Fluid Dynamics and Surface Pressure Fluctuations of Turbulent Boundary Layers Over Sparse Roughness

Nathaniel D. Varano

Dissertation submitted to the Faculty of the
Virginia Polytechnic Institute and State University
in partial fulfillment of the requirements for the degree of

Doctor of Philosophy
in
Aerospace Engineering

Roger L. Simpson, Chair
William J. Devenport
William H. Mason
Saad A. Ragab
Christopher J. Roy

January 29, 2010
Blacksburg, Virginia

Keywords: turbulence, boundary layer, surface pressure, roughness, laser Doppler velocimetry, skin friction

Fluid Dynamics and Surface Pressure Fluctuations of Turbulent Boundary Layers Over Sparse Roughness

Nathaniel D. Varano

(ABSTRACT)

Turbulent boundary layers over rough surfaces are a common, yet often overlooked, problem of practical engineering importance. Development of correlations between boundary layer parameters that can be used in turbulence models and the surface geometry is the only practical option for solving these problems. Experiments have been performed on a two-dimensional zero pressure gradient turbulent boundary layer over sparsely spaced hemispherical roughness elements of 2 mm diameter. Laser Doppler velocimetry was used to measure all three components of velocity. The friction velocity was calculated using an integral momentum balance. Comparisons were made with various fitting methods that assume the von Kármán constant is appropriate for rough walls. Results indicate that this is not the case, and that the slope of the semi-logarithmic portion of the mean streamwise profile may be a function of the ratio of inner and outer length scales. Comparisons were also made between various correlations that relate the surface geometry to the behavior of the mean velocity profile. In general, the existing correlations achieved a reasonable agreement with the data within the estimated uncertainties.

A detailed study of the local turbulent structure around the roughness elements was performed. It was found that, in contrast to 'sharper-edged' elements such as cylinders, an elevated region of TKE and Reynolds shear stress was found downstream of the element below the peak. This can be explained by the delay in separation of the flow coming over the top of the element due to the smooth curvature of the element.

Surface pressure fluctuation measurements were made as well using a dual microphone noise reduction technique. There have only been a few past experiments on the surface pressure fluctuations under rough wall boundary layers. However, it has been shown that the spectra of the wall fluctuations can be used to predict the far-field noise spectrum [1, 2]. Therefore it is been the goal of this research to verify existing correlations between the surface pressure fluctuation spectrum and the surface geometry as well as develop new correlations that provide insight into the interactions between the turbulent motions in the flow surface pressure.

Acknowledgments

I must first give thanks to The Lord for sustaining me throughout the process of obtaining this degree. I also thank my advisor, Prof. Roger Simpson, for his generous support and guidance. His presence in my life has taught me to be, not only a better researcher and engineer, but also a better person. Many thanks to Andrew Hopkins with whom I worked very closely on this research project. His contribution to this work has been invaluable. Dr. Todd Lowe has been an incredible source of knowledge and expertise over the years and I am grateful for his assistance, guidance, and patience. I thank also Joe Derlaga, Deirdre Hunter, Max Rusche, Gwibo Byun, Edgar Orsi, and the many others who have assisted me in this work at one time or another. I also thank the capable men in the AOE machine shop without whose skill I would not have accomplished this research. I also thank my PhD committee members for their guidance and patience. Finally, I offer a special thanks to my parents David and Lori who have selflessly supported me throughout my life and Cameron Burkholder who is my biggest fan.

Contents

Nomenclature

$\bar{\epsilon}$	Bias error
$\bar{f}$	Mean frequency of statistically converged number of bursts
$\bar{S}$	Value of the fringe spacing that corresponds to $\bar{f}$
δ	Boundary layer thickness
$\delta(\cdot)$	Denotes uncertainty in any quantity $(\cdot)$
ΔU^+	Roughness function
δx, δy, δz	Uncertainty in position
ϵ	Error in origin/Displacement height
ϵ_A	Error in computed window coefficient
$\epsilon_{\hat{t}}$	Error in computed peak time
$\frac{Df}{Dt}$	Signal chirp
γ	Coordinate along the beam pair bisector
γ_0	Location along beam pair bisector that corresponds to center of receiving volume
γ_w	Beam waist position along beam pair bisector
$\hat{b}$	Beam pair bisector unit vector
$\hat{e}$	Measurement direction unit vector
$\hat{f}$	Measure of frequency, fraction of half the non-dimensional sample rate
$\hat{m}$, $\hat{n}$	Beam unit vectors
$\hat{Q}$	Non-dimensional sample rate
$\hat{t}$	Non-dimensional time

$\hat{t}_p$ Non-dimensional burst peak time

κ von Kármán Constant

Λ Ratio of total volume over surface (to height k) to effective volume of roughness elements

λ Frontal surface area to planform area

λ Wavelength of light

$\{\Delta X\}$ Required change to the state vector from Newton's nonlinear method

$\{G\}$ System of nonlinear equations for Newton's method

$\{X\}$ State vector for Newton's nonlinear method

μ Dynamic viscosity

ν Kinematic viscosity

$\omega(t)$ Burst envelope

randn($\hat{t}$) Random number generator with normal distribution of mean zero and standard deviation one

$\overline{u^2}$, $\overline{v^2}$, $\overline{w^2}$ Reynolds normal stress components in streamwise, wall-normal, and spanwise directions respectively

$\overline{uv}$, $\overline{uw}$, $\overline{vw}$ Reynolds shearing stresses

ϕ Interior half angle of a beam pair

ρ Density

ρ_f Fluid density

ρ_p Seed particle density

σ Sample standard deviation

τ Time constant

τ_w Wall shear stress

$\vec{a}$ Acceleration

$\vec{U}$ Velocity vector

$\vec{x}(t)$ Position vector

$\vec{x}_?$ Unknown position within the measurement volume

$\vec{x}_r$ Reference position vector

$\vec{x}_V$ Center of intersection volume

$\vec{x}_{avg}$ Average position of particles trajectory within the measurement volume

a Half height of measurement volume

A, B, C Burst window coefficients

A_f Frontal area

A_p Plan form area, area of a roughness 'cell'

A_w Frontal wetted area

B Intercept constant in the law of the wall

b Dimensional intercept of semi-logarithmic region of mean velocity profile

b Element spanwise length

C_1 Simulated burst signal level

C_f Skin friction coefficient

C_n Time dependent noise level

C_o Time independent noise level

d pipe diameter

d_p Seed particle diameter

d_w Beam waist diameter

d_{fiber} Core diameter of fiber optic cable

d_{lens} Lens diameter

d_{meas} Measurement volume diameter

f Friction factor

f Measured frequency

$f(\cdot)$ Geometric roughness function

f_I	Image focal length (fiber side)
f_O	Object focal length (measurement volume side)
G	System of nonlinear equations
$g(y')$	Probability distribution of wall-normal crossing locations
H_{DS}	Downstream extent of roughness element separation region
J	Jacobian matrix
k	Roughness height
k_c	Characteristic roughness length scale
k_s	Equivalent sand grain roughness
l	Frequency spectral line number
l	Turbulence mixing length
M	Number of parameters in model equation used for curve fit
M	Number of simulations performed
m	Chirp spectral line number
m	Constant wall-normal velocity gradient in sublayer
m	Dimensional slope of semi-logarithmic region of mean velocity profile
m	Magnification factor
m	Simulation number
N	Number of points used in curve fit
N	Sample size
N	Total number of samples in discreet signal
$n(\hat{t})$	Simulated burst noise
NA	Numerical aperture
p	mean pressure
p_c	Coherent portion of surface pressure fluctuations

p_t	Turbulent portion of surface pressure fluctuations
p_∞	Freestream static pressure
P_{atm}	Atmospheric pressure
P_{dym}	Dynamic pressure
R	Ideal gas constant
R	hemisphere or cylinder radius
Re_d	Reynolds number based on pipe diameter
S	Fringe spacing
s	spacing between roughness elements in a 'cell'
$s(\hat{t})$	Simulated burst signal
s_k	Value of discreet signal at k^{th} sample number
S_{avg}	Average fringe spacing along particle trajectory
S_{est}	Estimate of the sample standard deviation
SD	Spectral density
T	Temperature
t	Time
$t_?$	Time when the particles passes through $\vec{x}_?$
t_a, t_b	Limits of integration for computation of S_{avg}
t_p	Peak time of a burst
t_r	Reference time
t_{95}	Student's correction for small sample size at a 95 percent level of confidence
U	Mean streamwise velocity component
U	Streamwise mean velocity component
U,V,W	Mean components of velocity
u,v,w	Fluctuating components of velocity

U',V',W' Instantaneous velocity components in tunnel coordinates

$U_\perp$ Velocity perpendicular to intersection volume fringes

U_e Edge velocity

U_p Velocity derived from pitot probe measurement

U_R Streamwise mean velocity component over a rough wall

U_S Streamwise mean velocity component over a smooth wall

u_τ Friction velocity

V Mean wall-normal velocity component

V_E Volume of roughness element

V_T Total volume of roughness elements and their wakes

x_r,y_r,z_r Reference position components

x_s Position of laser sheet (in main flow direction) within measurement volume

y Wall-normal coordinate

y' Coordinate with it origin at the geometric center of the measurement volume

Y_1 Some distance above the wall

y_d Encoder datum location

y_e Wall-normal position of the LDV measurement volume indicated by the encoder

y_s Distance from true wall location to geometric center of the measurement volume

TKE Turbulent kinetic energy

List of Figures

List of Tables

Chapter 1

Introduction

1.1 Motivation

Turbulent boundary layers over rough surfaces are a common occurrence, and the effect of a particular rough surface on the boundary layer is a practical engineering problem of great importance. Wear roughens the surfaces of turbomachinery blades, which affects drag and heat transfer rates [4]. The accretion of ice on an airplane wing affects boundary layer separation and can lead to stall [5]. Fouling in pipes [6] and biofouling on ship hulls [7] have been engineering problems since the eighteenth century [8]. The additional fuel needed to overcome the increased drag due to biofouling on ships is estimated to cost millions of dollars each year [9]. The modification of the atmospheric boundary layer by landscape and urban roughness is also a problem of interest. Increasingly, buildings and bridges are being designed with wind climate and air quality in mind [10, 11]. Generally, a rough surface causes an increase in skin friction compared with a smooth surface. However, certain carefully designed rough surfaces can actually reduce the skin friction below that of a smooth wall by as much as eight percent [12]. More recently, the noise generated by rough surfaces on submarines has become of interest to the navy. Indeed, this work has been funded through the Hydroacoustics Group of the Office of Naval Research.

All research on boundary layers over rough surfaces has the same broad goal: To attain the ability to predict quantitatively how the boundary layer will be affected by a rough surface of arbitrary geometry. The scale of the roughness geometry is generally very small compared with the boundary layer thickness. Therefore, numerical solutions to practical problems that attempt to resolve the rough surface in detail are impossibly expensive [13]. Thus, this goal is only practically achieved when any arbitrary rough surface can be characterized by a finite set of parameters that capture the global effect of the roughness on the boundary layer through experimentally determined correlations. These correlations might be for direct estimates of boundary layer quantities of interest such as the skin friction coefficient or boundary layer thickness. However, it is more likely that these correlations must be incorporated into turbulence models that are used to close the Reynolds averaged Navier-Stokes (RANS)

equations.

1.2 Previous Research

1.2.1 Rough-Flow Regimes

In his seminal 1933 experiments, Nikuradse [6] studied the effect of sandgrain roughness on the resistance of fully developed pipe flow. He discovered three rough-flow regimes: hydraulically smooth, fully rough, and transitionally rough. Each regime depends on the relative height of the roughness elements to the sublayer height. If the roughness elements are small compared with the viscous sublayer height, viscous drag is dominant and the surface-flow interaction is considered hydraulically smooth. If the roughness elements are large compared to the sublayer height, the form drag on the elements is dominant and the surface-flow interaction is considered fully rough. In the fully rough regime, Nikuradse found that the skin friction coefficient (C_f) becomes independent of the bulk velocity (or edge velocity for external boundary layers, U_e). The skin friction coefficient can be written in terms of the friction velocity, ($u_\tau \equiv \sqrt{\tau_w/\rho}$).

$$C_f \equiv \frac{\tau_w}{1/2\rho U_e^2} = 2\left(\frac{u_\tau}{U_e}\right)^2 \tag{1.2.1}$$

The surface-flow interaction is considered transitionally rough when the size of the roughness elements are on the same order as the sublayer height. In this regime, both viscous drag and form drag contribute to the total drag on the surface.

In his 1954 paper [14], Hama points out that the surface-flow interaction regimes depend on downstream location. For external boundary layers, the sublayer height increases with downstream location. This means that for a given roughness geometry and edge velocity, the surface-flow interaction will change from fully rough to transitionally rough to hydrodynamically smooth as the boundary layer evolves downstream. This is not true for fully developed interior flows, such as Nikuradse's pipe flow experiments, where the boundary layer is self-similar and no longer a function of downstream location. This simple yet important difference is often overlooked in the literature, and has contributed to some confusion on the topic of outer-layer similarity (discussed in section 1.2.4).

Jiménez emphasizes another important rough-flow regime in his 2004 review paper [15]. If the roughness height extends well into the boundary layer, the semi-log region can be significantly modified due to the presence of the roughness. In this regime it is possible that the boundary layer is modified to such an extent that the it behaves like flow around surface mounted obstacles. Jiménez states this regime is established when the ratio of boundary layer thickness to roughness height (δ/k) is less than 40, but that its effects may be present for $\delta/k < 80$.

1.2.2 Turbulence Structure

If a surface contains elements that are spaced at sufficiently large distances, the total drag on the surface is a linear combination of the increased drag due to each element. This is a case of 'single' or 'isolated' elements. George [16] and Bennington [17] both conducted experiments on single 3-D elements. They found that a horseshoe vortex is formed in front of each element. The ensuing trailing vorticies cause a downwash of fluid downstream of the element that increases the local skin friction. The element wakes extend tens of element diameters downstream. This flow behavior is contrasted by the flow around patches of elements (called fetches) that are spaced closely enough for their wakes to interact with the flow around elements further downstream. In this case, the total drag is not simply a linear combination of drag due to similarly shaped isolated elements.

The flow structure due to the latter rough surface described above can be broken down further into two broad categories. When Nikuradse [6] conducted his pipe flow experiments, he discovered that the value of the skin friction coefficient in the fully rough regime could be scaled on the ratio of the roughness length scale (usually denoted by k) to pipe diameter (d). However, there were some cases for which the k/d scaling did not work. Perry *et al.* [18] pointed out that these cases scaled on the pipe diameter alone, and coined the names 'k-type' and 'd-type' roughness. For d-type roughness the spacing between individual elements was so small that low momentum fluid becomes trapped in recirculation regions in the cavities between the elements (although ejections do still occur occasionally). In this case the height of the elements is no longer an important parameter.

Riblets are another type of rough surface distinct from k- or d-type roughness. Surfaces of this type are usually comprised of streamwise grooves that are sufficiently small to disrupt the formation of turbulent eddies near the wall. This disruption can lead to drag reduction and some researchers have attempted to reach an optimal design. Bechert *et al.* [12] claims to have achieved an 8.2% reduction in drag compared to a smooth wall.

There is a fundamental difference in the flow structure caused by 2-D and 3-D roughness elements. Bandyopadhyay and Watson [19] indicate a primary difference is the direction of the near-wall transport of shear-stress, which is outward from the wall for flow over 2-D roughness elements. George [16] made extensive measurements of the flow structure for k-type 3-D roughness. His measurements reveal that the flow separates and reattaches downstream of each element. Low momentum fluid is aspirated upwards directly behind the element. This leads to a collision of high and low momentum fluid that results in elevated levels of turbulent kinetic energy (TKE) production downstream of the element peak. (Figure 1.1).

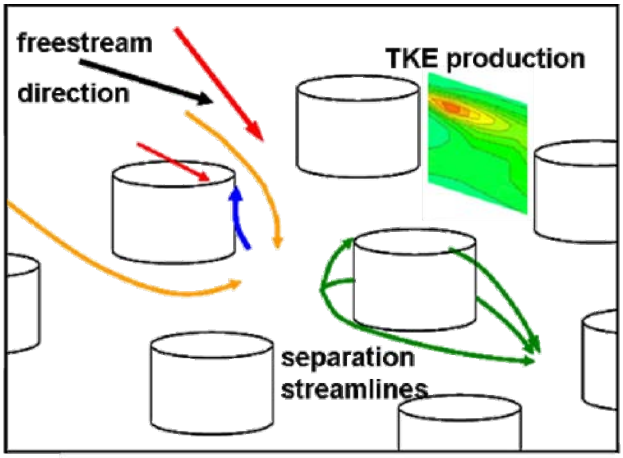

Figure 1.1: Turbulent Structure over k-type 3-D Roughness

1.2.3 Effect of Roughness on the Mean Flow

The most prevalent effect of surface roughness on the boundary layer is a downward shift in the semi-log region of the normalized mean velocity profile (normalized on u_τ and the kinematic viscosity ν). This downward shift was first described by Prandtl [20] in 1933. However, in 1954 Clauser [21] represented this downward shift in what has become the most commonly used form, ΔU^+.

$$\frac{U}{u_\tau} = \frac{1}{\kappa} \ln \left[\frac{(y+\epsilon)u_\tau}{\nu} \right] + B - \Delta U^+ \tag{1.2.2}$$

The coefficients κ and B are usually assumed to be invariant for smooth and rough walls. However, the validity of this assumption is called into question by several researchers [22, 23, 24, 25]. Furthermore, κ is known to be a function of Reynolds number for low values ($\mathrm{Re}_\theta < 6000$) [26].

Another effect of surface roughness is to cause a displacement of the mean streamlines away from the wall due to the presence of the roughness elements and their wakes. This effect can be accounted for by including a constant wall-normal shift (ϵ) or 'displacement height' in equation 1.2.2. Figure 1.3 shows how ϵ is incorporated into the law of the wall for rough walls. Essentially, it is assumed that the semilogarithmic portion of the normalized mean velocity profile for a rough wall (U_R^+) at any height above the wall (y^+) is equal to the normalized profile for a smooth wall (U_S^+) at a height of ($y^+ + \epsilon^+$) minus the roughness function (ΔU^+).

$$U_R^+(y^+) = U_S^+(y^+ + \epsilon^+) - \Delta U^+. \tag{1.2.3}$$

The '+' superscript indicates normalization on u_τ and ν. It is noteworthy that $U_R^+(y^+ - \epsilon^+) = U_S^+(y^+) - \Delta U^+$ is also valid though less practical.

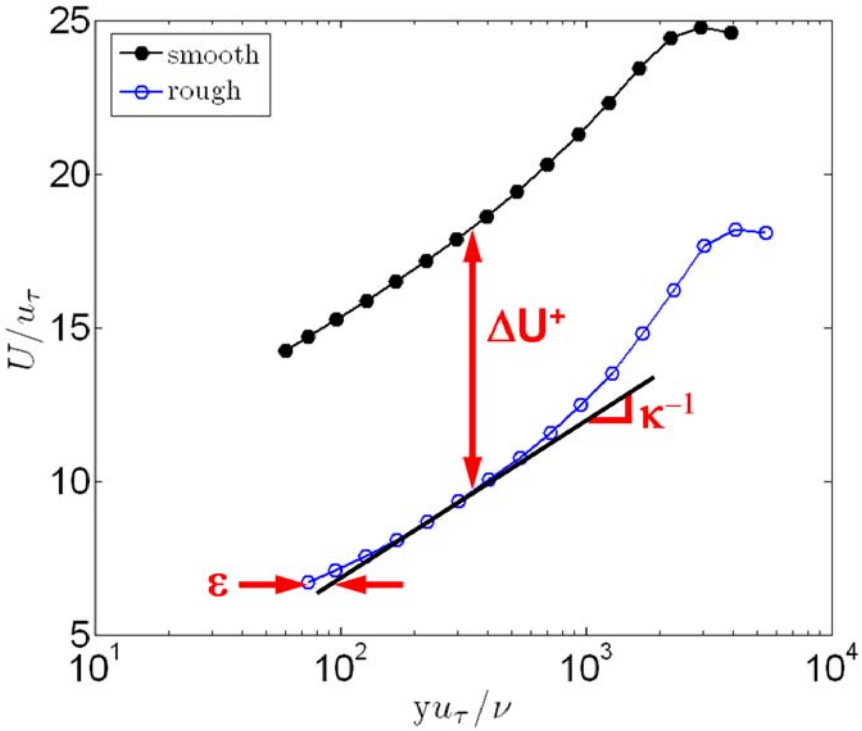

Figure 1.2: Effect of a Rough Surface on the Mean Flow

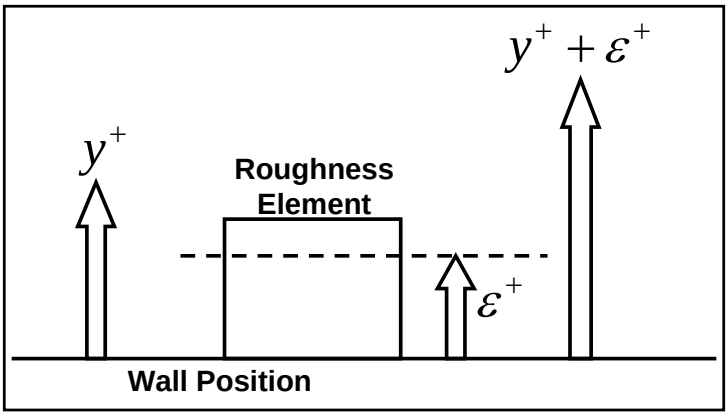

Figure 1.3: Explanation of ϵ parameter

1.2.4 Outer Layer Similarity

Townsend [27] derived his 'attached-eddy hypothesis' for fully developed channel flow. It was interpreted by Perry and Abell [28] to mean that the sole effect of roughness on the boundary layer is to modify the wall stress but leave the rest of the boundary layer unaffected (at high Reynolds number). This is known as outer layer similarity and does not apply near the wall (on the order of the roughness heights) where the presence of each element will significantly modify the local flow.

There are a number of researchers who support [29, 30, 31] and refute [32, 33, 34, 35, 36] Townsend's hypothesis as interpreted by Perry and Abell. Interestingly, those who support it base their conclusions on experiments or numerical simulations of fully developed interior flows. Those who refute it tend to use external boundary layers in their evidence. Bakken *et al.* [37] suggests a fundamental difference between fully developed interior flows and external turbulent boundary layers that may make outer layer similarity more likely for fully developed flow. In fact, Townsend himself suggests this fact in his original theory due to the self-similarity of pipe and channel flow while external boundary layer are only approximately self-similar.

1.2.5 Modeling Roughness

Originally, the increased resistance in pipes due to roughness was modeled directly by experimentally correlating the friction factor (f) with the Reynolds number based on pipe diameter (Re_d) and a characteristic roughness scale k_c. Moody [38] compiled the work of several researchers to form the now famous Moody diagram. His diagram contains correlations for the smooth, transitionally rough, and fully rough regimes.

For external boundary layers, the most common approach for modeling the effect of roughness is to assume a form for ΔU^+ in equation 1.2.2.

$$\Delta U^+ = \frac{1}{\kappa} \ln \frac{k_c u_\tau}{\nu} + f(\cdot) \tag{1.2.4}$$

The assumed form of the roughness function ΔU^+ in equation 1.2.4 will remove all dependence on the viscosity when substituted into equation 1.2.2. Therefore, this form of the ΔU^+ requires the flow to be fully rough to be valid. The value of k_c is usually taken to be the roughness element height k. The function $f(\cdot)$ is only a function of the surface geometry.

Early experiments by Schlichting [39] revealed that the spacing as well as the height of the elements affects the boundary layer. He found that the ratio of element frontal area to the planform area (λ) was an important parameter for scaling his results. Later, other researchers [40, 41, 42] confirmed that $f(\cdot)$ is a strong function of λ. Two clear regions emerged from their analysis indicating a dense and sparse type spacing of roughness. Bettermann [40]

and Dvorak [41] proposed correlations for $f(\cdot)$ for densely and sparsely spaced rough surfaces respectively. Their correlations were functions of the element streamwise width and the element spacing. Simpson [43] modified their correlations to be only functions of λ.

$$f(\lambda) = 12.24 \ln \lambda^{-1} - 17.35 \,, \;\; \lambda^{-1} < 5 \tag{1.2.5}$$

$$f(\lambda) = -2.85 \ln \lambda^{-1} + 5.95 \,, \;\; \lambda^{-1} > 5 \tag{1.2.6}$$

Later, Waigh and Kind [42] included additional parameters in their correlation but found them to only weakly influence $f(\cdot)$. The ratio of element frontal wetted area to element frontal area is denoted by A_w/A_f, and the ratio of element height to width is denoted by k/b. They also conclude that λ alone is not a good discriminator between the densely and sparsely spaced regimes. Instead they used the ratio of the total volume over the surface (to height k) to effective volume of roughness elements, Λ.[1]

$$f(\lambda, k/b, A_w/A_f) = 4.586 \ln \lambda^{-1} (k/b)^{0.87} (A_w/A_f)^{0.44} - 7.59 \,, \;\; \Lambda < 6 \tag{1.2.7}$$

$$f(\lambda, k/b, A_w/A_f) = -2.50 \ln \lambda^{-1} (k/b)^{0.55} (A_w/A_f)^{1.38} + 5.78 \,, \;\; \Lambda > 6 \tag{1.2.8}$$

Moore [24] was the first to discover the effect of the displacement height and he assumed $\epsilon \approx 2/3k$. Jackson (1981) states that ϵ is the height at which the mean drag on the surface appears to act [44]. However, this quantity is challenging to estimate *a priori*. Stewart [45] used the volume of the roughness elements and their wakes to estimate ϵ and achieved reasonable results. He used the roughness element volume (V_E) and the upstream and downstream separation regions to compute the total displacement volume V_T. He modeled the separation regions as half cone shapes that extend upstream by the element height k and downstream by some value H_{DS} determined from measurement. The displacement height is then computed as the volume of displaced fluid over the planform area A_p. For discreet regularly spaced roughness the result is equation 1.2.9.

$$\epsilon = V_T/A_p = 1/A_p \left(1/6\pi k^3 + V_E + 1/6\pi k^2 H_{DS} \right) \tag{1.2.9}$$

1.2.6 Measuring Skin Friction

Any attempt to develop or validate models of boundary layer over rough surfaces will rely on an accurate measure of the skin friction. There are two general categories found

[1] Values for A_p appear to be computed incorrectly (SEE fig.(1) in reference [42]).

in the literature for measuring the skin friction: fitting methods and independent methods. Fitting methods require making assumptions about the boundary layer profile. Independent methods make no such assumptions, but are generally more challenging to perform.

Independent Methods

Independent methods can be broadly categorized by whether or not they require velocity profile measurements (other than the freestream speed). The most common methods that do not require such measurements include measuring the pressure drop in fully developed pipe or channel flow [37, 46, 47, 31, 6, 48], using a mechanical force balance [49, 50, 51, 12, 52, 53], or embedding pressure taps directly in roughness elements [54, 11, 55, 18]. All these methods suffer from various challenges. Embedding pressure taps in roughness elements can only measure the form drag on specific elements and requires large 2-D elements. Force balances are usually too large to give local skin friction values and become increasingly difficult to use as they are made smaller in size. Relating the pressure drop and pipe diameter (d) to the wall shear stress (τ_w) via equation 1.2.10 is probably the most robust method, but requires a fully developed interior flow.

$$\tau_w = \frac{d}{4}\frac{dp}{dx} \tag{1.2.10}$$

Independent methods that require velocity profile measurements to compute the skin friction all use some form of the momentum integral equation. The most rigorous form found in the literature is used by Brzek *et al.* [56]. It is important to note that C_f represents the total drag on the surface and includes form drag on the elements.

$$\begin{aligned}\frac{C_f}{2} =& -\frac{1}{U_e^2}\frac{\partial}{\partial x}\int_0^{Y_1} U^2 dy + \frac{U(Y_1)}{U_e^2}\frac{\partial}{\partial x}\int_0^{Y_1} U dy - \frac{1}{U_e^2}\frac{\partial}{\partial x}\int_0^{Y_1} \overline{u^2} - \overline{v^2} dy \\ & - \frac{1}{U_e^2}\left(\overline{uv} - \nu\frac{\partial U}{\partial y}\right)\Bigg|_{Y_1} + \frac{1}{U_e}\frac{dU_e}{dx}Y_1\end{aligned} \tag{1.2.11}$$

Equation 1.2.11 can be derived by applying the principle of conservation of momentum to a control volume in a 2-D boundary layer. It is assumed that the control volume is positioned in a plane of symmetry such that the total spanwise flux of streamwise momentum into the control volume is negligible. The streamwise viscous term is also assumed to be negligible. The integrals are evaluated from the wall to some arbitrary distance above the wall Y_1. The mean streamwise velocity is denoted by U. The Reynolds normal stresses are denoted by $\overline{u^2}$ and $\overline{v^2}$. The Reynolds shear stress $\overline{uv}$ and the viscous stress term are evaluated at $y = Y_1$. Integrating the continuity equation with respect to y (equation 1.2.12) provides a way to remove the mean wall-normal velocity component V from the second term of equation 1.2.11.

$$V = -\frac{\partial}{\partial x}\int_0^{Y_1} U dy \tag{1.2.12}$$

The quantity $\overline{v^2}$ enters into equation 1.2.11 via the differential form of the y-momentum equation in order to account for the variation of the mean pressure with distance from the wall. All terms in the y-momentum equation are considered negligible except $\overline{v^2}$ and the pressure gradient term. Integrating the y-momentum equation with respect to y gives equation 1.2.13.

$$p(y) = p_\infty - \rho\overline{v^2} \tag{1.2.13}$$

The final term of equation 1.2.11 is formed by differentiating Bernoulli's equation with respect to x (equation 1.2.14).

$$\frac{1}{\rho}\frac{p_\infty}{dx} = -U_e\frac{dU_e}{dx} \tag{1.2.14}$$

Past researchers used various forms of equation 1.2.11. If the integrals are evaluated from the wall to the boundary layer thickness (δ), equation 1.2.15 is the result. This form is written in terms of the displacement thickness δ^* and the momentum thickness θ.

$$\frac{C_f}{2} = \frac{d\theta}{dx} - \frac{1}{U_e^2}\frac{\partial}{\partial x}\int_0^\delta (\overline{u^2} - \overline{v^2})dy + [2\theta + \delta^*]\frac{1}{U_e}\frac{dU_e}{dx} \tag{1.2.15}$$

$$\delta^* \equiv \int_0^\delta (1 - \frac{U}{U_e})dy \tag{1.2.16}$$

$$\theta \equiv \int_0^\delta \frac{U}{U_e}(1 - \frac{U}{U_e})dy \tag{1.2.17}$$

Frequently in the literature, the normal stress term in equation 1.2.15 are assumed negligible. Then, for a zero pressure gradient the skin friction coefficient can be written simply as equation 1.2.18.

$$\frac{C_f}{2} = \frac{d\theta}{dx} \tag{1.2.18}$$

Another common approach is to assume that all x-derivative terms in equation 1.2.11 are negligible and evaluate the remaining Reynolds stress and viscous stress terms in the constant shear stress region of the boundary layer. Brzek *et al.* [56] found that the Reynolds shear stress can contain up to 96-98% of the total wall shear in this region, so often the viscous stress is also assumed negligle. This approach 'extrapolates' the stress in this region to the wall and is hence termed the 'stress extrapolation' method.

Fitting Methods

Fitting methods involve measuring a boundary layer profile and optimizing the value for the friction velocity (u_τ) and some parameters such that a normalized profile will have a predefined shape. Fitting methods always suffer from having to make assumptions about the shape of the boundary layer profile. Clauser [21] was the first to utilize this type of method. He fit the slope of the semi-logarithmic region of the mean streamwise profile to canonical law-of-the-wall. His method was extended to find ΔU^+ and ϵ as well. Hama [14] suggested the use of the velocity defect law, which he broke into two parts (equation 1.2.19). The velocity defect law does not contain ΔU^+, and therefore reduces the number of unknowns to u_τ and ϵ. His method assumes a constant smooth wall value for the strength of the wake.

$$U_e^+ - U^+ = \begin{cases} -\frac{1}{\kappa}\ln\left(\frac{(y+\epsilon)u_\tau}{\delta^* U_e}\right) - 0.6 & \frac{y+\epsilon}{\delta} < 0.15 \\ 9.6\left[1-\frac{y+\epsilon}{\delta}\right] & \frac{y+\epsilon}{\delta} \geq 0.15 \end{cases} \tag{1.2.19}$$

Krogstad et al. (1992) developed the most commonly used fit method to allow for a variable wake strength [57] (Π) in the velocity defect law. A least squares approach is used to optimize values of u_τ, ϵ, and Π in equation 1.2.20.

$$\frac{U}{U_e} = 1 + \frac{u_\tau}{\kappa U_e}\left\{\ln\left(\frac{y+\epsilon}{\delta}\right) - (1+6\Pi)\left[1-\left(\frac{y+\epsilon}{\delta}\right)^2\right] + (1+4\Pi)\left[1-\left(\frac{y+\epsilon}{\delta}\right)^3\right]\right\} \tag{1.2.20}$$

1.2.7 Surface Pressure Fluctuations

Interest in surface pressure fluctuations (SPF) is due primarily to their relationship to the far-field acoustic noise generated when a boundary layer flows over a rough surface. Recently, Glegg and Devenport [1], starting from Lighthill's analogy, rigorously show that the far-field noise spectrum is a function of the surface pressure spectrum and the roughness geometry. Their analysis is limited to homogeneously distributed SPF and roughness elements that do not extend beyond the semilogarithmic layer. Their finding was experimentally confirmed by Smith *et al.* [2] in a wall jet facility. While these findings are impressive, the challenge to predict the surface pressure spectrum still remains. If SPF spectra can be modeled as a function of boundary layer parameters, predictable turbulent statistics, and the roughness geometry then it follows that far-field noise predictions can be made as well.

The review of Goody and Simpson [58], show that spectra of smooth wall SPF collapse at high frequencies when scaled on inner boundary layer variables (ν/u_τ, u_τ, and τ_w). The spectra decay as ω^{-5} in this high frequency range. In the low frequency region they found little collapse could be achieved with a range of outer variables (δ, δ^*, u_τ, U_e, τ_w, and $1/2\rho U_e^2$). Good collapse was achieved in the mid-frequency range when scaled on τ_w regardless of the

time scale used. However, the slope of this region was found to be between -0.7 and -0.8. This is lower than the theoretical value of -1, derived from dimensional analysis in the overlap region.

Previous scaling efforts to relate the SPF spectrum for a rough surface to the geometry date back to the early 1970's. Blake [59] measured the SPF for turbulent boundary layers over surfaces roughened by sand grains in sparse and dense configurations. He suggests that the high frequency spectra scales on the mean roughness height ($\bar{k}$) and the friction velocity (u_τ) while the smooth wall scaling still holds for the low frequency region.

$$\Phi(\omega) = \frac{\tau_w^2 \bar{k}}{u_\tau} G_1\left(\frac{\omega \bar{k}}{u_\tau}\right) \tag{1.2.21}$$

$$\Phi(\omega) = \rho^2 U_e^3 \delta^* G_2\left(\frac{\omega \delta^*}{U_e}\right) \tag{1.2.22}$$

Blake also claimed that $2\sqrt{\overline{p^2}}/\rho U_e^2 \cong 3.4 C_f$ for rough and smooth wall flows. His conclusions might be tainted however, by the small ratio of δ/k for his measurements.

Experiments by Aupperle and Lambert [60] were also of boundary layers over sand grain roughened surfaces. Again, δ/k values were small. They concluded that the SPF spectrum should be scaled on the skin friction coefficient and the equivalent sandgrain roughness k_s, which can be related to ΔU^+ via equation 1.2.24.

$$\Phi(\omega) = \frac{C_f \tau_w^2 k_s}{u_\tau} G\left(\frac{\omega k_s}{u_\tau}\right) \tag{1.2.23}$$

$$\Delta U^+ = 1/\kappa \ln(k_s u_\tau/\nu) - 3.5 \tag{1.2.24}$$

More recently Smith [61] conducted experiments in a wall jet facility. He found that the above scaling only achieve decent collapse in the overlap region when the surface-flow interaction is in the fully rough regime. He also suggested the following empirical correlation.

$$\Phi(\omega) = \frac{(k^+)^{1.325} k_s \tau_w^2 C_f Re_\delta^{0.5}}{u_\tau} G\left(\frac{\omega k_s}{(k^+)^{0.825} u_\tau}\right) \tag{1.2.25}$$

Finally, Alexander [62] measured SPF over discreet hemispherical roughness of 1 mm and 3 mm heights. He found that the scaling method of Glegg and Devenport [1] was successful for the 1 mm case. However, the local flow around the 3 mm hemispheres caused the SPF spectrum to be a function of position and hence not homogeneous. Therefore, a collapse was not achieved.

1.3 Scope and Aim of this Research

As explained previously, there are many different flow regimes and categories for which the boundary layer behaves in a fundamentally distinct way. Therefore, it is important to be specific when deciding the scope of an experiment so that the results are interpreted correctly. The scope of this research is limited to two-dimensional zero pressure gradient turbulent boundary layer over three-dimensional, k-type, sparse, fully described roughness elements in the fully rough regime with sufficiently large δ/k values.

When considering the sheer number of roughness related experiments that have been performed over the past century or more, it is easy to assume that producing new and relevant contributions to the field is unlikely. However, upon closer inspection one finds that many researchers are attempting to solve complicated problems relating to boundary layers over surface roughness, while the simplest problems are still not completely understood. A review of past experiments was conducted to determine what work has already been done within the limited scope proposed. Of the 72 experiments reviewed, table 1.1 lists the only three that met the criteria listed above and contained sufficient information in their publications to extract skin friction measurements and velocity profiles. A review of 72 experiments is by no means an exhaustive review, but it is certainly representative of the bulk of the work published on this topic. The complete list of experiments reviewed is given in appendix A.

Given the limited amount of data available, the aim of this research is to make measurements of the mean velocity, turbulent statistics, and fluctuating wall pressure and correlate the results of these measurements with the rough surface geometry. Specifically, to understand the effect element spacing has on the mean velocity profile and the surface pressure spectrum. Another goal of this research to determine a simple and accurate way of measuring the skin friction. Specifically, to determine if fitting methods are correct. This also implies that a goal of this research is to verify that the von Kármán constant is appropriate for rough wall boundary layers. Given the extent to which κ is assumed constant in the literature, this is a particularly relevant issue. It is also a goal to contribute to the limited amount of data available to verify existing models for the mean flow and surface pressure spectrum.

Reference	Geometry	δ/k	λ^{-1}
George [63, 16]	Cylinders	40 - 134	10, 20, 40
Kerevanian [64]	Cylinders	13 - 55	7 - 95
Stewart [45]	Gaussian spikes, Cylinders	17 - 111	10 - 110

Table 1.1: List of previous experiments that are within the scope of the present research

Chapter 2

Instrumentation

2.1 Laser Doppler Velocimetry

2.1.1 Principles of LDV

The primary advantage of Laser Doppler Velocimetry (LDV) is its ability to make measurements without obstructing the flow. The principle of Differential LDV is based on the Doppler shifting of two intersecting beams of coherent light. This region of intersection is called the intersection volume. When a seed particle passes through the intersection volume the Doppler shifted scattered light will constructively and destructively interfere on a square law detector to form a signal of high and low intensity at a much lower and measurable frequency than the Doppler frequency. This frequency is directly related to the velocity of the seed particle ($\vec{U}$).

A more practical approach to understanding LDV is to model the Doppler shift effect as if there were real fringes formed in space by the interference of the two beams of coherent light. The light scattered by a seed particle creates a signal with a frequency determined by the distance between these fringes S and the velocity of the particle. This scattered light is collected by optical components focused at a region within the intersection volume. This region is called a receiving volume. The presence of both an intersection volume and a receiving volume is called a measurement volume. The measured intensity of the scattered light is referred to as a burst signal. The frequency f of the burst signal is directly related to the particle's velocity component in the measurement direction $\hat{e}$. The measurement direction is perpendicular to the fringes.

$$\vec{U} \cdot \hat{e} = fS \tag{2.1.1}$$

Although Miles [65] derived an analytical expression for the fringe spacing S as a function of the beam crossing geometry, a calibration is preferred due to the uncertainty in the beam

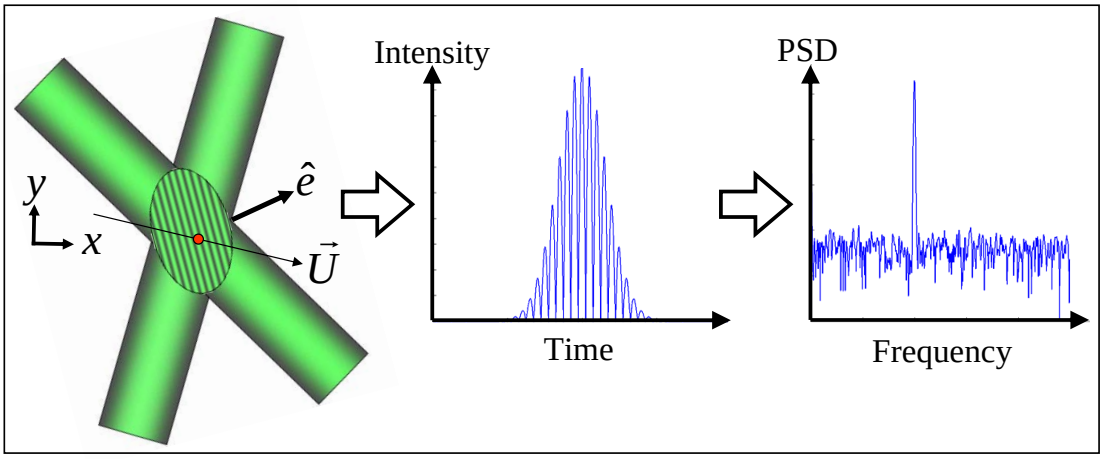

Figure 2.1: Velocity Measurement

waist diameters. A calibration is performed simply enough by measuring the mean frequency of a statistically converged number of bursts $\bar{f}$ in a known velocity field. Equation 2.1.2 can be used to solve for S.

$$S = \frac{\vec{U} \cdot \hat{e}}{\bar{f}} \tag{2.1.2}$$

The measured velocity of interest is not that of the seed particle, but rather of the flow. Deviation of the seed particle velocity from the flow velocity can be modeled as a first order system [66], where the time constant τ is a function of the particle and fluid densities (ρ_p and ρ_f respectively), the fluid viscosity μ, and the particle diameter d_p. If τ is less than the Kolmogorov time scale, the particle will follow the flow well.

$$\tau = \frac{d_p^2(\rho_p + \frac{1}{2}\rho_f)}{18\mu} \tag{2.1.3}$$

Equation 2.1.3 indicates that, in general, smaller particles have shorter time constants. However, a larger seed particle will scatter more light [67, 68] and hence give a stronger burst signal. Therefore the optimal seed particle should be as large as possible, but still small enough so τ is less than the Kolmogorov time scale.

To measure all three velocity components, three pairs of overlapping fringes are required. This results in a linear set of three equations.

$$\vec{U} \cdot \hat{e}_i = f_i S_i \ , \quad i = 1, 2, 3 \tag{2.1.4}$$

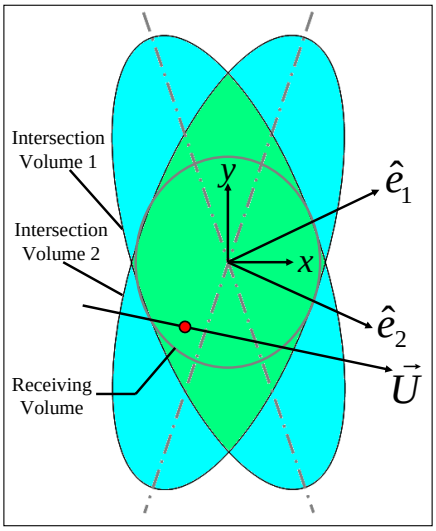

Figure 2.2: An example of two overlapping intersection volumes and a receiving volume

The subscript i refers to each set of fringes. It does not infer summation notation. The orientation of the three overlapping beam pairs must be chosen such that the measurement direction matrix $\hat{e}$ is not singular. An independent calibration can be performed for each S_i as explained for one component systems previously.

2.1.2 LDV Apparatus

Two LDV systems were used in this research, but the majority of measurements were made with the 'Long System'. The Long System is a subsystem of the probe designed by Dr. Semih Ölçmen [69] and used by Dr. Jacob George [16]. Several modifications were made to the probe for this research. The Comprehensive LDV (CompLDV) was the second system used in this research. It was developed by Dr. K. T. Lowe [70, 71], and is designed to measure all components of particle velocity, position, and acceleration. Only the Long System is described here, but details concerning the CompLDV can be found in section B.2.

The Long System

LDV systems are comprised of four basic components: the optical table, the probe, the receiving table, and A/D conversion. An optical table is used to condition the beams before sending them, via optical fibers, to the probe. The probe focuses the beams to create the measurement volume and collect the scattered light signal. The receiving table converts the light signal into an electrical signal. The analog electrical signals are then converted to digital signals for processing. The traverse mechanism and seeding apparatus are also described below.

The Long System uses two 5 W Argon-Ion lasers (Coherent Innova I90 C-5). Only the green (514.5 nm) beams are used from each laser. One beam is split using a 60 MHz Bragg cell. The other is split with an 80 MHz Bragg cell. The unshifted beam of that pair is split again with a 40 MHz Bragg cell. The Bragg cell power supplies are adjusted to ensure all three beams (unshifted, 80 MHz and 60 MHz shifted) have equal power. Each of the five beams are focused into a 4 μm diameter polarization preserving fiber optic cable (Corning Alcoa-Fujikura SM8-P-4/125-ST/NY-9000) via a Newport Single-Mode Fiber Coupler. The fiber optic cables carry the light from the optical table to the probe.

Several modifications were made to the Long System probe for this research. The probe includes two transmitting heads, comprised of five 6 mm focal length plano-convex lenses and two 88.3 mm focal length plano-convex lenses. Two Parker Automation linear stages were added under each head to allow for precise adjustment in the two directions parallel to the tunnel floor. The linear stages in the original design were retained to allow for adjustment in the vertical direction as well. The receiving lens assembly was completely redesigned to increase the amount of scattered light that is detected. Two Thor Labs achromat lenses of 2 inch diameter were used. The receiving fiber with a 62.5 μm core diameter and the 50 μm estimated measurement volume diameter results in a desired magnification factor of 1.25 via equation 2.1.5. In order to ensure proper access to the wind tunnel the first lens has a focal length (f_O) of 200 mm. The second lens must therefore have a focal length (f_I) of 250 mm to achieve the desired magnification factor via equation 2.1.5. However, the diameter of the second lens d_{lens} and f_I result in a numerical aperture of 0.10 via equation 2.1.6. This is smaller than the numerical aperture of the receiving fiber (0.27) and means the amount of collectible light from the measurement volume is not maximized. To achieve optimal collection for these values of f_O and f_I greater lens diameters are required.

$$m = \frac{d_{fiber}}{d_{meas}} = \frac{f_I}{f_O} \tag{2.1.5}$$

$$NA = \frac{d_{lens}/2}{\sqrt{f_I^2 + (d_{lens}/2)^2}} \tag{2.1.6}$$

Once the modifications to the Long System were completed the measurement volume size was roughly estimated from measurements. The streamwise and spanwise size of the measurement volume were computed by measuring the mean burst window size in the wind tunnel freestream. The vertical length of the measurement volume was computed similarly, but using a jet flow directed downward perpendicular to the tunnel flow. The effective dimensions of the measurement volume were found to be approximately 80 μm in the streamwise and spanwise directions and 405 μm in the wall normal direction.

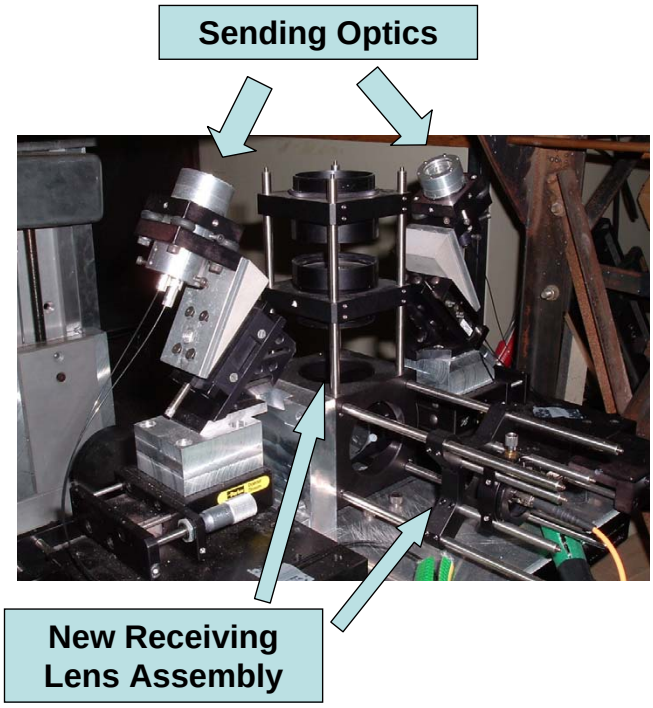

Figure 2.3: LDV probe with new receiving lens assembly

The receiving fiber carries the collected light to the receiving table where the light signal is converted to a voltage signal. An interference narrow bandpass filter is used to prevent unwanted contamination of the light signal by extraneous wavelengths. After passing through the interference filter, the light passes into a photomultiplier tube (PMT), where the light is converted into an electrical current. The PMT is powered by Brandenburg model 477 power supplies. A Sonoma Instrument model 315 amplifier is used to convert and amplify the current signal from the PMTs to a voltage signal. The signal from the PMT is extremely weak and so electronic noise interference is a serious issue. Special care is taken to shield the cables that transport the signals to the amplifiers. The analog signal is lowpass filtered with a cut-off frequency of 100 MHz to remove any aliasing that might otherwise occur. The signal is also highpass filtered with a cut-off frequency of 5 MHz.

Data acquisition is managed on a standard PC. An 8 bit Strategic Test board (model UF.258) samples at 250 megasamples/second (MS/s). There are two modes of data acquisition: continuous sampling and triggered sampling. At this sample rate, continuous sampling can be maintained for 0.54 seconds before the on-board RAM must write to disk storage. Continous sampling achieves the highest burst data rate (shortest time between recorded bursts), because the card waits to write data to storage until its onboard memory is full. However, continuous sampling results in a greater information density and a vastly greater amount of storage per burst is required. Triggered sampling means that only bursts signals that reach a specified voltage level are written to file. A National Instruments 5112 board (NI) is used to record the time of each burst. This is achieved by sending the 'trigger out' signal from the Strategic Test board directly into the 'trigger in' channel of the NI board. For this research triggered sampling was used exclusively.

Traverse

The LDV traverse mechanism is an important part of the overall design. It must be able to move the entire weight of the LDV probe (approximately 25 lbs) with minimal vibration. It should also be precise to a fraction of a millimeter, especially for the wall normal direction where precision on the order of microns is needed. The range of the traverse should be five to six inches in all three directions.

The previous traverse system was design for an LDV that required a large platform. Hence, the design incorporated several quarter inch aluminum plates (30x42 inches). Although a large platform was no longer need, this traverse system was used with the current LDV probe. However, during operation this design suffered from vibrations that contributed to misalignment of the LDV. These vibrations were due to the lack of stiffness of the aluminum plates. A new traverse system was designed to remove the aluminum plates and increase the stability of the entire system, while using many of the components of the previous system.

The primary components of the traverse are three BiSlide Positioning Slides from Velmex Inc. Each is capable of 300 lb static loads and can withstand a maximum 500 lb-in cantilever load with only a 0.0055 degree deflection. The Positioning Slides have a resolution of 0.005±0.0025 mm and are driven by Slo-Syn stepper motors (type M092-FD-447). All three are electronically controlled by a Velmex Inc VP9000 Controller. For increased precision, the vertical component is also measured using an Acu-Rite ENC 150 Encoder with an accuracy of 3 microns (at 20 C^o). The encoder uses a Quick-Chek digital readout.

The x-axis positioning slide was directly stacked on top of the z-axis positioning slide. Care was taken so the combined center of mass of the x-axis positioning slide and LDV probe would be located over the midpoint of the z-axis positioning slide to minimize cantilever loads. A 30000 Worm Gear Drive Heavy Load-Carrying rotation stage (6 inch table diameter) made by the Daedal Division of Parker Automation with a resolution of 0.002 degrees was mounted on the x-axis positioning slide using an quarter inch aluminum plate as a base. The rotation stage was bolted to the plate.

The z-axis positions slide is mounted in an aluminum cross member that spans the vertical traverse support beams. The first iteration of the new design used a single standard aluminum C-channel 4 inches wide and 38 inches long. The aluminum C-channel was the least rigid component of the traverse system. It was especially vulnerable to minor-axis cantilever loads. The rotation of the CompLDV probe from the true x-z plane was measured using a Mitutoyo Pro 360 Digital Protractor for the entire range of the traverse system. The maximum rotation was found to be greater than 0.4±0.1 deg. This rotation was deemed excessive. Vibration of the system when traversed in the x-direction was also excessive. The system was modified to incorporate a second C-channel to increase stiffness. The maximum rotation was found to be 0.2±0.1 deg, but remained constant over most of the traverse range. With an LDV probe mounted to the traverse, shims are used to ensure the plane of the LDV probe is horizontal with respect to the wind tunnel floor to within 0.1±0.1 deg.

Seeding

Seed particles are made by forcing compressed air through Laskin nozzles which are located in a sealed container partially filled with dioctyl phthalate (DOP). The pressure inside the nozzles is regulated and adjusted according to the level of seeding desired. The nozzles are submerged in the DOP and are designed to create small pockets of atomized seed. The atomized seed rises to the surface and due to the pressure within the container is forced out through a tube to another sealed container where larger particles are collected. The remaining seed passes through a tube to another vessel called a VAPCON. The device was first developed by Liu *et al.* in 1966 [72]. The VAPCON is made of a manifold that distributes the aerosol into four stainless-steel tubes. The first section of the tubes is heated to a nominal external temperature of 770°F by the use of heating tape. The temperature can be regulated by controlling the voltage across the tape using Variac A/C regulators. The high temp in

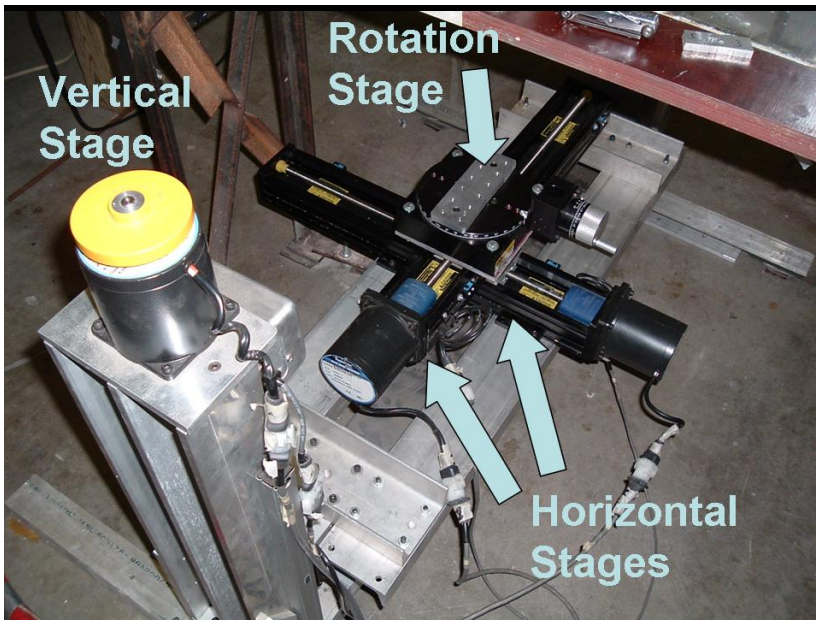

Figure 2.4: LDV traverse mechanism with double C-channel cross members

the initial section of the tubes vaporizes the DOP particles. As the mixture moves through the rest of the tubes it cools and the vapor condenses into uniformly sized particles. The seed particles are combined in a second manifold and are carried via copper tubing into the wind tunnel plenum chamber and released.

K.T. Lowe [71] describes at length the process for measuring the diameter of the seed particles. He found the mean diameter to be 0.61 ± 0.07 μm for an external VAPCON temperature of 770°F. The particle diameter was insensitive to the pressure level inside the system. Using equation 2.1.3, the particle time constant is 1 μs for typical wind tunnel conditions. This suggests that Lagrangian fluctuations of a particle's velocity will not be attenuated by more than 3 dB out to 160 kHz.

2.1.3 Data Acquisition and Signal Processing

Data Acquisition

LabView is used to interface with the Strategic Test DAQ card and properly write both channels of raw data to file. LabView is also used to control the traverse which can be automated to move the LDV measurement volume to specified locations for data collection. Automation of data acquisition is desirable because several hours are normally required to measure just one boundary layer profile. A boundary layer profile is usually made up of approximately twenty points. Each point is made up of files, usually between fifteen and fifty for each channel of data. Each file contains a certain number of burst signals.

Most boundary layer profiles require vast storage space, on the order of tens of Gigabytes each. Therefore, the most common method of acquiring data is to only store data that contain a burst signal and discard the rest. This is accomplished by instructing the DAQ card to write data from its onboard memory to storage only when a trigger event occurs, usually when the amplitude on one channel reaches some threshold value or trigger level. The trigger level and number of samples to store is specified in advance. The trigger level is usually specified to be approximately three quarters of the average burst amplitude. The number of samples is chosen to be approximately twice the average burst width. An equal number of samples before and after the trigger event are written to storage. Thus, the burst signal is nominally centered in the data written to file. The time when the trigger event occurred is written to storage as well.

Raw Processing

The shifted Doppler frequencies are extracted from the burst signals using a fast Fourier transform (FFT). The burst is centered in a processing window that is roughly twice the burst period width. The signal is not zero-padded however, as this offers little improvement for typical signal-to-noise ratios seen in the data per Shinpaugh *et al.* [73]. Shinpaugh *et al.* also show that a three-point Gaussian interpolation is best suited to determine the location of the Doppler signal peak between spectral lines. Before writing the measured frequencies to file, the associated bragg frequency is subtracted from each. The signal-to-noise ratio (SNR_1) for each signal is written to file as well and is defined here as shown below.

$$\mathrm{SNR}_1 \equiv 10 log_{10}\left[\frac{\text{spectral peak value}}{(\text{spectral noise density}) \times (\text{signal bandwidth})}\right] \tag{2.1.7}$$

To minimize the number of poor Doppler signals retained for further processing, the frequencies extracted from each burst measured at a point in the boundary layer profile are plotted against SNR_1 (figure 2.5). This allows the user to identify the noise floor and the frequency bands of interest for each point in the profile. Any burst containing a signal that does not exceed the user-specified minimum SNR_1 value or does not fall within the user-specified frequency band for that signal is removed. This step is important in mitigating any strong non-white spurious noise signals (usually occurring at radio or bragg frequencies) due to faulty shielding. This process is also performed to remove poor chirp signals when measuring flow accelerations (see B.1).

Post Processing

The extracted burst frequencies are used to compute the velocity components via a linear set of three equations (equation 2.1.8). The fringe spacing S is found from calibration as described in section 2.1.5 and the measurement direction vectors $\hat{e}$ can be measured per section 2.1.4.

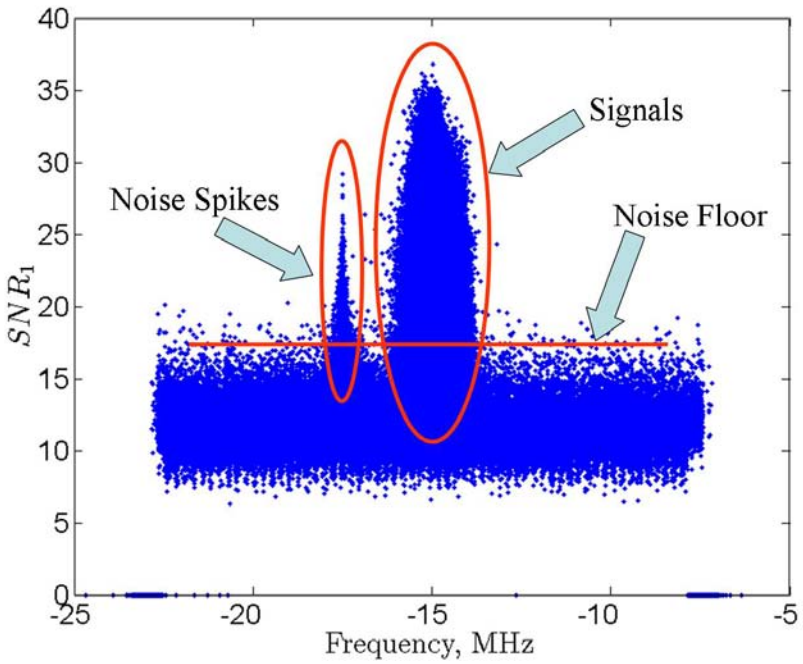

Figure 2.5: SNR_1 vs. Frequency for use in clipping

$$\vec{U} \cdot \hat{e}_i = f_i S_i \ , \quad i = 1, 2, 3 \tag{2.1.8}$$

Once velocities have been computed for each point in a profile, another round of clipping is performed graphically to mitigate spurious data points. Histograms of each velocity component reveal outliers and where the effect of noise begins to corrupt the data (i.e. where the histograms begin to level off).

2.1.4 Beam Angle Measurement

The beam vectors are measured by securing a sheet of plain white paper over the glass section of the wind tunnel floor with a streamwise and spanwise scale. When the beams shine up through the glass they scatter light through the paper. The beam spots can be marked with a fine tip pen, or a digital camera (secured directly over the tunnel floor aiming down) can be used to photograph the beam spots on the paper.

The first step is to identify a reference coordinate system. The simplest choice is the coordinate system that is aligned with the three orthogonal directions along which the traverse mechanism moves the LDV probe. One beam of light is allowed to shine through the paper and its initial position is marked. The LDV probe is then traversed in the downstream direction about an inch and its final position is marked. The line defined by these two points

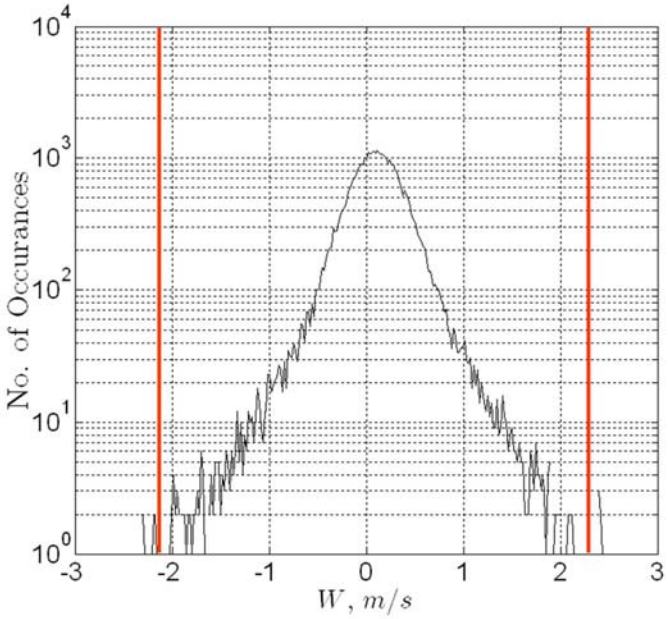

Figure 2.6: Example of velocity histogram for clipping. The noise floor is evident where the histogram begins to level off. Data between the vertical lines is accepted the rest is discarded.

defines the streamwise direction of the coordinate system. Usually, however, additional intermediate positions are marked as well to minimize uncertainties. The final position of the beam defines the origin of the coordinate system. The LDV probe is then traversed in the positive spanwise and the process is repeated to define the spanwise direction of the coordinate system.

The next step is to mark the location of the measurement volume in the plane of the paper. To do this all the beams are allowed to shine through the paper and the LDV probe is traversed in the vertical direction such that the beam positions on the paper collapse to a single point. The probe is then traversed in the plane of the paper so that this point is located in the center of the tunnel. This location is marked. The LDV probe is then traversed vertically approximately 50 mm which causes the positions of each beam on the paper to spread out. These positions are marked and the vertical distance traversed is recorded using the encoder that is mounted directly to the traverse system. Usually the probe is traversed vertically to another location and the process is repeated to provide a redundant measurement for lower uncertainty.

The coordinates (with respect to the origin) of each beam position and measurement volume position are measured by choosing the beam spot location from the digital picture. This can be done accurately with an estimated uncertainty of $\delta x = \delta z = \pm 0.2$ mm The vertical components have already been measured with the encoder with an uncertainty of $\delta y = \pm 0.005$ mm. The origin is shifted to the measurement volume position by subtracting its vector from all the beam vectors. Since all three components of each beam is known, their unit vectors ($\hat{m}$ and $\hat{n}$) are easily computed.

$$\hat{m} = \frac{x_m}{\sqrt{x_m^2 + y_m^2 + z_m^2}}\hat{i} + \frac{y_m}{\sqrt{x_m^2 + y_m^2 + z_m^2}}\hat{j} + \frac{z_m}{\sqrt{x_m^2 + y_m^2 + z_m^2}}\hat{k} \tag{2.1.9}$$

The measurement direction ($\hat{e}$), beam bisector direction ($\hat{b}$), and interior half angle (ϕ) of each beam pair can therefore be computed from the following formulas.

$$\hat{e} = (\hat{m} \times \hat{n}) \times \frac{1}{2}(\hat{m} + \hat{n}) \tag{2.1.10}$$

$$\hat{b} = \frac{1}{2}(\hat{m} + \hat{n}) \tag{2.1.11}$$

$$\phi = \frac{1}{2}\cos^{-1}(\hat{m} \cdot \hat{n}) \tag{2.1.12}$$

The measurement direction vector and the beam bisector both rely on the cross product and hence there is some sign ambiguity. It was decided that the streamwise component of the measurement direction should always point downstream and the beam bisector should always point away from the probe.

θ_{40}	$\pm 0.4^\circ$
θ_{60}	$\pm 0.5^\circ$
θ_{80}	$\pm 0.3^\circ$

Table 2.1: Beam angle uncertainty for the Long System. Beam pairs denoted by their Bragg shift frequency

The uncertainty in every component of $\hat{e}$ was computed. However, only the equation for the streamwise component is shown here in equation 2.1.13.

$$\delta e_x = \left[\left(\frac{\partial e_x}{\partial x_m} \delta x_m \right)^2 + \left(\frac{\partial e_x}{\partial y_m} \delta y_m \right)^2 + \left(\frac{\partial e_x}{\partial z_m} \delta z_m \right)^2 + \left(\frac{\partial e_x}{\partial x_n} \delta x_n \right)^2 + \left(\frac{\partial e_x}{\partial y_n} \delta y_n \right)^2 + \left(\frac{\partial e_x}{\partial z_n} \delta z_n \right)^2 \right]^{1/2} \tag{2.1.13}$$

The uncertainty in the components of $\vec{x}_m$ and $\vec{x}_n$ are $\sqrt{2}$ times the uncertainty in the beam spot measurement. This is due to the fact that to measure one component of a vector two spot measurements are required.

It is easier to interpret the results when the uncertainty is quantified in terms of the angle (θ) between the true and measured value of $\hat{e}$. Using equation 2.1.14 this angle is computed for each of the three beam pairs used in the Long System and shown in table 2.1. Each beam pair is designated by their Bragg shift frequency: 40 Mhz, 60 Mhz, and 80 Mhz.

$$\theta = \pm \arccos \left(\hat{e} \cdot \frac{\hat{e} + \delta\hat{e}}{\|\hat{e} + \delta\hat{e}\|} \right) \tag{2.1.14}$$

2.1.5 Uncertainty and Calibration

The uncertainty of the LDV is found from examination of equation 2.1.1 were the term $\vec{U} \cdot \hat{e}$ is replaced with the velocity perpendicular to the fringes $U_\perp$ for convenience. The uncertainty in $U_\perp$ is comprised of components from the uncertainty in the frequency measurement δf and uncertainty in the fringe spacing δS.

$$\delta U_\perp = \sqrt{(S\delta f)^2 + (f\delta S)^2} \tag{2.1.15}$$

An estimate for the uncertainty in the frequency measurement for the typical noise levels experienced by the Long System is $\delta f = 0.1/D$ from Shinpaugh *et al.* [73]. The burst

duration D decreases as the speed of the seed particle increases leading to greater uncertainty in the frequency measurement. For the conditions for which the Long System was employed, 28 m/s is the highest velocity measured. Given the measurement volume width of 80 μm from section 2.1.2, a reasonable estimate of the uncertainty in the frequency is $\delta f = 0.1/(80x10^{-6}\text{ m}/28\text{m/s}) = \pm 35$ kHz. Typical fringe spacings for the Long System are $S = 11$ μm. Thus, the contribution to $\delta U_\perp$ from δf is $\pm S\delta f = \pm 0.385$ m/s. It is important to note that this is the contribution to the instantaneous velocity measurement and not the mean. The remaining contribution to $\delta U_\perp$ is a result of δS which is related to calibration uncertainties.

Simple Calibration Method

The simplest way of calibrating the fringe spacing makes use of equation 2.1.2. The fringe spacing can then be written in terms of the components of the calibration velocity.

$$S = \frac{U_x e_x + U_y e_y + U_z e_z}{\bar{f}} \tag{2.1.16}$$

To calibrate the Long system the measurement volume is positioned on the centerline of the test section in the freestream, where a Pitot-static probe and liquid manometer are used to measure the velocity U_p. The LDV is rotated approximately 45° to balance the components U_x and U_z. Equation 2.1.16 can be written in terms of this rotation angle ϕ. Note that the vertical component of the calibration velocity is defined to be zero.

$$S = \left(e_x \cos\phi + e_z \sin\phi\right) \frac{U_p}{\bar{f}} \tag{2.1.17}$$

Uncertainties arises from four sources: the calibration velocity U_p, the angle ϕ, the measurement direction vector $\hat{e}$, and the mean frequency measured $\bar{f}$. The smallest contributor to δS is the uncertainty in $\bar{f}$. The uncertainty in the mean frequency is $\delta\bar{f} = \delta f/\sqrt{N}$, where N is the number of bursts for which the mean is computed. Typically 100,000 bursts are recorded during calibration so the uncertainty in the mean frequency is $\delta\bar{f} = \pm 111$ Hz. The uncertainties in the components of $\hat{e}$ were computed as explained in section 2.1.4. The uncertainty in the rotation angle was $\delta\phi = \pm 0.005°$ due to the vernier scale on the rotation stage of the traverse mechanism. The uncertainty in U_p required additional analysis.

Using the Pitot-static probe and liquid manometer to measure the freestream velocity involved measurements of the tunnel dynamic pressure P_{dym}, atmospheric pressure P_{atm}, and the tunnel temperature T in equation 2.1.18. The ideal gas constant is denoted by R.

$$U_p = \sqrt{2RTP_{dym}/P_{atm}} \tag{2.1.18}$$

The uncertainties in the measured quantities are $\delta P_{dym} = \pm 0.005$ inH_2O, $\delta P_{atm} = \pm 0.05$ mBar, and $\delta T = \pm 1$ C^o. Given these values the uncertainty in the velocity measured with the Pitot probe is $\delta U_p = \pm 0.062$ m/s via equation 2.1.19.

$$\delta U_p = \sqrt{\left(\frac{\partial U_p}{\partial P_{dym}}\delta P_{dym}\right)^2 + \left(\frac{\partial U_p}{\partial P_{atm}}\delta P_{atm}\right)^2 + \left(\frac{\partial U_p}{\partial T}\delta T\right)^2} \tag{2.1.19}$$

$$\frac{\partial U_p}{\partial P_{atm}} = \frac{1}{2}\left[2\frac{RT}{P_{atm}}\right]^{\frac{1}{2}} P_{dym}^{-\frac{1}{2}} \tag{2.1.20}$$

$$\frac{\partial U_p}{\partial P_{atm}} = -\frac{1}{2}\left[2RTP_{dym}\right]^{\frac{1}{2}} P_{atm}^{-\frac{3}{2}} \tag{2.1.21}$$

$$\frac{\partial U_p}{\partial T} = \frac{1}{2}\left[2R\frac{P_{dym}}{P_{atm}}\right]^{\frac{1}{2}} T^{-\frac{1}{2}} \tag{2.1.22}$$

The uncertainty in the fringe spacing is written in equation 2.1.23. The sensitivities of the uncertainty to the independent variables are shown below. The overall uncertainty in S is dominated by the uncertainties in the measurement directions $\hat{e}$. The results for each beam pair used in the Long System is shown in table 2.2. Each pair is designated by their Bragg shift frequency.

$$\delta S = \left[\left(\frac{\partial S}{\partial U_p}\delta U_p\right)^2 + \left(\frac{\partial S}{\partial e_x}\delta e_x\right)^2 + \left(\frac{\partial S}{\partial e_z}\delta e_z\right)^2 + \left(\frac{\partial S}{\partial \bar{f}}\delta \bar{f}\right)^2 + \left(\frac{\partial S}{\partial \phi}\delta \phi\right)^2\right]^{1/2} \tag{2.1.23}$$

$$\frac{\partial S}{\partial U_p} = \frac{e_x \cos\phi + e_z \sin\phi}{\bar{f}} \tag{2.1.24}$$

$$\frac{\partial S}{\partial e_x} = \frac{U_p \cos\phi}{\bar{f}} \tag{2.1.25}$$

$$\frac{\partial S}{\partial e_z} = \frac{U_p \sin\phi}{\bar{f}} \tag{2.1.26}$$

$$\frac{\partial S}{\partial \bar{f}} = -\left(e_x \cos\phi + e_z \sin\phi\right)\frac{U_p}{\bar{f}^2} \tag{2.1.27}$$

$$\frac{\partial S}{\partial \phi} = -\frac{e_x U_p \sin\phi}{\bar{f}} + \frac{e_z U_p \sin\phi}{\bar{f}} \tag{2.1.28}$$

New Calibration Method

A new calibration method was devised to mitigate the effect of the uncertainty in beam angle measurement. The method leveraged the fact that LDV probe could be rotated to a high degree of accuracy. The new method couples the calibration of the fringe spacing

Beam Pair.	Calibration Method	
	Simple	Coupled
δS_{40}	± 0.154 μm	± 0.035 μm
δS_{60}	± 0.143	± 0.033
δS_{80}	± 0.093	± 0.028

Table 2.2: Fringe spacing uncertainty estimates. Comparison between simple and new calibration methods

with the beam angle measurement by rewriting equation 2.1.17 in terms of the independent variables e_x/S and e_z/S.

$$\left(\cos\phi\frac{e_x}{S}+\sin\phi\frac{e_z}{S}\right)=\frac{\bar{f}}{U_p} \tag{2.1.29}$$

If a calibration is done at two values of ϕ, then a coupled set of linear equations can be written.

$$\begin{bmatrix} \cos\phi_1 & \sin\phi_1 \\ \cos\phi_2 & \sin\phi_2 \end{bmatrix}\begin{Bmatrix} e_x/S \\ e_z/S \end{Bmatrix}=\begin{Bmatrix} \bar{f}_1/U_p \\ \bar{f}_2/U_p \end{Bmatrix} \tag{2.1.30}$$

An additional equation is used to solve for S which comes from the identity $e_x^2+e_y^2+e_z^2=1$. Note that a value for e_y is still needed due to the fact that the LDV probe could only be rotated about the y-axis. The e_y component can be estimated from the 'Simple Calibration Method' explained in the previous section.

$$S=\left[\frac{1-e_y^2}{\left(e_x/S\right)^2+\left(e_z/S\right)^2}\right]^{1/2} \tag{2.1.31}$$

The uncertainty is S is then found via equation 2.1.32. Equations for the sensitivities were derived by substituting the solution to equation 2.1.30 into equation 2.1.31 and computing the partial derivatives. However, they are far too lengthy to be included here.

$$\delta S=\left[\left(\frac{\partial S}{\partial\phi_1}\delta\phi\right)^2+\left(\frac{\partial S}{\partial\phi_2}\delta\phi\right)^2+\left(\frac{\partial S}{\partial\bar{f}_1}\delta\bar{f}\right)^2+\left(\frac{\partial S}{\partial\bar{f}_2}\delta\bar{f}\right)^2+\left(\frac{\partial S}{\partial U_p}\delta U_p\right)^2+\left(\frac{\partial S}{\partial e_y}\delta e_y\right)^2\right]^{1/2} \tag{2.1.32}$$

The results of the uncertainty analysis for the fringe spacing is shown in table 2.2. Each beam pair is designated by their Bragg shift frequency. As shown, the new calibration method offers a significant reduction in the uncertainty in the fringe spacing.

Term	Uncertainty (w/ bias)	
$\delta U'$	± 0.324 (0.513)	m/s
$\delta V'$	± 0.577 (0.912)	
$\delta W'$	± 0.438 (0.957)	
δU	± 0.003 (0.397)	
δV	± 0.005 (0.706)	
δW	± 0.004 (0.851)	
$\delta\overline{u^2}$	± 0.063 (0.127)	m^2/s^2
$\delta\overline{v^2}$	± 0.072 (0.144)	
$\delta\overline{w^2}$	± 0.073 (0.213)	
$\delta\overline{uv}$	± 0.060 (0.119)	
$\delta\overline{uw}$	± 0.051 (0.136)	
$\delta\overline{vw}$	± 0.055 (0.124)	

Table 2.3: Uncertainty in measured terms

Uncertainty in Velocity Components

The uncertainty in the velocity perpendicular to the fringes is computed via equation 2.1.15 using the values for δS found from the coupled calibration method. This uncertainty along with uncertainty in the measurement directions were propagated through equations 2.1.4 to find the uncertainties in the instantaneous velocity components U', V', and W'. The uncertainties in the mean values are significantly lower as computed from $\delta U = 1.96\delta U'/\sqrt{N}$. However, although δS is due to random errors inherent in the calibration process, it behaves as an unknown bias in the measured data. Therefore, $f\delta S$ in equation 2.1.15 poses a lower limit for the uncertainties in the means. However, its effect is not seen from measurement-to-measurement only calibration-to-calibration, and it has a small effect on the higher moments. Table 2.3 lists the uncertainty bounds for various quantities including the mean quantities with and without the calibration uncertainty included (i. e. $\delta\hat{e} = \delta S = 0$).

2.2 Microphones

The microphones used to measure the fluctuating surface pressure were Endevco Miniature Piezoresistive Pressure Transducers (model 8507C-2). These pressure transducers have a flat frequency response from 0 to 70 kHz, a sensitivity of 0.0233 mV/Pa, and a full scale range of 300 mV. The microphone has an outer diameter of 2.42 mm and was inserted into a pinhole mask with a pinhole diameter of 0.5 mm to limit spatial averaging. For the conditions of these experiments the wave speed is assumed to be no greater than 14 m/s. Given the

pinhole diameter, this results in a 28 kHz bound on the highest frequency measurable due to spatial averaging. However, the resonant peak of the pinhole mask was found to be at a lower frequency, but never less than 20 kHz. Fortunately, for the present experiments, pressure fluctuations above 20 kHz contain negligible energy.

The signal from the microphone is amplified 100 times by a Measurements Group Strain Gauge Conditioning Amplifier (model 2310). The amplified signal is passed through a National Instruments Shielded Connector Block (model NI-SCB-68) before being digitized by a 16-bit National Instruments DAQ card (model NI-PCI-6013) in a standard PC. The DAQ card has a 10 volt range. The amplified signal is sampled at 65536 Hz for 8 seconds which results in 524288 samples. The samples are written to file for further processing.

The wind tunnel facility (see 2.3) in which these surface pressure fluctuations are measured is not acoustically treated. Consequently, they contain unwanted contributions from a fan, motor, or other tunnel components. Vibrations of the tunnel structure itself can also be a large contribution. To remove these unwanted components from the surface pressure spectra and isolate only the portion due to the turbulence, a two identical microphones were used simultaneously as proposed by Simpson *et al.* [74]. This method is valid if the pressure fluctuations can be broken up into a turbulent component (p_t) and a coherent component (p_c) that is propagating through the tunnel structure and the flow.

$$p(t) = p_t(t) + p_c(t) \tag{2.2.1}$$

It is not necessary for p_c to be periodic, only coherent in the direction perpendicular to the flow direction. The unwanted contributions listed above all meet this criteria. If two transducers are mounted on the surface at the same streamwise location but at different spanwise locations, they will both measure the same value of p_c. The unwanted coherent portion can then be eliminated by subtracting the two signals.

$$p_2(t) - p_1(t) = p_{t,2}(t) - p_{t,1}(t) \tag{2.2.2}$$

If the distance between the transducers is greater than the largest coherent turbulent motions in the flow, then each of the measured turbulent components are uncorrelated ($\overline{p_{t,2}p_{t,1}} = 0$). Therefore, if both transducers experience the same type of flow, the mean square of equation 2.2.2 becomes twice the mean square of the turbulent contribution measured by one transducer.

$$\overline{(p_2 - p_1)^2} = 2\overline{p_{t,1}^2} = 2\overline{p_{t,2}^2} \tag{2.2.3}$$

This result means the spectra of the turbulent portion of the surface pressure fluctuations can be isolated and measured.

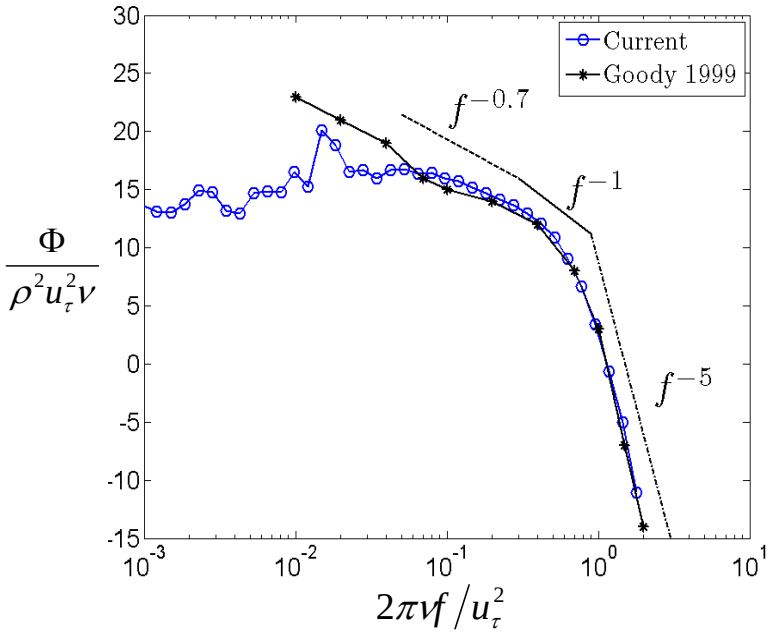

Figure 2.7: Single-sided PSD for smooth wall at 20 m/s

Processing of the raw signals to compute the isolated wall pressure spectra is relatively simple. The first step is to digitally amplify or attenuate one of the transducer signals to ensure the mean square values of both signals are equal. This minimizes any differences between the transducers and amplifiers. Next one signal is subtracted from the other, and the discrete Fourier transform of the result is computed. The spectra values are then divided in half due to equation 2.2.3. Bin averaging is used to smooth the result. Figure 2.7 shows data taken using this technique in the current wind tunnel on the smooth wall at 20 m/s compared with previous data from Goody and Simpson [75] taken in a different facility with a time delay noise reduction scheme suggested by Agarwal and Simpson [76]. The agreement is quite good. In fact, the current technique performs better at the low frequencies.

2.3 Small Boundary Layer Wind Tunnel

All measurements were made in the Virginia Tech Small Boundary Layer Wind Tunnel. Bennington [17] gives a detailed description. Only crucial information is included here. The test section has a cross-section of approximately 24x10 cm and is 200 cm long. The test section roof is made of Plexiglas, removable, and its height can be adjusted at four locations to control the pressure gradient and the overall tunnel speed to some extent. The primary speed control is a butterfly valve located upstream of the plenum chamber. Both the tunnel floor and ceiling are equipped with ports that allow Pitot probe access. A Pitot probe with a liquid manometer is used to measure the tunnel speed when adjustments to the butterfly

valve need to be made. During testing the roof is sealed with plastic tape to ensure there are no leaks. Measurements of the pressure gradient for each test case are given in section 3.1.

The boundary layer trip arrangement of Bennington [17] is used with some modification. A 0.125 inch square rod spanning the width of the test section is placed on the tunnel roof right after the contraction. A second identical rod is placed 2 inches downstream of the first. A piece of silicon-carbide Norton 20-grit sandpaper is placed between the rods spanning the width of the tunnel. For a freestream speed of $\sim$27 m/s, this trip arrangement produced an $\sim$43 mm thick boundary layer $\sim$1 m downstream of the contraction. The ratio of displacement thickness to momentum thickness (δ^*/θ) was 1.41. Bennington [17] shows that there is an $\sim$12 cm wide region where the boundary layers on the side walls do not affect the rest of the flow for the same approximate streamwise location of these measurements. All measurements were taken near the test section centerline. Measurements of the two-dimensionality of the flow for each test case are given in section 3.1.

The floor has an insert made of float glass 71 cm long that spans the width of the test section and allows for LDV access. The leading edge of the glass insert is located 76.2 cm downstream from the leading edge of the test section. The constant use of the seeding substance (Dioctyl Phthalate) necessitates frequent cleaning of the glass. An access hatch in the roof is removed during cleaning.

The DOP also clogs the screens upstream of the contraction used to decrease the turbulence level. The downstream-most screen is cleaned daily by removing the front 51 cm of the test section roof. There are two other screens located further upstream, but access to them is impossible without dismantling the contraction.

2.4 Roughness Fetches

The rough surfaces considered in these experiments were all made of 2 mm diameter hemispheres in a straight configuration. The element spacings were chosen to be in the sparse regime of the $f(\lambda)$ plot discussed in section 1.2.5. Hemispherical elements were chosen for several reasons. First, they are easier to manufacture than other discreet element such as cylinders or pyramids. Because they have no sharp edges, it is thought hemispheres are closer to typical roughness shapes found in nature. Finally, they are a case study for the Hydroacoustics Group at the Office of Naval Research.

Fetches of roughness elements were placed on the ceiling of the small boundary layer tunnel. This allowed complete LDV access from the floor, even allowing measurements to be made directly over top the roughness elements. If the roughness were located on the tunnel floor certain sections of the roughness substrate would have to be removed to keep the beams from being blocked. This would create steps that could influence the local flow structure. Placing

ID	k (mm)	s (mm)	A_f (mm^2)	A_p (mm^2)	λ^{-1}
Fetch 1	1.0	4.0	1.57	16.00	10.2
Fetch 2	1.0	5.5	1.57	30.25	19.3
Fetch 3	1.0	8.0	1.57	64.00	40.7
Fetch 4	1.0	11.0	1.57	121.00	77.0

Table 2.4: Geometric Parameters of Surfaces Roughened with Hemispheres

the roughness on the ceiling avoided this issue. The roughness fetches were 142 cm long and began just downstream of the boundary layer trips. The trip arrangement of Bennington [17] was used. All measurements were taken between 94 and 118 cm downstream of the trips.

The majority of the roughness fetches were made from molded rubber. The molds were made by the AOE machine shop and a company named Advanced Prototype Molding manufactured the rubber parts in 8.5 x 16 inch sections of 1/8 inch thickness. The rubber fetches were flexible, durable, and could be cut easily into desired shapes. However, many of the hemispheres contained a small hole near their tops. It was assumed that these small imperfections had little impact on the flow [77].

The sections of the roughness fetch over which LDV measurements were made utilized a front surface mirror to minimize the flare and aid in estimating the wall position (see section 3.3). Two different approaches were used. The first was used only for fetch 2 from table 2.4, and employed a small section of hard plastic machined by the AOE machine shop into the correct hemispherical shapes mounted on a substrate. A small circular section of the part was milled out and a front surface mirror (12.5 mm dia, 1 mm thick) was glued into the recess. Four hemispherical elements were cut from the plastic part and each was glued onto the mirror to maintain the pattern of the overall fetch. Also, to accommodate placement of the microphones for surface pressure fluctuation measurements, two square inserts were milled into the underside of the substrate. The remaining substrate material was only 2 mm thick. At the center of each insert a hole was machined through the remaining substrate to allow the microphone block to be traversed to various locations around a roughness element.

The embedded mirror in the plastic substrate had a number of drawbacks. It is very difficult the ensure that the mirror and the surface of the substrate are flush within 100 microns. Gluing individual hemispherical elements in the proper roughness pattern onto the mirror was also a challenge. Finally, the quality of the machined hemispheres was unimpressive. To remedy these issues a 1/8 inch thick polished aluminum mirror was used. A piece of aluminum was cut to size ($\sim$10x1.5 inches) and was wet sanded by hand using 220 to 1500 grit sandpaper. The aluminum was polished to a mirror finish using *Mother's Mag and Aluminum Polish* on a microfiber towel with an orbital sander. The AOE machine shop then used a CNC machine to drill two concentric holes for each roughness element location.

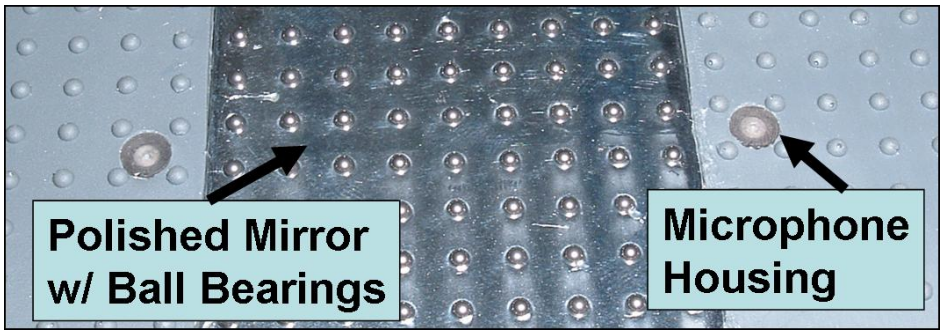

Figure 2.8: Polished metal mirror with embedded ball bearings and microphone housings

The outer hole has a diameter of 2 mm and is 0.661 mm deep. A through hole of 1.5 mm diameter was made at the center of the first hole. A final round of polishing is completed before the 2 mm diameter chromed aluminum balls are individually glued into the holes using Hardman 24 hour epoxy, a syringe, and tweezers. The dimensions of the holes are such that the ball bearing forms a hemisphere with the mirror's surface. Although the polished mirror quality was inferior to the optical quality mirror, its performance was sufficient. The pinhole masks for the microphones were embedded in the rubber fetches (in the middle of a cell of elements) approximately 2 inches apart.

Chapter 3

Results

3.1 Summary of Test Cases

Boundary layer measurements were made on the four fetches described in table 2.4 and on the smooth wall. Measurements were made at two freestream speeds of nominally 20 and 27 m/s. The same boundary layer measurements were made on three different days for each case. All parameters for each day are listed in table 3.1. The boundary layer thickness (δ) was estimated to occur where the local mean streamwise velocity was 99% of the freestream velocity. Definitions of the displacement thickness (δ^*) and momentum thickness (θ) are given in equations 1.2.16 and 1.2.17 respectively. The condition of fully rough surface-flow interaction is assumed to exist for all the rough test cases measured due to the relatively small change in C_f for the relatively large change in U_e for each roughness fetch.

The tunnel roof height was adjusted slightly for each case to ensure there was a zero pressure gradient in the test section. While adjustments to the roof were being made a Pitot static probe was used to measure the pressure gradient using access ports in the test section floor. A streamwise LDV profile was then taken along the centerline of the tunnel to ensure the maximum freestream velocity varied no more than 0.2 across the test section (see figure 3.1). (This procedure was performed on case 1, but the data was not retained and is therefore not shown in figure 3.1).

As explained in section 2.3, the flow was largely two-dimensional. Figure 3.2 shows the mean velocity components for all the cases measured. The absolute maximum spanwise velocity measured over all test cases was 0.25 m/s.

Case No.	Fetch ID	Day	U_e (m/s)	δ (mm)	δ^* (mm)	θ (mm)	C_f x1000
1	Smooth	1	26.9	42.9	4.82	3.44	2.877
		2	26.8	42.8	5.24	3.73	2.640
		3	26.1	42.4	4.26	3.01	2.924
2	Smooth	1	20.3	45.0	5.98	4.18	2.281
		2	20.2	45.0	5.44	3.90	2.350
		3	20.3	43.9	5.49	3.97	2.346
3	Fetch 1	1	27.4	60.3	13.15	8.28	3.545
		2	27.5	65.0	13.44	8.54	3.368
		3	27.4	64.9	13.95	8.83	3.363
4	Fetch 1	1	20.4	60.2	12.01	7.69	3.667
		2	20.5	64.9	12.74	8.17	3.434
		3	20.5	67.0	12.89	8.20	3.442
5	Fetch 2	1	27.2	44.3	8.38	5.19	4.168
		2	27.1	44.4	8.55	5.39	3.981
		3	26.9	44.5	8.98	5.55	3.851
6	Fetch 2	1	19.7	45.0	8.22	5.15	3.688
		2	19.6	43.7	7.56	4.73	3.993
		3	19.5	44.9	8.05	5.01	3.773
7	Fetch 3	1	27.5	32.8	5.27	3.42	3.932
		2	27.4	29.2	5.10	3.26	3.883
		3	27.4	29.2	4.88	3.22	3.937
8	Fetch 3	1	20.2	46.9	7.11	4.74	3.771
		2	20.2	49.1	7.46	5.16	3.564
		3	20.0	49.7	7.39	5.08	3.680
9	Fetch 4	1	27.5	59.2	7.77	5.61	3.078
		2	27.1	60.0	8.76	6.15	3.105
		3	27.0	60.0	8.86	6.17	3.154
10	Fetch 4	1	20.4	50.1	6.95	4.82	3.253
		2	20.4	54.7	7.48	5.22	3.320
		3	20.3	54.8	7.63	5.38	3.271

Table 3.1: Measured Boundary Layer Parameters

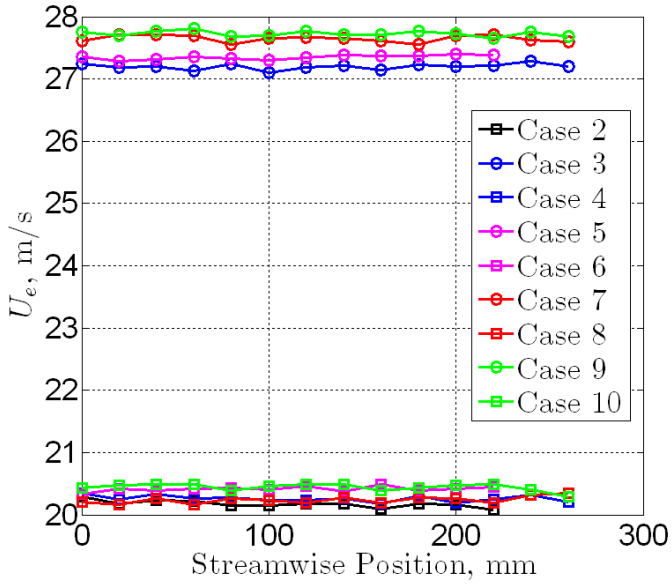

Figure 3.1: Freestream Variation with Streamwise Position

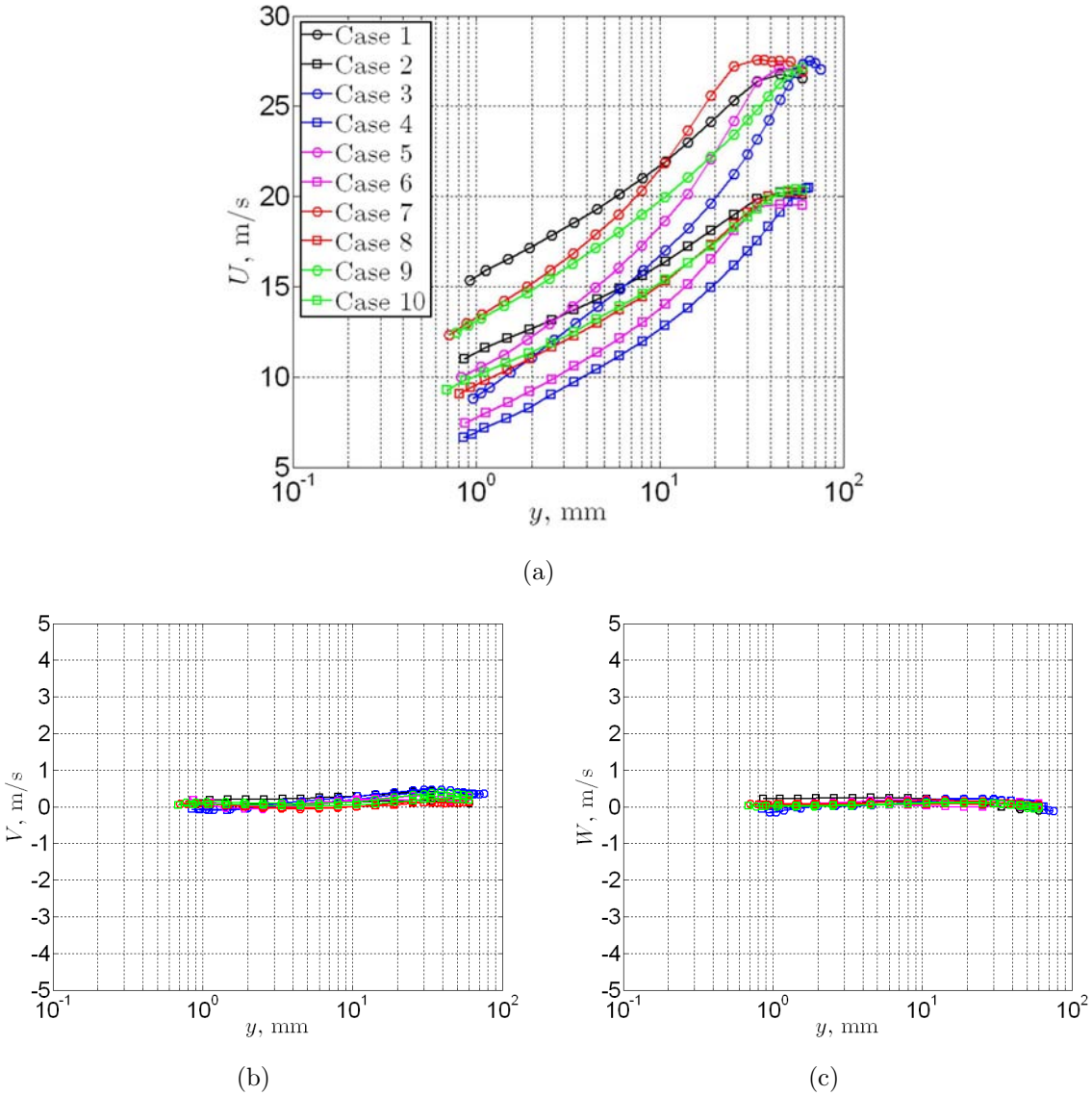

Figure 3.2: Mean U, V, and W profiles for all test cases

Quantity	Percent Difference
U	<0.2%
$\overline{u^2}$, $\overline{v^2}$, $\overline{w^2}$	<1.5%
$\overline{uv}$	<2.0%

Table 3.2: Percent difference between standard method of averaging and the method of Simpson and Chew [3]

3.2 Inter-arrival Time Bias

The standard method for computing the mean and higher moments of a sample of LDV data is given in equations 3.2.1 and 3.2.2.

$$U = \frac{\sum_{i=1}^{N} U_i}{N} \tag{3.2.1}$$

$$\overline{U^n} = \frac{\sum_{i=1}^{N} (U_i - U)^n}{N} \tag{3.2.2}$$

However, due to the inter-arrival time of the seed particles at the measurement volume. This inter-arrival time bias is due to the fact that more particles carried with higher velocity fluid will pass through the measurement volume than those carried by low velocity fluid. Simpson and Chew [3] suggest an alternative method for computing the means and higher moments to eliminate this bias, given in equations 3.2.3 and 3.2.4.

$$U = \frac{\sum_{i=1}^{N-1} U_i \Delta t_i}{\sum_{i=1}^{N-1} \Delta t_i} \tag{3.2.3}$$

$$\overline{U^n} = \frac{\sum_{i=1}^{N-1} (U_i - U)^n \Delta t_i}{\sum_{i=1}^{N-1} \Delta t_i} \tag{3.2.4}$$

Both the standard method and the method of Simpson and Chew were performed. It was found that the correlations coefficient between each velocity component and the inter-arrival time Δt was negligibly small (less than 0.02). This lack of correlation is due to the fact that data rate for the Long System is hardware limited and so the data is essentially randomly sampled in time which eliminates the bias. The inter-arrival time bias correction is really only appropriate for high data rates when the data rate is limited by particle concentration. Table 3.2 shows that the percent difference between both methods of averaging is neglibily small as expected. Therefore, all means and higher moments presented were computed using the standard method.

3.3 Uncertainties

The contributions to uncertainty estimates discussed in section 2.1.5 are concerned with the LDV operating parameters and calibration. However, other factors have contributed to the uncertainties in the values reported in these results. The consistency of the wind tunnel (section 2.3) was an issue. Although every attempt was made to maintain a constant temperature in the tunnel test section, the temperature could vary slowly throughout the day. The atmospheric pressure also varied throughout the day and certainly day-to-day. Although these effects were considered small, the boundary layer development over the trips and upstream portions of the roughness fetches could be affected more than realized. Tests were conducted to check repeatability of measured profiles. Noticeable difference were found between profiles measured on different days. Also, profiles measured in the early evening sometimes gave unusual results due to the relatively abrupt change in temperature and atmospheric pressure over a few hours. To mitigate these effects, most of the data was taken between the hours of 10am and 5pm. During this time three boundary layer profiles could be measured.

In order to clean the glass on the tunnel floor for clear LDV access, a small hatch in the tunnel roof directly above the test section had to be removed each day. How removal and replacement of this hatch affected repeatability of profiles was studied extensively and found to be negligible. However, complete repeatability could not be guaranteed. Care was also taken to ensure the roughness fetches were as free as possible from gaps and protrusions of the substrate at joints between parts. Still, although the tunnel roof had negligible curvature, it was not flat due to the necessary accommodation of the pressure gradient and some gaps were unavoidable. The area around the tunnel hatch was especially challenging since the molded roughness fetches had to be cut to accommodate the hatch.

Upstream of the test section there are several screens that are used to decrease the turbulence intensity of the incoming flow. After days of prolonged exposure to seed particles these screens become saturated, at which point the freestream turbulence intensity increases and the mean flow rate decreases. These screens were cleaned daily to mitigate the problem, but this issue may still contribute to the overall uncertainties in the data.

Another area for concern was the boundary layer thickness relative to the test section height. In most cases the boundary layers on the top and bottom surfaces of the test section were merging and the potential core was very small or non-existent. The flow in the tunnel was far from fully developed, however, it is certain that there was some interaction between the boundary layers on the top and bottom walls.

In order to quantify the global uncertainty of these results all measurements were repeated over three days. Estimates of the global uncertainty bounds were found using the sample standard deviation (σ) with Student's correction $t_{95} = 12.706$ to account for the small sample

Case No.	95% Confidence Interval				
	U_e (m/s)	δ (mm)	δ^* (mm)	θ (mm)	C_f x1000
1	±3.19	±1.99	±3.60	±2.65	±1.117
2	0.37	4.93	2.19	1.06	0.284
3	0.45	19.75	2.95	2.00	0.760
4	0.24	25.59	3.47	2.11	0.970
5	1.11	0.76	2.28	1.30	1.169
6	0.49	5.44	2.50	1.55	1.155
7	0.49	15.25	1.41	0.78	0.219
8	0.80	10.69	1.36	1.64	0.761
9	1.94	3.55	4.42	2.34	0.283
10	0.39	19.75	2.61	2.11	0.254

Table 3.3: Uncertainty of boundary layer parameters with 95% confidence interval

size $N = 3$ at a 95 percent level of confidence. However, for such a small sample size a 95 percent of confidence on the uncertainty bounds has limited practical value. For perspective, the uncertainty bounds were also computed for an 80 percent confidence level ($t_{80} = 3.078$).

$$\delta(\cdot) = \pm t_{95} \frac{\sigma}{\sqrt{N}} \tag{3.3.1}$$

Case No.	80% Confidence Interval				
	U_e (m/s)	δ (mm)	δ^* (mm)	θ (mm)	C_f x1000
1	±0.77	±0.48	±0.87	±0.64	±0.271
2	0.09	1.19	0.53	0.26	0.069
3	0.11	4.78	0.72	0.49	0.184
4	0.06	6.20	0.84	0.51	0.235
5	0.27	0.18	0.55	0.31	0.283
6	0.12	1.32	0.61	0.38	0.280
7	0.12	3.70	0.34	0.19	0.053
8	0.19	2.59	0.33	0.40	0.184
9	0.47	0.86	1.07	0.57	0.068
10	0.10	4.79	0.63	0.51	0.062

Table 3.4: Uncertainty of boundary layer parameters with 80% confidence interval

Positioning of the LDV probe at the desired streamwise (x) and spanwise (z) location was done by eye. Two beams from each LDV head were partially launched such that their spot size on the tunnel ceiling was small. The traverse system, discussed at length in section 2.1.2,

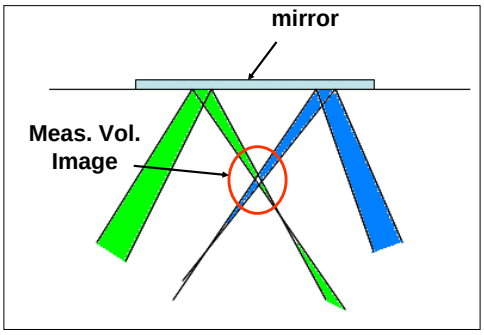

Figure 3.3: Sketch of wall finding technique. A mirror is used to create a reflection or image of the measurement volume

was adjusted vertically until the beam spots merged. The beam spot was then positioned in the desired location in reference to the local roughness elements. Estimated uncertainty in the x and z position with respect to the local roughness element is ± 0.2mm or about 1/10 the element base diameter.

The wall-normal coordinate y was much more certain due to a digital encoder capable of position resolution of $< \pm 0.005$mm. The wall position was less certain and is always a challenge to determine for any laser based flow measurement system. A novel approach for wall finding was used that resulted in excellent uncertainty bounds of ± 0.03mm for the present measurements. The LDV beams were reflected off a polished aluminum mirror (section 2.4) to create an image of the measurement volume. By making measurements with both the image and the real measurement volume in the same locations, the true wall location can be inferred (see figures 3.4 and 3.5). The uncertainty in wall position could be decreased even further if an optical quality mirror is used.

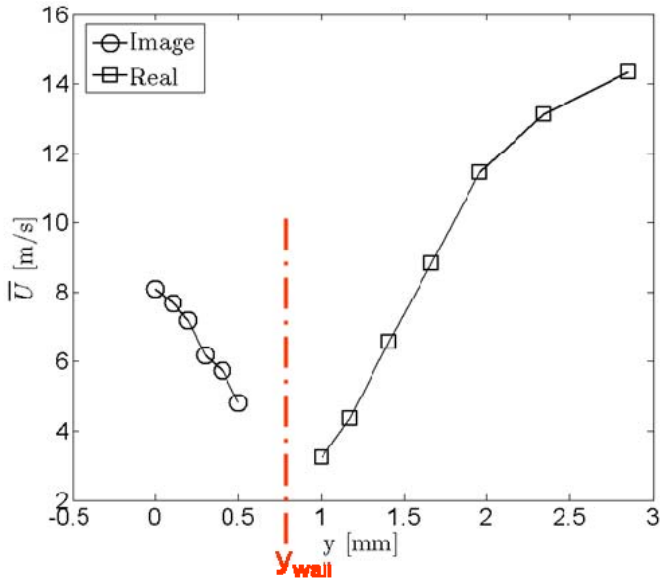

Figure 3.4: Velocity measured with real and image of measurement volume. Position of symmetry indicates wall position

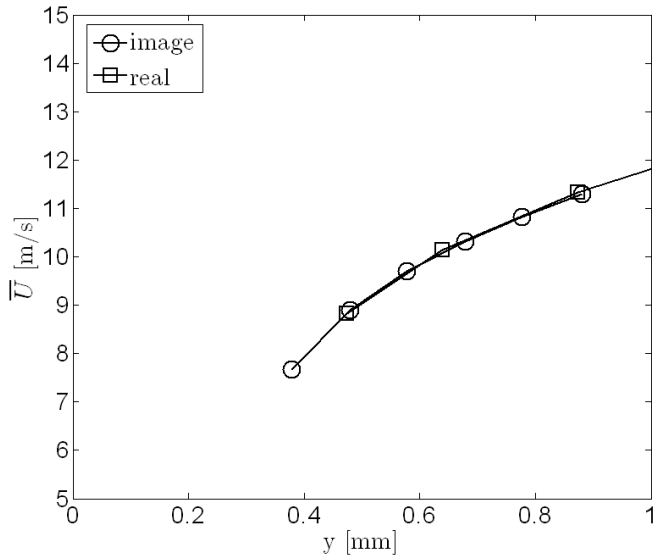

Figure 3.5: Velocity profile measured with real and image of measurement volume overlayed

3.4 Skin Friction Measurements

3.4.1 Integral Momentum Balance

The skin friction coefficients in table 3.1 were measured using an integral momentum balance similar to equation 1.2.11 with some slight differences.

$$\frac{C_f}{2} = \underbrace{-\frac{\partial}{\partial x}\int_0^{Y_1}\frac{U^2}{U_e^2}dy + \frac{U(Y_1)}{U_e}\frac{\partial}{\partial x}\int_0^{Y_1}\frac{U}{U_e}dy}_{\text{convection}} \underbrace{-\frac{\partial}{\partial x}\int_0^{Y_1}\frac{\overline{u^2}-\overline{v^2}}{U_e^2}dy}_{\text{normal stress}} \underbrace{-\frac{\overline{uv}}{U_e^2}}_{\text{shear stress}} + \underbrace{\frac{\nu}{U_e^2}\frac{\partial U}{\partial y}\bigg|_{Y_1}}_{\text{viscous stress}} \tag{3.4.1}$$

Equation 3.4.1 assumes the flow is two dimensional, the pressure gradient is zero, and the viscous stress due to gradients in the streamwise direction is negligible. The continuity equation has been used to eliminate the mean wall-normal velocity component from the convection term. In the normal stress term, $\overline{v^2}$ is a result of using the y-momentum equation to account for the variation of pressure with y. The integrals are evaluated from the wall to some arbitrary distance above the wall, Y_1. The Reynolds shear stress term and the viscous term are both evaluated at Y_1. The x-derivatives are evaluated by measuring a boundary layer profile at three streamwise locations each separated by approximately 100 mm and performing a linear fit. The profile locations are at the center of a roughness cell along a symmetry plane where the assumption of two-dimensionality is valid.

Due to figure 3.1, the pressure gradient was assumed to be negligible at every instant in time, and hence the pressure gradient term was not included in equation 3.4.1. However, the consistency of the small boundary layer wind tunnel was an issue, and U_e was not a constant over the course of several hours. Unfortunately, the three profiles required to compute the x-derivatives in equation 3.4.1 took six to eight hours to complete. Not only did U_e change in time, but the entire profile also changed slightly and ultimately contributed to the final uncertainty discussed in section 3.3. In order to minimize these effects, the U_e terms were brought into the x-derivatives in equation 3.4.1. This gave a skin friction coefficient that had less variation over the range of the boundary layer thickness, which is physically correct.

Figure 3.6 show results of this measurement technique for case 3 and case 4. As reported by Brzek *et al.* [56], the Reynolds shear stress is the dominant term near the wall, the convective term dominates away from the wall, and the remaining terms are negligible. As mentioned, the total skin friction should be a constant over the entire boundary layer, so the average value was taken in the constant region to limit uncertainties (see figure 3.6(b). The three boundary layer profiles that comprise a single skin friction estimate were measured on the same day. The entire procedure described above was repeated on two additional days. The results are give in table 3.1.

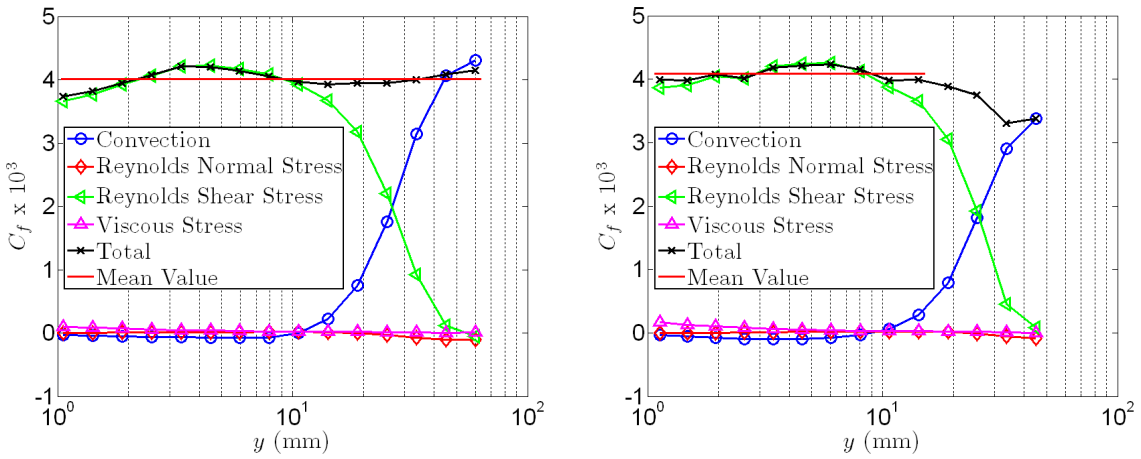

(a) Case 3 (b) Case 4

Figure 3.6: C_f Budget for Cases 3 and 4. Note that for case 4, the average C_f value is taken only over the range where it is nearest a constant value

These results give good evidence that the Reynolds shear stress term in the plateau region is a solid estimate of the wall shear. Table 3.5 compares estimates of the friction velocity computed using the measured skin friction coefficient and the average value of the Reynolds shear stress in the plateau region. The values differ by less than 4% for all cases studied.

Case No.	Day	u_τ (m/s)	
		$U_e\sqrt{C_f/2}$	$\sqrt{-\overline{uv}}$
1	1	1.019	0.977
	2	0.973	0.966
	3	0.997	0.998
2	1	0.685	0.702
	2	0.692	0.700
	3	0.694	0.691
3	1	1.153	1.134
	2	1.128	1.134
	3	1.123	1.099
4	1	0.874	0.865
	2	0.848	0.831
	3	0.849	0.839
5	1	1.241	1.258
	2	1.209	1.235
	3	1.180	1.201
6	1	0.844	0.863
	2	0.874	0.844
	3	0.848	0.862
7	1	1.221	1.211
	2	1.208	1.198
	3	1.217	1.204
8	1	0.878	0.869
	2	0.853	0.859
	3	0.859	0.846
9	1	1.080	1.090
	2	1.068	1.050
	3	1.074	1.055
10	1	0.823	0.833
	2	0.830	0.828
	3	0.821	0.818

Table 3.5: Measured Boundary Layer Parameters

3.4.2 Smooth Wall Sublayer Fit

In order to obtain further verification that the Reynolds shear stress is an accurate measure of the total wall shear, measurements of a 2D smooth wall turbulent boundary layer were made on the floor of the tunnel test section. Since the floor of the tunnel is simply a glass plate, wall flare was negligible and LDV measurements could be made down into the sublayer. In the sublayer, the shear stress at the wall can be approximated as equation 3.4.2 due to the no-slip boundary condition.

$$\frac{\tau_w}{\rho} = \nu \frac{\partial U}{\partial y} \tag{3.4.2}$$

Since the wall shear is a constant, the velocity gradient must also be a constant in the sublayer. This means the velocity profile in the sublayer can be modeled as equation 3.4.3, where $m = \partial U/\partial y$.

$$U = my \tag{3.4.3}$$

By performing a linear fit to a measured set of U and y values, the wall shear can be measured. However, as the LDV measurement volume moves closer to the wall the y values recorded by the encoder need to be corrected to account for measurement volume truncation (see appendix C).

Although only a single smooth wall profile was examined, the friction velocity estimated from the Reynolds shear stress and the sublayer fit agree remarkably well. A simple fit to the semi-log portion of the mean velocity profile (described in section 3.5) also yielded a similar result.

Method	u_τ (m/s)
Sublayer Fit (uniform dist.)	0.889
Reynolds Shear Stress $\sqrt{-\overline{uv}}$	0.878
Log-Layer Fit ($\kappa = 0.41$)	0.850

Table 3.6: Smooth wall test

3.5 Fitting Methods

All fitting methods utilize model equations for the mean boundary layer profile. Therefore, any estimate of u_τ or other quantities derived from them include intrinsic assumptions, namely, that the model equation is a good representation of the actual velocity profile. Nonetheless, they offer a relatively simple means of obtaining u_τ and other parameters such as ΔU^+ and ϵ. The following sections explain three different models and the algorithms used to fit them to portions of the measured mean boundary layer profiles.

3.5.1 Simple Fit Method

The 'Simple Fit Method' (SFM) for estimating the friction velocity uses the dimensional form of the 'law-of-the-wall' (equation 3.5.1). A linear fit is performed to U vs. $\ln y$ to extract the parameters m and b, which are functions of u_τ, ΔU^+, and κ.

$$U = m \ln y + b \tag{3.5.1}$$

$$m = \frac{u_\tau}{\kappa} \tag{3.5.2}$$

$$b = \frac{u_\tau}{\kappa} \ln \frac{u_\tau}{\nu} - u_\tau (B - \Delta U^+) \tag{3.5.3}$$

Equation 3.5.1 is only applicable in the semi-logarithmic portion of the mean velocity profile. This region can be difficult to find for rough walls because the presence of the roughness elements and their wakes can distort this region near the wall. For each profile, the region where the correlation coefficient between the fit and the data was a maximum was found for a given number of sequential data points. The number of sequential data points used in the fit was also varied from three to the total (N) and the process was repeated for each number. The correlation coefficient is not a sufficient parameter to determine the number of points that results in the best fit. For such a few number of data points used, the correlation coefficient will always decrease as the number of points used is increased. This is due to the uncertainty in the measured data. However, including a greater number of data points in the fit is desirable to obtain more correct values for m and b, as long as the model equation is valid in the region over which the fit occurs. Hence, the estimate of the sample standard deviation (S_{est}) is used to help determine the best fit, where β_i is the residual between the data point and the value estimated by the curve fit and M is the number of parameters in the model equation.

$$S_{est} = \frac{1}{N - M} \sum_{i=1}^{N} \beta_i^2 \tag{3.5.4}$$

Figure 3.7 shows the estimate of the sample standard deviation vs. number of points used in the fit. The number of points that resulted in a 'best fit' was usually assumed to occur at

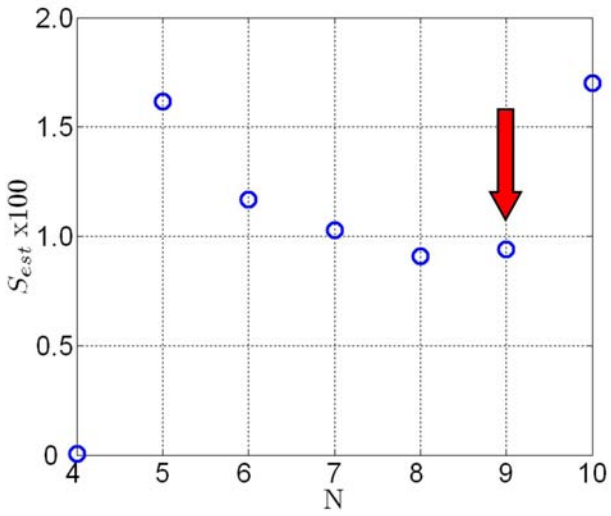

Figure 3.7: Estimated sample standard deviation vs. Number of points used in fit. Red arrow indicates the number of points considered optimum for this case.

a local minimum or just before a 'dramatic' increase in S_{est}, however some human judgment was required.

3.5.2 Simple Fit Method with ϵ

When the parameter ϵ is included in the model equation, an iterative approach is needed to perform a fit to the measured data. A least-squares approach was used to generate a system of nonlinear equations that were solved for m, b, and ϵ. Newton's method (equation 3.5.6) was used to solve these equations. The solution was insensitive to the initial parameter values and convergence was assumed to occur when ($\|-J^{-1}G\|$ <1x10^{-10}). The same procedure described for the SFM for finding the best region and optimal number of points was performed for this method as well.

$$\{G\} = \begin{Bmatrix} m\sum\left[\ln(y_i+\epsilon)\right]^2 - \sum U_i \ln(y_i+\epsilon) + b\sum\ln(y_i+\epsilon) \\ bN - \sum U_i + m\sum\ln(y_i+\epsilon) \\ m\sum\frac{\ln(y_i+\epsilon)}{y_i+\epsilon} - \sum\frac{U_i}{y_i+\epsilon} + b\sum\frac{1}{y_i+\epsilon} \end{Bmatrix} = \{0\} \tag{3.5.5}$$

$$\begin{Bmatrix} m \\ b \\ \epsilon \end{Bmatrix}_{k+1} = \begin{Bmatrix} m \\ b \\ \epsilon \end{Bmatrix}_{k} - [J]^{-1}\{G\} \tag{3.5.6}$$

$$
\begin{aligned}
J(1,1) &= \sum \left[\ln(y_i+\epsilon)\right]^2 \\
J(1,2) &= \sum \ln(y_i+\epsilon) \\
J(1,3) &= 2m\sum \tfrac{\ln(y_i+\epsilon)}{y_i+\epsilon} - \sum \tfrac{U_i}{y_i+\epsilon} + b\sum \tfrac{1}{y_i+\epsilon} \\
J(2,1) &= \sum \ln(y_i+\epsilon) \\
J(2,2) &= N \\
J(2,3) &= m\sum \tfrac{1}{y_i+\epsilon} \\
J(3,1) &= \sum \tfrac{\ln(y_i+\epsilon)}{y_i+\epsilon} \\
J(3,2) &= \sum \tfrac{1}{y_i+\epsilon} \\
J(3,3) &= (m-b)\left[\sum \tfrac{1}{(y_i+\epsilon)^2}\right] - m\sum \tfrac{\ln(y_i+\epsilon)}{(y_i+\epsilon)^2} + \sum \tfrac{U_i}{(y_i+\epsilon)^2}
\end{aligned}
\tag{3.5.7}
$$

3.5.3 Krogstad Fit Method

As mentioned in section 1.2.6, the method of Krogstad *et al.* [57] is a common fit method in the literature. It was used in the present work as well to assess it's performance. A least squares approach is used to optimize values of u_τ, ϵ, and Π in equation 3.5.8. The approach was identical to the previous section, however, the solution convergence was much more sensitive to the initial parameter values. Since equation 3.5.8 can be assumed valid through most of the boundary layer and since convergence was as issue, the procedure for finding the best region and optimal number of points was not performed. It should be noted that values for U_e and δ were required and a value for κ must be assumed.

$$
\frac{U}{U_e} = 1 + \frac{u_\tau}{\kappa U_e}\left\{\ln\left(\frac{y+\epsilon}{\delta}\right) - (1+6\Pi)\left[1-\left(\frac{y+\epsilon}{\delta}\right)^2\right] + (1+4\Pi)\left[1-\left(\frac{y+\epsilon}{\delta}\right)^3\right]\right\} \tag{3.5.8}
$$

3.5.4 Comparison to Independent Measure

Recall that three boundary layer profiles were measured on each of three different days for each case, and that the profiles on a given day were each separated by ∼100 mm. Each fitting method described above was applied to the center profile from each of the three days and the results averaged together. A typical result is shown in figure 3.8. The results for the friction velocity are shown in table 3.7 along with the results obtained from the integral momentum balance explained in section 3.4.1. The friction velocity estimates from the SFM and the SFM with ϵ were found using $u_\tau = m\kappa$. For all fitting methods it was assumed that $\kappa = 0.41$.

The results show that the fitting methods consistently overestimate the friction velocity for the rough wall cases (3-10). Including ϵ in the SFM seems to increase the error, however, the Krogstad method can sometimes give results similar to the SFM. Figure 3.9 shows a comparison between the u_τ estimates from the integral momentum balance, SFM, and

Case No.	Day	u_τ (m/s)			
		Int. Mom. Bal.	SFM	SFM w/ ϵ	Krogstad
1	1	1.019	1.144	1.379	1.216
	2	0.973	1.106	1.369	1.211
	3	0.997	1.147	1.297	-
2	1	0.685	0.794	1.010	1.005
	2	0.692	0.791	1.058	0.113
	3	0.694	0.743	1.047	0.830
3	1	1.153	1.392	1.520	1.129
	2	1.128	1.383	1.525	1.209
	3	1.123	1.378	1.473	1.099
4	1	0.874	1.022	1.285	1.028
	2	0.848	1.052	1.255	1.043
	3	0.849	1.034	1.181	1.045
5	1	1.241	1.395	1.878	1.769
	2	1.209	1.469	1.923	1.654
	3	1.180	1.364	1.780	1.527
6	1	0.844	1.017	1.352	1.290
	2	0.874	1.048	1.355	1.438
	3	0.848	1.060	1.320	1.444
7	1	1.221	1.201	1.840	2.107
	2	1.208	1.238	1.787	1.704
	3	1.217	1.273	1.793	1.504
8	1	0.878	0.949	1.106	1.104
	2	0.853	0.808	1.050	1.071
	3	0.859	0.965	1.072	1.070
9	1	1.080	1.348	1.564	1.413
	2	1.068	1.321	1.511	1.251
	3	1.074	1.329	1.538	1.311
10	1	0.823	1.049	1.202	1.063
	2	0.830	1.036	1.182	1.116
	3	0.821	0.964	1.156	1.051

Table 3.7: Comparison of fitting methods

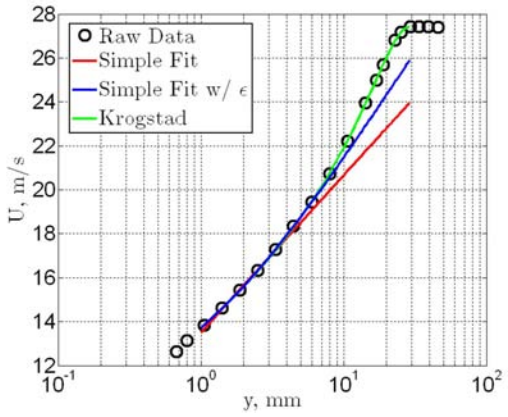

Figure 3.8: Typical result from fitting methods. Results shown from Case 7.

SFM w/ ϵ. It is clear from the segregation of the data that random uncertainty alone cannot be to blame for the poor agreement. This suggests that either the functional form of equation 1.2.2 is not valid or the model constants are in error.

The results of the fitting methods are highly dependent on the assumed value for κ. Therefore, due to the fact that the fitting methods all over predict u_τ, using an assumed value of $\kappa = 0.41$, it would seem the smooth wall von Kármán constant is not appropriate for rough walls. It should be noted that the SFM agrees fairly well with the smooth wall results from the integral momentum balance. However, the other fitting methods still produce a high estimate. This may be due to the uncertainty associated with estimating small ϵ values.

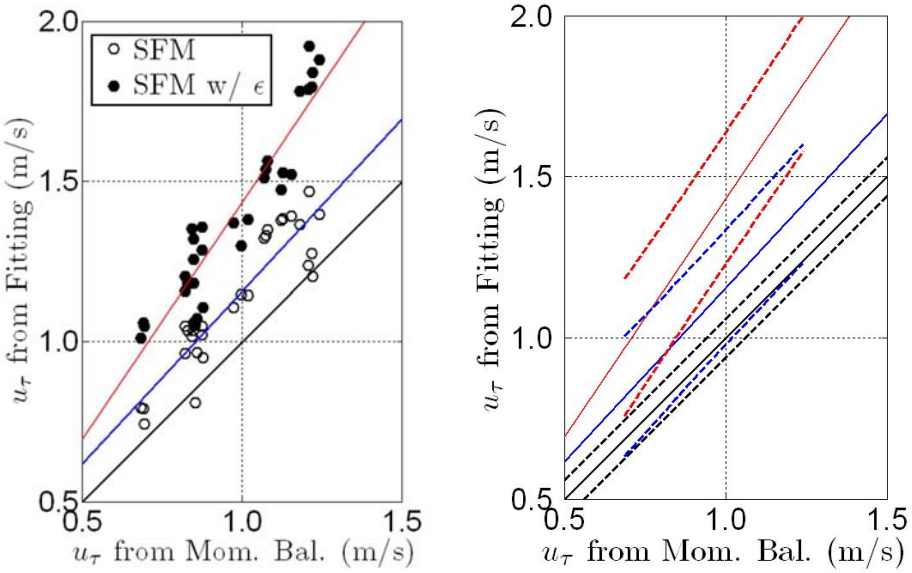

Figure 3.9: Comparison of friction velocity estimates from momentum balance and fitting methods. Solid red and blue lines from linear regression. Black line has slope of one. Dashed lines indicate uncertainty bounds at 95%.

3.6 Scaling the Boundary Layer Profile

One representative mean velocity profile measured on one day is plotted in figure 3.10(a) for each case. Figure 3.10(b) shows the same profiles normalized on inner variables, where u_τ is measured from the integral momentum balance. The effect of the rough surface can be seen in the downward shift ΔU^+ as explained in section 1.2.3. Although case 1 is designated as smooth, the apparent ΔU^+ would suggest there is some small amount of surface roughness present. This is not surprising as the tunnel roof section (section 2.3) is not completely smooth to the touch. However, at the lower speed of 20 m/s measured in case 2, there appears to be little effect of the roughness. Of course, as explained in section 1.2.1, it is expected that as U_e decreases the surface-flow interaction tends toward hydrodynamically smooth.

In order to examine the applicability of the form of equation 1.2.2 to model rough wall turbulent boundary layers, the SFM and SFM w/ ϵ were applied to the mean velocity profiles. The constant κ was assumed to be 0.41 and a value for u_τ was computed via equation 3.5.2. Equation 3.5.3 was used to solve for ΔU^+. The results are shown in figure 3.11. When the SFM is applied and the displacement height ϵ is ignored, the data collapses only in a small portion of the semilog region. However, if ϵ is included, the collapse is excellent over most of the semilog region. This gives support to the validity of the function form of equation 1.2.2. However, this collapse was only achieved by choosing an optimum value of u_τ for an assumed value of κ. As seen from section 3.5 if u_τ is estimated in this way it does not reflect the true value of the skin friction.

The mean velocity profiles are again shown in figure 3.12. This time the correct value of u_τ is used and the SFM and SFM w/ ϵ are used only to measured ΔU^+ and ϵ. As can be seen, the normalized profiles have a rather poor collapse overall. Although, if ϵ is included a better collapse is achieved. If it can be assumed that the measured value of u_τ is correct with reasonable certainty, then this result implies that κ cannot be a constant value in equation 1.2.2. Therefore, the challenge is to relate not only ΔU^+ and ϵ to the rough surface geometry, but potentially κ as well.

3.7 Modeling Roughness

Now that the functional form of equation 1.2.2 has been verified in section 3.6, correlations for κ, ΔU^+, and ϵ are required. All three have been measured via SFM and the SFM w/ ϵ as discussed in section 3.5. The usual model for ΔU^+ is given in equation 1.2.4. It is repeated here for convenience. The parameter $f(\cdot)$ is a function of the rough geometry alone. Its value can be computed by combining equation 3.5.3 and 3.7.1, which results in equation 3.7.2 below.

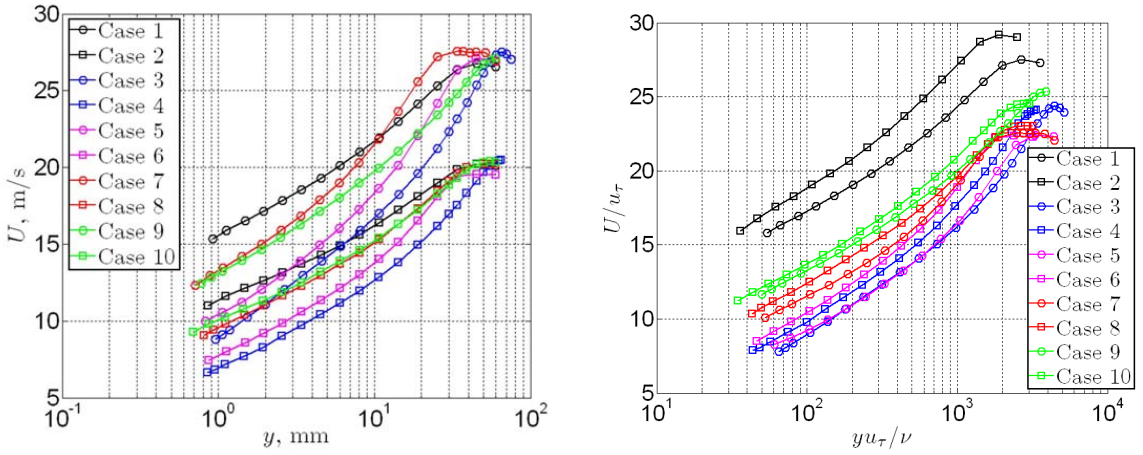

(a) Dimensional streamwise velocity profiles

(b) Profiles normalized on u_τ from momentum balance

Figure 3.10: Dimensional and normalized mean velocity profiles

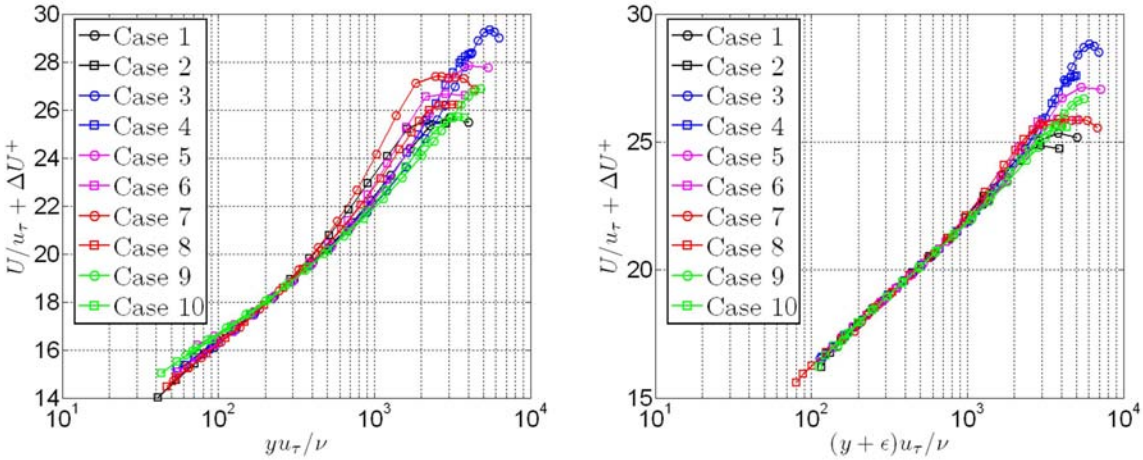

(a) u_τ and ΔU^+ from SFM

(b) u_τ and ΔU^+ from SFM w ϵ

Figure 3.11: Streamwise velocity profiles normalized on inner variables estimated from fitting methods

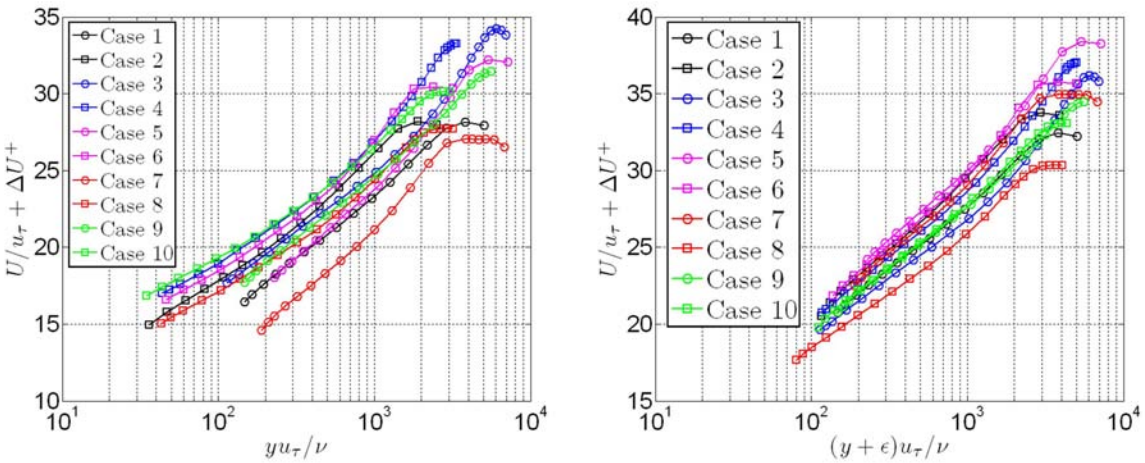

(a) u_τ from Mom. Bal., ΔU^+ from SFM (b) u_τ from Mom. Bal., ΔU^+ from SFM w/ ϵ

Figure 3.12: Streamwise velocity profiles normalized on inner variables

$$\Delta U^+ = \frac{1}{\kappa} \ln \frac{k_s u_\tau}{\nu} + f(\cdot) \tag{3.7.1}$$

$$f(\cdot) = \frac{b}{u_\tau} - \frac{1}{\kappa} \ln \left(\frac{k u_\tau}{\nu} \right) + B \tag{3.7.2}$$

Results from the fitting methods are presented in table 3.8. Both methods give two values of $f(\cdot)$ depending on whether or not u_τ is measured using the integral momentum balance or estimated by assuming $\kappa = 0.41$ via equation 3.5.2.

3.7.1 The von Kármán Constant

As figure 3.13 shows, the uncertainty in measured values of κ is perhaps too high to construct a reliable correlation. However, it is quite possible that κ would be a function of δ/k, which represents a ratio of outer to inner scales of turbulent motion. This same concept of overlapping inner and outer scales is used in the derivation of the law of the wall. For the smooth wall the inner scale was entirely based on the wall shear and the viscosity. This however is not the case if the surface-flow interaction is fully rough. Instead, the wall law should be independent of viscosity. There is no reason therefore that κ should remain a constant for rough wall flows. In fact, Townsend [27] attempts to mathematically estimate κ by modeling the near wall turbulent flow as an attached 'double-cone' eddy and equating the rate of transfer of energy from the mean flow and the rate of energy loss due to smaller eddies. His solution was dependent on the inclination of this attached eddy. If κ does in fact depend on the structure of the near wall turbulence which is modified by a rough wall, then it is not unthinkable to expect κ to be partially a function of the roughness geometry as well as the outer scales of the flow. The roughness length scale used here is the height k.

Case No.	Day	Simple Fit Method				Simple Fit Method w/ ϵ			
		κ	$f(\cdot)$	κ	$f(\cdot)$	κ	$f(\cdot)$	κ	$f(\cdot)$
3	1	0.340	-2.44	0.410	-1.17	0.311	-1.77	0.410	-0.14
	2	0.334	-2.77	0.410	-1.34	0.303	-2.11	0.410	-0.26
	3	0.334	-2.64	0.410	-1.23	0.312	-2.15	0.410	-0.45
4	1	0.351	-2.77	0.410	-1.65	0.279	-1.15	0.410	0.81
	2	0.331	-2.77	0.410	-1.26	0.277	-1.34	0.410	0.72
	3	0.337	-2.68	0.410	-1.31	0.295	-1.71	0.410	0.18
5	1	0.365	-3.07	0.410	-2.18	0.271	-0.96	0.410	1.06
	2	0.337	-2.95	0.410	-1.54	0.258	-0.68	0.410	1.43
	3	0.355	-3.14	0.410	-2.04	0.272	-1.23	0.410	0.87
6	1	0.340	-3.75	0.410	-2.26	0.256	-1.61	0.410	0.87
	2	0.342	-3.53	0.410	-2.12	0.264	-1.65	0.410	0.71
	3	0.328	-3.54	0.410	-1.83	0.263	-1.72	0.410	0.68
7	1	0.417	-5.82	0.410	-6.00	0.272	-3.40	0.410	-0.57
	2	0.400	-5.78	0.410	-5.53	0.277	-3.71	0.410	-0.89
	3	0.392	-6.10	0.410	-5.61	0.278	-4.08	0.410	-1.16
8	1	0.379	-5.78	0.410	-4.97	0.325	-4.90	0.410	-2.86
	2	0.433	-6.35	0.410	-6.98	0.333	-5.01	0.410	-3.13
	3	0.365	-5.74	0.410	-4.57	0.329	-5.05	0.410	-3.05
9	1	0.328	-6.93	0.410	-4.56	0.283	-5.55	0.410	-2.28
	2	0.331	-6.52	0.410	-4.32	0.290	-5.27	0.410	-2.26
	3	0.331	-6.21	0.410	-4.06	0.286	-4.81	0.410	-1.85
10	1	0.322	-6.69	0.410	-4.17	0.281	-5.37	0.410	-2.11
	2	0.328	-6.31	0.410	-4.06	0.288	-5.05	0.410	-2.06
	3	0.349	-6.71	0.410	-4.97	0.291	-5.24	0.410	-2.27

Table 3.8: Comparison of modeling parameters for different fitting methods

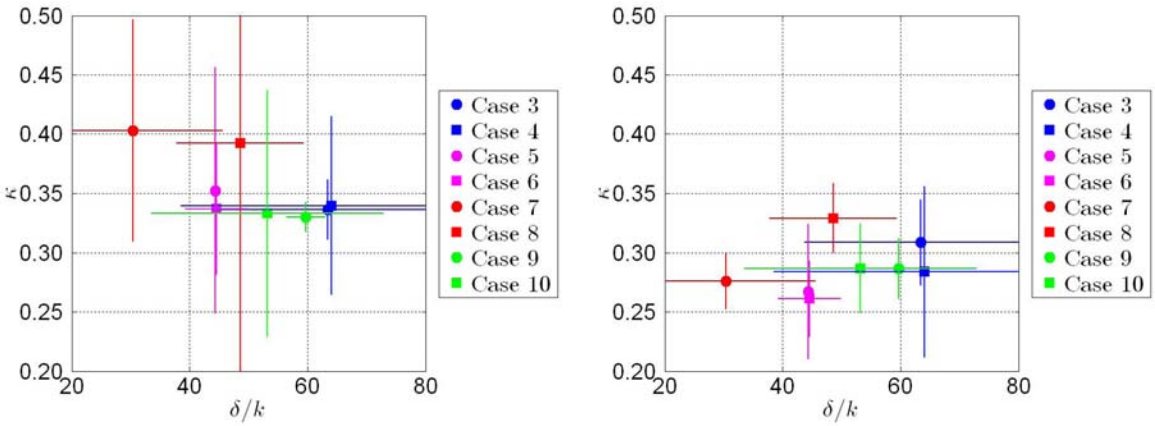

(a) SFM (b) SFM w/ ϵ

Figure 3.13: Estimated κ values with uncertainties for 95% confidence level

It is worth noting that when ϵ is included in the analysis, the estimated values for κ are much more certain. This makes intuitive sense, because the region over which a good fit can occur without considering ϵ is small. Although there is still significant scatter in the data, it appears that a smooth wall value for κ is not appropriate for this data. Perhaps a slight trend can be inferred as well, when this data is plotted with data from other researchers (figure 3.14). As δ/k becomes smaller, κ departs further from its smooth wall value. This is expected if indeed the above hypothesis is true. If the roughness modifies the turbulent structure in such a way that κ is modified, then as the roughness elements become larger and larger they would modify a larger portion of the boundary layer and hence have a greater effect on κ.

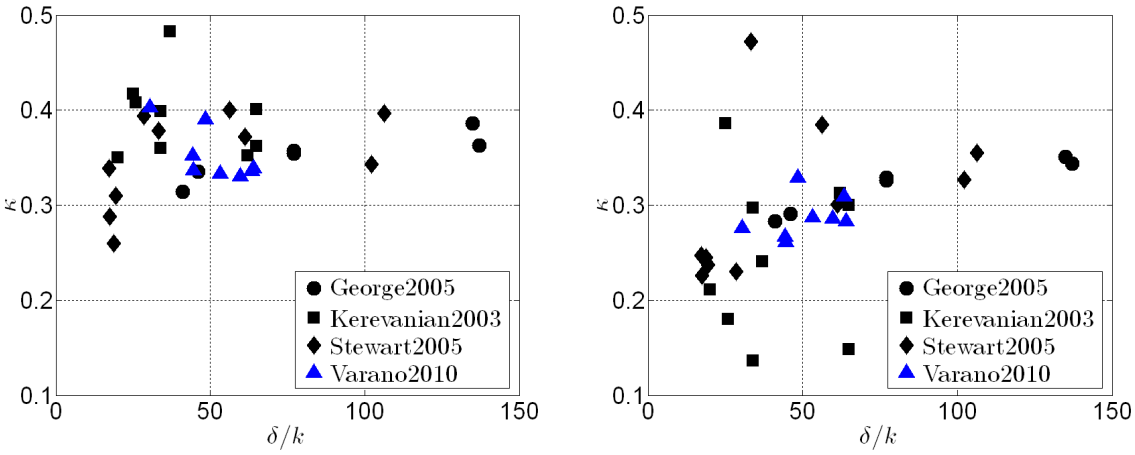

(a) SFM (b) SFM w/ ϵ

Figure 3.14: Estimated κ values with other available data

3.7.2 The Roughness Function $f(\cdot)$

The estimates for $f(\cdot)$ in table 3.8 are plotted in figure 3.15 with uncertainty estimates at a 95 percent confidence level. The high uncertainty reveals the challenge in trying to develop correlations for this term. Uncertainty levels are affected primarially by the estimate of u_τ and the fitting method. It appears that when the fitting method is used to compute u_τ instead of the momentum balance, the uncertainty is slightly higher.

When plotted with data from other researchers, the difference between different fitting methods is apparent. This reinforces the necessity to measure u_τ by some independent method. Figure 1.2.6 and figure 1.2.8 examine the correlations of Dvorak and Waigh respectively from section 1.2.5. They are given again here for convenience. Considering the uncertainty levels, the scatter in the data for both cases is perhaps as good of a collapse as one can expect. This suggests serious limitations to the possibility of being able to know $f(\cdot)$ *a priori* simply by knowing the surface geometry.

$$f(\lambda) = -2.85 \ln \lambda + 5.95 \,, \;\; \lambda > 5 \tag{3.7.3}$$

$$f(\lambda, k/b, A_w/A_f) = -2.50 \ln \lambda^{-1} (k/b)^{0.55} (A_w/A_f)^1.38 + 5.78 \,, \;\; \Lambda > 6 \tag{3.7.4}$$

It is possible that a different roughness length scale should be used in equation 3.7.2 instead of the roughness height k. Since taller elements will disproportionately contribute to the drag it is possible that a higher moment of the surface elevation would be an appropriate scale. Direct numerical simulations of Ikeda et al. [78] seem to indicate that the second moment of the surface elevation is correct. Equations 3.7.5 and 3.7.6 give expressions for the characteristic roughness length scale for hemispherical and cylindrical elements respectively based on the second moment of the surface elevation, The radius of each is denoted by R and s^2 is the planform area of a roughness 'cell'. Keeping dimensional considerations in mind, the cube root is employed. Figure 3.18 shows the results of these efforts. In general, there is no better collapse using this new length scale. However, uncertainties in the measured values of $f(\cdot)$ are considerable and are sure to limit the collapse of successful scaling parameters.

$$\left(\overline{y^3}\right)^{1/3}_{hemi} = \frac{2\pi}{5} \frac{R^5}{s^2} \tag{3.7.5}$$

$$\left(\overline{y^3}\right)^{1/3}_{cyl} = \left(\frac{\pi R^2}{s^2}\right)^{1/3} k \tag{3.7.6}$$

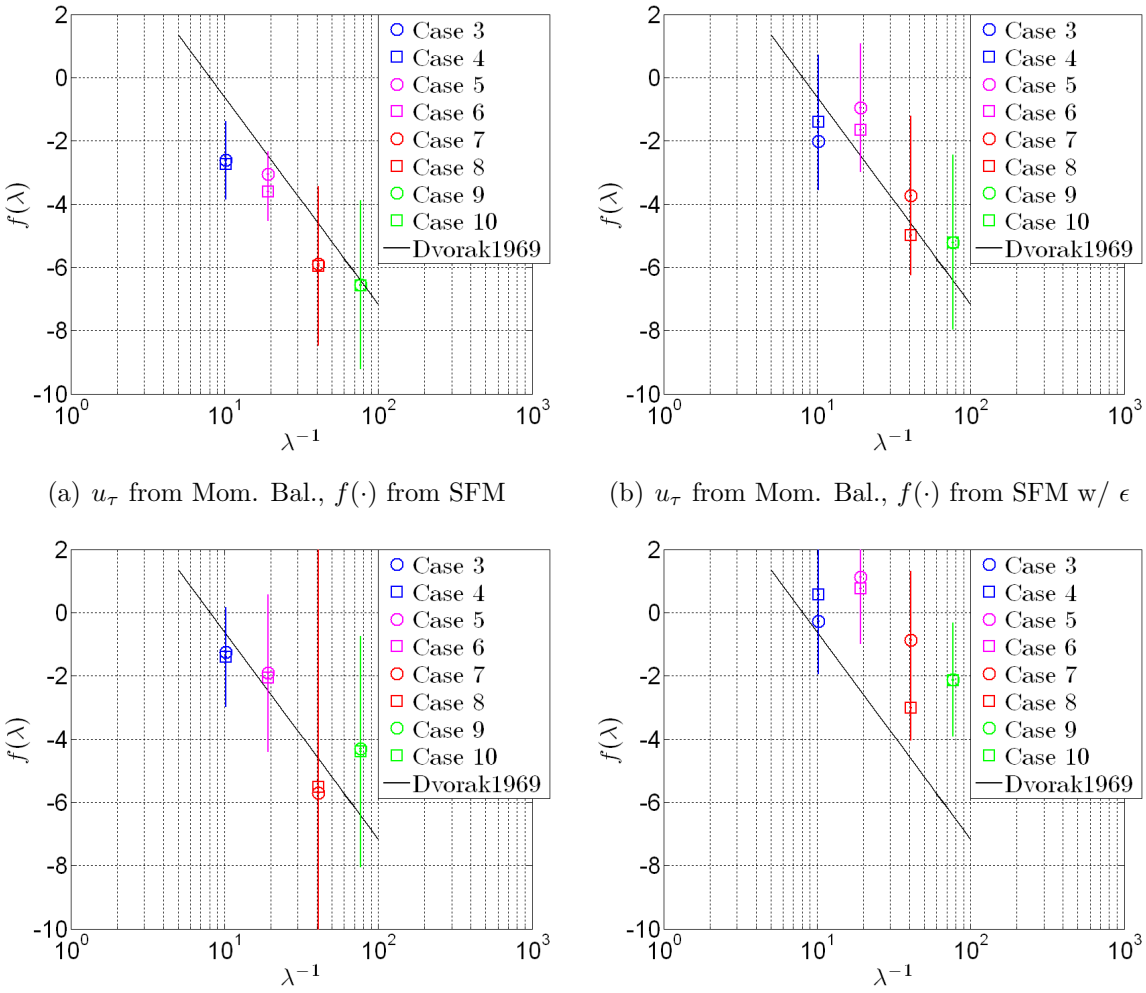

(a) u_τ from Mom. Bal., $f(\cdot)$ from SFM

(b) u_τ from Mom. Bal., $f(\cdot)$ from SFM w/ ϵ

(c) u_τ and $f(\cdot)$ from SFM

(d) u_τ and $f(\cdot)$ from SFM w/ ϵ

Figure 3.15: Estimated $f(\lambda)$ values with uncertainties for 95% confidence level

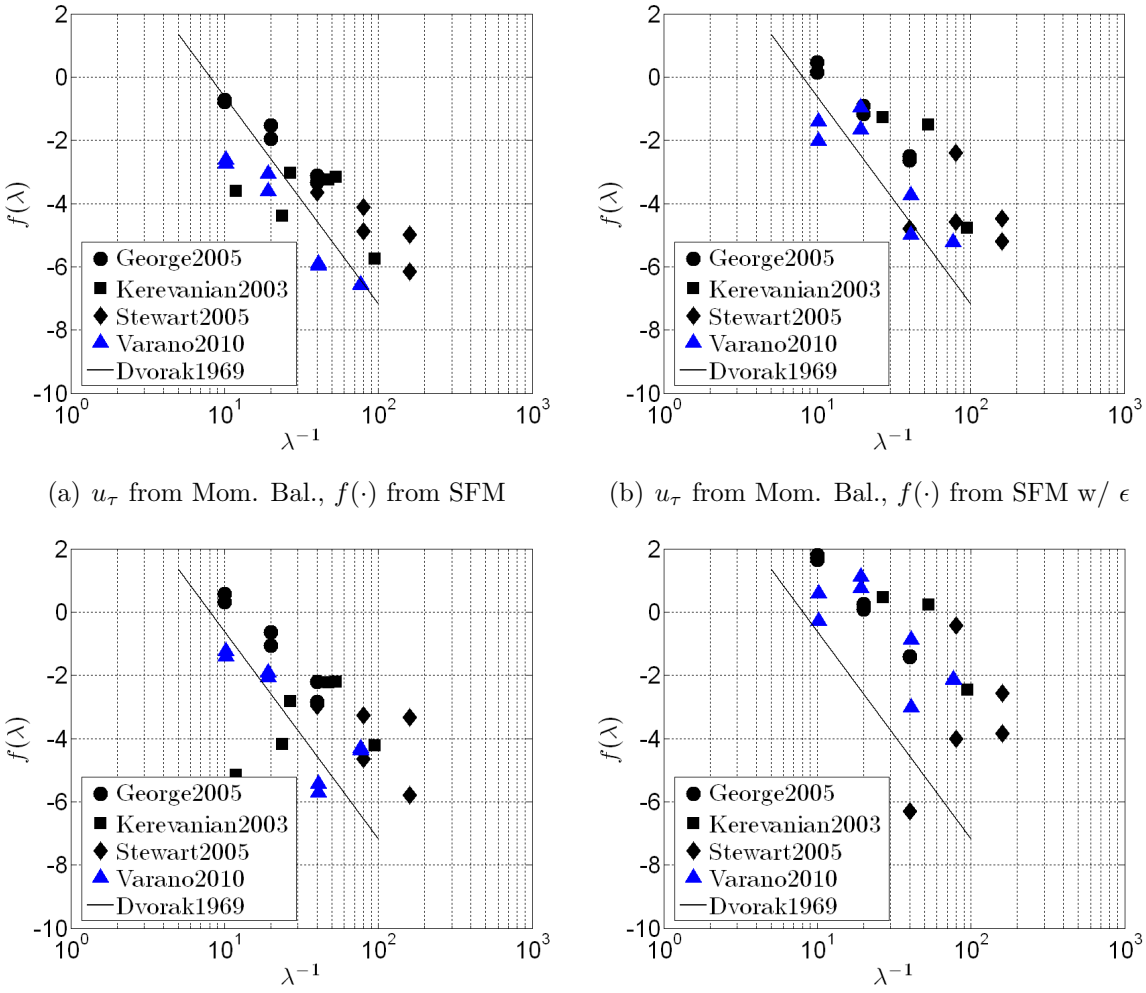

(a) u_τ from Mom. Bal., $f(\cdot)$ from SFM

(b) u_τ from Mom. Bal., $f(\cdot)$ from SFM w/ ϵ

(c) u_τ and $f(\cdot)$ from SFM

(d) u_τ and $f(\cdot)$ from SFM w/ ϵ

Figure 3.16: Estimated $f(\lambda)$ values with other available data and Dvorak's correlation

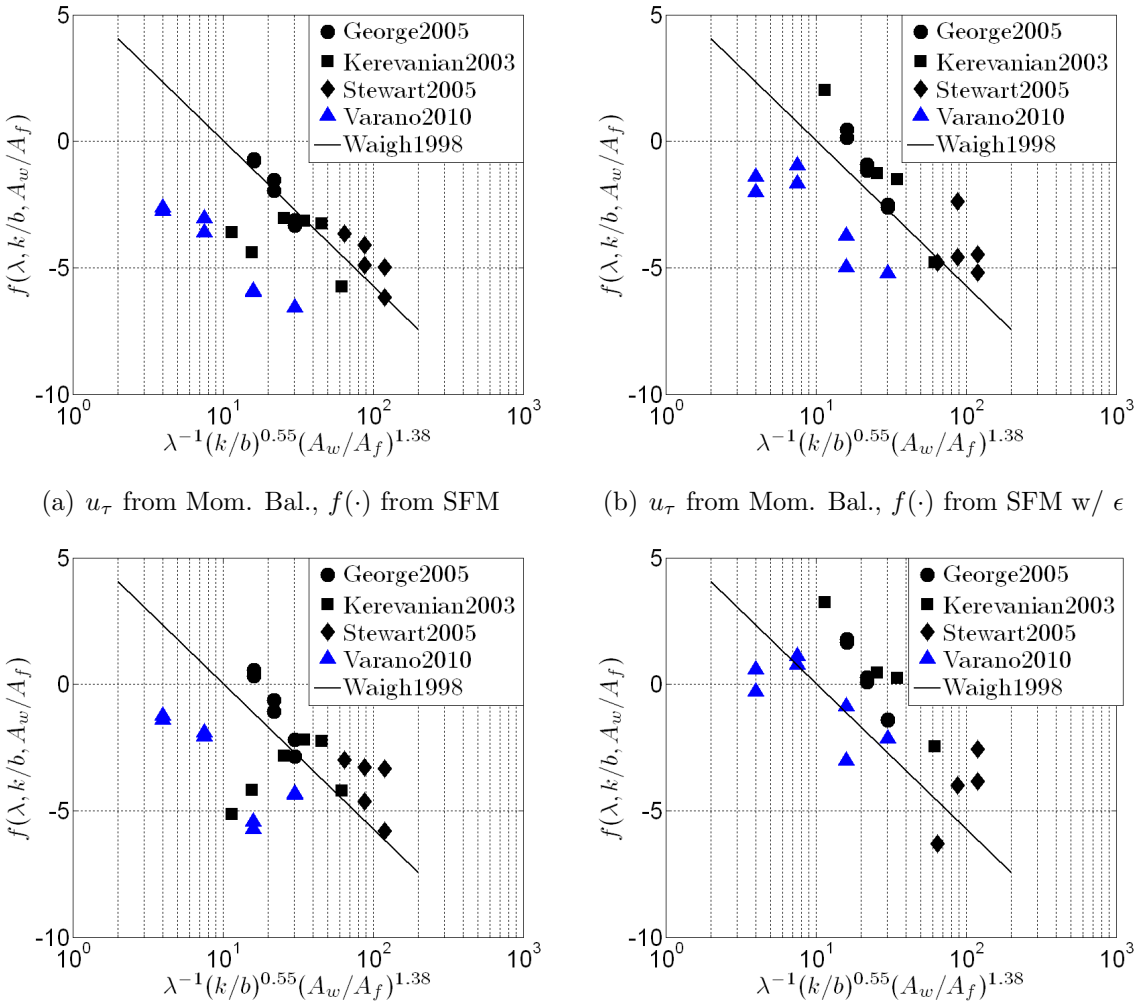

(a) u_τ from Mom. Bal., $f(\cdot)$ from SFM

(b) u_τ from Mom. Bal., $f(\cdot)$ from SFM w/ ϵ

(c) u_τ and $f(\cdot)$ from SFM

(d) u_τ and $f(\cdot)$ from SFM w/ ϵ

Figure 3.17: Estimated $f(\cdot)$ values with other available data and Waigh's correlation

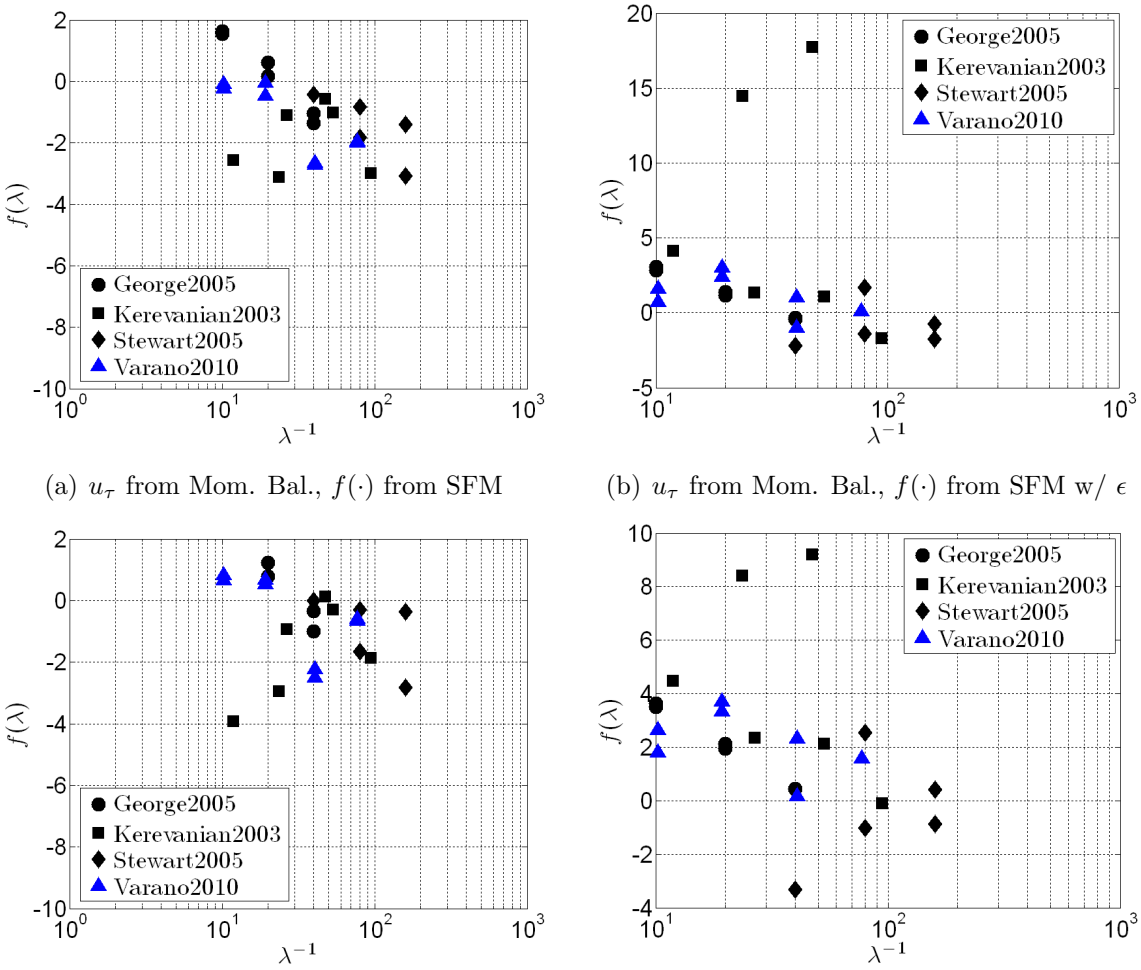

(a) u_τ from Mom. Bal., $f(\cdot)$ from SFM

(b) u_τ from Mom. Bal., $f(\cdot)$ from SFM w/ ϵ

(c) u_τ and $f(\cdot)$ from SFM

(d) u_τ and $f(\cdot)$ from SFM w/ ϵ

Figure 3.18: Estimated $f(\lambda)$ values with other available data and $k_c = \left(\overline{y^3}\right)^{1/3}$

3.7.3 The Displacement Height, ϵ

The computed values for displacement height from the SFM w/ ϵ and Krogstad method are given in table 3.9. It is worth mentioning that u_τ does not have any effect when using the SFM w/ ϵ compute ϵ. The scatter in the data from day to day is very high, and the large values of ϵ for the smooth wall cases is particularly revealing. This makes developing any correlation difficult, but nevertheless an attempt is made here.

As explained in section 1.2.5, Stewart [45] estimated ϵ as the volume of the roughness elements and separation regions over the planform area. The challenge then, is to estimate the downstream extent of the separation region H_{DS}. Although LDV measurements were not made near enough to the wall estimate H_{DS}, it was possible to extract the information from oil flow visualizations. The flow visualizations were not intentional, but instead a side effect of the seed particles used for the LDV measurements (see section 2.1.2). Over time, seed particles were deposited around the roughness elements such that the separation regions become visible as shown in figure 3.19. From these photographs H_{DS} was estimated to be 5 mm. For fetches 1 and 2 (4.0 and 5.5 mm spacing respectively) the separation regions extended to the downstream elements, therefore the volume was approximated as a hemisphere that extends infinitely downstream. This resulted in equation 3.7.8.

Figure 3.21 plots the present results with some available data from the literature. Although there is considerable scatter, a possible trend can be observed. The scatter and the mean value of ϵ increases for increasing values of the roughness height k. This supports the hypothesis of that ϵ is a measure the displacement of the mean streamlines of the flow above the surface. The increased scatter probably is probably a result of local flow effects due to the presence near which a profile was made.

$$\epsilon = V_T/A_p = 1/A_p \left(1/6\pi k^3 + V_E + 1/6 * \pi k^2 H_{DS}\right) \tag{3.7.7}$$

$$\epsilon = 1/A_p \left(1/2\pi k^2 s\right) \tag{3.7.8}$$

Much of the data from this research revealed ϵ to be a positive number only when the model equation (equation 1.2.2) is expressed in terms of $(y + \epsilon)$. This indicates that the measured mean velocity profile deviates from the law of the wall in such a way that the normalized mean velocity is increased near the wall. However, if ϵ_1 is defined as the height at which the boundary layer away from the wall 'perceives' the wall location, then physically it would seem intuitive that the model equation should be written in terms of $(y - \epsilon_1)$ and ϵ_1 be a positive value in general. However, for this hypothesis to be consistent with the measured data, the model equation needs to be modified. To facilitate this modification a mixing length l is defined in equation 3.7.9, where a characteristic smallest eddy size (k_c) based on the roughness height is incorporated into the traditional mixing length formulation.

Case No.	V_T/A_p (mm)	SFM w/ ϵ (mm)			Krogstad (mm)		
		Day 1	Day 2	Day 3	Day 1	Day 2	Day 3
1	0.000	0.913	0.860	0.489	0.470	0.506	-
2	0.000	0.838	0.953	0.981	0.658	1.555	0.906
3	0.393	0.348	0.281	0.239	-0.310	-0.252	-0.381
4	0.393	0.701	0.690	0.455	0.104	0.185	0.138
5	0.286	0.977	1.133	0.866	1.019	0.834	0.562
6	0.286	0.916	0.813	0.897	0.985	1.309	1.770
7	0.082	0.984	0.819	0.838	1.884	0.952	0.547
8	0.082	0.394	0.647	0.358	0.494	0.750	0.436
9	0.043	0.883	0.841	0.956	0.554	0.273	0.432
10	0.043	0.862	0.859	0.819	0.500	0.745	0.578

Table 3.9: Displacement height from fitting methods

$$l = k_c + \kappa(y - \epsilon_1) \tag{3.7.9}$$

If this new mixing length formulation is used in equation 3.7.10 to express the friction velocity, then by integration, a new wall law can be found (equation 3.7.11) which incorporates information about the roughness length scales.

$$u_\tau^2 = l^2 \left(\frac{\partial U}{\partial y}\right)^2 \tag{3.7.10}$$

$$\frac{U}{u_\tau} = \frac{1}{\kappa} ln \left|k_c + \kappa \left(y - \epsilon_1\right)\right| + \frac{1}{\kappa} ln \left|\frac{u_\tau}{\nu\kappa}\right| + B - \Delta U^+ \tag{3.7.11}$$

By equating the terms inside the first logarithms of equations 1.2.2 and 3.7.11, it is possible to form an expression for ϵ_1 in terms of the measured value of ϵ and κ. Computed values of ϵ_1 are given in table 3.10 for various values of k_c for the hemispherical roughness elements, including several fractions of the roughness height k and $(\overline{y^3})^{1/3}$ computed from equation 3.7.5. It appears $k_c = k/3$ gives the most reasonable results.

$$\epsilon_1 = \frac{k_c}{\kappa} - \epsilon \tag{3.7.12}$$

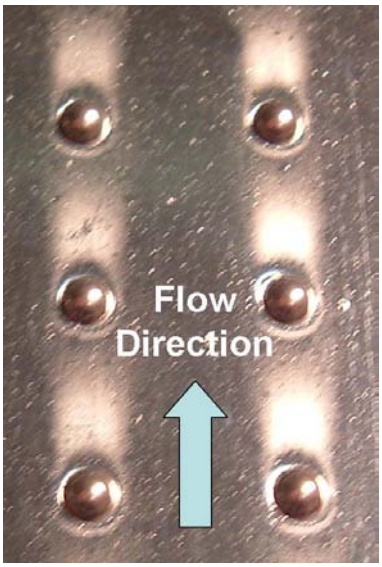

Figure 3.19: Flow visualization of separation regions behind hemispheres. Fetch 3, 8.0 mm spacing.

Case No.	ϵ_1, mm			
	k	$k/2$	$k/3$	$(\overline{y^3})^{1/3}$
3	2.948	1.329	0.790	1.097
4	2.913	1.149	0.561	0.896
5	2.757	0.883	0.258	0.306
6	2.953	1.039	0.401	0.450
7	2.746	0.933	0.328	0.098
8	2.573	1.053	0.547	0.354
9	2.599	0.853	0.271	-0.131
10	2.643	0.898	0.317	-0.085

Table 3.10: Displacement height for new semilog law formulation, ϵ_1, with various values of the roughness height used.

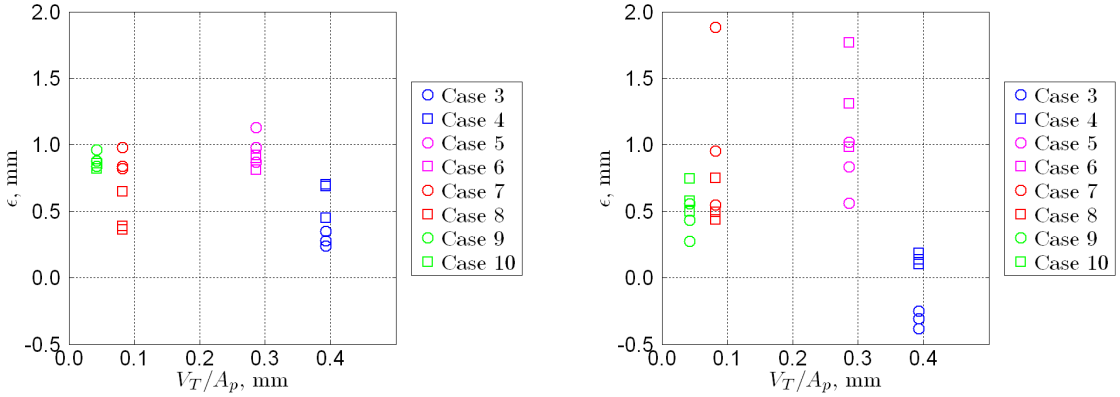

(a) SFM w/ ϵ (b) Krogstad fit method

Figure 3.20: Displacement height estimates from SFM w/ ϵ

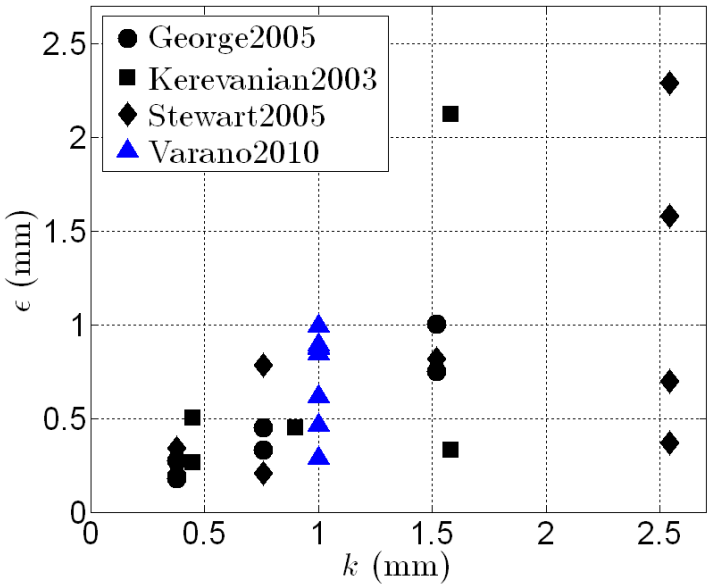

Figure 3.21: Displacement height estimated from SFM w/ ϵ with other available data

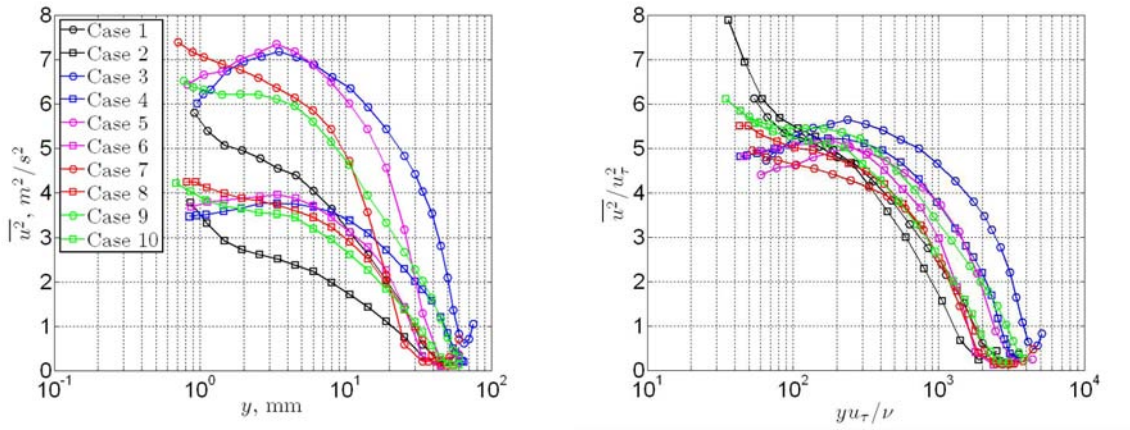

(a) Dimensional (b) Normalized

Figure 3.22: Reynolds normal stress $\overline{u^2}$

3.8 Reynolds Stresses

Figures 3.22 through 3.27 show profiles of the Reynolds stresses in dimensional and normalized form. Normalization is performed using u_τ computed from the integral momentum balance as explained in section 3.4.1. There are a few things of note concerning the Reynolds stresses. First, although data is not available very near the wall for these profiles, it appears that the peak in the $\overline{u^2}$ profile is nonexistent for the roughest cases (cases 3-6). This could indicate .... There also seems to be little difference in the magnitude of the $\overline{u^2}$ profiles for the lower speed cases, but a segregation between the more and less rough cases at the high speed. Second, the $\overline{v^2}$ profiles seem to scale very well on inner variables as expected, although a collapse of the $\overline{w^2}$ profiles is less impressive. Finally, the profiles of the Reynolds shearing stress $\overline{uv}$ show good collapse in the constant region. This simply shows that the Reynolds stress $\sqrt{-\overline{uv}}$ is a good approximation for the friction velocity as explained in section 3.4.1. Also, it is worth noting that the constant region is larger for the more rough cases (cases 3-6). This indicates that the roughness is increasing the overlap region of the boundary layer.

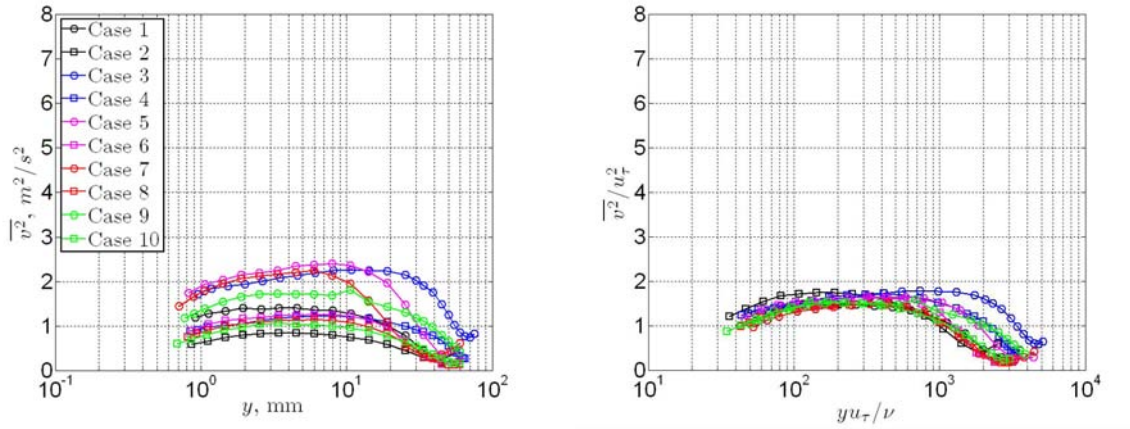

(a) Dimensional (b) Normalized

Figure 3.23: Reynolds normal stress $\overline{v^2}$

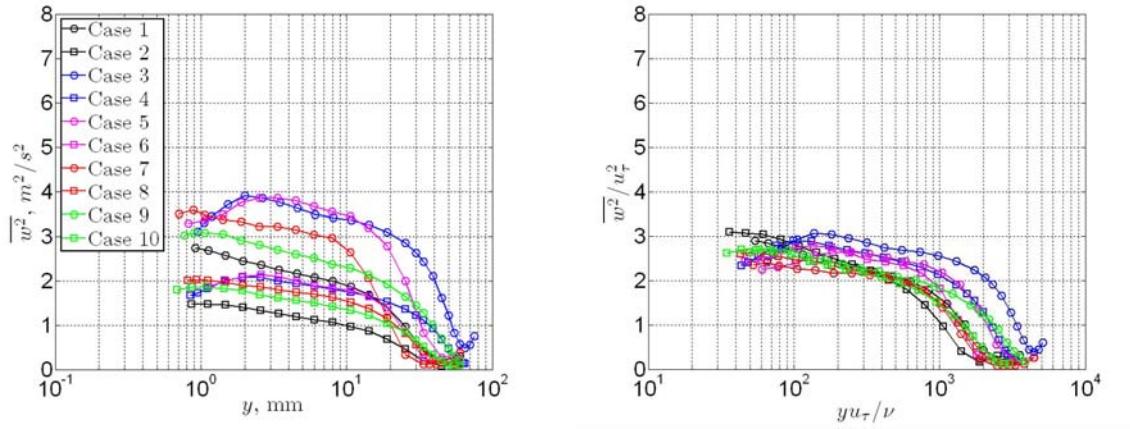

(a) Dimensional (b) Normalized

Figure 3.24: Reynolds normal stress $\overline{w^2}$

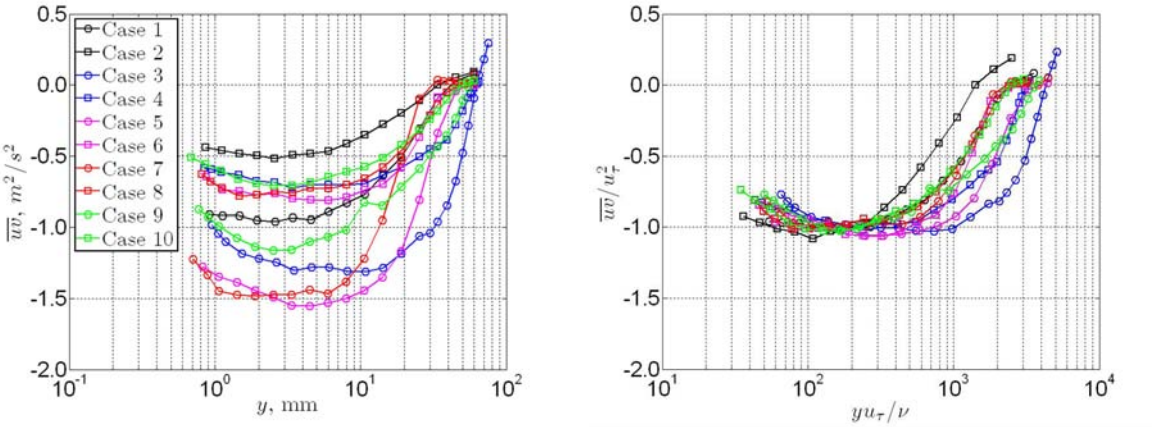

(a) Dimensional (b) Normalized

Figure 3.25: Reynolds shear stress $\overline{uv}$

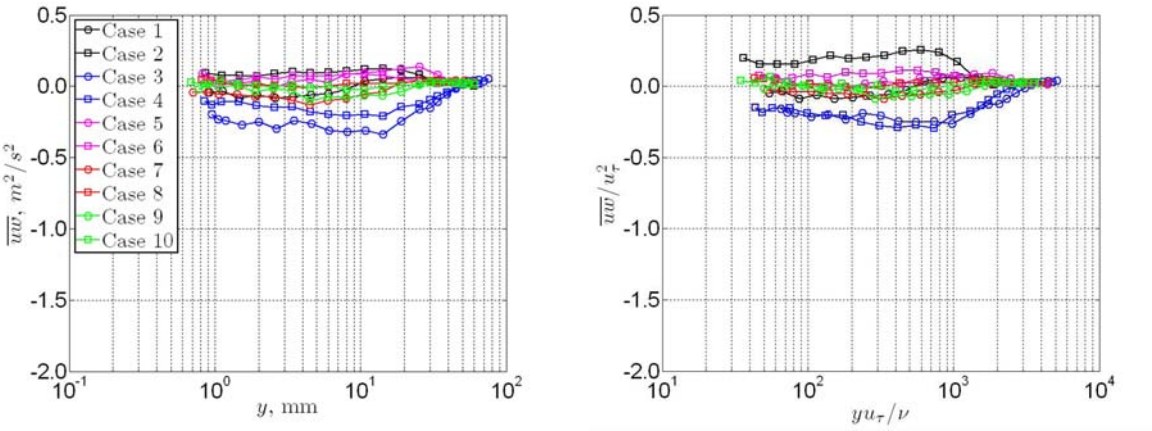

(a) Dimensional (b) Normalized

Figure 3.26: Reynolds shear stress $\overline{uw}$

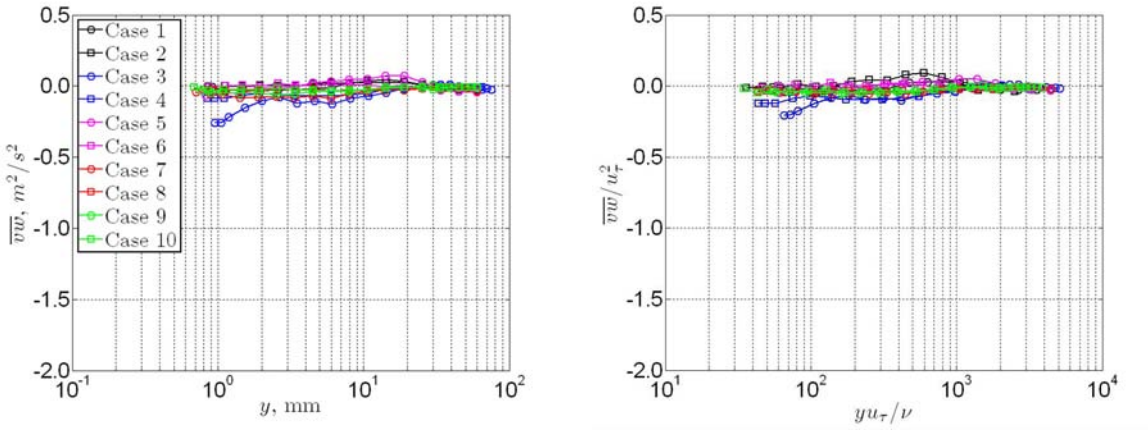

(a) Dimensional (b) Normalized

Figure 3.27: Reynolds shear stress $\overline{vw}$

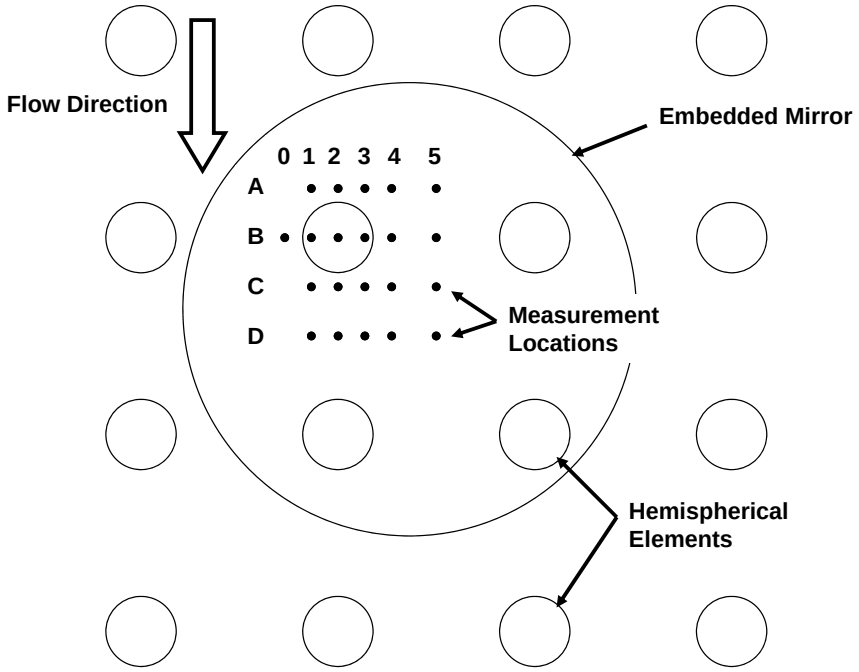

Figure 3.28: Locations of local flow measurements for Fetch 2

3.9 Local Effects

3.9.1 Measurement Locations

To interrogate the local flow structure around roughness elements, twenty-one partial boundary layer profiles were measured inside an element 'cell' for case 5. The measurement locations are shown in figure 3.28 and their coordinates are listed in table 3.11. Figure 3.29 shows the relative position of the contour planes. It is important to note that because the roughness fetches were attached to the ceiling of the wind tunnel, measurements could be made directly above the roughness element.

Row ID	Column Number					
	0	1	2	3	4	5
A	-	(-1.38,0.75)	(-1.38,0.00)	(-1.38,-0.75)	(-1.38,-1.50)	(-1.38,-2.75)
B	(0.00,1.50)	(0.00,0.75)	(0.00,0.00)	(0.00,-0.75)	(0.00,-1.50)	(0.00,-2.75)
C	-	(1.38,0.75)	(1.38,0.00)	(1.38,-0.75)	(1.38,-1.50)	(1.38,-2.75)
D	-	(2.75,0.75)	(2.75,0.00)	(2.75,-0.75)	(2.75,-1.50)	(2.75,-2.75)

Table 3.11: Table of local flow measurement locations (x,z) for Case 5. Units in millimeters.

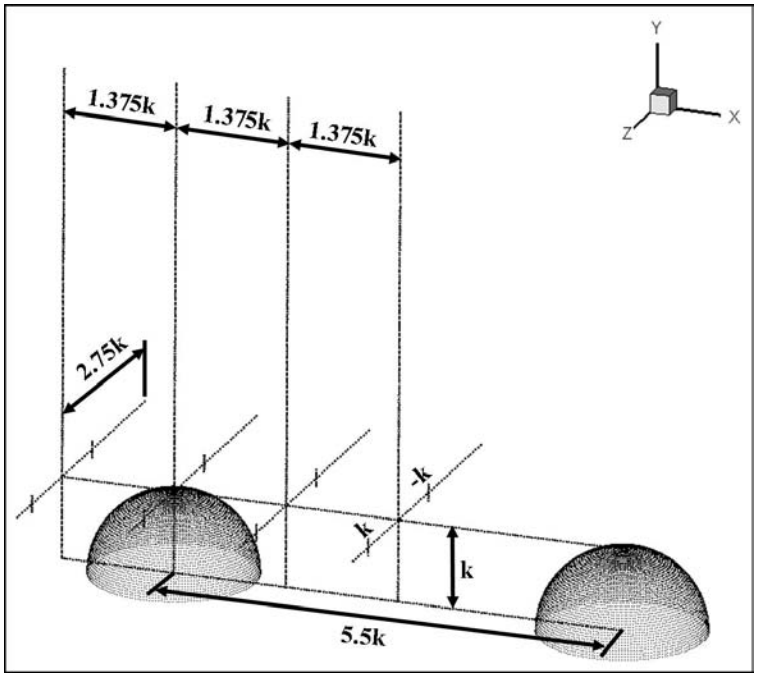

Figure 3.29: Dimensions of contour plots for Case 5

3.9.2 First and Second Moments

Figures 3.30 through 3.32 show contours of the mean velocities U, V, and W respectively. Figure 3.30 shows a typical variation of U with distance from wall. Figure 3.31 shows a relatively large value of positive V upstream and directly over the roughness element as flow is pushed upwards due to the presence of the roughness element. Downstream of the element, however, V becomes negative with a minimum occurring directly downstream of the element just below the element height. As the wall is approached the magnitude of V approaches zero to satisfy the boundary conditions. Figure 3.32 shows that fluid also moves towards the centerline from both spanwise directions.

Figures 3.33 through 3.39 represent the Reynolds stress terms (although the sign of the cross correlation terms have not been changed). Figures 3.33 through 3.35 show $\overline{u^2}$, $\overline{v^2}$, and $\overline{w^2}$ all have elevated levels downstream of the element. This is also true for the turbulent kinetic energy (TKE) which is equal to $\left(\overline{u^2}+\overline{v^2}+\overline{w^2}\right)/2$. However, while $\overline{u^2}$ has a maximum at the element height, both $\overline{v^2}$ and $\overline{w^2}$ have maxima that occur below the element peak at approximately $0.75k$. The $\overline{u^2}$ production $(-\overline{uv}\frac{\partial U}{\partial y})$ is plotted in figure 3.40 and interestingly shows that a maximum exists well above the element peak ($\sim 1.5k$) that extends from k to $2k$. The production weakens as it is convected downstream, but still extends upwards approximately $2k$. Figure 3.37 shows that $\overline{uv}$ reaches a minimum downstream of the element, just below the peak. As the flow is convected downstream the $\overline{uv}$ levels weaken. Slightly elevated levels of $\overline{uv}$ can be detected over top the element and extending downstream. The $-\overline{uv}$ production $(\overline{v^2}\frac{\partial U}{\partial y})$ is shown in figure 3.41 to have a maximum just above the element peak extending from k to $2k$. The production weakens as the flow is convected downstream.

At a distance of three to four element heights above the wall position, the mean flow and turbulence statistics collapse to the same profile in the outer region. This confirms the data of previous researchers [16, 45]. When compared with a smooth wall the rough wall Reynolds number is increased due to the roughness for a given downstream measurement location and freestream speed. This increase in Reynolds number is reflected in the outer layer by an increase is the Reynolds stresses.

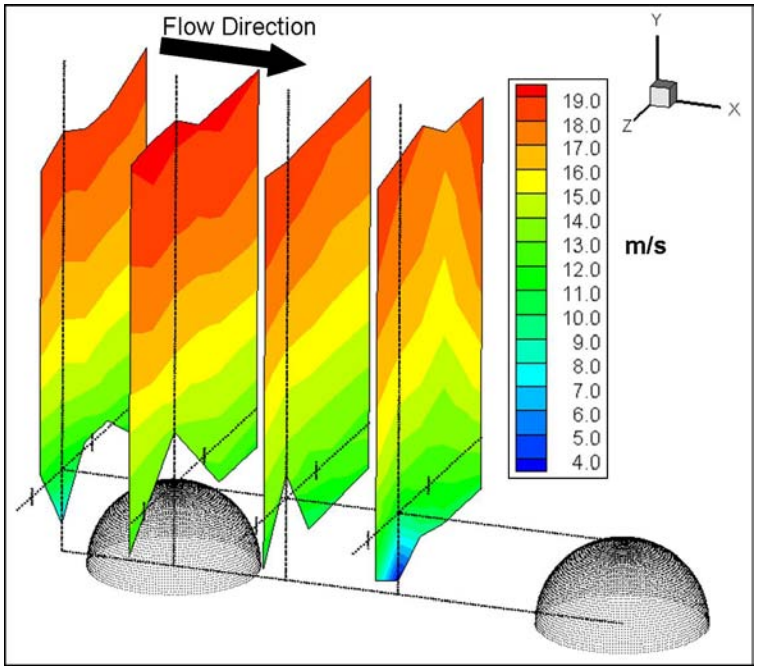

Figure 3.30: Contour plot of mean streamwise velocity for Case 5

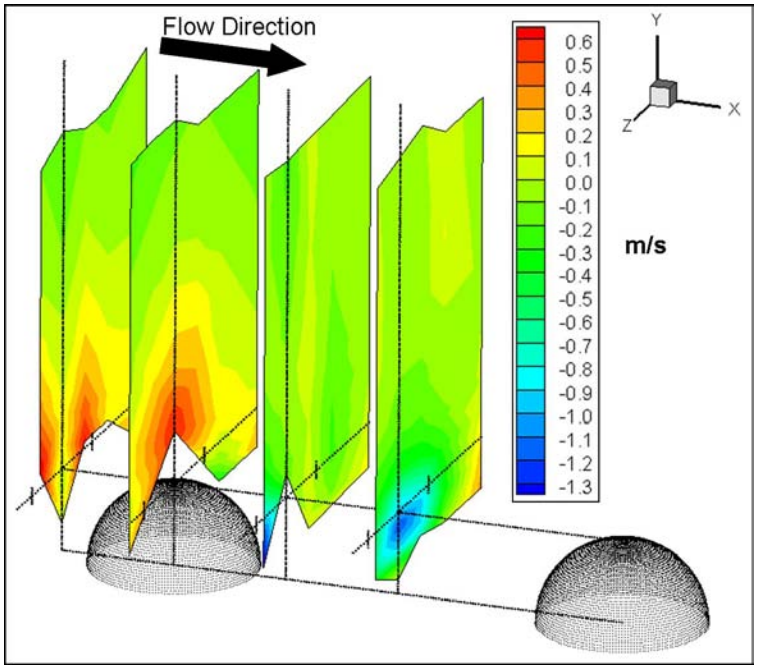

Figure 3.31: Contour plot of mean wall-normal velocity for Case 5

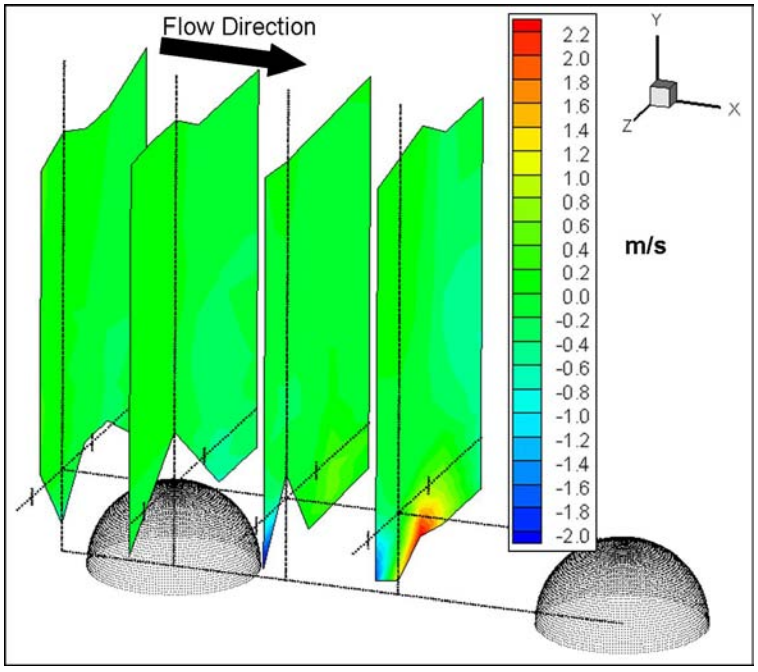

Figure 3.32: Contour plot of mean spanwise velocity for Case 5

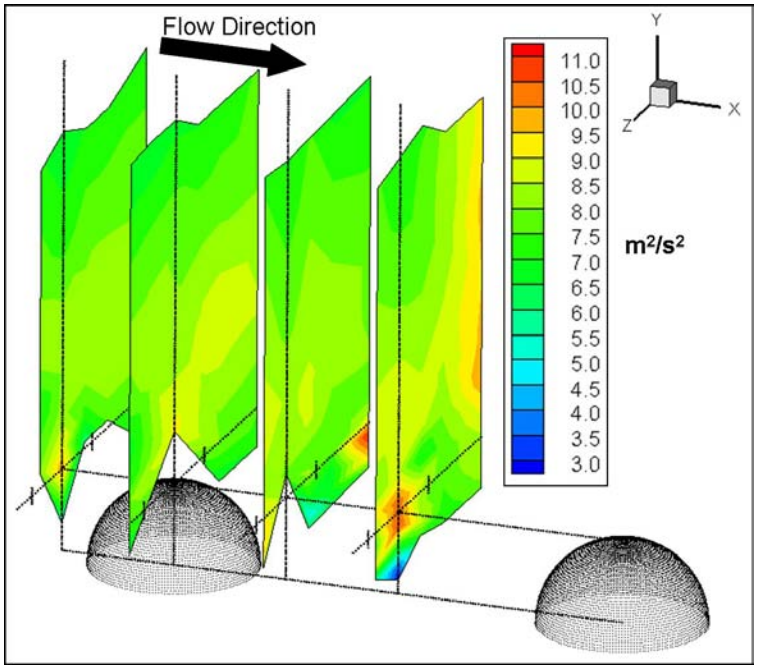

Figure 3.33: Contour plot of $\overline{u^2}$ for Case 5

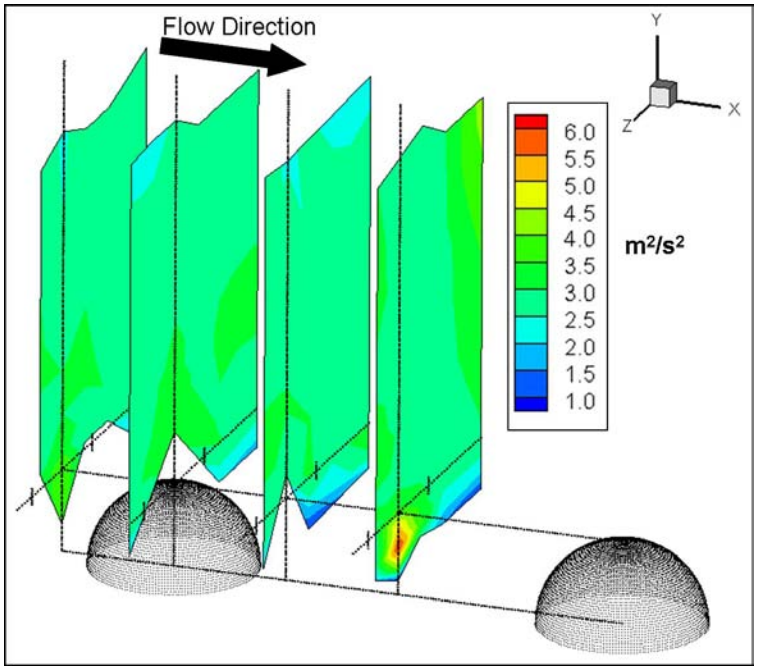

Figure 3.34: Contour plot of $\overline{v^2}$ for Case 5

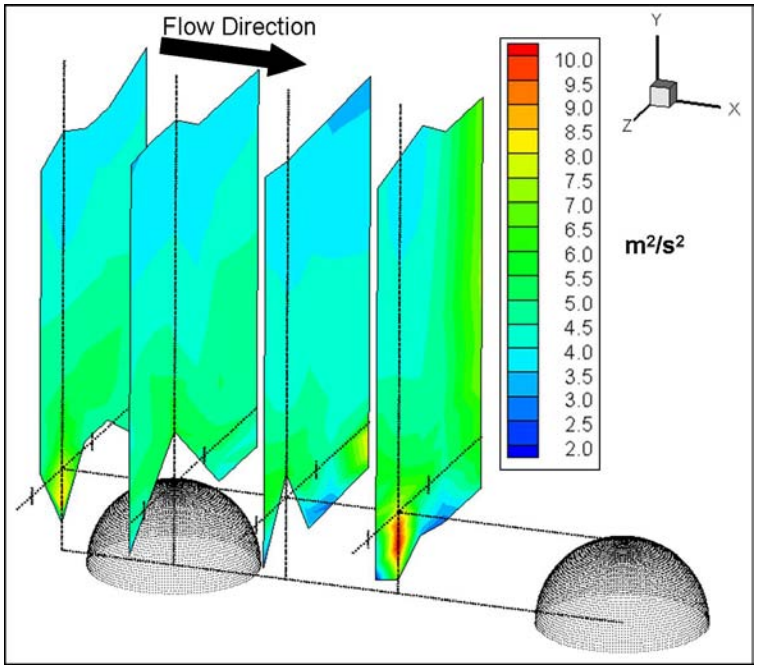

Figure 3.35: Contour plot of $\overline{w^2}$ for Case 5

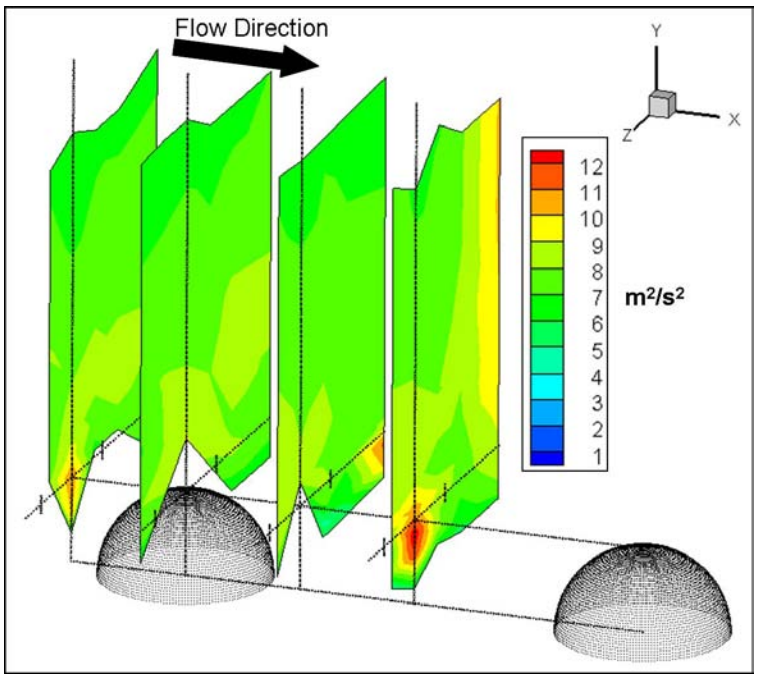

Figure 3.36: Contour plot of TKE ($\left(\overline{u^2}+\overline{v^2}+\overline{w^2}\right)/2$) for Case 5

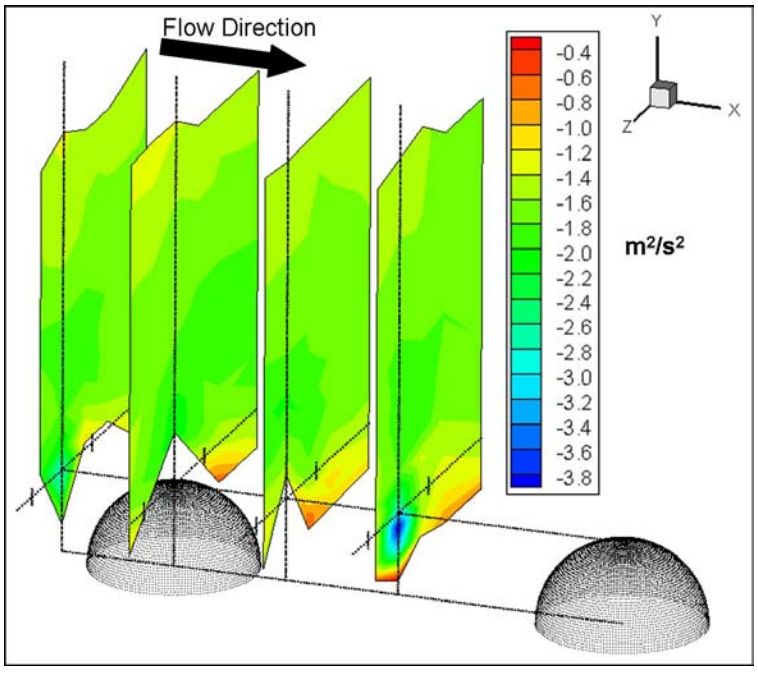

Figure 3.37: Contour plot of $\overline{uv}$ for Case 5

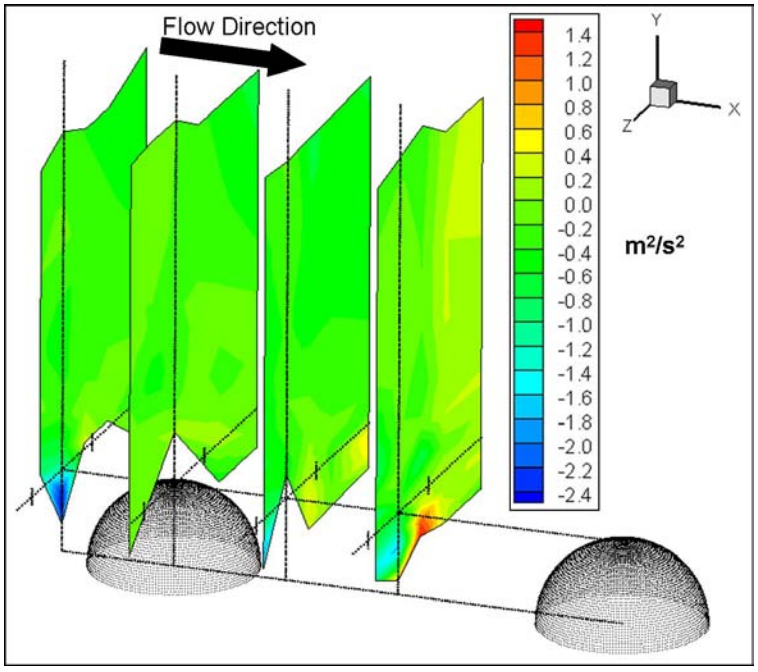

Figure 3.38: Contour plot of $\overline{uw}$ for Case 5

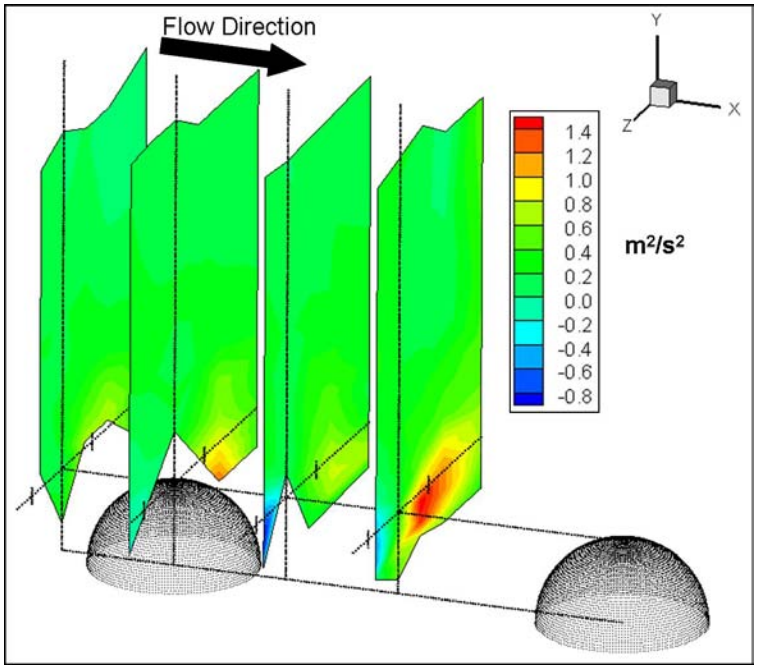

Figure 3.39: Contour plot of $\overline{vw}$ for Case 5

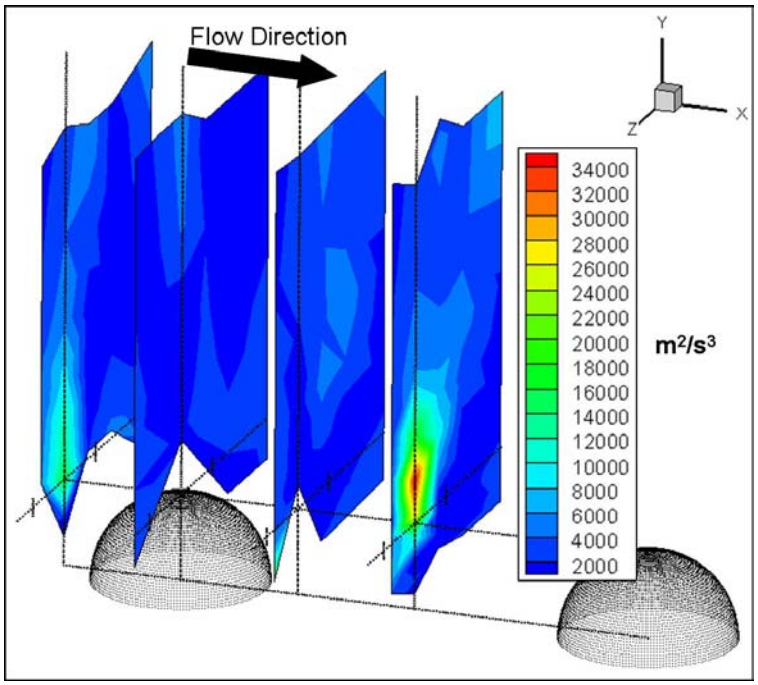

Figure 3.40: Contour plot of $\overline{u^2}$ production for Case 5, $-\overline{uv}\frac{\partial U}{\partial y}$

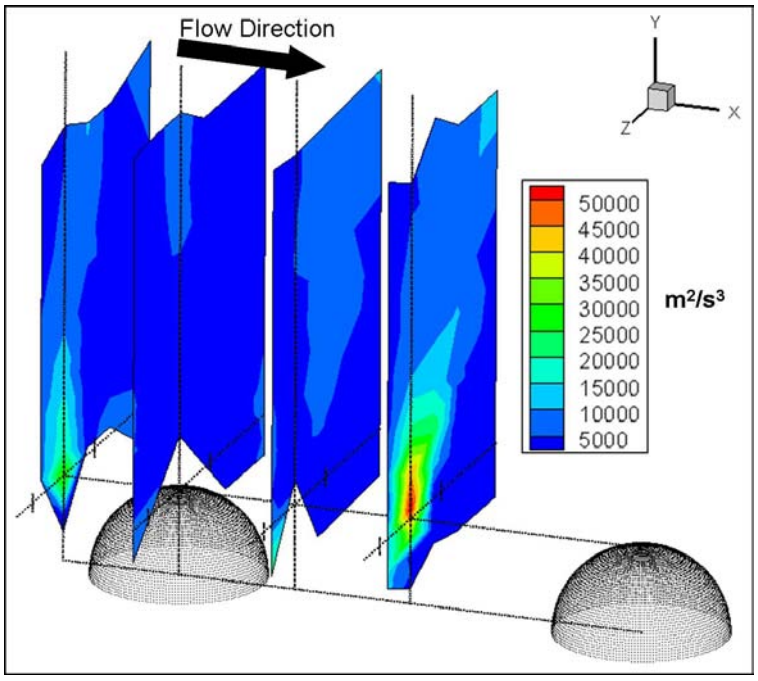

Figure 3.41: Contour plot of $-\overline{uv}$ production for Case 5, $\overline{v^2}\partial U/\partial y$

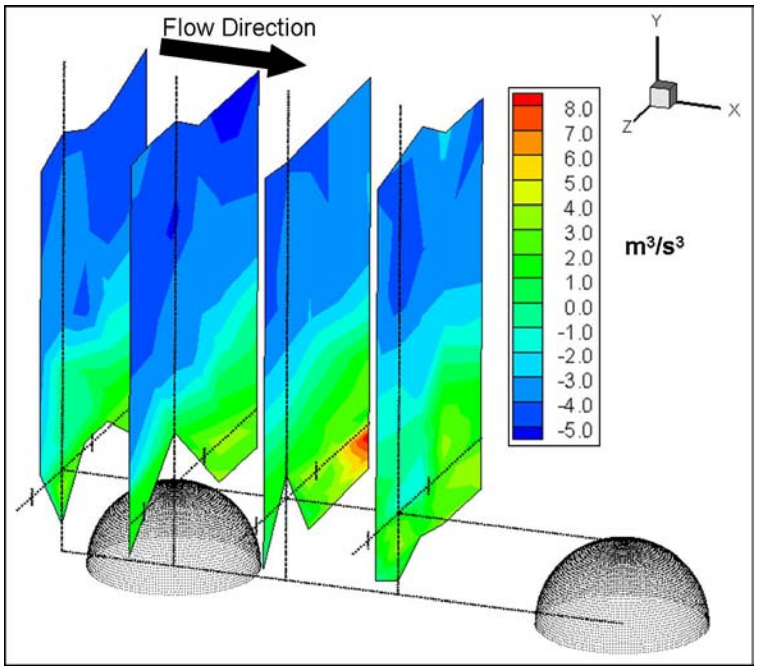

Figure 3.42: Contour plot of $\overline{u^3}$ for Case 5

3.9.3 Triple Products

The turbulence triple products are defined as $\overline{u_i u_j u_k}$ using subscript notation. They can be interpreted as components of normal stress transport. For example, $\overline{u^2 u}$ represents the average streamwise velocity fluctuation relative to the mean streamwise velocity that convects the streamwise normal stress $\overline{u^2}$. The sign of $\overline{u^2 u}$ is entirely determined by u, since u^2 is positive definite.

Figures 3.42 through 3.51 show the triple products for the profiles. Figure 3.42 shows that $\overline{u^2 u}$ changes sign at approximately $2k$ regardless of the streamwise and spanwise coordinates. Above $\sim 2k$, $\overline{u^2}$ is convected at speeds less than the local U. The opposite is true below $\sim 2k$. Figure 3.43 shows that $\overline{u^2 v}$ is generally positive except downstream of the roughness element. A local minimum exists downstream of the element at $\sim 0.5k$.

Figure 3.45 shows $\overline{v^2 u}$ has has a maximum and minimum in the same plane, downstream of the element. The minimum is just below the element height, and the maximum is just below $\sim 0.5k$. Both these regions decrease in magnitude as the flow moves downstream. Figure 3.46 reveals that $\overline{v^2 v}$ has a maximum downstream of the element just below the element height. This also weakens as the flow moves downstream. Figure 3.47 suggests that $\overline{v^2}$ moves toward the centerline downstream of the element at fluctuating values of $|w| < |W|$.

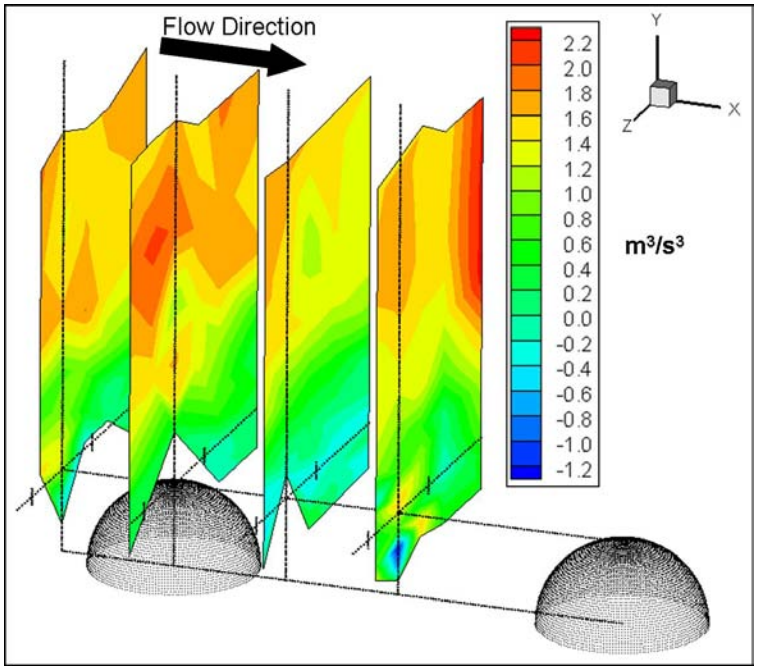

Figure 3.43: Contour plot of $\overline{u^2 v}$ for Case 5

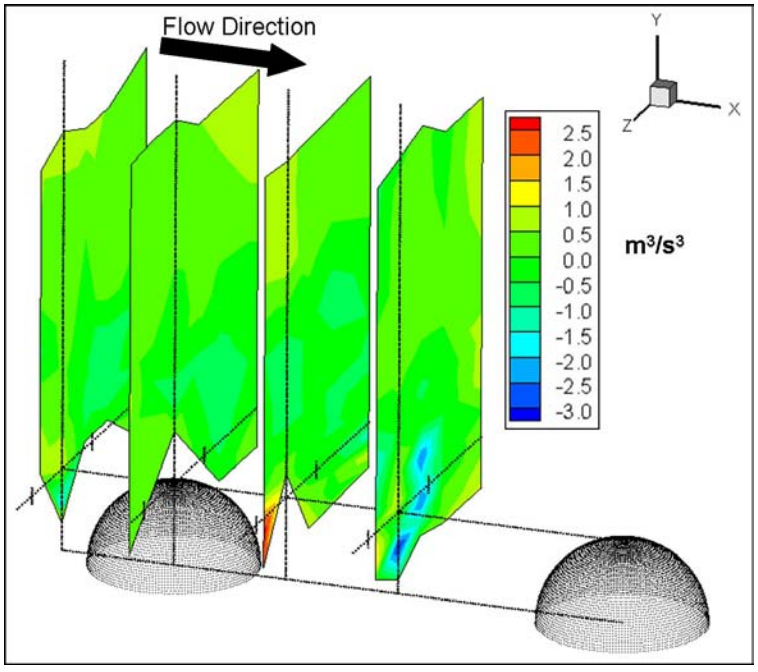

Figure 3.44: Contour plot of $\overline{u^2 w}$ for Case 5

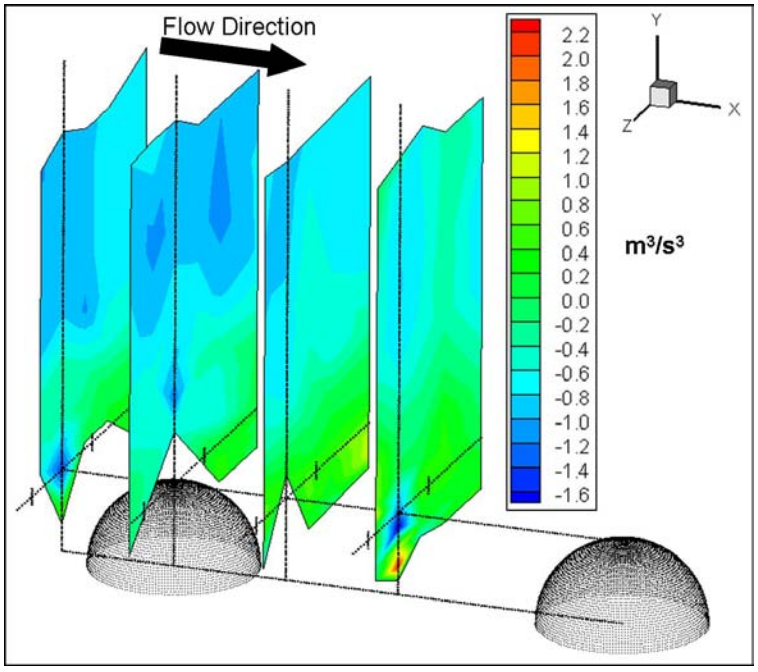

Figure 3.45: Contour plot of $\overline{v^2 u}$ for Case 5

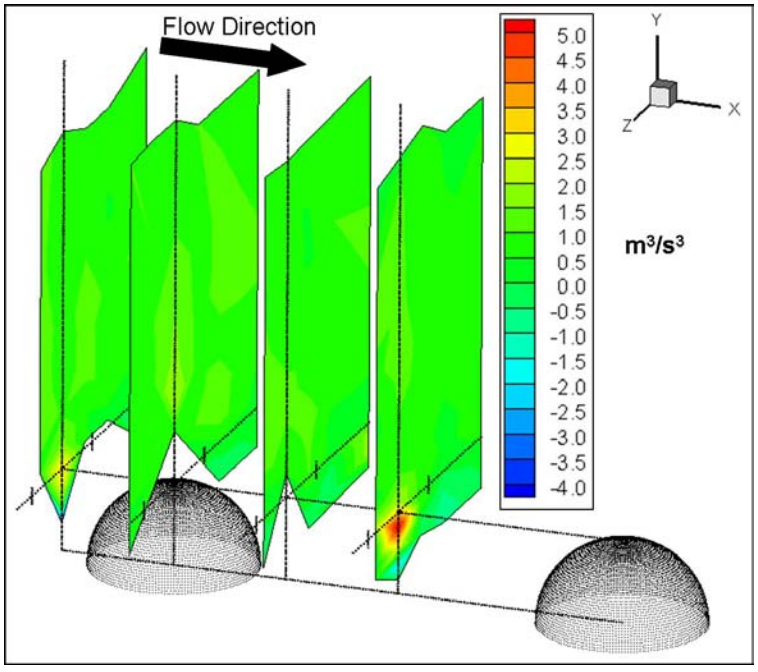

Figure 3.46: Contour plot of $\overline{v^3}$ for Case 5

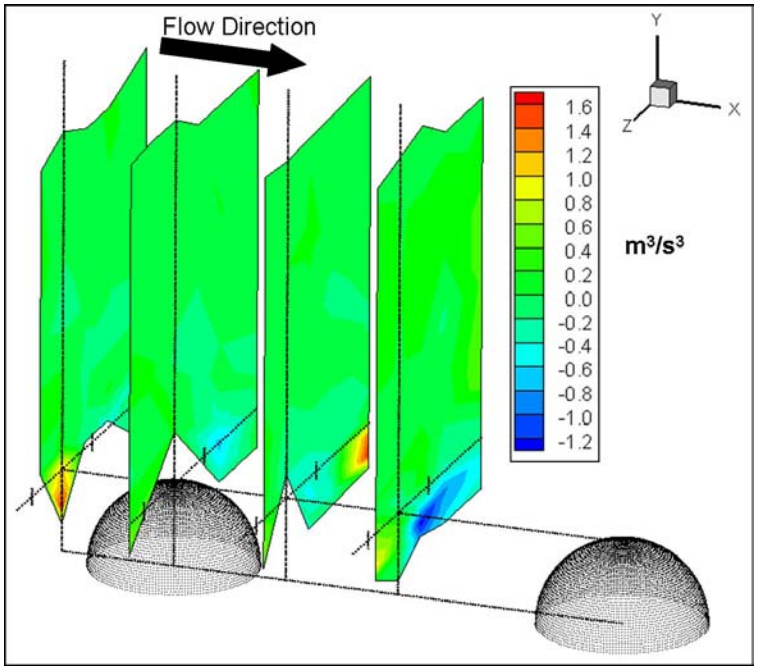

Figure 3.47: Contour plot of $\overline{v^2 w}$ for Case 5

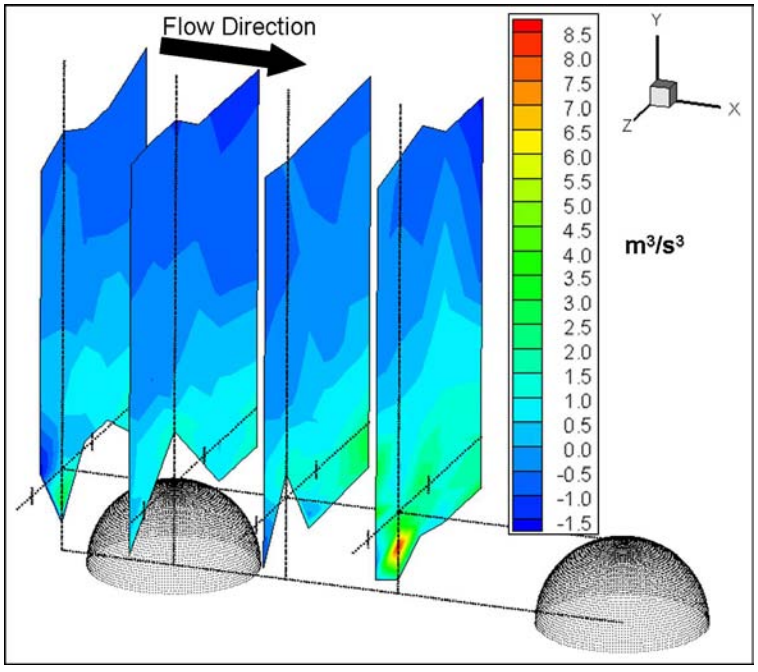

Figure 3.48: Contour plot of $\overline{w^2 u}$ for Case 5

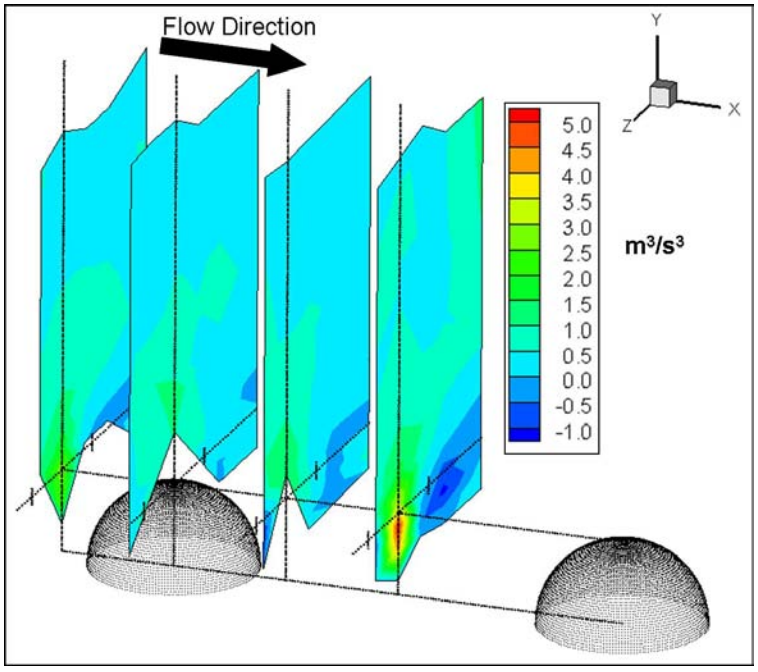

Figure 3.49: Contour plot of $\overline{w^2 v}$ for Case 5

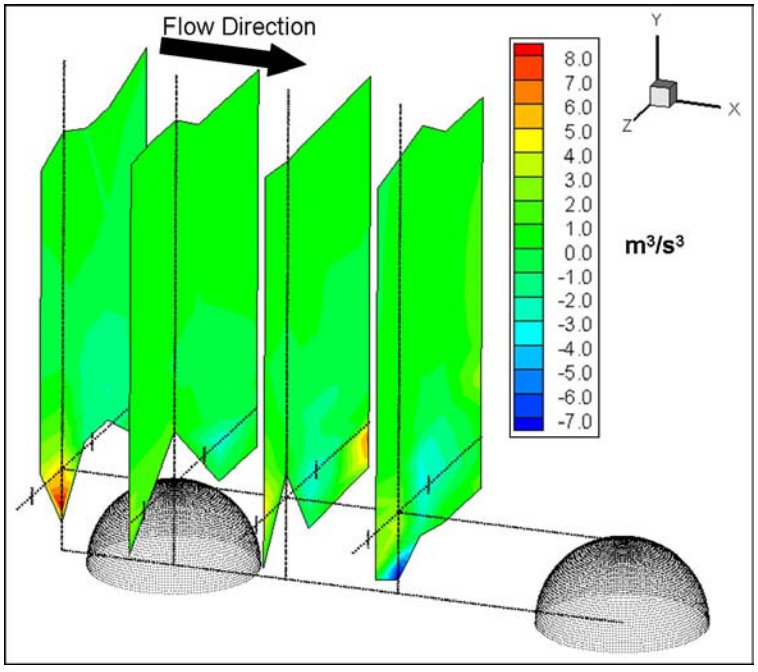

Figure 3.50: Contour plot of $\overline{w^3}$ for Case 5

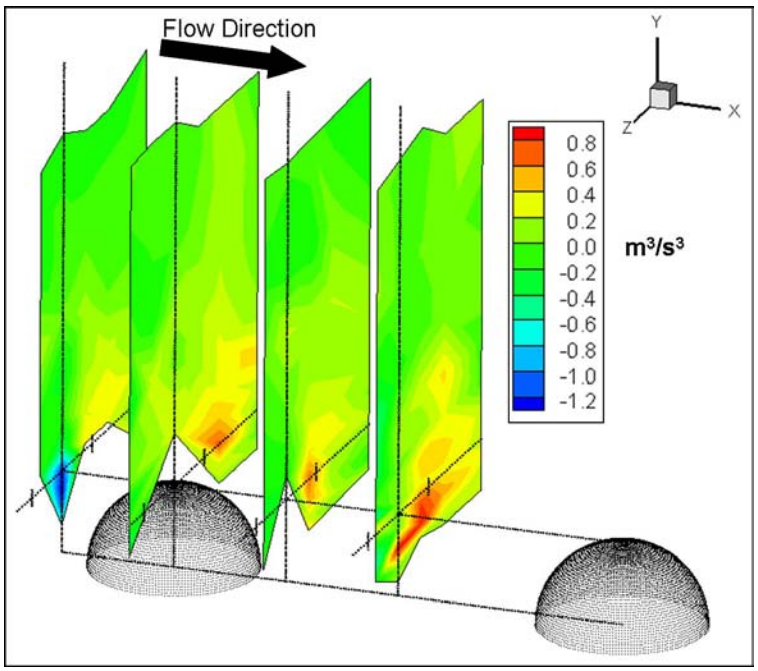

Figure 3.51: Contour plot of $\overline{uvw}$ for Case 5

3.9.4 Sweeps and Ejections

To gain insight into how the sweep and ejection motions affect the turbulence structure, the data was conditionally averaged. Sweeping motions are associated with the second quadrant of the u-v joint probability distribution function. Ejections are defined as the fourth quadrant. Both sweeps and ejections contribute to the increased surface drag due to the turbulent motion. The motions that correspond to the first and third quadrants are defined as interactions and are relatively weak inactive motions that produce negative values of the Reynolds shear stress $-\overline{uv}$. Figure 3.52 shows contours of the ratio of the number of sweep, ejection, and interaction events to total number of events measured. In general, sweeps and ejections occur equally as often (32% of the time) and interactions are about 5% more common. However, downstream of the element just below the element height (where the high levels of TKE and Reynolds shear stress exist) the sweep, ejection, and interaction events occur equally as often. By comparison, with smooth walls the sweeps and ejection events each occur about 10% of the time, so rough walls are causing a greater energy exchange between the inner and outer flow.

The mean flow angle between the streamwise and wall-normal velocity components is defined as $\theta = \tan^{-1}(V/U)$. Figure 3.53 shows that θ is near zero everywhere, except upstream of the element where the flow is pushed upwards due to the presence of the element and downstream of the element where it reaches a minimum at $\sim 0.75k$. Figures 3.54(a) and 3.54(b) show the mean flow angle conditionally averaged on sweep and ejection events respectively. For sweep events θ reaches -19° downstream of the element at a height of $\sim 0.5k$. Ejection events reach θ values of 10° to 14° upstream of the element as the flow moves over the element. A local maximum is found downstream of the element near the wall.

Figures 3.55 through 3.62 show contours of the Reynolds stresses and TKE conditionally averaged on sweep and ejection events. These figures show that sweep and ejection events contribute about equally to the Reynolds stresses and TKE everywhere. However, $\overline{u^2}$ and $-\overline{uv}$ production maximums are effected more by sweeping motions as shown in figures 3.61 and 3.62 respectively, and the location of these maximums differ for sweeps and ejections. The location of maximum production for sweeps occurs slightly closer to the wall while the opposite is true for ejections. However, in any case, the maximum occurs downstream of the element below the element height.

Figures 3.63 through 3.71 show contours of triple products conditionally averaged on sweep and ejection events. Terms $\overline{u^2u}$, $\overline{u^2v}$, and $\overline{u^2w}$ contained contributions from sweeps and ejection events that were similar in magnitude but of opposite sense. Ejections events are slightly stronger than sweep events for $\overline{v^2u}$ and $\overline{v^2v}$ terms. Also, the local maximum of the absolute value for both sweeps and ejections for these terms occur downstream of the element. However, the local maximum of the absolute value for the ejections events

cause slightly stronger values than the sweep events. The $\overline{v^2 w}$ term shows clear structure downstream of the element for sweep events as $\overline{v^2}$ is convected toward the centerline and decelerates. The opposite occurs for ejection events, however the magnitudes are weaker.

Figures 3.72 through 3.80 show contours of triple products formed from instantaneous velocities, not fluctuating velocities, conditionally averaged on sweep and ejection events. These terms include information about the mean flow as well as the fluctuating turbulence. For terms $\overline{U^2 U}$, $\overline{U^2 V}$, and $\overline{U^2 W}$ the sweep events are stronger in magnitude than the ejection events. For the $\overline{V^2 U}$ term the magnitude due to sweep events are again greater with a strong local maximum occuring downstream of the element just below the element height. The magnitudes due to ejection events have a local minimum in roughly the same location. However, there is a strong local maximum directly overtop of the roughness element. This is due to the strong mean V velocity there due to the presence of the element. The $\overline{V^2 V}$ term experiences a sign change between sweep and ejection events as expected. Ejections result in a positive value and again cause a local maximum overtop of the element. Sweep events cause a local minimum downstream of the element approximately $0.5k$ from the wall. In general, the magnitude of $\overline{V^2 V}$ is larger for ejection events, but this is not true in the regions of local maximum where sweeps events dominate.

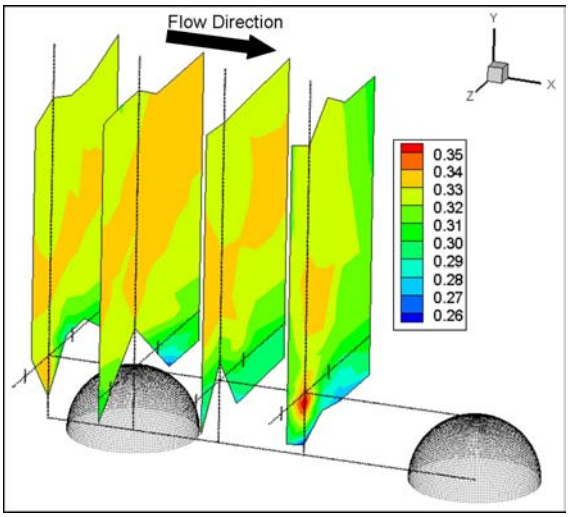

(a) Sweeps

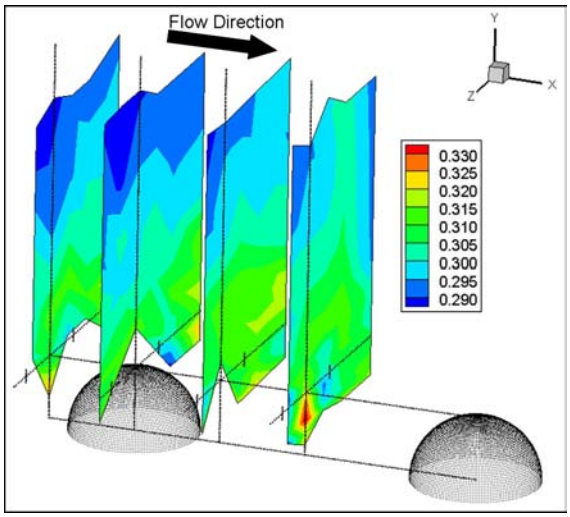

(b) Ejections

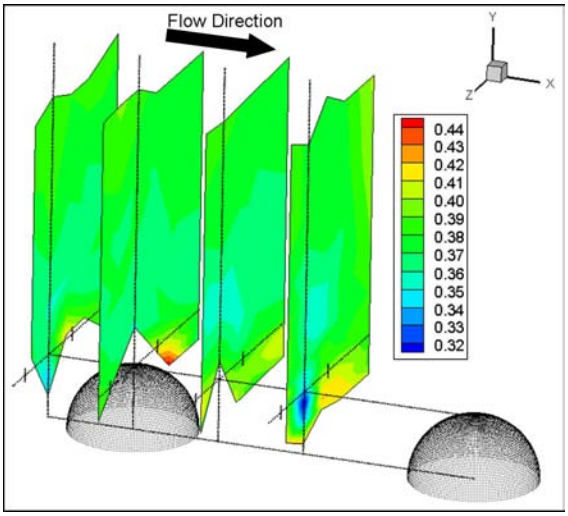

(c) Interactions

Figure 3.52: Contour plots of the ratio of number of sweep, ejection, and interaction events measured to total number of events measured for Case 5

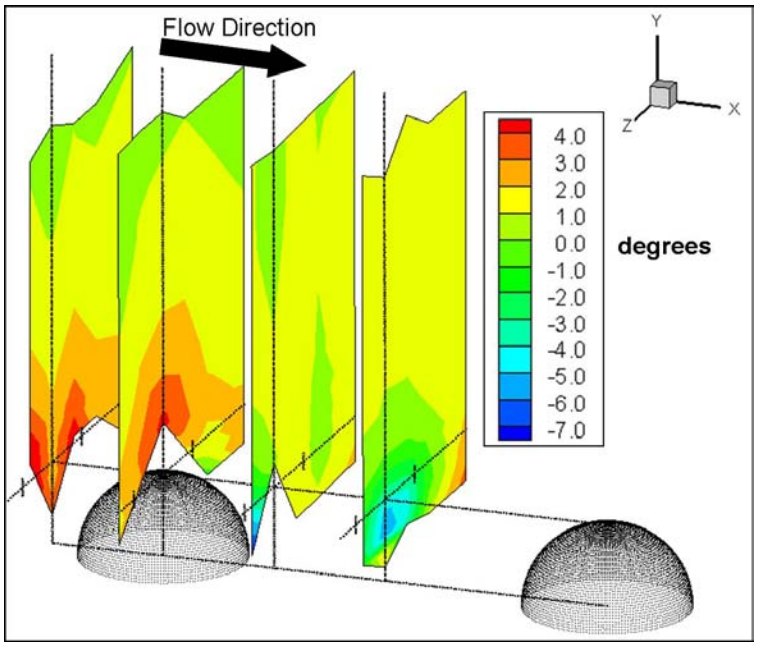

Figure 3.53: Contour plot of mean flow angle ($\tan^{-1}(V/U)$) in degrees for Case 5

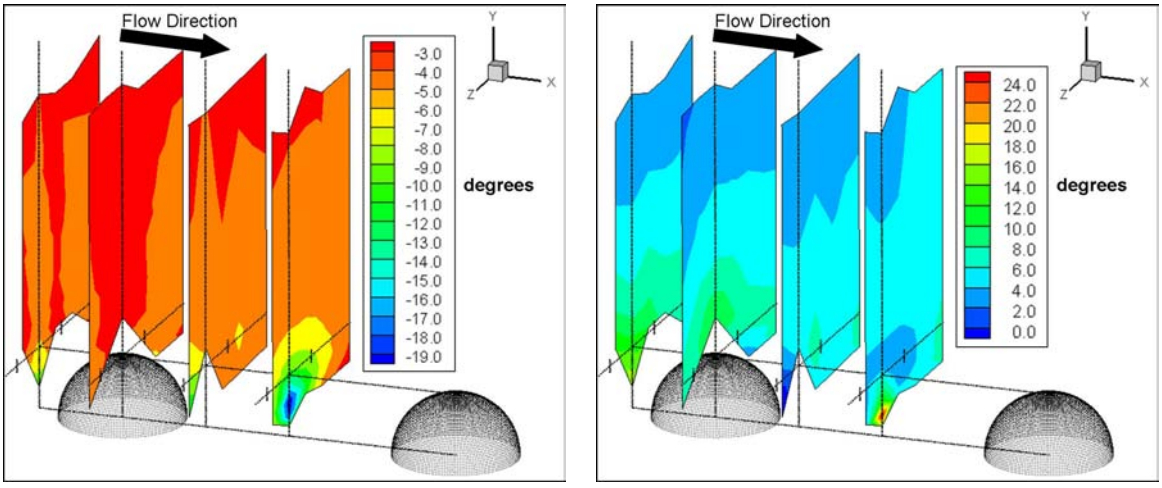

(a) Sweeps (b) Ejections

Figure 3.54: Contour plot of mean flow angle ($\tan^{-1}(V/U)$) in degrees conditonally averaged on sweep and ejection events for Case 5

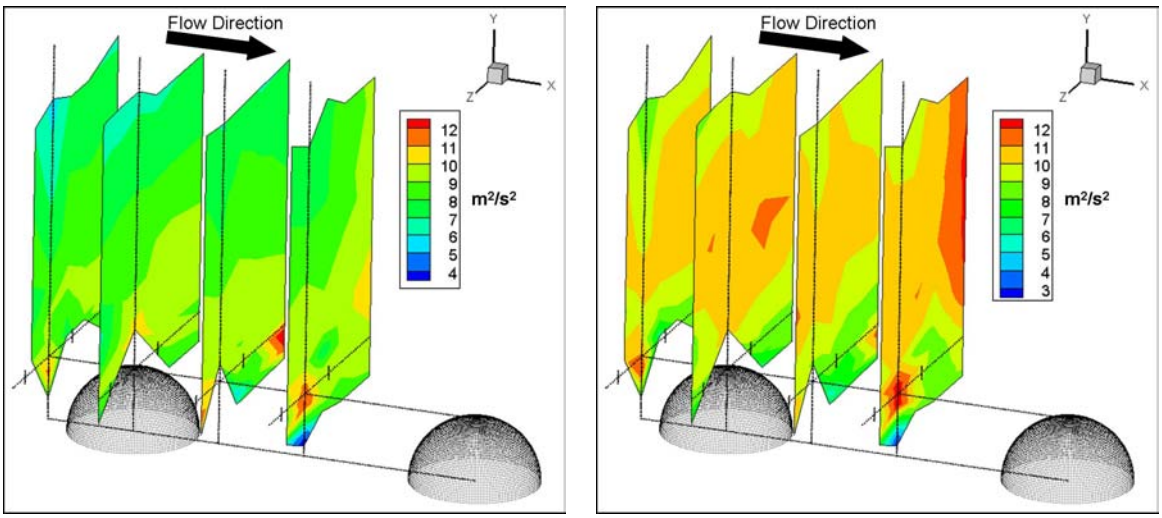

(a) Sweeps (b) Ejections

Figure 3.55: Contour plot of $\overline{u^2}$ conditionally averaged on sweep and ejection events for Case 5

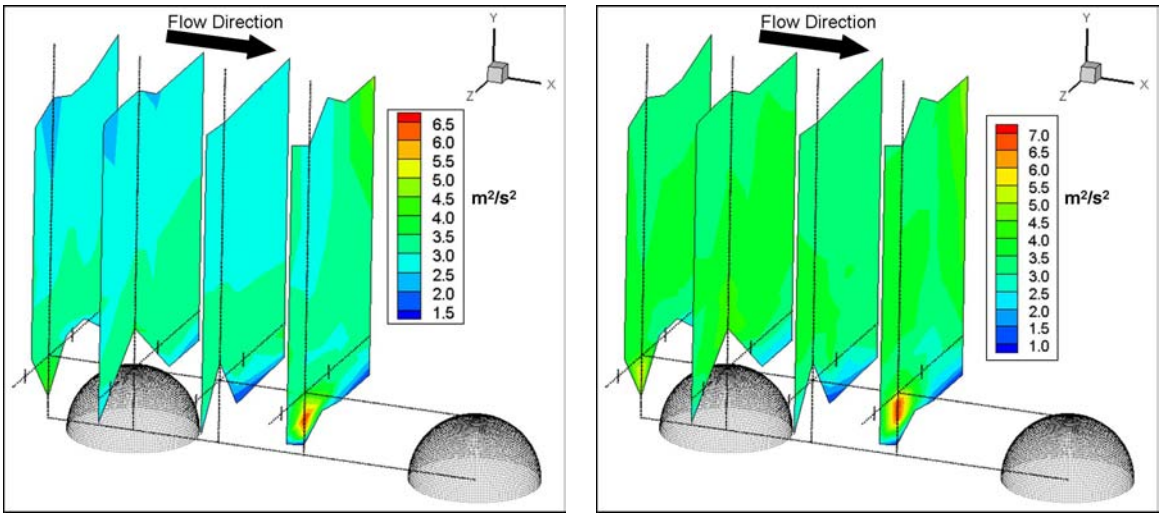

(a) Sweeps (b) Ejections

Figure 3.56: Contour plot of $\overline{v^2}$ conditionally averaged on sweep and ejection events for Case 5

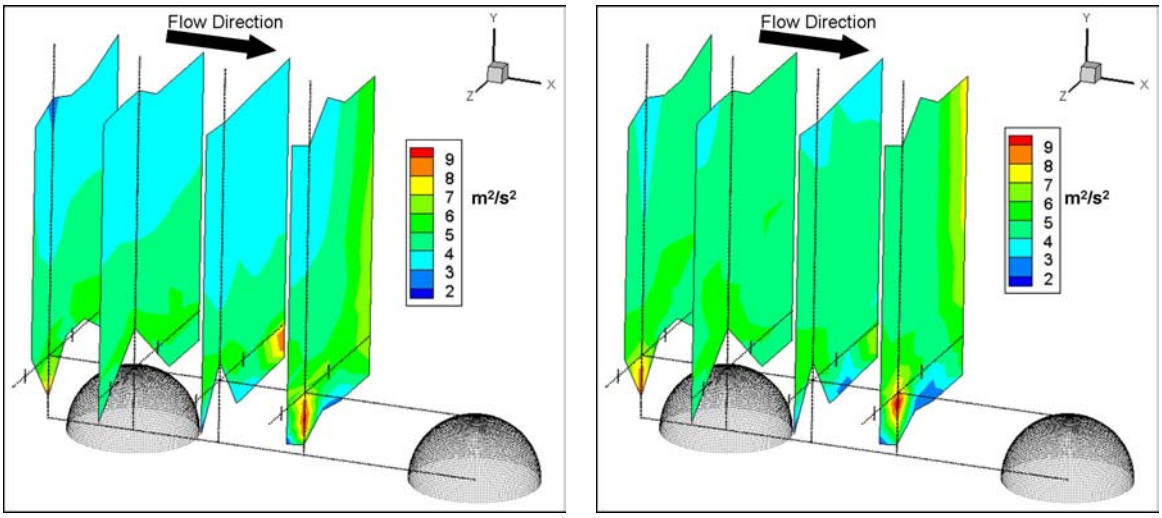

(a) Sweeps (b) Ejections

Figure 3.57: Contour plot of $\overline{w^2}$ conditionally averaged on sweep and ejection events for Case 5

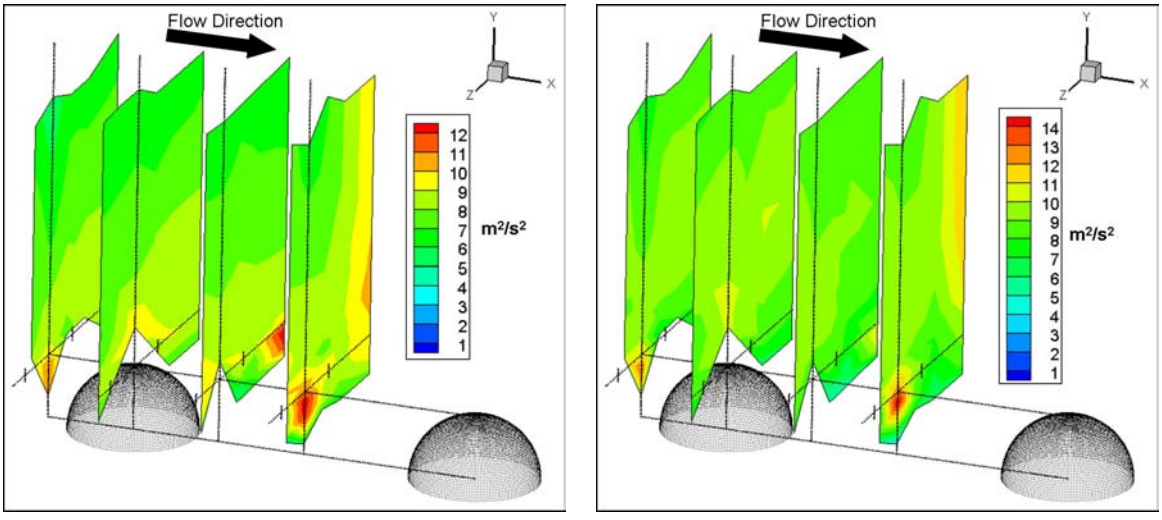

(a) Sweeps (b) Ejections

Figure 3.58: Contour plot of TKE ($\left(\overline{u^2}+\overline{v^2}+\overline{w^2}\right)/2$) conditionally averaged on sweep and ejection events for Case 5

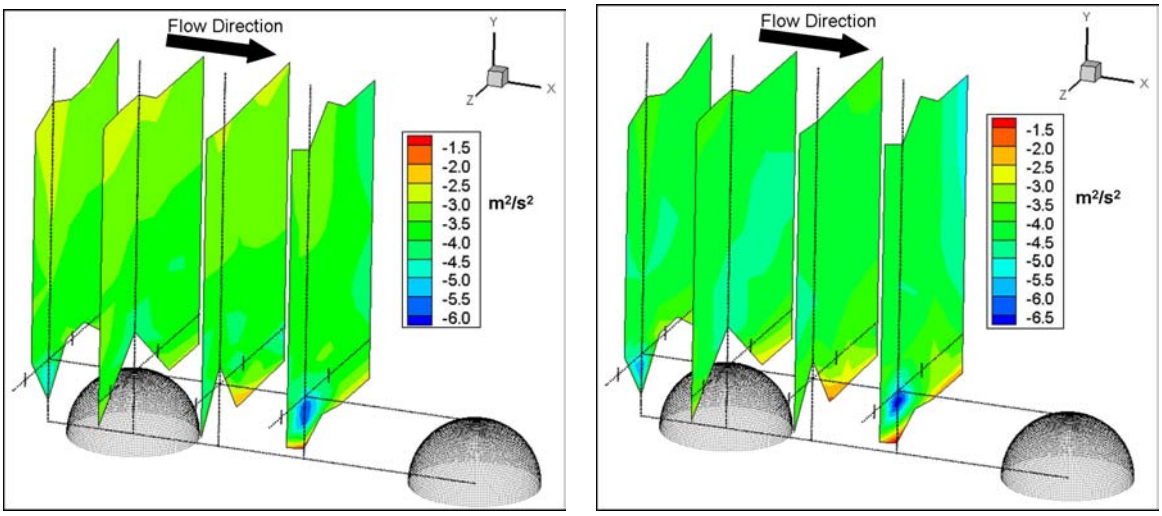

(a) Sweeps (b) Ejections

Figure 3.59: Contour plot of $\overline{uv}$ conditionally averaged on sweep and ejection events for Case 5

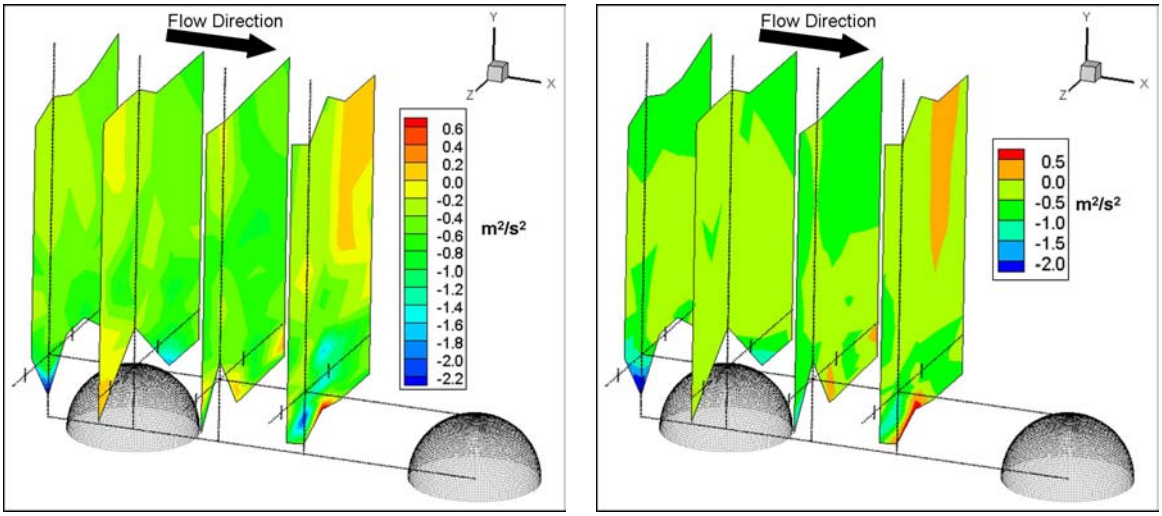

(a) Sweeps (b) Ejections

Figure 3.60: Contour plot of $\overline{uw}$ conditionally averaged on sweep and ejection events for Case 5

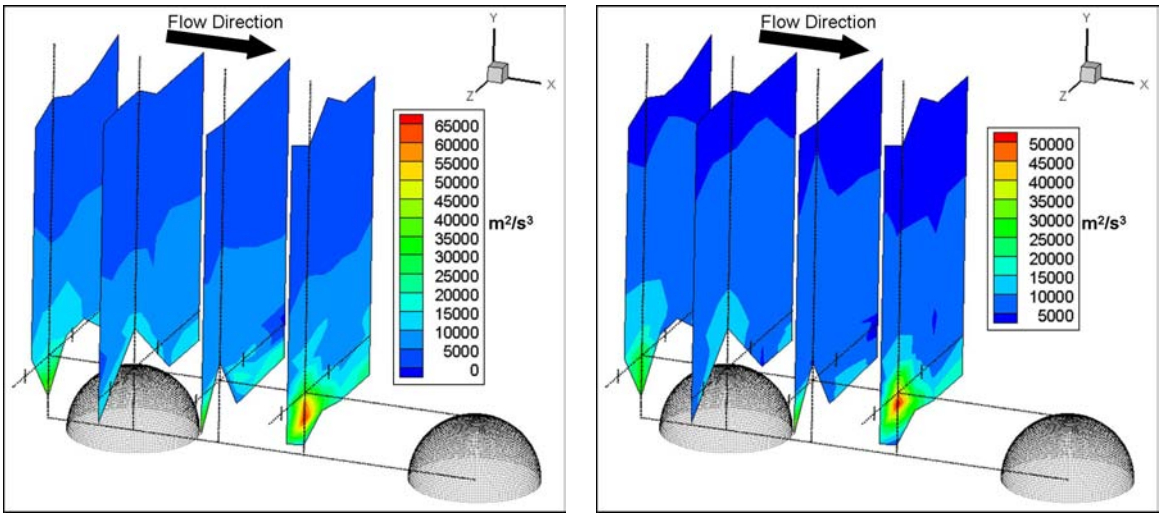

(a) Sweeps (b) Ejections

Figure 3.61: Contour plot of $\overline{u^2}$ production ($-\overline{uv}\frac{\partial U}{\partial y}$) conditionally averaged on sweep and ejection events for Case 5

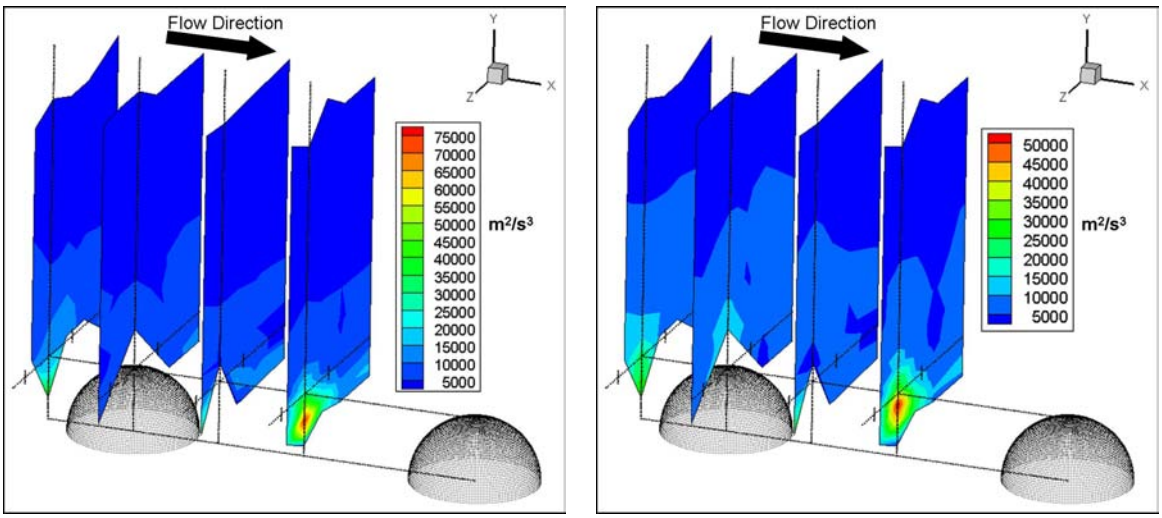

(a) Sweeps (b) Ejections

Figure 3.62: Contour plot of $\overline{-uv}$ production ($\overline{v^2}\frac{\partial U}{\partial y}$) conditionally averaged on sweep and ejection events for Case 5

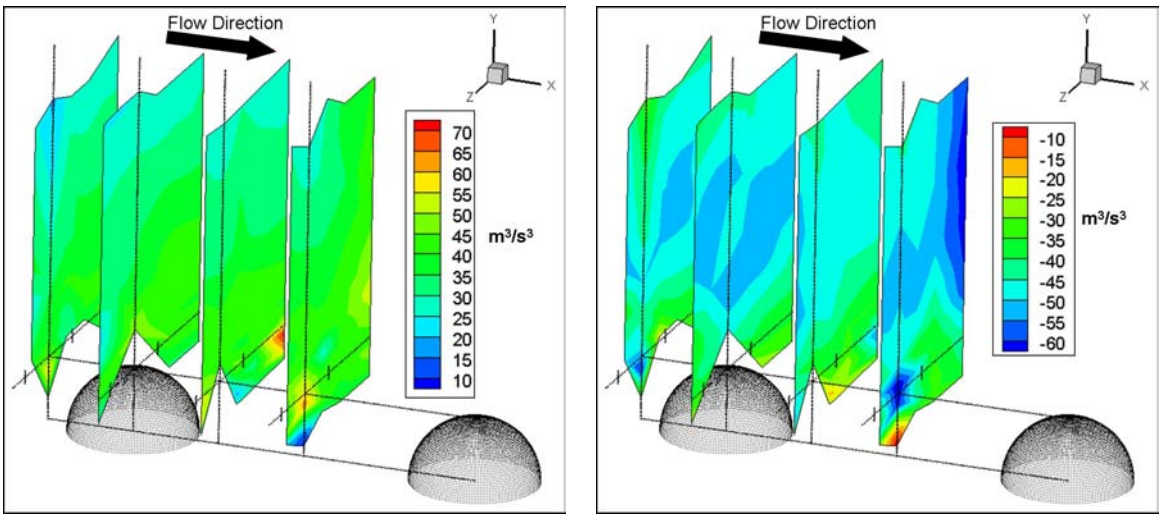

(a) Sweeps (b) Ejections

Figure 3.63: Contour plots of $\overline{u^2u}$ conditionally averaged on sweep and ejection events for Case 5

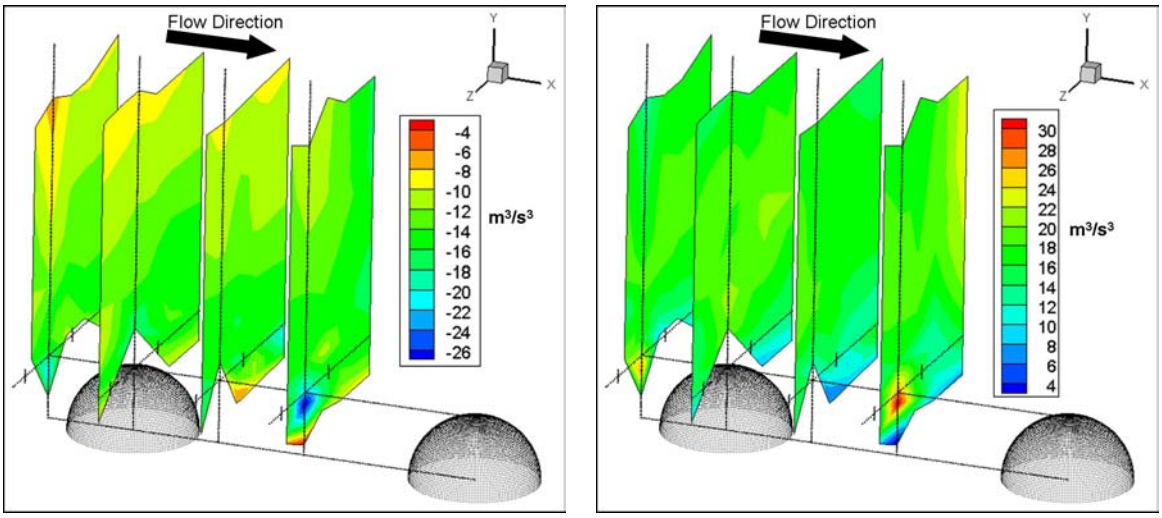

(a) Sweeps (b) Ejections

Figure 3.64: Contour plots of $\overline{u^2v}$ conditionally averaged on sweep and ejection events for Case 5

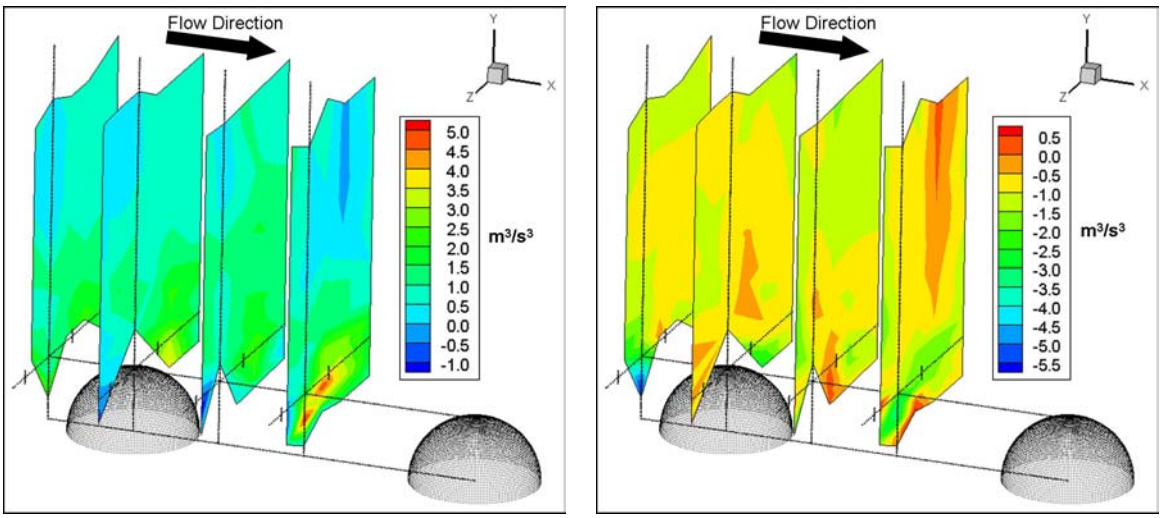

(a) Sweeps (b) Ejections

Figure 3.65: Contour plots of $\overline{u^2 w}$ conditionally averaged on sweep and ejection events for Case 5

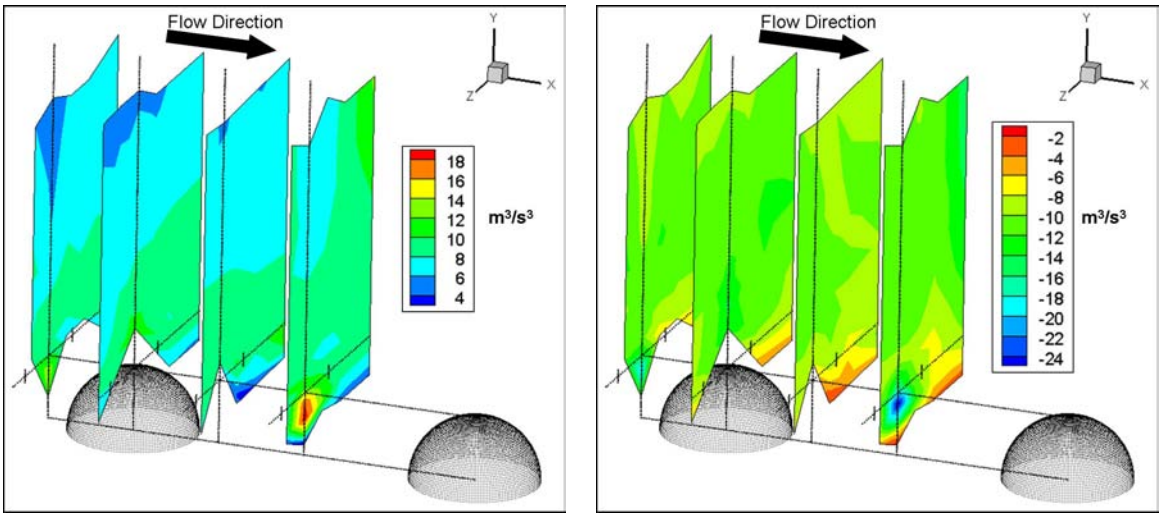

(a) Sweeps (b) Ejections

Figure 3.66: Contour plots of $\overline{v^2 u}$ conditionally averaged on sweep and ejection events for Case 5

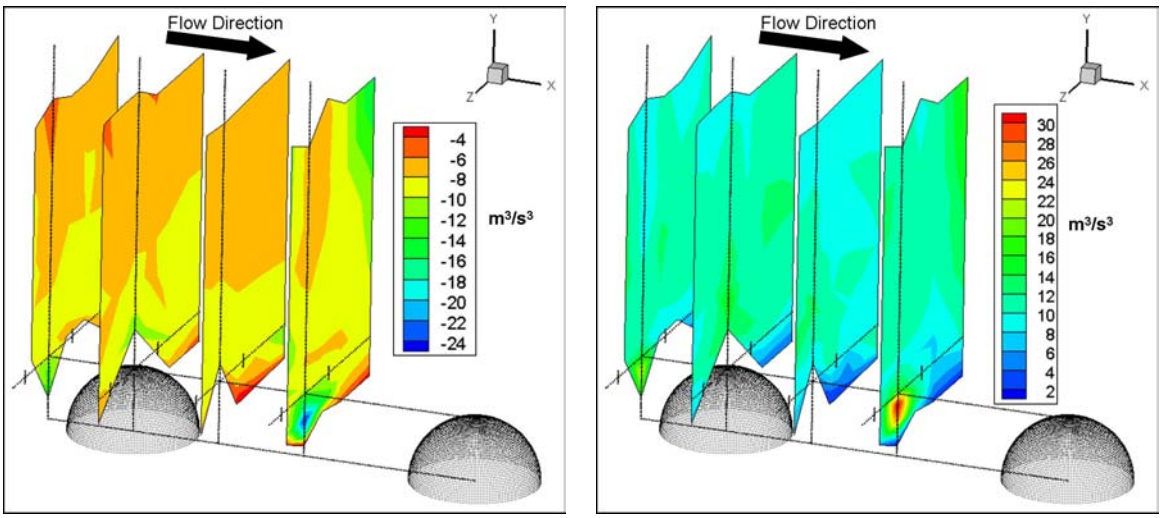

(a) Sweeps (b) Ejections

Figure 3.67: Contour plots of $\overline{v^2 v}$ conditionally averaged on sweep and ejection events for Case 5

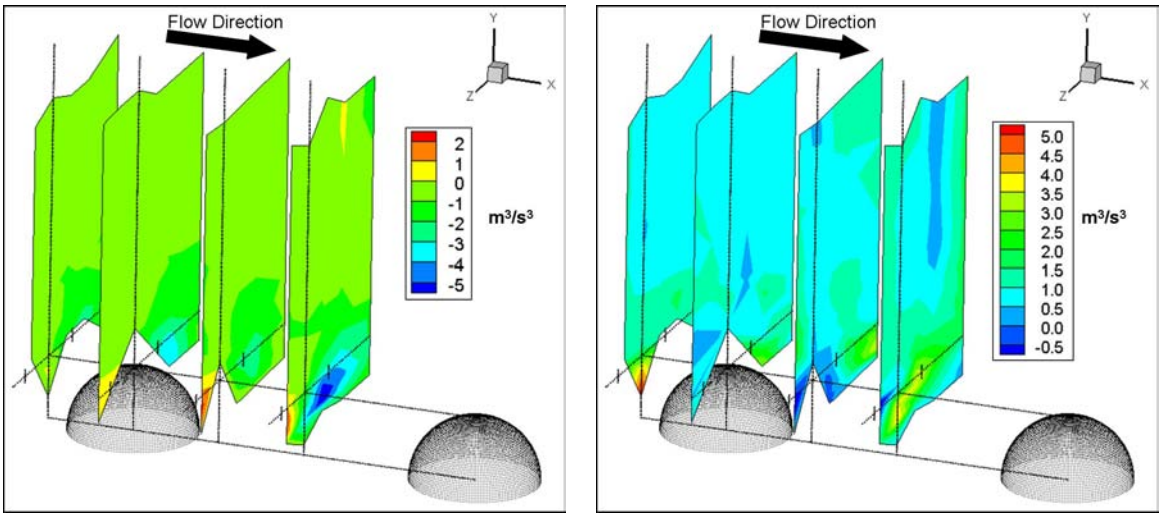

(a) Sweeps (b) Ejections

Figure 3.68: Contour plots of $\overline{v^2 w}$ conditionally averaged on sweep and ejection events for Case 5

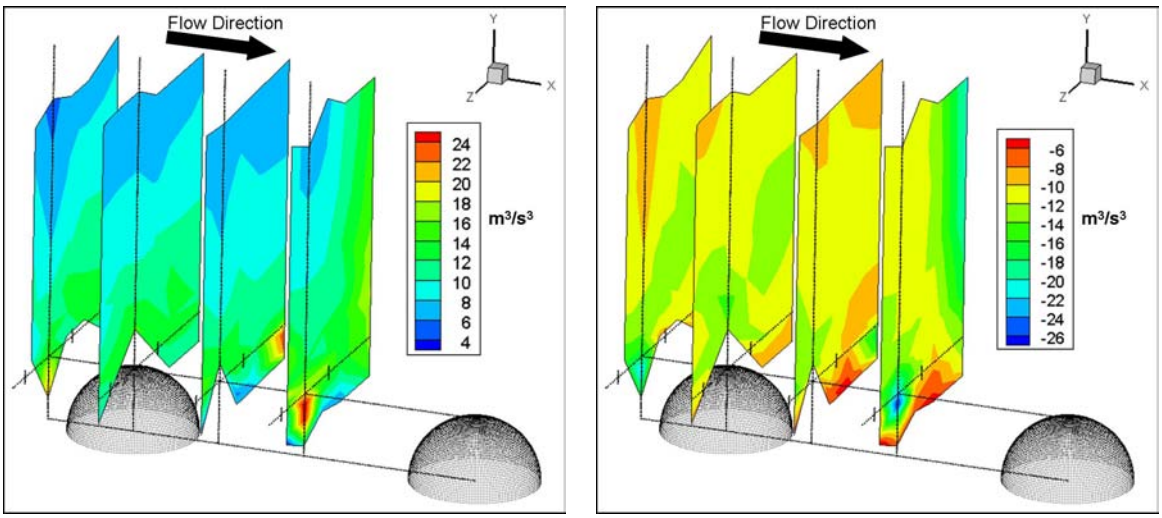

(a) Sweeps (b) Ejections

Figure 3.69: Contour plots of $\overline{w^2u}$ conditionally averaged on sweep and ejection events for Case 5

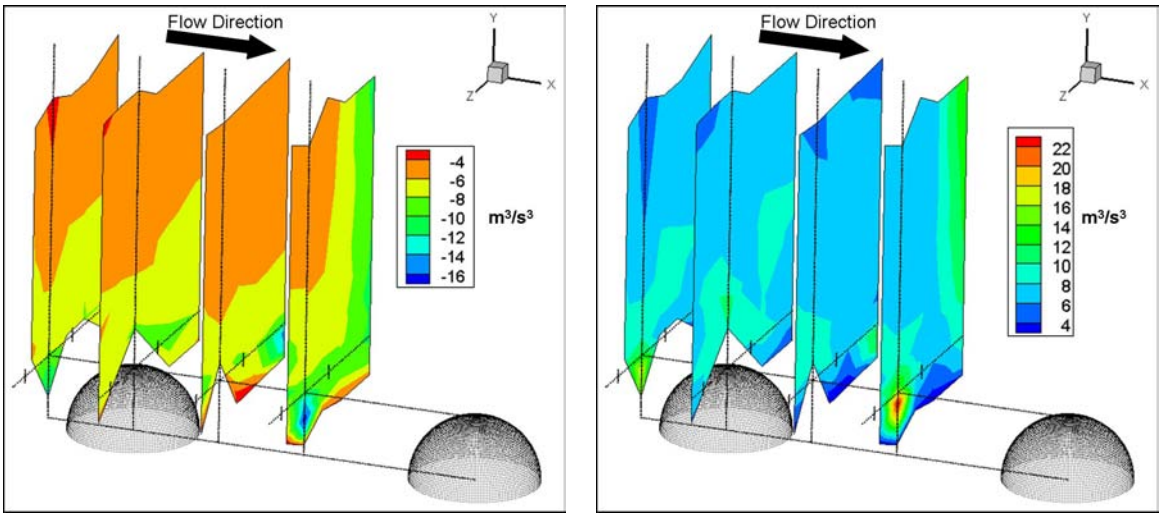

(a) Sweeps (b) Ejections

Figure 3.70: Contour plots of $\overline{w^2v}$ conditionally averaged on sweep and ejection events for Case 5

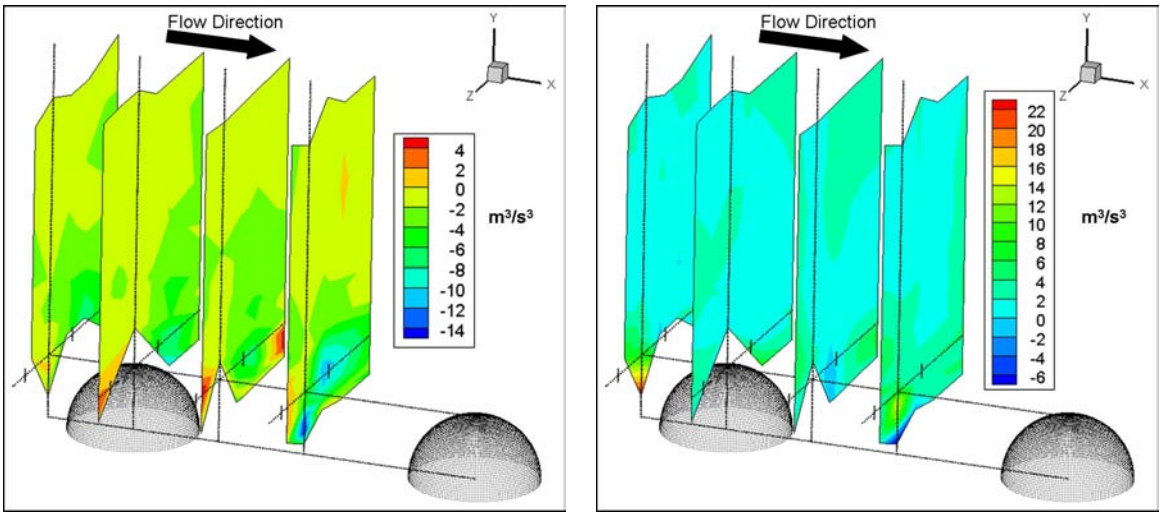

(a) Sweeps (b) Ejections

Figure 3.71: Contour plots of $\overline{w^2 w}$ conditionally averaged on sweep and ejection events for Case 5

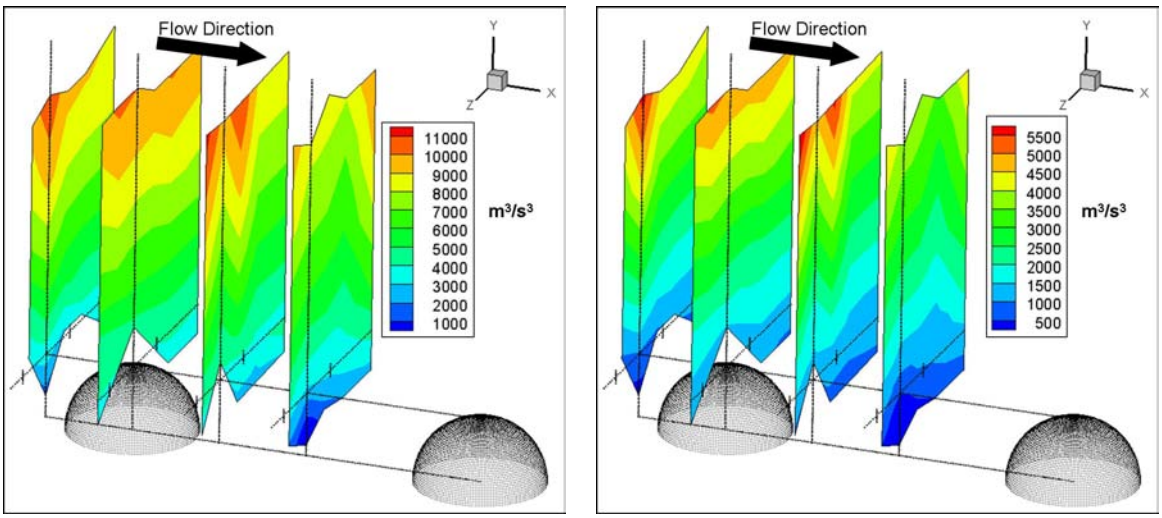

(a) Sweeps (b) Ejections

Figure 3.72: Contour plots of $\overline{U^2U}$ conditionally averaged on sweep and ejection events for Case 5

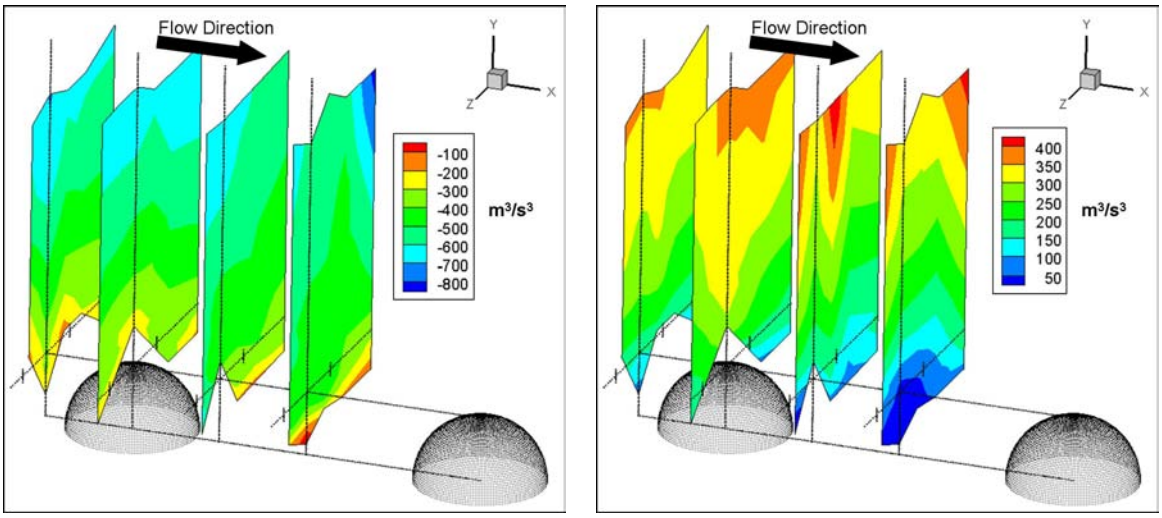

(a) Sweeps (b) Ejections

Figure 3.73: Contour plots of $\overline{U^2V}$ conditionally averaged on sweep and ejection events for Case 5

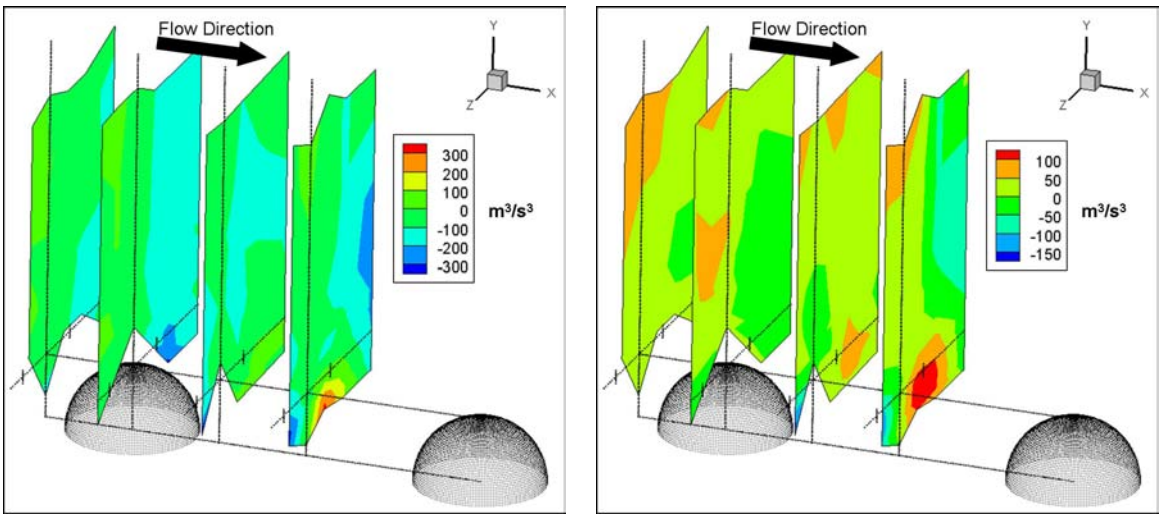

(a) Sweeps (b) Ejections

Figure 3.74: Contour plots of $\overline{U^2W}$ conditionally averaged on sweep and ejection events for Case 5

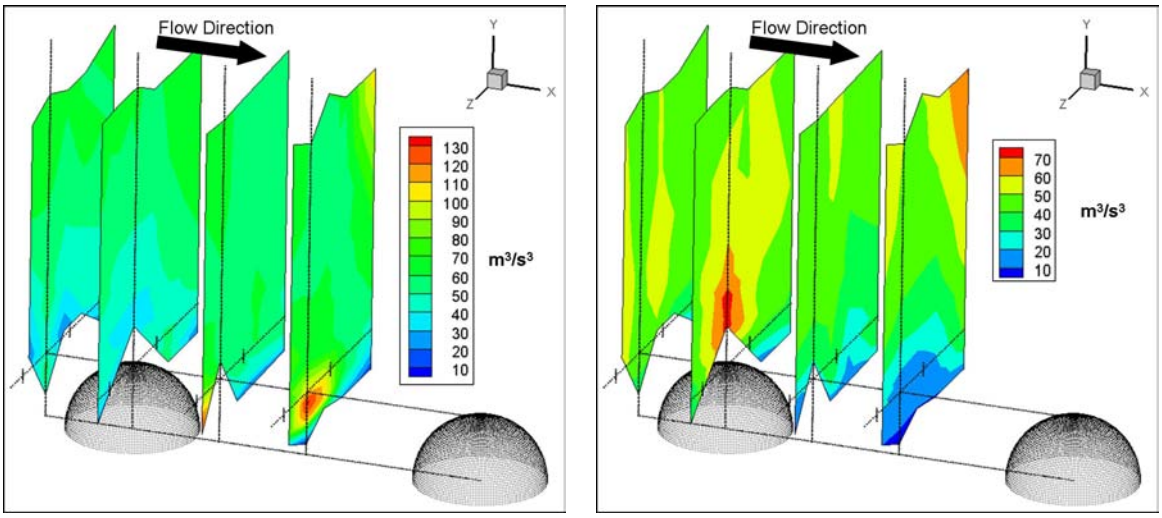

(a) Sweeps (b) Ejections

Figure 3.75: Contour plots of $\overline{V^2U}$ conditionally averaged on sweep and ejection events for Case 5

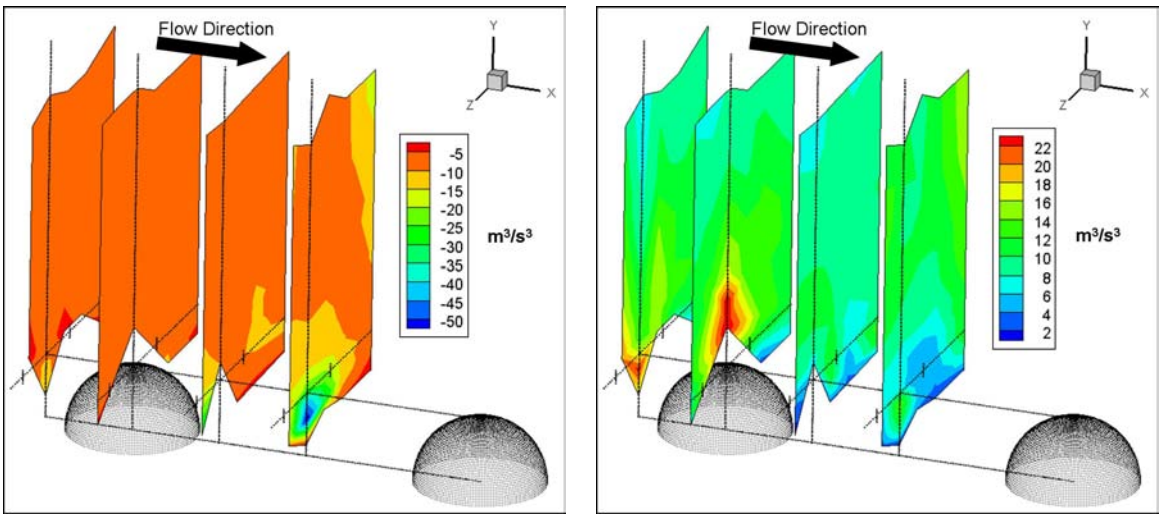

(a) Sweeps (b) Ejections

Figure 3.76: Contour plots of $\overline{V^2V}$ conditionally averaged on sweep and ejection events for Case 5

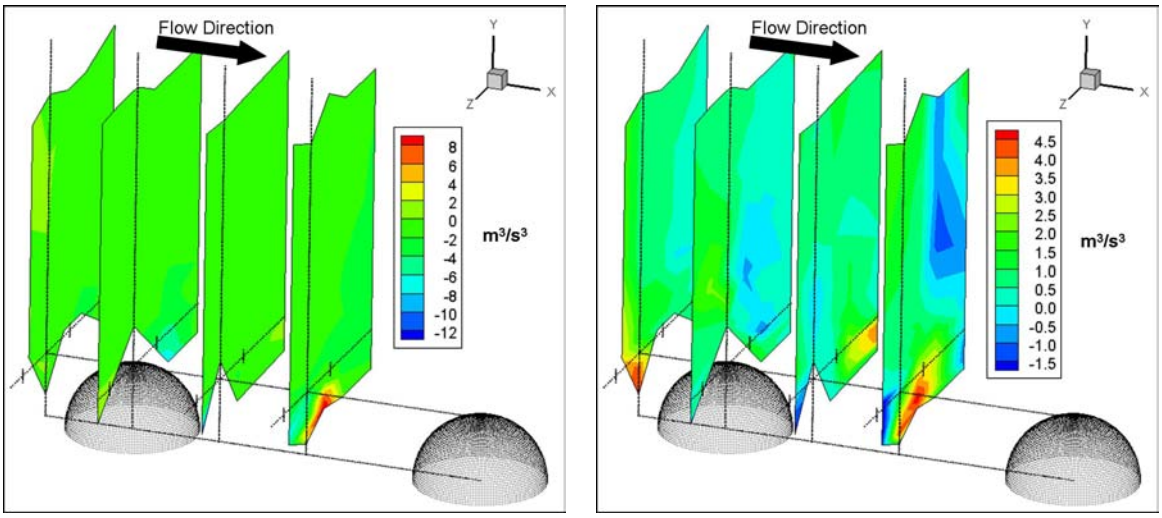

(a) Sweeps (b) Ejections

Figure 3.77: Contour plots of $\overline{V^2W}$ conditionally averaged on sweep and ejection events for Case 5

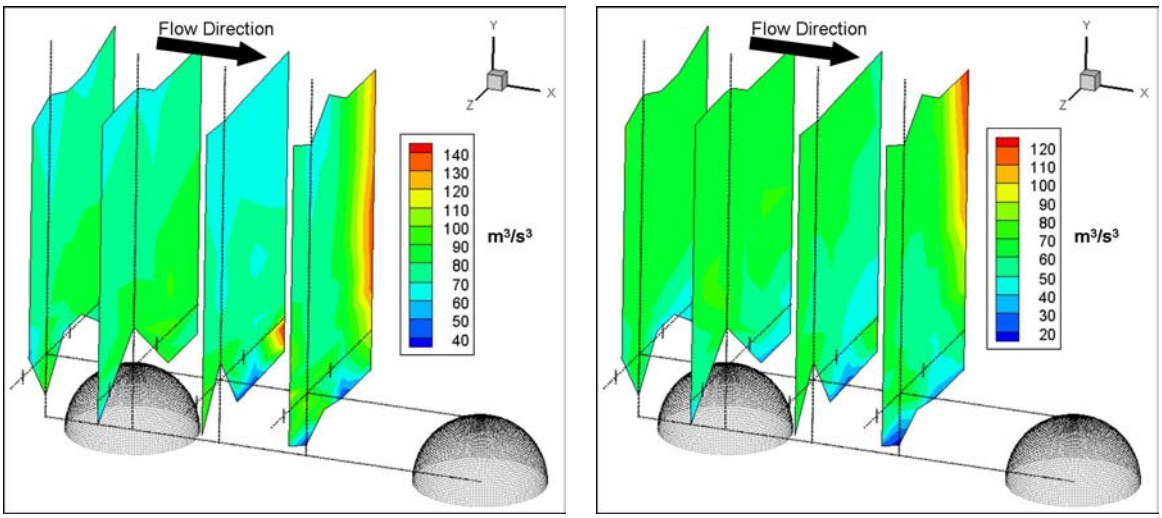

(a) Sweeps (b) Ejections

Figure 3.78: Contour plots of $\overline{W^2U}$ conditionally averaged on sweep and ejection events for Case 5

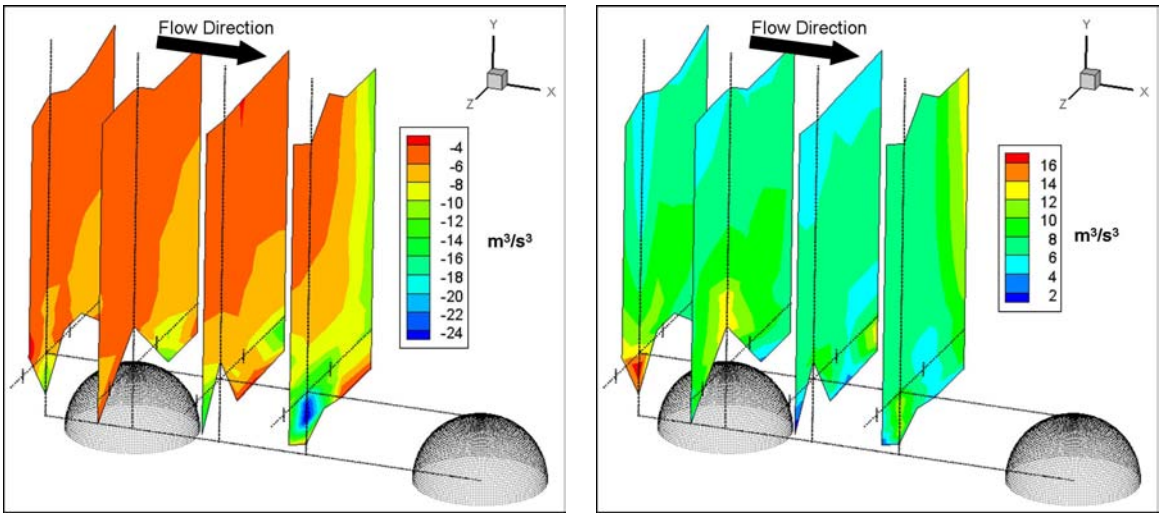

(a) Sweeps (b) Ejections

Figure 3.79: Contour plots of $\overline{W^2V}$ conditionally averaged on sweep and ejection events for Case 5

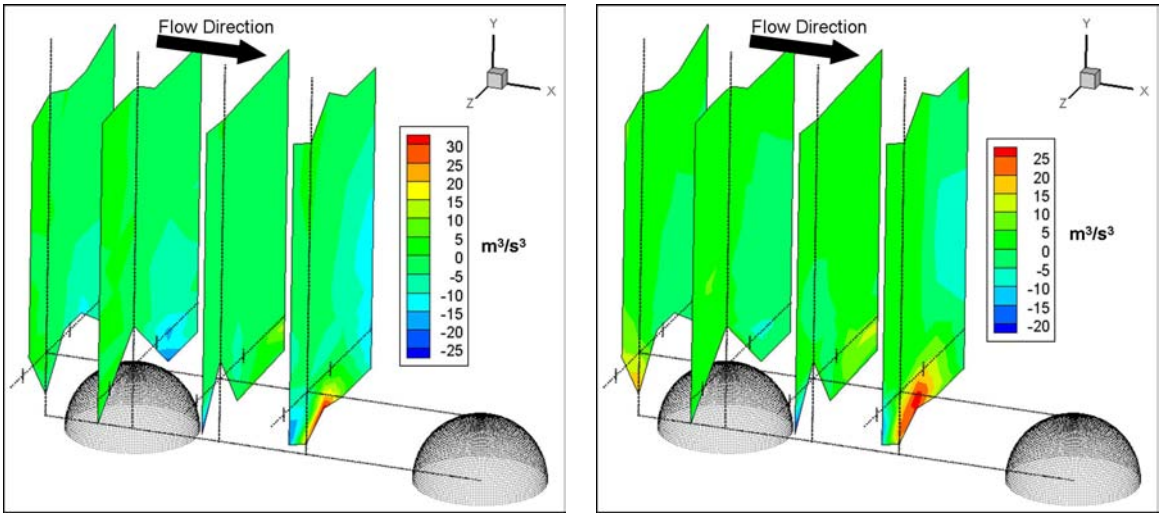

(a) Sweeps (b) Ejections

Figure 3.80: Contour plots of $\overline{W^2W}$ conditionally averaged on sweep and ejection events for Case 5

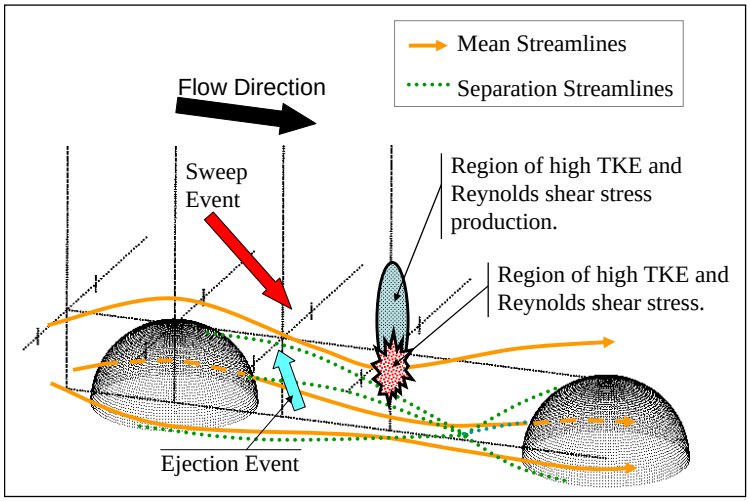

Figure 3.81: Conceptual Model of Turbulence Structure

3.9.5 Conceptual Model

Based on the aforementioned measurements and other studies [16, 45], a conceptual model of the turbulence structure can be realized (figure 3.81). The hemispherical elements cause a separation region that, for case 5, reattaches downstream before colliding with the downstream element. There is a smaller separation region upstream of the element. The presence of the element forces the mean flow lines upward away from the wall as fluid passes over the element as well as around the sides of the element, but to a lesser degree. Sweeping motions carry high momentum fluid from further out in the boundary layer down toward the wall. When this fluid impinges on the roughness elements a strong shear layer is created downstream of the element. High levels of TKE and Reynolds shearing stress exist in this region. In contrast to cylindrical roughness elements however [16], where this region is located one element height above the wall, this region is located at 75% of the hemisphere height about the wall. This can be explained by the hemispherical elements' lack of sharp edges, which causes the flow to remain attached longer as it passes of the top of the hemisphere. There also exists a high region of TKE and Reynolds shear stress production extending upwards away from the wall to about twice the element height due to the presence of a high mean velocity gradient. This is also in contrast to the cylindrical elements which have much higher levels of TKE and Reynolds stress in the shear region. This is again due to the sharp edge that forms the cylinder top. At a distance of three to four element heights above the wall position, the mean flow and turbulence statistics collapse to the same profile in the outer region. This confirms the data of the previous researchers [16, 45]. When compared with a smooth wall the rough wall Reynolds number is increased due to the roughness for a given downstream measurement location and freestream speed. This increase in Reynolds number is reflected in the outer layer by an increase is the Reynolds stresses and triple products.

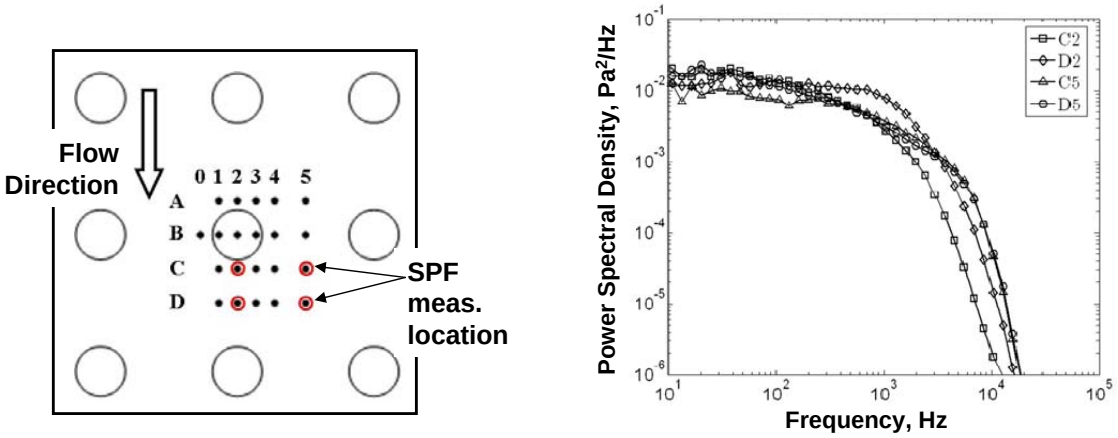

(a) SPF measurement locations

(b) Measured SPF spectra

Figure 3.82: Effect of local flow field on surface pressure fluctuations

3.10 Surface Pressure Spectra

Surface pressure fluctuation (SPF) measurements were made at four different locations for case 3 (5.5 mm spacing, 27 m/s). It was found that the local flow field around a roughness element influenced the SPF spectrum if the measurement location was in the separation region of the element. The mid and high frequency range was significantly modified, but the low frequencies were left largely unaffected. The two SPF spectrum measured at different locations on the centerline between columns of elements collapsed extremely well. Figure 3.82 shows the measurement locations and the results. The significantly higher power measured at location D2 at around 1000 Hz can be explained qualitatively as due to the high turbulence levels near that sensor location (see figure 3.81). With this information, it was decided to make all other SPF measurements at the cell center as far from the roughness elements as possible (location D5).

Table 3.12 shows the mean square pressure level for all cases. This value can be found by integrating the power spectral density over all frequencies. Figure 3.83 is a plot of sound pressure level (SPL) vs. frequency. There is a clear ω^{-5} region for all the cases, and nearly all cases have a ω^{-1} region. Only the smooth wall and sparsest rough cases (cases 1, 2, 9, and 10) do not clearly have this region. This is possibly for two reasons. The first is because the Reynolds number for the cases mentioned is too low to have a distinct overlap region. The second is that the reasoning behind the derivation of an ω^{-1} region is based on self-similar (equilibrium) arguments which for an external boundary layer is only approximate. Goody and Simpson [58] show that in fact, for smooth walls, the power on ω in this region is really between -0.7 and -0.8. However, self-similarity and equilibrium is a much better approximation for boundary layers in the fully rough regime and therefore a ω^{-1} is more likely.

Case No.	$\overline{p^2}$x10^{-7} Pa^2	$\overline{p^2}/(\rho u_\tau^2)^2x10^{-7}$
1	0.824	0.696
2	0.268	0.981
3	2.089	1.058
4	0.638	1.019
5	1.867	0.724
6	0.695	1.072
7	1.961	0.752
8	0.539	0.810
9	1.604	1.005
10	0.381	0.691

Table 3.12: $\overline{p^2}$ values for all cases

The ω^{-5} region can be explained by considering an approximate form of the Poisson equation, where Ω is a volume and r is the distance to any point in the volume to the location where p is measured.

$$p \approx \frac{\rho}{\pi} \oint_\Omega \left[\frac{\partial U}{\partial y} \frac{\partial v}{\partial x} \right] \frac{d\Omega}{r} \tag{3.10.1}$$

It is extremely difficult to measure $\partial v/\partial x$. However it can be modeled by assuming v can be represented as a traveling wave ($v = v_w \cos(\omega t - k_1 x)$), where v_w is the value of v at a given frequency and k_1 is the wave number in the stream-wise direction. The x-derivative of v can then be written as follows.

$$\frac{\partial v}{\partial x} = k_1 v_w \sin(\omega t - k_1 x) \tag{3.10.2}$$

Since the behavior of the fluctuating pressure at a given frequency is inversely proportional to distance from the wall [79], the near-wall turbulence dominates the high frequency region. The turbulent fluctuations near the wall in the viscous subrange produce a k_1^{-7} variation in energy. This means $v_w \propto k^{-\frac{7}{2}}$ in this region and $k_1 v_w \propto k_1^{\frac{5}{2}}$. By assuming that the phase of the turbulent structures for each k_1 is nearly the same accross the sublayer, equation 3.10.1 can be integrated without altering the frequency dependence of v_ω. Therefore by squaring equation 3.10.1 the spectral density of the wall pressure fluctuations at high frequency varies as $\Phi \propto k_1^{-5} \propto \omega^{-5}$

The inner scaling of Blake is shown in figure 3.84 with four different estimates of the friction velocity: the integral momentum balance, the SFM, the SFM w/ ϵ, and the method of Krogstad (see section 3.5). The average values over the three days of measurement are used for each method. The differences are only slight, however, the integral momentum

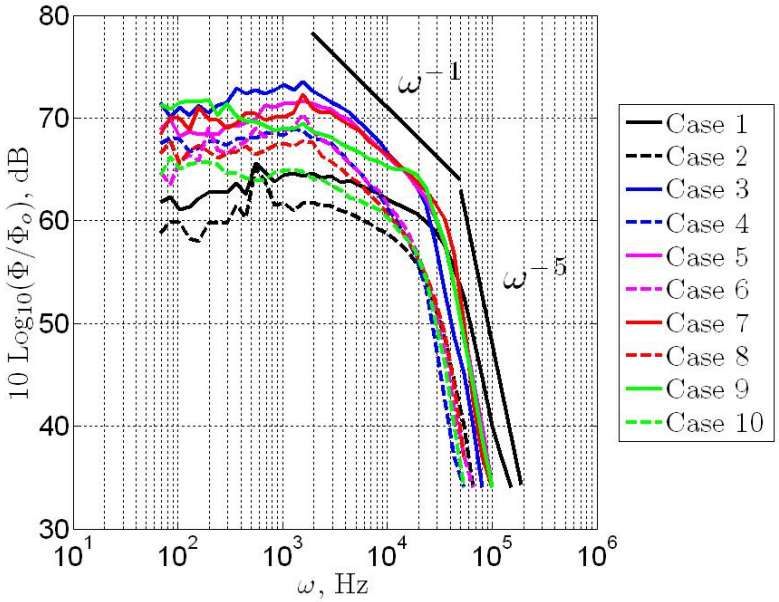

Figure 3.83: SPF spectra measurements in dimensional form, $\Phi_o = (20\text{x}10^{-6})^2$ Pa^{2}s

balance produces the best collapse. The fit methods have noticeably less collapse, especially for Krogstad's method. This is expected as the uncertainties for the fit methods are generally higher. In light of this information, the integral momentum balance will be used throughout the rest of this section to estimate the skin friction were needed.

The inner scaling of Blake appears to produce a good collapse of the SPF spectra in the high frequencies where the smallest turbulent eddies are described by the wall shear and the roughness length scale. However, if the flow-surface interaction is in the fully rough regime then the friction velocity should be proportional to the edge velocity ($u_\tau \propto U_e$). Rearranging Blake's inner scaling and substituting this proportionality yields the following relationship.

$$\frac{\Phi u_\tau}{\tau_w^2 k} = \frac{\Phi}{\rho^2 u_\tau^3 k} \propto \frac{\Phi}{\rho^2 U_e^3 k} \tag{3.10.3}$$

Figure 3.85 shows that a scaling on U_e does in fact produce a good collapse at high frequencies. This is further evidence that the flow-surface interaction is indeed fully rough. It also reveals that the element spacing is not an important parameter for high frequency scaling.

The scaling of Aupperle and Lambert do not collapse all the roughness cases as seen in figure 3.86. Since the equivalent sand grain length scale k_s is used in their formulation, it is necessary to perform a fit to measure ΔU^+ as explained in section 1.2.7. Figures 3.86(a) and 3.86(b) use the SFM and SFM w/ ϵ methods respectively. Neither collapse the data as well as Blake's scaling. However, the SFM seems to collapse the densest and sparest cases

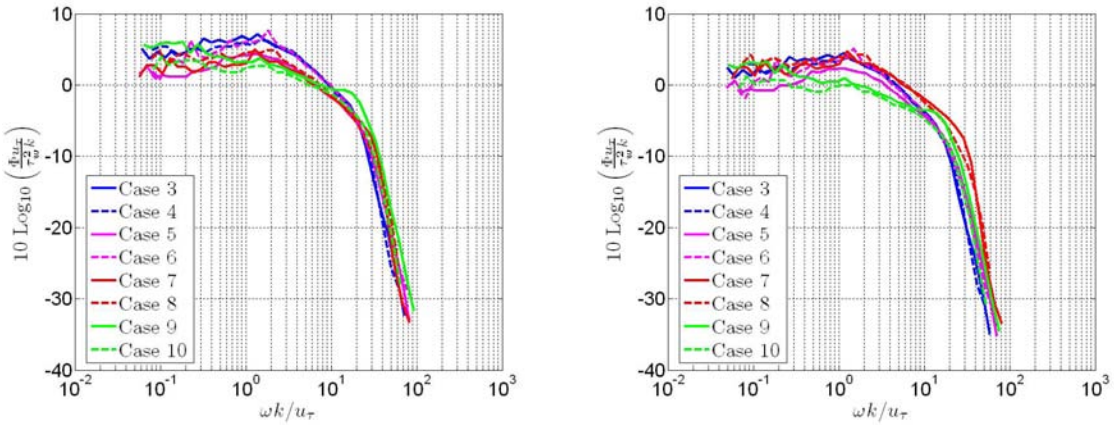

(a) Int. Mom. Bal.

(b) SFM

(c) SFM w/ ϵ

(d) Krogstad

Figure 3.84: SPF spectra normalized with inner scaling of Blake (1970). $\frac{\Phi u_\tau}{\tau_w^2 \bar{k}}$ vs. $\omega\bar{k}/u_\tau$. Estimates of the friction velocity from a) the integral momentum balance, b) the SFM, c) the SFM w/ *epsilon*, and d) the method of Krogstad

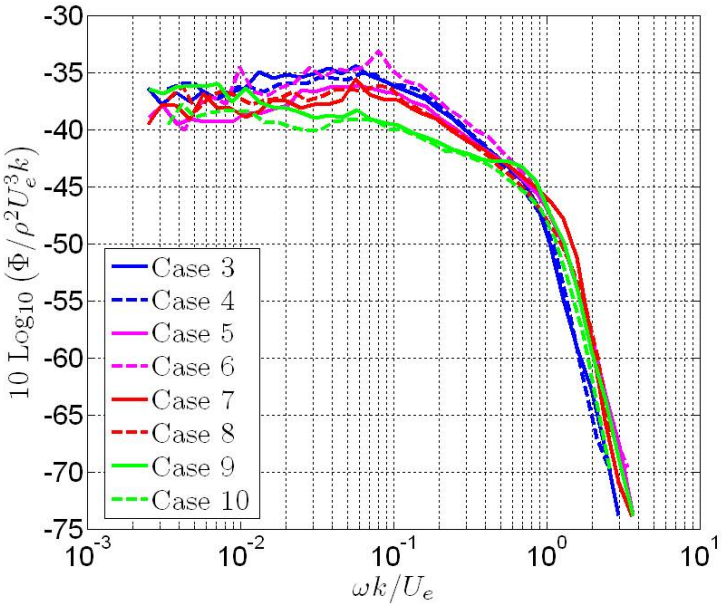

Figure 3.85: SPF spectra measurements normalized on U_e and k, $(\Phi/\rho^2U_e^3k)$ vs. $\omega k/U_e$

separately. Perhaps this has something to do with the differences between the separation regions as mentioned in section 3.6.

As discussed by Bradshaw [79] the behavior of the fluctuating pressure at a given frequency is due to $U_c/2\pi y$, where y is the distance from the wall to the location of the turbulence structure and U_c is the wave speed. This means that at low frequencies the spectral density should depend on global boundary layer parameters such as δ and U_e, and not on motions happening near the wall. Figure 3.88 shows the outer layer scaling suggested by Goody [80] in his 2004 review paper. It is note worthy that the smooth wall cases (1 and 2) are included since there is no dependence on the wall geometry in this scaling. There is, however, poor collapse at the low frequencies may be contributed to the merging boundary layers from the tunnel floor and ceiling.

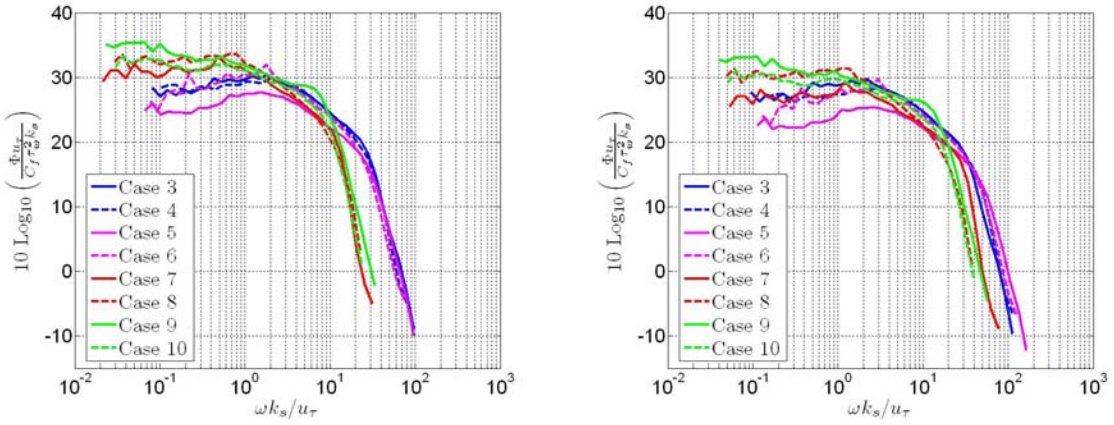

(a) SFM (b) SFM w/ ϵ

Figure 3.86: SPF spectra normalized with inner scaling of Aupperle and Lambert (1970). $\frac{\Phi u_\tau}{C_f \tau_w^2 k_s}$ vs. $\omega k_s/u_\tau$

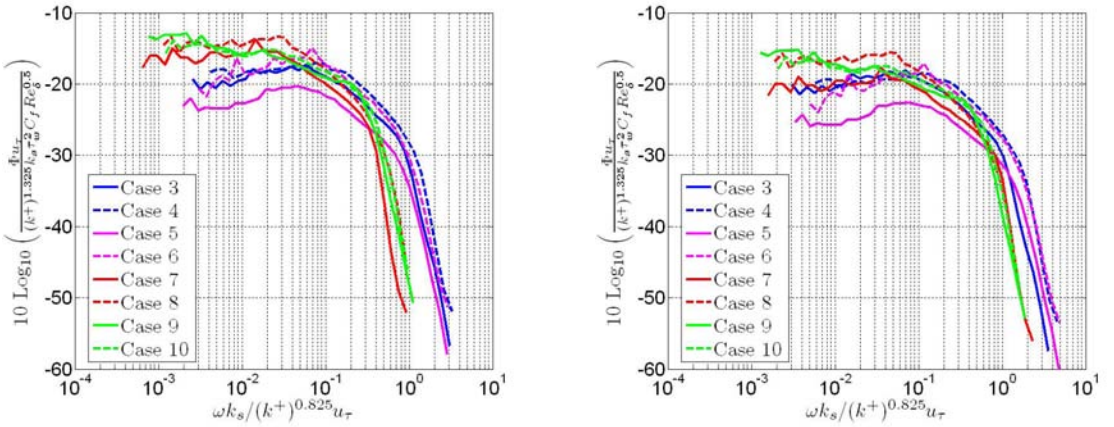

(a) SFM (b) SFM w/ ϵ

Figure 3.87: SPF spectra normalized with scaling of Smith (2008b). $\frac{\Phi u_\tau}{(k^+)^{1.325} k_s \tau_w^2 C_f Re_\delta^{0.5}}$ vs. $\omega k_s/(k^+)^{0.825} u_\tau$

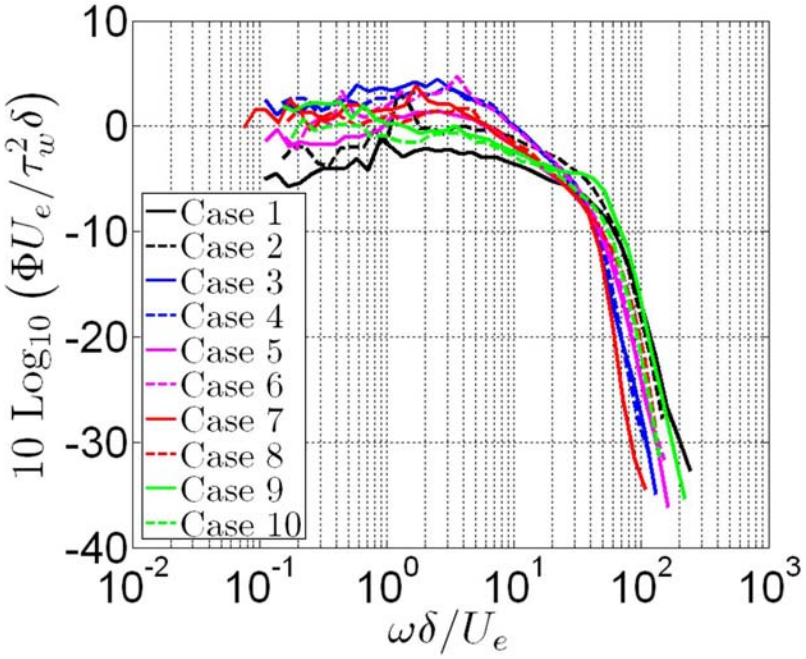

Figure 3.88: SPF spectra measurements normalized on outer variables, $(\Phi U_e/\tau_w^2\delta)$ vs. $\omega\delta/U_e$

Chapter 4

Summary, Conclusions, and Future Work

4.1 Summary of Experiments

Turbulent boundary layers over rough surfaces are a common, yet often overlooked, problem of practical engineering importance. Development of correlations between boundary layer parameters that can be used in turbulence models and the surface geometry is the only practical option for solving these problems. An extensive review of the literature reveals that correlations for even the simplest case of a 2D zero pressure gradient turbulent boundary layer have yet to be fully developed, although significant progress has been made. The most common model for the streamwise mean flow is given in equations 4.1.1 and 4.1.2.

$$\frac{U}{u_\tau} = \frac{1}{\kappa} \ln \left[\frac{(y+\epsilon)u_\tau}{\nu} \right] + B - \Delta U^+ \tag{4.1.1}$$

$$\Delta U^+ = \frac{1}{\kappa} \ln \frac{k_c u_\tau}{\nu} + f(\cdot) \tag{4.1.2}$$

The effect of the shift in mean streamlines due to the presence of the roughness element and their wakes is expressed as ϵ. The model equation for the roughness function ΔU^+ only applies when the surface-flow interaction is considered fully rough. This occurs when the viscous sublayer is completely destroyed by the roughness elements and the viscous contribution to the surface drag is minor compared to the form drag on the elements. The function $f(\cdot)$ is only a function of the surface geometry. Correlations for $f(\cdot)$ have been developed revealing a sparse and dense regime. It was a goal of this research to examine the performance of these correlations for the sparse regime. This research also attempted to explore the relationship between ϵ and the roughness geometry as well.

Many other researchers use the model equation (4.1.1) assuming κ is the smooth wall von Kármán constant. There is no physical reason why this assumption should be true, but it

does allow for simple estimation of the friction velocity u_τ. A goal of this research was to examine the validity of a constant κ by performing an independent measure of u_τ.

There have only been a very few experiments of the surface pressure fluctuations performed on rough wall boundary layers. However, it has been shown that the spectra of the wall fluctuations can be used to predict the far-field noise spectrum [1, 2]. Therefore it has been the goal of this research to verify existing correlations between the surface pressure fluctuation spectrum and the surface geometry as well as develop new correlations that provide insight into the interactions between the turbulent motions and the wall pressure.

Experiments have been performed on fetches of hemispherical roughness elements of 2 mm diameter. The elements were arranged in a straight configuration. Four different spacings were considered of 4.0, 5.5, 8.0, and 11.0 mm. Experiments were conducted in the Virginia Tech Small Boundary Layer Wind Tunnel. Flow measurements were conducted with a laser Doppler velocimeter capable of measuring all three components of velocity. Extensive uncertainty analysis was performed and it was determined that an unknown bias due to calibration was a large contributor to any error in the measurements. However, it was determined that the largest source of uncertainty in these measurements was the wind tunnel itself. Changes in tunnel conditions over the course of an experiment could cause errors in the measured quantities. To mitigate and quantify these effects all the LDV measurements were repeated three times over the course of three days. Surface pressure fluctuation measurements were made two Endevco Miniature Piezoresistive Pressure Transducers. Two transducers were used in a noise-reduction scheme since the wind tunnel was not acoustically treated.

4.2 Conclusions

The friction velocity was estimated from a form of the integral momentum equation. Budgets of u_τ across the boundary layer revealed that $\sqrt{-\overline{uv}}$ is a good approximation of the friction velocity to within less than 4 percent. The friction velocity was also estimated using three fitting methods: a simple fit (SFM) to the semi-log region of the mean velocity profile, a simple fit that included the ϵ parameter (SFM w/ ϵ), and the fit method of Krogstad [57]. The method of Krogstad is an iterative method, and was found to be very sensitive to the value of the initial guess. It was found that all the fit methods, with an assumed κ value of 0.41, overestimated the friction velocity. Uncertainty in the measurements alone, could not be blamed for the discrepancy. Therefore, it was concluded that κ is not a constant for rough wall boundary layers.

It is reasonable to hypothesize that the variation in κ is dependent on the ratio of outer to inner length scales of the flow. After all, this same argument is used to explain the existence of the semilogarithmic region of the mean velocity profile, where an overlapping of these scales occur. It is reasonable to consider that if the inner length scales of the boundary layer

are significantly modified due to the presence of the roughness elements, that the slope of this region might as well. Since κ is a measure of the slope, it follows that it should be a function of the ratio of these length scales. The measured data tentatively confirm this hypothesis. Although significantly limited by uncertainties, when plotted with data from other researchers a trend begins to emerge. An overall decrease in the value of κ can be detected with a decrease in the ratio of δ/k. This trend is more pronounced if the SFM w/ ϵ is used (see figure 3.14(b) and appears to decrease below 0.3 for $\delta/k < 40$.

Values for $f(\cdot)$ can be computed several different ways depending on the fit method used to estimate ΔU^+ and whether u_τ is measured using the integral momentum balance or a fit method. The correlations of Dvorak [41] and Waigh and Kind [42] have been examined using values for $f(\cdot)$ computed four different ways. Values for $f(\cdot)$ are considerably less certain when a fit method is used to evaluate u_τ. When u_τ is measured from the integral momentum balance the uncertainty is reduced. In addition, when the SPF w/ ϵ is used to estimate ΔU^+, Dvorak's correlation falls within the uncertainty bounds. However, when only the SPF is used, measured values are over predicted by the correlation. In general, when compared with data from other researchers, the values of $f(\cdot)$ are always lower for both Dvorak's and Waigh and Kind's correlations. Since none of the data from the other researchers included hemispheres, this may indicate that there is still another set of parameters for which $f(\cdot)$ may be a function. However, due to the limited amount of data and its uncertainty, discovering these parameters will be challenging. In fact, given the uncertainty in u_τ measured across the literature, it may be that better collapse cannot be achieved.

Values for the displacement height ϵ were found using an iterative fitting method. Although uncertainty in the values were high, it was clear that for the present data the model equation must be written in terms of $(y + \epsilon)$ to achieve a positive value for ϵ. This however is not consistent with the physical interpretation of the displacement height, which is the upward displacement of mean streamlines due to the presence of the roughness elements. To achieve consistency with this interpretation, the model equation is modified to include a roughness length scale (k_c) contribution to the mixing length ($l = k_c + \kappa(y - \epsilon_1)$). Several values for k_c based on the surface geometry were considered. However, a value of $k_c = k/3$ produced the most reasonable results.

A study of the local turbulence structure around hemispherical roughness elements was performed for Case 5. It was found that, in contrast to 'sharper-edged' elements such as cylinders, an elevated region of TKE and Reynolds shear stress was found downstream of the element at $0.75k$. This can be explained by the delay in separation of the flow coming over the top of the element due to the smooth curvature of the element. Also in contrast to cylindrical elements, an elevated region of shear stress production extended away from the wall a distance of approximately twice the element height. This is attributed to the relatively high mean velocity gradient at that location. It was also found that sweep and ejection events each occur 32% of the time. This is a significant difference from the smooth wall case, where

sweep and ejection events each only occur about 10% of the time, comfirming the increased mixing in the boundary layer due to rough surface.

The surface pressure spectrum was found to collapse well at high frequencies using the scaling of Blake [59]. Blake's scaling involves inner variables, namely u_τ. However, since the surface-flow interaction for these experiments is fully rough, the friction velocity is proportional to the freestream velocity. Indeed, good collapse is achieved at high frequency when u_τ is replaced by U_e in Blake's scaling. When the scaling of Aupperle and Lambert [60] is tried collapse at the high frequencies is not achieved.

The most important conclusions from this work are summarized below.

- The Reynolds shear stress in the constant region is a good estimate of the skin friction.
- Fitting methods over-estimate the skin friction.
- The von Kármán 'constant' may not be valid for rough walls.
- The slope of the semi-log region (κ) may depend on a ratio of inner and outer length scales.
- The displacement height (ϵ) should be included in the law-of-the-wall for rough wall boundary layers.
- A new model equation for the mean flow is suggested to achieve consistency with the traditional definition of the displacement height.

$$\frac{U}{u_\tau} = \frac{1}{\kappa} ln \left| \frac{k}{3} + \kappa \left(y - \epsilon_1 \right) \right| + \frac{1}{\kappa} ln \left| \frac{u_\tau}{\nu \kappa} \right| + B - \Delta U^+ \tag{4.2.1}$$

- In contrast to 'sharper-edged' elements such as cylinders, an elevated region of TKE and Reynolds shear stress was found downstream of the element at $0.75k$ indicating a delay in separation of the the flow over the top of the element.
- An elevated region of shear stress production extended away from the wall a distance of approximately twice the element height.
- Blake's scaling achieves the best collapse of the rough wall pressure spectra at high frequencies.

4.3 Future Work

The present research only examined the effect of element spacing on the boundary layer. More work is needed to examine the effect of element size, shape, and configuration. Future work should also take into account irregular roughness that can only be described statistically, however, this is a more challenging problem. Now that the validity of a universally constant κ has been questioned, all future measurements should not rely on a fit method to estimate u_τ. Until more work can be done with accurate independent measures of u_τ it will be unlikely that better correlations can be developed for $f(\cdot)$

The displacement height is a difficult quantity to measure but should be examined in more detail. This research used only one measurement location within a roughness 'cell'. However, ϵ really represents the spatially averaged effect of the roughness and this should be taken into account when conducting further experiments. Experiments in larger facilities capable of larger boundary layers would allow for larger roughness elements which would be useful in limiting uncertainties in measurements of ϵ.

Although the scaling of Blake produced a good collapse of the surface pressure spectra at high frequencies, the low-frequencies need to be correlated as well. Future work should also examine the effect of roughness size and shape. If the smooth and rough wall pressure spectrum can also be collapsed, fresh insights into the turbulent length scales would be gained.

Appendix A

List of Reviewed Experiments

Table A.1: List of Reviewed Experiments

Reference	**Flow Conditions**	**Geometry**	**Skin Friction**
Acharya *el al.* [49]	2D ZPG TBL	cast aluminum, simulated turbomachinery blade roughness, wire mesh	force balance
Akinlade *et al.* [81]	2D ZPG TBL	sandgrain, perforated plate, woven wire mesh	Krogstad [57] fit method
Andreopoulos and Bradshaw [82]	2D ZPG TBL	sandgrain	shear stress extrapolation
Antonia and Luxton [54]	2D ZPG TBL	2D square rods	pressure taps in elements
Bakken *et al.* [37]	2D fully developed channel flow	2D square rods, perforated plates	pressure drop
Bandyopadhyay [50]	2D ZPG TBL	2D bars, sandgrain	force balance
Bandyopadhyay and Watson [19]	2D ZPG TBL	2D spanwise grooves	force balance
Bechert *et al.* [51]	2D ZPG TBL	3D riblets	force balance
Bechert *et al.* [12]	2D ZPG TBL	streamwise triangular and scalloped riblets, thin vertical ribs	force balance
Bergstrom *et al.* [33]	2D ZPG TBL	sandgrain, perforated plate, woven wire mesh	Krogstad [57] fit method

Continued on next page

Table A.1 – continued from previous page

Reference	**Flow Conditions**	**Geometry**	**Skin Friction**
Bergstrom *et al.* [83]	2D ZPG TBL	circular perforations, wire screen, sandgrain	Krogstad [57] fit method
Bettermann [84]	2D ZPG TBL	2D spanwise square ribs integral momentum balance	
Brzek *et al.* [56]	2D ZPG TBL	sandgrain	integral momentum balance
Cheng and Castro [11]	2D ZPG TBL	rectangular blocks	pressure taps in elements
Colebrook and White [46]	fully developed pipe flow	sandgrain	pressure drop
Djenidi *et al.* [85]	2D pressure driven channel flow	2D square cavities	integral momentum balance
Flack *et al.* [86]	2D ZPG TBL	sandgrain, woven mesh	shear stress extrapolation
Furuya and Fujita [87]	2D ZPG TBL	wire screen, sandgrain	integral momentum balance
Furuya *et al.* [88]	2D ZPG TBL	2D and 3D spanwise wires	integral momentum balance, pressure taps in elements
Gartshore and De Croos [89]	2D ZPG TBL	3D rectangular thin vertical strips	force balance
George [16]	2D ZPG TBL	3D cylindrical elements	shear stress extrapolation
George and Simpson [63]	2D ZPG TBL	3D cylindrical elements	shear stress extrapolation
George and Simpson [90]	3D (wing-body junction) TBL	3D cylindrical elements	shear stress extrapolation
Grass [91]	2D open channel flow	sandgrain, round pebbles	shear stress extrapolation
Hama [14]	2D ZPG TBL	mesh screens	integral momentum balance
Hosni *et al.* [92]	2D ZPG TBL	3D hemispheres	integral momentum balance
Keirsbulck *et al.* [93]	2D ZPG TBL	2D spanwise square ribs	Krogstad [57] fit method

Continued on next page

Table A.1 – continued from previous page

Reference	**Flow Conditions**	**Geometry**	**Skin Friction**
Keirsbulck *et al.* [34]	2D ZPG TBL	2D square rods	Krogstad [57] fit method
Kerevanian *et al.* [64]	2D ZPG, adverse and favorable pressure gradient TBL	3D cylindrical elements	integral momentum balance
Kotay *et al.* [94]	2D ZPG TBL	circular perforations, wire screen, sandgrain	power law fit method
Krogstad et al. [47]	2D fully developed channel flow	2D square rod roughness	pressure drop
Krogstad *et al.* [57]	2D ZPG TBL	woven mesh screen	Krogstad [57] fit method
Krogstad and Antonia [95]	2D ZPG TBL	woven mesh screen, 2D lateral rods	Krogstad [57] fit method
Kunkel *et al.* [30]	fully developed pipe flow	honed roughness	uncertain, likely pressure drop
Lee and Soliman [55]	2D ZPG TBL	cubic roughness elements	pressure taps in elements
Li *et al.* [96]	2D ZPG and non-zero pressure gradients	sandgrain	oil-film interferometry
Ligrani and Moffat [97]	2D ZPG TBL	densely packed spheres	integral momentum balance
Marshall [98]	2D ZPG? TBL	3D cylindrical elements	integral momentum balance, force balance on individual element
Mikhailova *et al.* [99]	2D non-ZPG TBL	sandgrain	sublayer fit (viscous stresses only)
Moore [24]	2D ZPG TBL	2D spanwise square ribs	integral momentum balance
Nakagawa and Hanratty [100]	fully developed channel flow	sinusoidal wavy wall	shear stress extrapolation or pressure drop
Nakagawa *et al.* [31]	fully developed channel flow	2D sinusoidal wave roughness	pressure drop, shear stress extrapolation
Nikuradse [6]	fully developed pipe flow	sandgrain	pressure drop

Continued on next page

Table A.1 – continued from previous page

Reference	**Flow Conditions**	**Geometry**	**Skin Friction**
Perry and Joubert [101]	2D adverse pressure gradient TBL	2D spanwise square ribs	integral momentum balance
Perry and Li [102]	2D ZPG TBL	mesh roughness, narrow spanwise grooves	shear stress extrapolation
Perry *et al.* [103]	2D ZPG TBL	2D wavy wall, 3D diamond mesh	shear stress extrapolation, integral momentum balance
Perry *et al.* [18]	2D ZPG and adverse pressure gradient TBL	2D spanwise rods	pressure taps in elements
Pineau *et al.* [52]	2D ZPG TBL, 2D channel flow	2D spanwise square ribs	pressure drop (channel), force balance
Poggi *et al.* [36]	open channel TBL	wire screen	Krogstad [57] fit method
Raupach *et al.* [104]	2D ZPG TBL	3D cylindrical elements	shear stress extrapolation, integral momentum balance
van Rij *et al.* [105]	fully developed channel flow	sandgrain, sandgrain with smooth patches	pressure drop
Schetz and Nerney [53]	axisymetric body	porous surface 'similar in feel' to sandpaper	force balance
Schultz [106]	2D near ZPG TBL	sandgrain, algae	shear stress extrapolation
Schultz and Flack [77]	2D ZPG TBL	close-packed spheres, additional fine grit	shear stress extrapolation
Schultz and Flack [107]	2D ZPG TBL	sandgrain	shear stress extrapolation
Sirovich and Karlsson [108]	2D fully developed channel flow	upstream pointing 'V's'	pressure drop
Smalley *et al.* [109]	2D ZPG TBL	2D spanwise cylindrical rods	shear stress extrapolation
Stewart [45]	2D ZPG TBL	3D Gaussian spikes, circular cylinders	shear stress extrapolation
Subramanian *et al.* [110]	2D ZPG TBL	irregular roughness of scaled replica of an eroded gas turbine blade	surface pressure taps

Continued on next page

Table A.1 – continued from previous page

Reference	**Flow Conditions**	**Geometry**	**Skin Friction**
Tachie *et al.* [111]	2D shallow TBL	sandgrain, perforated plate, woven wire mesh	Krogstad [57] fit method
Tomkins [25]	2D ZPG? TBL	short fetch of hemispherical elements	shear stress extrapolation
Tsuji [112]	2D ZPG TBL	sandgrain	integral momentum balance
Webb *et al.* [48]	fully developed pipe flow	square ribs	pressure drop

Appendix B

Advanced LDV Principles and Apparatus

This appendix describes work that is distinct from the aim of this research, as outlined in section 1.3, but no less challenging or practical. It is included here as an appendix to maintain the flow and focus of this dissertation. The following sections contain valuable theoretical concepts and developments in LDV, a description of hardware used to explore these theories, a description of the novel algorithms used in signal processing, as well as the results of signal simulations used to examine their performance.

B.1 Advanced Principles of LDV

This section is a continuation of section 2.1.1. Here more advanced topics, such as sub-measurement volume position resolution and particle acceleration measurement are discussed in detail. This section contains novel efforts to provide a more complete theoretical framework of the more complicated principles in LDV.

Position Resolution

Much work has been done by other researchers to resolve the seed particle's position as it passes through the measurement volume [70, 113, 114, 115, 116, 117, 118, 119, 120]. Most previous work was limited to measuring only one or two components of velocity and one component of position within the measurement volume. However, the present work builds on the developments of Lowe and Simpson [70], which allows for simultaneous measurement of all three components of position as well as the three components of velocity.

Beam pairs that are crossed at off-waist positions will no longer have parallel fringes. Instead, they nominally vary monotonically across the measurement volume in a converging or diverging pattern.

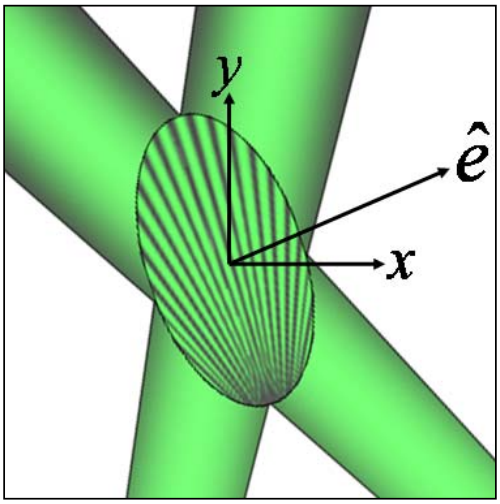

Figure B.1: An example of diverging fringes

If this variation is a known function of position it is possible to measure the seed particle's trajectory, $\vec{x}(t)$. If the reference time (t_r) is chosen to coincide with the peak intensity of a burst from a particular intersection volume, then the intercept vector ($\vec{x}(t_r) = \vec{x}_r$) will be in the plane of maximum intensity of the intersection volume.

$$\vec{x}(t) = \vec{U}(t - t_r) + \vec{x}_r \tag{B.1.1}$$

Since the fringe spacing is now a function of position within the measurement volume, the fringe spacing used in equation 2.1.4 must be modified to include this effect. The correct value to use is the average fringe spacing the seed particle sees as it moves through the measurement volume, S_{avg}. This is computed by integrating the fringe spacing along the particle's trajectory using the burst envelope $\omega(t)$ as a windowing function (equation B.1.3). Equations B.1.2 and B.1.3 are a coupled non-linear set of six. The solution of which is the seed particle's trajectory, equation B.1.1. Six intersection volumes are needed in total - three for each component of $\vec{U}$ and three more for each component of $\vec{x}_r$. If the fringe variations are indeed monotonic and the particle does not circulate within the measurement volume, the solution to these equations will be unique.

$$\vec{U} \cdot \hat{e}_i = f_i S_{avg,i} \ , \quad i = 1, 2, \ldots, 6 \tag{B.1.2}$$

$$S_{avg,i} = \frac{\int_{t_a}^{t_b} S_i(\vec{x}(t))\omega_i(t)dt}{\int_{t_a}^{t_b} \omega_i(t)dt} \ , \quad i = 1, 2, \ldots, 6 \tag{B.1.3}$$

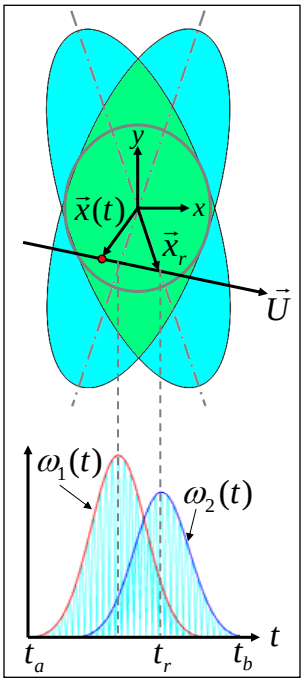

Figure B.2: An example of a seed particle's trajectory and corresponding burst signals

Laser Sheet

Nominally, the plane of the maximum intensity for a given beam pair corresponds to the plane perperdiculer to the intersection volume direction ($\hat{e}$) and intersecting the volume center. However, this is only true when each beam has the same intensity level, and can be rather difficult to ensure. The relative diameters of the two beams at their crossing location also affects the location of the plane of maximum intensity. Ensuring equal beam diameters is also challenging. If the location of the plane of maximum intensity is uncertain, then the intercept vector $\vec{x}_r$ will also be uncertain.

A more precise way to specify t_r is by shining a laser sheet through the measurement volume with known location. The thickness of the laser sheet is only a fraction of the measurement volume diameter. If the location of the sheet is chosen wisely, one unknown can be eliminated and the number of intersection volumes needed is reduced to five.

$$\vec{x}_r = \left\{ \begin{array}{c} x_s \\ y_r \\ z_r \end{array} \right\} \tag{B.1.4}$$

The laser sheet should be positioned perpendicular to the main flow direction so that the large majority of seed particles will pass through it. Otherwise, if a particle does not pass through the laser sheet, no solution exists.

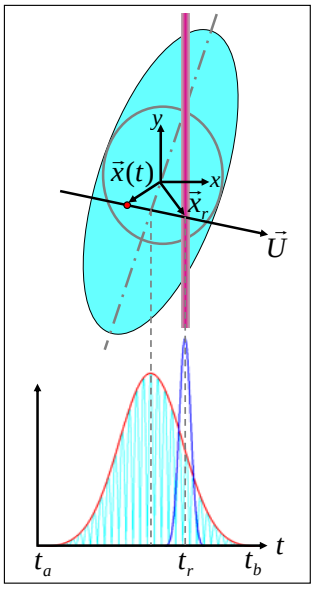

Figure B.3: An example of a seed particle's trajectory and corresponding burst signal with laser sheet

Calibrating for $S(\vec{x})$

A significant challenge is knowing the fringe spacing as a function of position within the measurement volume for all beam pairs. As discussed by Hopkins [121], it is possible to directly calibrate the fringe spacing as a function of position within the intersection volume. However, such efforts are costly.

For the ideal case of Gaussian beams, Miles [65] derived an analytical expression for the fringe spacing as a function of position within an intersection volume.

$$S(\gamma) = \frac{\lambda}{2\sin\phi}\left[1 + \frac{\gamma\cos^2\phi(\gamma\cos^2\phi - \gamma_w)}{\left(\frac{\pi d_w^2}{\lambda}\right)^2\cos^2\phi - \gamma_w(\gamma\cos^2\phi - \gamma_w)}\right],\ \gamma = (\vec{x} - \vec{x}_V)\cdot\hat{b} \qquad \text{(B.1.5)}$$

Equation B.1.5 is the special case where the beam waists diameters are identical ($d_{w,1} = d_{w,2} = d_w$) and the distance from the center of the intersection volume ($\vec{x}_V$) to the beam waists are also equal ($(\vec{x}_{w,2} - \vec{x}_V)\cdot\hat{b} = (\vec{x}_{w,1} - \vec{x}_V)\cdot\hat{b}$). Note that γ is in the direction of the beam pair bisector ($\hat{b}$) and that the fringe spacing is only a function of the component of position in this direction. Miles included a more general form of equation B.1.5 in his paper, one that accounts for the effects of unequal beam waist diameters and unequal beam diameters at the intersection point. These effects cause the fringe spacing to be a function of position in both the $\hat{b}$ and $\hat{e}$ directions. The following analysis can be applied in the same way for this more general case.

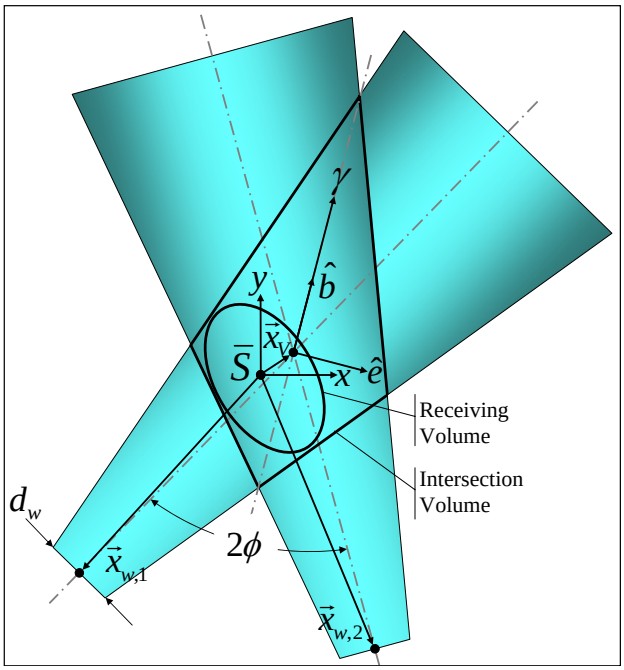

Figure B.4: The calibrated mean fringe spacing relationship to intersection and receiving volumes

The value of the fringe spacing at the center of the receiving volume is found through the calibration explained previously. Subsequently, the value of the fringe spacing computed using equation 2.1.2 is denoted by $\bar{S}$, as it corresponds to the mean frequency measured during calibration $\bar{f}$. It is assumed that $\bar{S} = S(\vec{x} = 0)$ for each beam pair. This assumption requires that the receiving volume is entirely contained within each of the intersection volumes and that the fringe variation within the receiving volume be linear. Since equation B.1.5 is near linear for small variations in γ, the fringe spacing as a function of position for all beam pairs can then be linearized about the center of the receiving volume.

$$S_i(\vec{x}) = \bar{S}_i + \nabla S_i|_{\vec{x}=0} \cdot \vec{x} \tag{B.1.6}$$

$$\nabla S|_{\vec{x}=0} = \left.\frac{dS}{d\gamma}\right|_{\gamma=\gamma_0} \hat{b}\,, \quad \gamma_0 = -\vec{x}_V \cdot \hat{b} \tag{B.1.7}$$

$$\left.\frac{dS}{d\gamma}\right|_{\gamma=\gamma_0} = \frac{\lambda}{2\sin\phi}\left\{\frac{\cos^2\phi(2\gamma_0\cos^2\phi-\gamma_w)}{\left(\frac{\pi d_w^2}{\lambda}\right)^2\cos^2\phi-\gamma_w(\gamma_0\cos^2\phi-\gamma_w)} + \frac{\gamma_0^2\gamma_w\cos^4\phi(\gamma_0\cos^2\phi-\gamma_w)}{\left[\left(\frac{\pi d_w^2}{\lambda}\right)^2\cos^2\phi-\gamma_w(\gamma_0\cos^2\phi-\gamma_w)\right]^2}\right\} \tag{B.1.8}$$

Since equation B.1.5 is written in the coordinate system of the intersection volume, the point about which the fringe gradient must be taken is unknown (γ_0). However, γ_0 can be found by iteratively solving equation B.1.5 where $\bar{S} = S(\gamma_0)$.

Linear Solver

Up to this point the governing equations describing the trajectory of the seed particle have been nonlinear. This nonlinearity arises from the necessity to integrate in time the fringe spacing experienced by the particle as it passes through the measurement volume. These equations, however, can be linearized by assuming $S_{avg} = S(\vec{x}_?)$, where $\vec{x}_?$ is some location within the measurement volume where the fringe spacing satisfies equation B.1.2. Linearizing the fringe spacing about the center of the receiving volume yields equation B.1.9.

$$\vec{U}\cdot\hat{e}_i = f_i\left[\bar{S}_i + \nabla S_i\cdot\vec{x}_?\right] \quad , \quad i = 1,2,\ldots,6 \tag{B.1.9}$$

The fringe spacing at the center of the receiving volume ($\bar{S}$) is calibrated as described previously. The fringe gradient (∇S) for each beam pair can be estimated from equation B.1.7. The frequency is the measured quantity and the remaining unknowns are $\vec{U}$ and $\vec{x}_?$ for each particle that passes through the measurement volume. Equation B.1.9 represents a linear set of six equations.

The process of linearizing equation B.1.2 has led to the assumption of a constant fringe gradient. This implies that $\vec{x}_? = \vec{x}_{avg}$, where $\vec{x}_{avg}$ is the average position of the seed particle as it passes through the measurement volume. For $\vec{x}_{avg}$ to be a point on the particle's trajectory ($\vec{x}(t)$), there must be negligible curvature in the trajectory. If this assumption does not hold $\vec{x}_{avg}$ has little meaning.

If $\vec{x}_{avg}$ is on $\vec{x}(t)$, then the solution to equation B.1.9 defines the particles trajectory through space. However, the time when the particle passes through $\vec{x}_{avg}$ is still unknown ($t_?$).

$$\vec{x}(t) = \vec{U}(t - t_?) + \vec{x}_{avg} \tag{B.1.10}$$

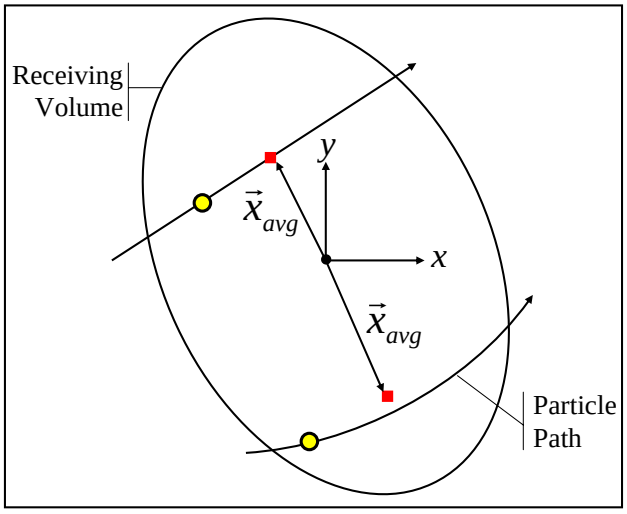

Figure B.5: Effect of curved path on $\vec{x}_{avg}$

However, a laser sheet can be used as a reference. If the sheet intersects the measurement volume in a plane perpendicular to the x-axis located at some distance x_s along the x-axis, then $t_?$ can be found by solving the following scalar equation.

$$x(t_?) = U(t_? - t_r) + x_s = x_{avg} \tag{B.1.11}$$

$$t_? = \frac{x_{avg} - x_s}{U} + t_r \tag{B.1.12}$$

Acceleration

The seed particle's acceleration can also be measured using LDV. In later sections on signal processing the method of extracting the rate of change of frequency, or chirp ($\frac{Df}{Dt}$), from a burst signal is discussed. This chirp signal is used to estimate the Lagrangian acceleration following a seed particle as it passes through the measurement volume. This is done by taking the substantial derivative of equation B.1.2.

$$\vec{x}(t) = \frac{\vec{a}}{2}(t^2 - t_r^2) + \vec{U}(t - t_r) + \vec{x}_r \tag{B.1.13}$$

$$\vec{a} \cdot \hat{e}_i = \frac{D\vec{U}}{Dt} \cdot \hat{e}_i = \frac{Df_i}{Dt} S_{avg,i} + f_i \frac{DS}{Dt}_{avg,i}, \quad i = 1, 2, \ldots, 6 \tag{B.1.14}$$

Equation B.1.14 represents six more equations that are weakly coupled to equations B.1.2 and must be solved simultaneously. The system is over constrained however and only three

of the six intersection volumes are needed to extract the acceleration. The time rate of change of fringe spacing following a seed particle $\frac{DS}{Dt}_{avg}$ can be computed similarly to S_{avg}.

$$\frac{DS_i}{Dt}_{avg} = \frac{\int_{t_a}^{t_b} \frac{D}{Dt} S_i(\vec{x}(t)) w_i(t) dt}{\int_{t_a}^{t_b} w_i(t) dt} \tag{B.1.15}$$

The laser sheet can still be used to remove one of the beam pairs as explained previously.

If the linear solver is used (i.e. $S_{avg} = S(\vec{x}_{avg})$), it is assumed the curvature of the particle's path is negligible. This assumption limits the magnitude of the particle's acceleration because the path curvature is a direct result of acceleration. The time rate of change of the fringe spacing can be computed as follows.

$$\frac{DS_i}{Dt}_{avg} = \vec{U} \cdot \nabla S_i \tag{B.1.16}$$

The fringe gradient (∇S) can be estimated from equation B.1.7. Using the linear solver decouples the acceleration equations from the velocity and position equations B.1.2. Therefore, the acceleration can be solved for separately once $\vec{U}$ and $\vec{x}_{avg}$ are known.

$$\vec{a} \cdot \hat{e}_i = \frac{Df_i}{Dt} \left[\bar{S}_i + \nabla S_i \cdot \vec{x}_{avg} \right] + f_i \left[\vec{U} \cdot \nabla S_i \right] \tag{B.1.17}$$

B.2 Comprehensive LDV

The Comprehensive LDV (CompLDV) was developed by Dr. K. T. Lowe [70, 71]. It is capable of measuring all components of velocity, position, and acceleration. The CompLDV was modified slightly for the present research.

Like most LDV systems, the CompLDV is made of the same basic components: the optical table, the probe, the receiving table, and A/D conversion. An optical table is used to condition the beams before sending them, via optical fibers, to the probe. The probe focuses the beams to create the measurement volume and collect the scattered light signal. The receiving table converts the light signal into an electrical signal. The analog electrical signals are then converted to digital signals for processing. Seed generation hardware is also described. The CompLDV uses the same traverse mechanism and seeding apparatus described in sections 2.1.2 and 2.1.2.

B.2.1 The Optical Table

The optical table supports two 5 W Argon-Ion lasers (Coherent Innova I90 C-5). They are used in multiline mode without an etalon. The coherency of the beams is approximately 2.5 cm. Prisms are used to split the beam from each laser into several beams of separate

wavelengths. Green (514.5 nm) and blue (488 nm) beams are used from each laser. One purple (476.5 nm) and one teal (496.5 nm) beam is used from one laser. The green, blue, and purple beams are acousto-optically modulated using IntraAction Corp. Bragg cells and power supplies. A Bragg cell will produce two beams for any particular color - one unshifted in frequency, the other shifted by a predetermined amount. The unshifted and shifted beam are called a beam pair, and will eventually make up an intersection volume. The purple beam is split using a 40 MHz Bragg cell, one blue and one green beam are split using 60 MHz Bragg cells, and the remaining blue and green beams are split using 80 MHz Bragg cells. The teal beam remains unshifted. There are now two green beam pairs, two blue beam pairs, one purple beam pair, and the remaining teal beam. Each of the eleven beams are focused into a 4 μm diameter polarization preserving fiber optic cable (Corning Alcoa-Fujikura SM8-P-4/125-ST/NY-9000) via a Newport Single-Mode Fiber Coupler. The fiber optic cables carry the light from the optical table to the probe.

B.2.2 The Probe

The CompLDV probe is composed of two aluminum heads, a mount for the laser sheet optics, and a receiving lens assembly. One head contains both blue beam pairs and the other contains both green pairs and the purple pair. The teal beam is used as the laser sheet. The interior angle between the surface normal direction of the heads was designed to be 90 degrees but was changed to 45 degrees to achieve greater access to the tunnel test section. The fiber optic cables are attached to the probe heads via fiber optic couplers and three axis traverse components that were added to the original design. Each coupler inserts into a three axis traverse component that allows for three axis adjustments of the fiber aperture for easy alignment. Each traverse component is mounted to a lens assembly that is secured to one of the aluminum heads. After exiting the fiber optic cable, each beam except teal is collimated and focused individually using two achromatic lenses. The beams are crossed at off-waist positions to create sets of converging and diverging fringes in the measurement volume. The 60 MHz green, 80 MHz blue, and 40 MHz purple pairs have diverging fringes. The 80 MHz green and 60 MHz blue pairs have converging fringes. The diameter of the beams at the intersection point (d_{meas}) is nominally 200 μm. Note that due to the coherency length of the lasers, the path length of each beam in a pair from the laser to the measurement volume must be equal to within 2.5 cm in order to form fringes. The teal beam exits its fiber optic cable and is focused into a laser sheet approximately 20 μm wide by a plano-convex lens. The laser sheet nominally intersects the measurement volume perpendicular to the streamwise direction in tunnel coordinates.

The receiving assembly was originally mounted perpendicular to the tunnel floor equidistant between the two heads. Due to the decreased interior angle between the two heads, however, it was necessary to mount the receiving assembly upstream of the heads at an angle of 29 degrees from vertical. The receiving lens assembly contains two 50.8 mm diameter achromat lens that are mounted in series with a fiber optic cable. The scattered light is

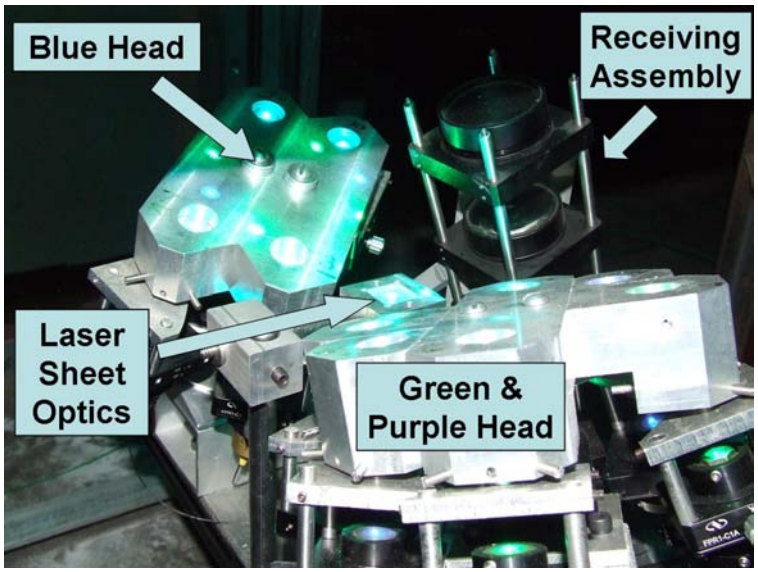

Figure B.6: CompLDV probe

collected and collimated by the first lens, which is focused on the measurement volume. The second lens focuses the columnated light into a multimode fiber with a 100 μm diameter core (d_{fiber}) and numerical aperture (NA) of 0.27. The focal length of the first lens (f_O) is 200 mm and the focal length of the second lens (f_I) is 100 mm. The focal lengths and diameter of the lenses (d_{lens}) satisfy the following equations for the numerical aperture and magnification factor (m) to achieve optimal light collection.

$$m = \frac{d_{fiber}}{d_{meas}} = \frac{f_I}{f_O} \tag{B.2.1}$$

$$NA = \frac{d_{lens}/2}{\sqrt{f_I^2 + (d_{lens}/2)^2}} \tag{B.2.2}$$

B.2.3 The Receiving Table

The collected scattered light is carried via fiber optic cable to the receiving table, where the light is again separated into the individual colors using chromatic separation optics. Interference narrow bandpass filters are used to prevent unwanted contamination of the light signal by extraneous wavelengths. After passing through the interference filters, each band of light passes into a photomultiplier tube (PMT), where the light is converted into an electrical current. The PMTs are powered by Brandenburg model 477 power supplies. Four Sonoma Instrument model 315 amplifiers are used to convert and amplify each current signal from the PMTs to a voltage. The signal from the PMTs is extremely weak and so electronic noise interference is a serious issue. Special care is taken to shield the cables that transport the signals to the amplifiers.

Only two digitizer channels are available, so the teal (496.5 nm), blue (488 nm), and purple (476.5 nm) band signals are analog combined. Before they are combined, the teal and purple bands are analog lowpass filtered with cut-off frequencies of 5 MHz and 50 MHz respectively. The blue band is highpass filtered at a 50 MHz cut-off frequency. The green (514.5 nm) band occupies the remaining channel and is analog lowpass filtered with a cut-off frequency of 100 MHz. The filtering scheme employed here removes any aliasing that might otherwise occur.

B.2.4 A/D Conversion

Data acquisition is managed with a standard PC. An 8 bit Strategic Test board (model UF.258) samples each channel at 250 megasamples/second (MS/s). There are two modes of data acquisition: continuous sampling and triggered sampling. At this sample rate, continuous sampling can be maintained for 0.54 seconds before the on-board RAM must write to disk storage. Continuous sampling achieves the highest burst data rate (shortest time between recorded bursts), because the card waits to write data to storage until its onboard memory is full. However, continuous sampling usually results in a lower average signal-to-noise ratio and a vastly greater amount of storage per burst is required. Triggered sampling means that only bursts signals that reach a specified voltage level are written to file. A National Instruments 5112 board (NI) is used to record the time of each burst. This is achieved by sending the 'trigger out' signal from the Strategic Test board directly into the 'trigger in' channel of the NI board.

B.2.5 Alignment Procedures

Proper alignment is crucial for any LDV system to achieve strong signals. Alignment procedures are similar but ultimately differ between systems. These procedures are always evolving as technology improves and most researchers have their own preferred methods. This section provides detailed explanation of the author's preferred method for aligning the CompLDV.

Each fiber is removed from its chuck and its beam is shined onto a flat smooth surface (i.e. the floor or a wall) at a distance of several feet. At this distance the beam diameter on the surface is about six to ten inches. The beam shape should look circular with a Gaussian intensity. There should be no dark spots or streaks in or around the beam. If these are present the fiber is lightly polished (with no beam shining). When the beam has the proper shape, the fiber is inserted back into its chuck. While in the chuck, the beam is again shined onto a flat surface at a distance of several feet to ensure that the chuck did not cause any change in beam shape or intensity. If changes are observed then the fiber was scratched during insertion into the chuck or the chuck is not holding the fiber properly.

Once it is determined that the beam shape is satisfactory, each chuck with fiber is inserted into its three-stage traverse with lens assembly attached. Each traverse is centered such that the beam passes through the center of its lens assembly. This is done by shining the beam onto a flat surface several feet away and adjusting the traverse until the beam center (brightest point) is centered in the image. If the image has dark spots or streaks the lens may be dirty and needs to be cleaned. If the image looks skewed or the beam center cannot be centered in the image the lens may not be sitting flat in the assembly and needs to be adjusted.

A beam from the optical table is launched into the receiving fiber which shines through the receiving optics into the wind tunnel. A piece of white polishing paper is placed on the floor of the tunnel (shiny side down) and the traverse is used to move the system vertically until the diameter of the beam on the paper is minimized. This is the waist of the receiving optics, and it is now intersecting with the tunnel floor. Next, each traverse component with lens assembly is inserted into the probe head. One by one the beams are launched and each lens assembly is adjusted until each beam intersects the waist of the receiving optics. Each assembly is securely fastened to the probe head by tightening the three all-thread screws for each. This step is an iterative process and requires some patience, it is important for all the beams to intersect as possible with the receiving optics' waist, because the finer adjustments of the traverse component does not have a large range.

Ensuring the polarization of each beam is properly aligned is important for creating strong fringe patterns in the measurement volume. The polishing paper is removed and each beam is allowed to shine onto a flat surface parallel with the tunnel floor. The flat surface should be several feet above the tunnel floor. A polarization indicator is used to detect the polarization direction which is nominally spanwise to the tunnel floor (dark streak is spanwise). The direction can be adjusted by simply rotating the chuck that holds the fiber optic cable. It is also important that the polarization looks sharp on the flat surface, not blurry. The polarization stability is tested by gently tugging on the fiber optic cable while viewing the polarization direction. The polarization direction will rotate slightly, but it should return to the correct position. If it does not, extra care is taken to secure the fiber optic cable to the probe traverse to minimize the amount of movement that can take place during data acquisition.

From this point onward alignment is too sensitive to be done by eye, so the beams must be magnified correctly to ensure accurate alignment. Magnification is done using an objective lens assembly mounted to a vertical traverse that can be placed on the wind tunnel floor. This effectively is a microscope, and it is used to magnify the image of the beams as they appear on the white polishing paper. The microscope's vertical traverse is used to bring the image into focus. This is a very important step and must be done every time the microscope is moved. A mirror can be used to reflect the image of the beams that the microscope projects onto a flat surface for viewing. This flat surface should be easily accessible because

the beam images will have to be examined closely. All further steps use the microscope to image the beams.

With a beam still launched back through the receiving optics a piece of white paper is again secured to the tunnel floor and the microscope device is put in place. The traverse system moves the probe vertically until the diameter of the beam on the paper is minimized. This is the waist of the receiving optics, and it is now intersecting with the tunnel floor and the encoder reading is set to zero. To have converging and diverging fringes the beams (except the laser sheet) must cross at off-waist positions. Beam pairs that make converging fringes are focused about 6mm beyond the measurement volume and vice versa for diverging fringes. When the probe is moved to the correct vertical position for a beam, the focus of each beam is adjusted until the diameter of its image is minimized. The beam is now focused. This process is repeated for each beam.

When all ten beams have the correct polarization direction and are all focused in the correct planes, they are ready to be crossed with the receiving volume. This is an extremely important step for obtaining strong signals and takes a certain level of experience. A beam is again launched into the receiving fiber and the zero-plane is again found as explained above. While imaging the beams with the microscope each beam is aligned with the beam launched through the receiving fiber. This is done one beam at a time. Not only do the beams need to cross with the receiving optics, but each beam must cross with its partner as well and both conditions are checked. Also some slight focusing adjustments usually need to be made to ensure that all the beams have the same diameter. Some of the beams look oval in shape. This is because the microscope is projecting the image of the beams on the white polishing paper and some of the beams intersect the paper at a shallow angle making their image look skewed. The target crossing point for these beams is the center of the oval.

The laser sheet is the last beam to be aligned. It is attached via C-clamps to the plate the CompLDV is mounted on. By adjusting the laser sheet optics vertically, it is focused in the plane of the measurement volume. The thickness of the laser sheet should be approximately a fifth the size of the diameter of the measurement volume. It is aligned in the center of the volume perpendicular to the streamwise direction.

B.2.6 LDV Signal Processing

Signal processing for laser Doppler velocimetry involves several steps and can be computationally expensive in terms of both time and storage space. The quality of the final LDV data is relatively sensitive to the processing techniques used. Much work has been done here and by other researchers to determine the best methods, although further improvements are certainly possible. This section includes details about data acquisition, frequency and chirp extraction, numerical solution methods for the LDV equations, and post processing techniques.

Data Acquisition

LabView is used to interface with the Strategic Test DAQ card and properly write both channels of raw data to file. LabView is also used to control the traverse which can be automated to move the LDV measurement volume to specified locations for data collection. Automation of data acquisition is desirable because several hours are normally required to measure just one boundary layer profile. A boundary layer profile is usually made up of approximately twenty points. Each point is made up of files, usually between fifteen and fifty for each channel of data. Each file contains a certain number of burst signals.

Most boundary layer profiles require vast storage space, on the order of tens of Gigabytes each. Therefore, the most common method of acquiring data is to only store data that contain a burst signal and discard the rest. This is accomplished by instructing the DAQ card to write data from its onboard memory to storage only when a trigger event occurs, usually when the amplitude on one channel reaches some minimum value or trigger level. The trigger level and number of samples to store is specified in advance. The trigger level is usually specified to be approximately three quarters of the average burst amplitude. The number of samples is chosen to be approximately twice the average burst width. An equal number of sample before and after the trigger event are written to storage. Thus, the burst signal is nominally centered in the data written to file. The time when the trigger event occured is written to storage as well.

Because the DAQ card must pause to write data from its onboard memory to storage for every burst, the data rate can be adversely affected. When the highest possible data rate is desired, such as for spectra measurements, this problem is alleviated by not triggering on each burst. Instead, after the first burst causes a trigger event the card is instructed to sample continuously until its onboard memory is full (0.54 seconds at $250\text{x}10^6$ samples per second per channel) before writing to file. After the card's onboard memory is filled, it writes a file to storage. The time of the initial trigger event is written to storage as well.

Raw Processing

Because of the large volume of data that must be processed for each boundary layer profile, a quick and robust burst recognition algorithm developed by Dr. Lowe [71] is used to identify good bursts for further processing. The burst recognition algorithm is implemented using C++. It is run on only one channel, because bursts on both channels should be coincident. The raw data is broken into bins of specified width and the samples that make up each bin are averaged together to give the bin value. This effectively acts as a computationally inexpensive low pass filter. The optimal bin width is determined by a seperate algorithm also developed by Dr. Lowe. A Gaussian fit is performed on each successive grouping of five bins. If the fit meets certain criteria the five points are accepted as a burst. The center sample number of the burst and width of the burst are written to a trigger file.

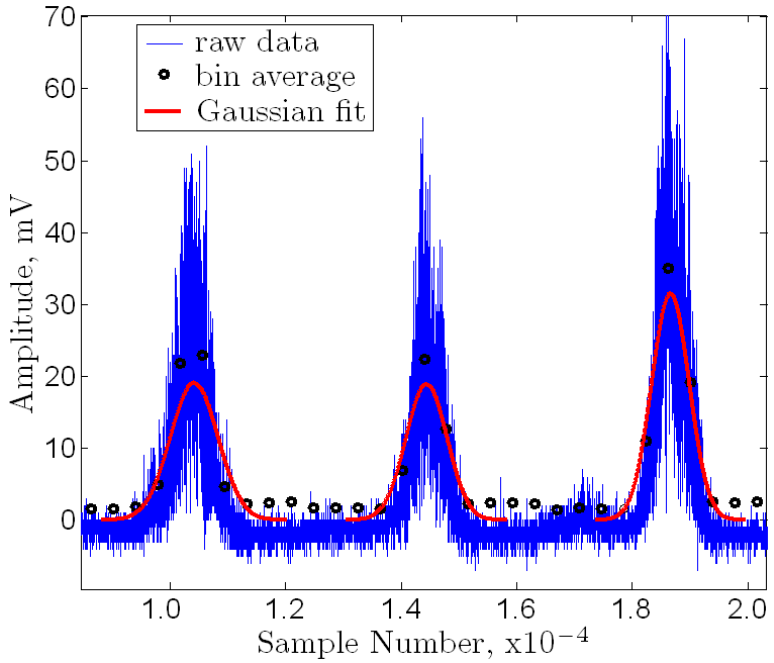

Figure B.7: Burst recognition algorithm using a five point Gaussian fit

With the location of the good bursts now identified in the trigger file, only raw data that contain Doppler information will be processed further. The shifted Doppler frequencies are extracted from the burst signals using a fast Fourier transform (FFT). The burst is centered in a processing window that is roughly twice the burst period wide. The signal is not zero-padded however, as this offers little improvement for typical signal-to-noise ratios seen in the data per Shinpaugh *et al.* [73]. Shinpaugh *et al.* also show that a three-point Gaussian interpolation is best suited to determine the location of the Doppler signal peak between spectral lines. Before writing the measured frequencies to file, the associated bragg frequency is subtracted from each. The signal-to-noise ratio (SNR_1) for each signal is written to file as well and is defined here as shown below.

$$\mathrm{SNR}_1 \equiv 10 log_{10}\left[\frac{\text{spectral peak value}}{(\text{spectral noise density}) \times (\text{signal bandwidth})}\right] \tag{B.2.3}$$

If the CompLDV is being used to measure accelerations then the time rate of change of frequency, or chirp, also needs to be extracted. This is done following the work of Dr. Lowe [71], which utilizes the discreet chirp Fourier transform (DCFT) to compute the spectral density (SD) in frequency-chirp space.

$$SD(l,m) = \sum_{k=0}^{N-1} s_k exp\left\{-i\left[\pi m\left(\frac{k-N/2}{N}\right)^2 + 2\pi l\left(\frac{k-N/2}{N}\right)\right]\right\} \tag{B.2.4}$$

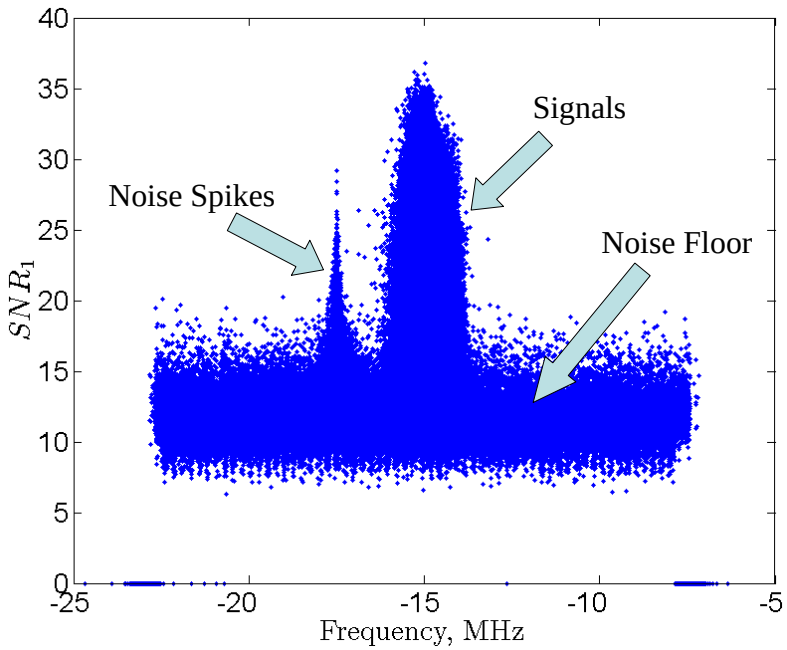

Figure B.8: SNR_1 vs. Frequency for use in clipping

The frequency and chirp spectral line numbers are denoted by l and m respectively. The total number of samples in the discreet signal s_k is denoted by N, where k denotes the sample index. Equation B.2.4 is computed along a range of chirp spectral lines (m index) for three frequency spectral lines (l index) adjacent to the frequency computed previously using the FFT, which was essentially an estimate of the frequency when the chirp is zero. Then spectral indices of the maximum spectral density is then found in the frequency-chirp space. To assertain more precisely the frequency and chirp, two interpolations are performed around this point. A Gaussian interpolation is used between the frequency spectral lines and a parabolic interpolation is used between chirp spectral lines. The chirps, frequencies, and SNR_1 values for each signal in a burst are written to file.

To minimize the number of poor Doppler signals retained for futher processing, the frequencies extracted from each burst measured at a point in the boundary layer profile are plotted against SNR_1 (figure B.8). This allows the user to identify the noise floor and the frequency bands of interest for each point in the profile. Any burst containing a signal that does not exceed the user specified minimum SNR_1 value or does not fall within the user specified frequency band for that signal is removed. This step is important in mitigating any strong non-white spurious noise signals (usually occuring at radio or bragg frequecies) allowed because of faulty shielding. This process is also performed to remove poor chirp signals when applicable.

In order for the CompLDV to measure particle positions or accelerations it is neccesary to know the burst envelope function ($\omega(t)$) for each of the five signals in equation B.1.3 as well as the peak time of the laser sheet burst (t_r). These signals were combined during data acquisition because only two channels were available on the DAQ card. They are separated here using digital filtering. For each of the five Doppler signals, bandpass filters with finite impulse response are created in MatLab. The passband is centered about the mean frequency of all the bursts measured at a point. The mean square of each channel is passed through the filters, the results are reversed in time, and then passed through the filters again to eliminate any phase distortions [122]. Five filtered signals result and each is divided into eleven bins and a Gaussian is fit to the middle five bins. The coefficients A, B, and C in equation B.2.5 are the result and are used to compute the peak time of the burst ($t_p = -B/2A$). The burst window is then normalized by the value at this time and can be written as a function of A and t_p. Poor quality bursts are ignored by ensuring that $A < 0$ and t_p is less then some predetermined fraction of the burst period (usually 20%).

$$\omega(t) = \frac{\exp(At^2 + Bt + C)}{\exp(At_p^2 + Bt_p + C)} = \exp\left[A(t - t_p)^2\right] \tag{B.2.5}$$

To find the time of the laser sheet a lowpass filter with finite impulse response is also created in MatLab and the signal is filtered as above to eliminiate phase distortions. The time at which the maximum value of the filtered signal occurs is defined to be t_r. Signal simulations were performed to quantify the uncertainty associated with the filtering process and are explained in detail in a section B.3.

Solvers

As explained in section B.1 and B.1, the CompLDV utilizes five intersection volumes and a laser sheet to measure three components of velocity and position by solving equations B.2.6 and B.2.7, where the subscript i represents the intersection volume.

$$\vec{U} \cdot \hat{e}_i = f_i S_{avg,i} \ , \quad i = 1, 2, \ldots, 5 \tag{B.2.6}$$

$$S_{avg,i} = \frac{\int_{t_a}^{t_b} S_i(\vec{x}(t))\omega_i(t)dt}{\int_{t_a}^{t_b} \omega_i(t)dt} \ , \quad i = 1, 2, \ldots, 5 \tag{B.2.7}$$

$$\vec{x}(t) = \begin{Bmatrix} U \\ V \\ W \end{Bmatrix} (t - t_s) + \begin{Bmatrix} x_s \\ y_r \\ z_r \end{Bmatrix} \tag{B.2.8}$$

These equations represent a set of nonlinear equations that are solved iteratively for the seed particle's trajectory, $\vec{x}(t)$, using Newton's method. The known quantites in the above equations are t_s, $\hat{e}_i$, $S_i(\vec{x})$, $\omega_i(t)$, f_i, and x_s. This leaves five remaining unknown quantites that are expressed as a state vector $\{X\}$.

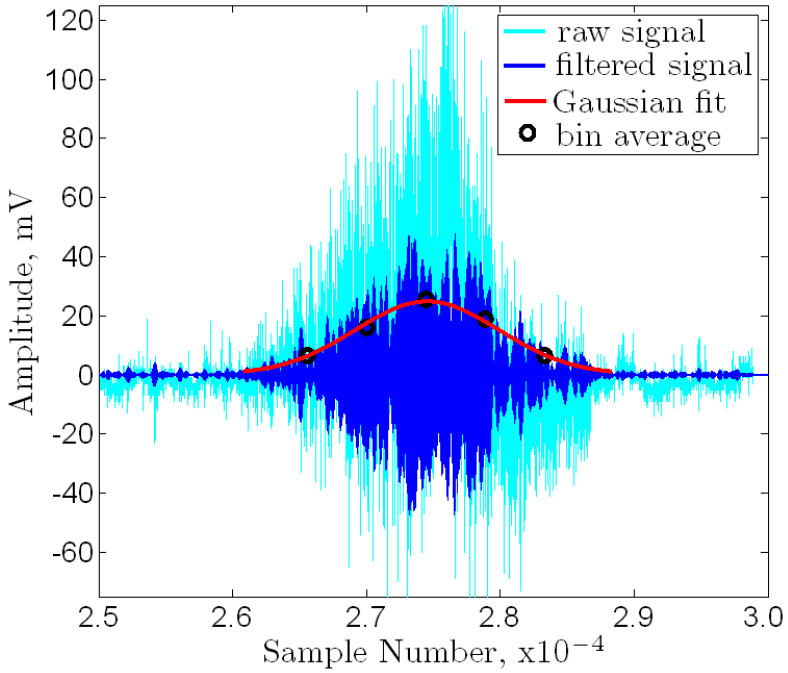

Figure B.9: Digitally filtered Doppler signal with Gaussian fit

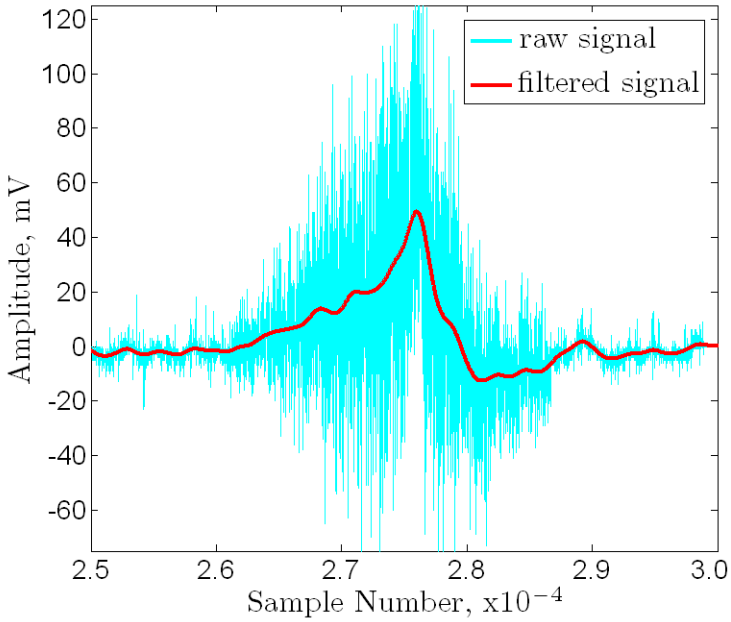

Figure B.10: Digitally filtered laser sheet signal

$$\{X\} = \left\{ \begin{array}{c} U \\ V \\ W \\ y_r \\ z_r \end{array} \right\} \tag{B.2.9}$$

Figure B.11 shows the steps for how Newton's method is applied to this problem. The first step is choose an initial guess for the unknown variables. This is done using the solution to the linearized LDV equations as discussed in section B.1. It is important to recall the assumptions that are made to linearize equation B.2.6. Furthermore, as the the CompLDV only utilizes five intersection volumes, an additional assumption that $x_{avg} = x_s$ must be made as well. Still, the solution to equation B.2.10 is a strong initial guess for Newton's method.

$$\left[\begin{array}{ccccc} e_{x,1} & e_{y,1} & e_{z,1} & f_1 \frac{\partial S_1}{\partial y}\Big|_{\vec{x}=0} & f_1 \frac{\partial S_1}{\partial z}\Big|_{\vec{x}=0} \\ e_{x,2} & e_{y,2} & e_{z,2} & f_2 \frac{\partial S_2}{\partial y}\Big|_{\vec{x}=0} & f_2 \frac{\partial S_2}{\partial z}\Big|_{\vec{x}=0} \\ e_{x,3} & e_{y,3} & e_{z,3} & f_3 \frac{\partial S_3}{\partial y}\Big|_{\vec{x}=0} & f_3 \frac{\partial S_3}{\partial z}\Big|_{\vec{x}=0} \\ e_{x,4} & e_{y,4} & e_{z,4} & f_4 \frac{\partial S_4}{\partial y}\Big|_{\vec{x}=0} & f_4 \frac{\partial S_4}{\partial z}\Big|_{\vec{x}=0} \\ e_{x,5} & e_{y,5} & e_{z,5} & f_5 \frac{\partial S_5}{\partial y}\Big|_{\vec{x}=0} & f_5 \frac{\partial S_5}{\partial z}\Big|_{\vec{x}=0} \end{array} \right] \left\{ \begin{array}{c} U \\ V \\ W \\ y_r \\ z_r \end{array} \right\} = \left\{ \begin{array}{c} f_1 S_1(0) \\ f_2 S_2(0) \\ f_3 S_3(0) \\ f_4 S_4(0) \\ f_5 S_5(0) \end{array} \right\} \tag{B.2.10}$$

Steps two and three are to compute the trajectory, $\vec{x}(t)$ and $S_{avg,i}$. If the seed particle's acceleration is also desired, then $(DS/Dt)_{avg_i}$ must be computed in the optional step four using equation B.1.15. Step five is to compute, $\{G\}$, which is simply B.2.6 rewritten.

$$G = \left\{ \begin{array}{c} G_1 \\ G_2 \\ G_3 \\ G_4 \\ G_5 \end{array} \right\} = \left\{ \begin{array}{c} \vec{U} \cdot \hat{e}_1 - f_1 S_{avg,1} \\ \vec{U} \cdot \hat{e}_2 - f_2 S_{avg,2} \\ \vec{U} \cdot \hat{e}_3 - f_3 S_{avg,3} \\ \vec{U} \cdot \hat{e}_4 - f_4 S_{avg,4} \\ \vec{U} \cdot \hat{e}_5 - f_5 S_{avg,5} \end{array} \right\} \tag{B.2.11}$$

Step six is to compute the Jacobian matrix of $\{G\}$, $[J_G]$. This is done numerically and equation B.2.12 is an example for one element of $[J_G]$. It should be noted that this step involves computing the elements of $\{G\}$, and therefore S_{avg}, an additional twenty five times in total.

$$\frac{\partial G_1}{\partial U} = \frac{G_1(U + \Delta U) - G_1(U)}{\Delta U} \tag{B.2.12}$$

Step seven is to apply Newton's nonlinear method and solve for the required change to the state vector, $\{\Delta X\}$. Step eight is to update the state variables ($\{X\}_{n+1} = \{X\}_n + \{\Delta X\}$).

$$\{\Delta X\} = -\left[J_G\right]^{-1}\{G\} \tag{B.2.13}$$

Step nine is an optional step that is performed if the particle acceleration is desired. Equation B.1.14 represents a coupled set of linear equations (one of each intersection volume) for the acceleration components. Since there are five intersection volumes, the system is over contrained. Only three are needed and usually one intersection volume of each color (green, blue, and purple) is used.

$$\begin{bmatrix} e_{x,1} & e_{y,1} & e_{z,1} \\ e_{x,2} & e_{y,2} & e_{z,2} \\ e_{x,3} & e_{y,3} & e_{z,3} \end{bmatrix} \begin{Bmatrix} a_x \\ a_y \\ a_z \end{Bmatrix} = \begin{Bmatrix} \frac{Df_1}{Dt} S_{avg,1} + f_1 \frac{DS}{Dt}_{avg,1} \\ \frac{Df_2}{Dt} S_{avg,2} + f_2 \frac{DS}{Dt}_{avg,2} \\ \frac{Df_3}{Dt} S_{avg,3} + f_3 \frac{DS}{Dt}_{avg,3} \end{Bmatrix} \tag{B.2.14}$$

Step ten is to check the convergence of the nonlinear solver. The error is defined as the norm of $\{\Delta X\}$. If the error is sufficiently small (usually $< 1 \times 10^{-10}$) the algorithm ends. If not, the trajectory $\vec{x}(t)$ is computed with the updated state variables and the procedure repeats from step two. If the acceleration is also being computed the trajectory must also include the additional acceleration term.

$$\vec{x}(t) = \begin{Bmatrix} a_x \\ a_y \\ a_z \end{Bmatrix} (t^2 - t_s^2) + \begin{Bmatrix} U \\ V \\ W \end{Bmatrix} (t - t_s) + \begin{Bmatrix} x_s \\ y_r \\ z_r \end{Bmatrix} \tag{B.2.15}$$

Post Processing

Once velocities, positions, and accelerations have been computed for each point in a profile, another round of clipping is performed graphically to mitigate supurious data points. Position clipping is performed on data taken with the CompLDV by plotting y_r vs. z_r and eliminating outliers. Histograms of each velocity component reveal outliers and where the effect of noise begins to corrupt the data (i.e. where the histograms begin to level off). Similarily, if applicable, histograms of the components of acceleration are also clipped. Figures B.12, B.13, and B.14 show examples of position, velocity, and acceleration clipping respectively.

B.3 Signal Simulations

B.3.1 Modeling the Burst Signal

In order to assess the errors associated with digitally filtering the burst signals and estimating the peak time (t_p) and window coefficient (A), signal simulations were performed in

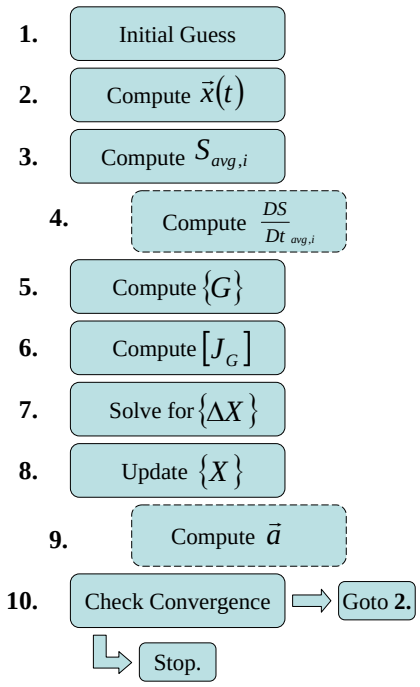

Figure B.11: Process chart of Newton nonlinear solver. Steps 4 and 9 are optional steps that are used to compute the acceleration.

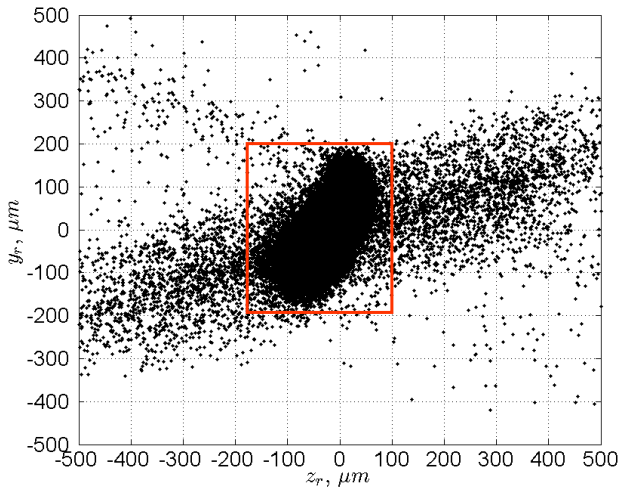

Figure B.12: Example of position clipping. The dark cluster of points contain most of the data and indicates the location and size of the measurement volume. Outliers are clearly visable. All data outside the box is discarded.

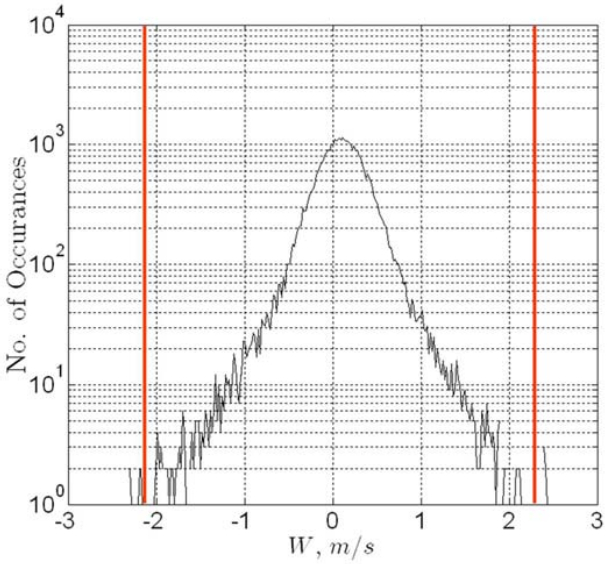

Figure B.13: Example of velocity histogram for clipping. The noise floor is evident where the histogram begins to level off. Data between the vertical lines is accepted the rest is discarded.

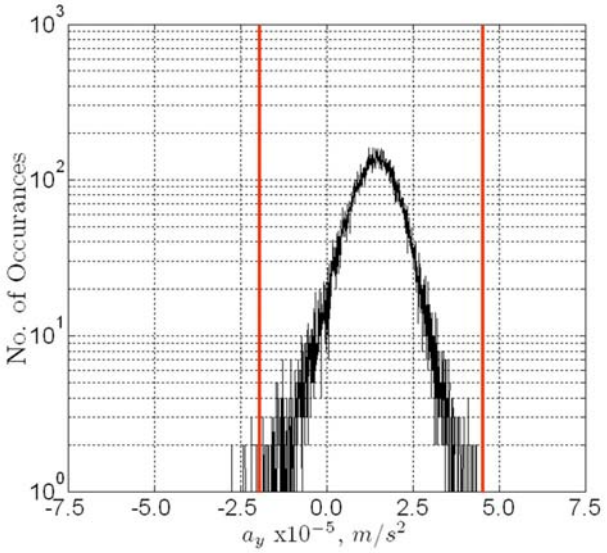

Figure B.14: Example of acceleration histogram for clipping. The noise floor is evident where the histogram begins to level off. Data between the vertical lines is accepted the rest is discarded.

MatLab. A burst signal was modeled as a Gaussian windowed cosine function with noise added (equation B.3.1).

$$s(\hat{t}) = C_1 \exp\left[A(\hat{t} - \hat{t}_p)^2\right] \cos(2\pi \hat{f}\hat{Q}/2\hat{t}) + n(\hat{t}) \tag{B.3.1}$$

$$n(\hat{t}) = \left[C_n \sqrt{\left|s(\hat{t})\right|} + C_o\right] \text{randn}(\hat{t}) \tag{B.3.2}$$

The burst signal is modeled in non-dimensional time $\hat{t} = t/T = -1 + 2(i-1)/(N-1)$, where T is half the burst period, N is the number of samples, and i is the sample index. The non-dimensional peak time is denoted by $\hat{t}_p$. The non-dimensional frequency ($\hat{f}\hat{Q}/2$) is measured as a fraction of half the non-dimensional sample rate ($\hat{Q}$), where $\hat{Q} = Q2T = N$ and $\hat{f}$ is a number between zero and one. A photomultiplier tube will contaminate a signal with shot noise. The noise, $n(\hat{(t)})$, is broadband, proportional to the square root of the photocathode current, and is described by Poisson statistics [67, 123]. Since the mean photon count for a PMT is large, the Poisson distribution can be approximated by a normal distribution. The function randn $\hat{t}$ randomly generates a number that follows a normal distribution with a mean of zero and a standard deviation of one. The time dependent noise level is denoted by C_n. A time independent noise level is also included in the model signal and is denoted by C_o. Figure B.15 shows a real and simulated burst signal.

For a given burst signal, the peak time and window coefficient are computed following the procedure described in section B.2.6. The error in the computed peak time ($\epsilon_{\hat{t}}$) and window coefficient (ϵ_A) are defined in equations B.3.3 and B.3.4 respectively.

$$\epsilon_{\hat{t}} \equiv (\hat{t}_{p,computed} - \hat{t}_{p,real}) \times 100\% \tag{B.3.3}$$

$$\epsilon_A \equiv \frac{A_{computed} - A_{real}}{A_{real}} \times 100\% \tag{B.3.4}$$

For a given number of simulations (M), the bias error ($\bar{\epsilon}$) is simply the mean error. The standard deviation of the error is denoted by $\sqrt{\overline{(\epsilon - \bar{\epsilon})^2}}$ and defined in equation B.3.5

$$\sqrt{\overline{(\epsilon - \bar{\epsilon})^2}} \equiv \sqrt{\frac{1}{M-1}\sum_{j=1}^{M}(\epsilon_j - \bar{\epsilon})^2} \tag{B.3.5}$$

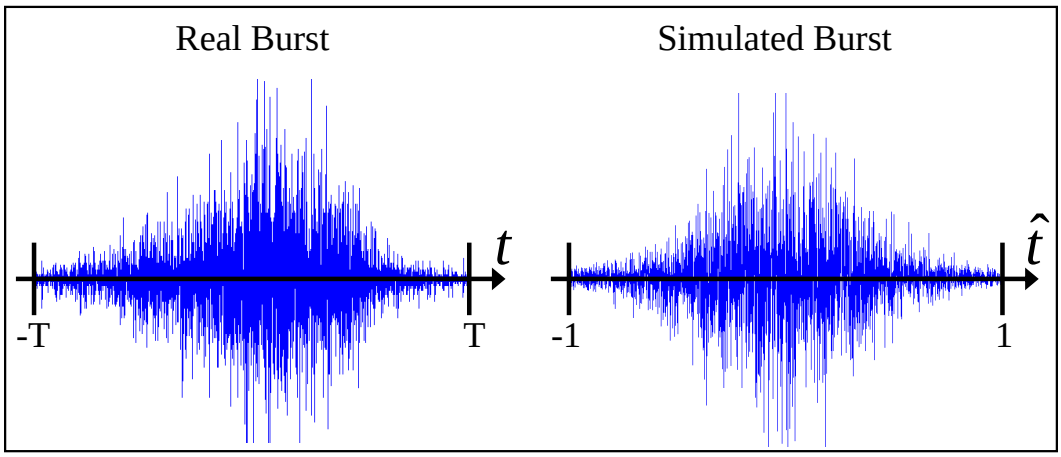

Figure B.15: Comparison of real and simulated burst signals

Parameters	Baseline	Perturbations from Baseline
Number of Samples (N)	4096	1024, 2048, 8192, 16384, 32768
Time Dependent Noise Level (C_n)	3.0	5.0, 4.0, 2.0, 1.0
Constant Noise Level (C_o)	0.15	0.00, 0.30, 0.45
Signal 1		
Fraction of half sample rate ($\hat{f}$)	0.55	0.15, 0.35, 0.75
Signal Window Coefficient (A)	-15	-5, -25, -35
Peak Time ($\hat{t}_p$)	0.10	-0.10, 0.05, 0.2
Peak Amplitude (C_1)	1.0	-
Filter Order	200	100, 300
Filter Bandwidth (fraction of half sample rate)	0.10	0.05, 0.15
Percentage of Burst for Gaussian Fit	45	71, 56, 38, 33

Figure B.16: Table of signal simulation parameters with constant peak time

B.3.2 Simulation Results

Extensive, but not exhaustive, simulations were performed to estimate the errors associated with the digital filtering and Gaussian fitting schemes described in section B.2.6. A baseline set of parameters, used to model the signal in equation B.3.1, were chosen to create in a typical burst signal. The parameters were perturbed one at a time from their baseline values, while all other parameters remained fixed. This was done to determine the affect of each parameter on the errors in question. The baseline values of the parameters and their perturbed values are listed in figure B.16.

Due to the random nature of the noise term, a large number of simulations needed to be run for each parameter set to ensure convergence of the error statistics. It was determined that

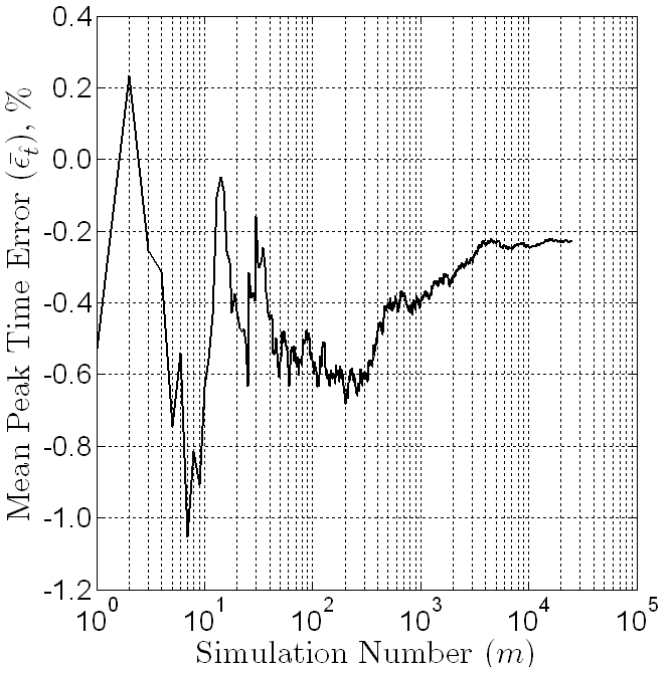

Figure B.17: Convergence history of signal simulations with baseline parameters

15,000 simulations was sufficient to achieve convergence, by plotting the mean error against the number of simulations over which the mean error was computed (figure B.17). The equation for the mean error as a function of simulation number (m) is given in equation B.3.6.

$$\bar{\epsilon}_{\hat{t},m} = \frac{\bar{\epsilon}_{\hat{t},m-1}(m-1) + \epsilon_{\hat{t},m}}{m} \tag{B.3.6}$$

The peak time and window coefficient errors showed little sensitivity to frequency (f) or filter order. Also noteworthy is the observation that as the bandwidth of the digital filter increases, the standard deviation of $\epsilon_{\hat{t}}$ decreases. However, $\bar{\epsilon}_{\hat{t}}$ grows with increasing bandwidth, and therefore, the bandwidth should be chosen to be the smallest interval that captures all realistic frequencies due to turbulent velocities at a given point in the flow. Most importantly, figure B.18 reveals that a bias in peak time error was present due to $\hat{t}_p$.

In order to remove any bias associated with the peak time of the model burst, $\hat{t}_p$ was allowed to vary randomly for each burst. In an effort to mimic real bursts, $\hat{t}_p$ followed a uniform distribution on the interval from -0.1 to 0.1. The baseline parameters and associated perturbations representing each simulation case is shown in figure B.19. The number of simulations run for each case was increased to 30,000 for these and all further cases.

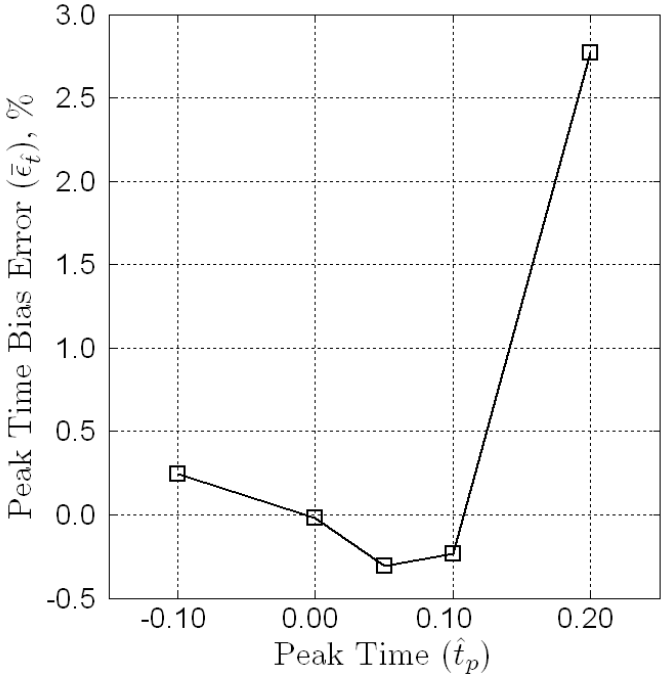

Figure B.18: Peak time bias vs. peak time

Parameters	Baseline	Perturbations from Baseline
Number of Samples (N)	4096	2048, 8192
Time Dependent Noise Level (C_n)	3.0	5.0, 4.0, 2.0, 1.0
Constant Noise Level (C_o)	0.15	0.00, 0.30, 0.45
Signal 1		
Fraction of half sample rate ($\hat{f}$)	0.55	-
Signal Window Coefficient (A)	-15	-
Peak Time ($\hat{t}_p$)	-0.1 to 0.1, uniform distribution	
Peak Amplitude (C_1)	1.0	-
Filter Order	200	-
Filter Bandwidth (fraction of half sample rate)	0.10	-
Percentage of Burst for Gaussian Fit	45	71, 56, 38, 33

Figure B.19: Table of signal simulation parameters with random peak time

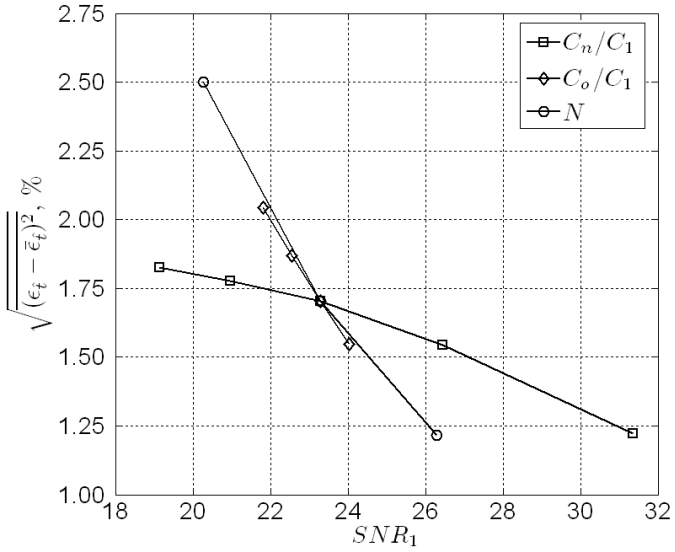

Figure B.20: $\sqrt{\overline{(\epsilon_{\hat{t}} - \bar{\epsilon}_{\hat{t}})^2}}$ vs. SNR_1. SNR_1 computed by varying parameters: C_n/C_1, C_o/C_1, and N about the baseline case.

Traditionally, an important parameter in signal processing is the signal-to-noise ratio, SNR_1, defined here in equation B.3.7. While represented in a different form, equation 2.1.7 is equivalent.

$$\text{SNR}_1 \equiv 10log_{10}\left[\frac{N\overline{s(\hat{t})^2}}{\overline{n(\hat{t})^2}}\right] \tag{B.3.7}$$

Three parameters affect SNR_1: C_n/C_1, C_o/C_1, and N. However, as is shown in figure B.20, $\sqrt{\overline{(\epsilon_{\hat{t}} - \bar{\epsilon}_{\hat{t}})^2}}$ is not a unique function of SNR_1.

Figure B.21 shows the standard deviation of the peak time error as a function of the percentage of the burst that is used for the Gaussian fit. The fitting procedure is explained in section B.2.6. The standard deviation of $\epsilon_{\hat{t}}$ levels off around 50% and is considered optimal.

While bias errors for the peak time are relatively low ($< 1\%$), the Gaussian window coefficient is subject to significant bias due to the noise, as seen in figure B.22. It may be possible to correct for this bias given some knowledge of SNR_1 and C_o for each burst. It is an interesting result that $\bar{\epsilon}_A$ is independent of N yet $\sqrt{\overline{(\epsilon_{\hat{A}} - \bar{\epsilon}_{\hat{A}})^2}}$ is greatly affected by it. However, $\sqrt{\overline{(\epsilon_{\hat{A}} - \bar{\epsilon}_{\hat{A}})^2}}$ is independent of C_o/C_1 yet $\bar{\epsilon}_A$ is greatly affected by it.

The CompLDV operates with two channels and there are multiple signals are on each channel. One channel carries two Doppler signals, the other carries three plus the DC signal

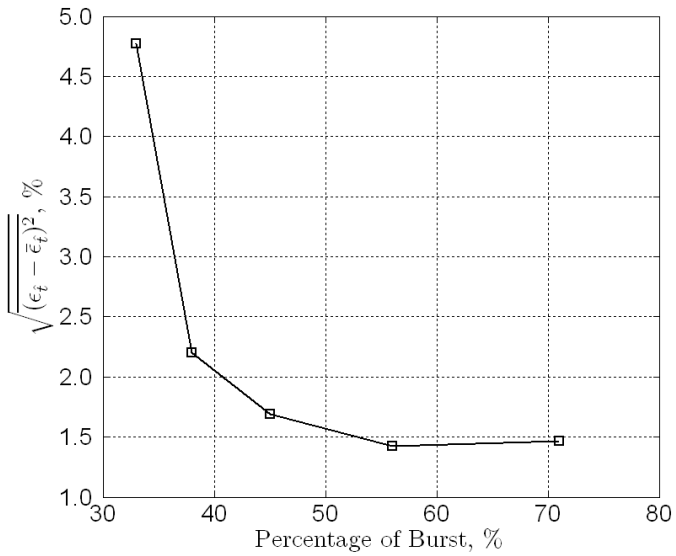

Figure B.21: $\sqrt{\overline{(\epsilon_{\hat{t}} - \bar{\epsilon}_{\hat{t}})^2}}$ vs. percentage of burst for Gaussian fit

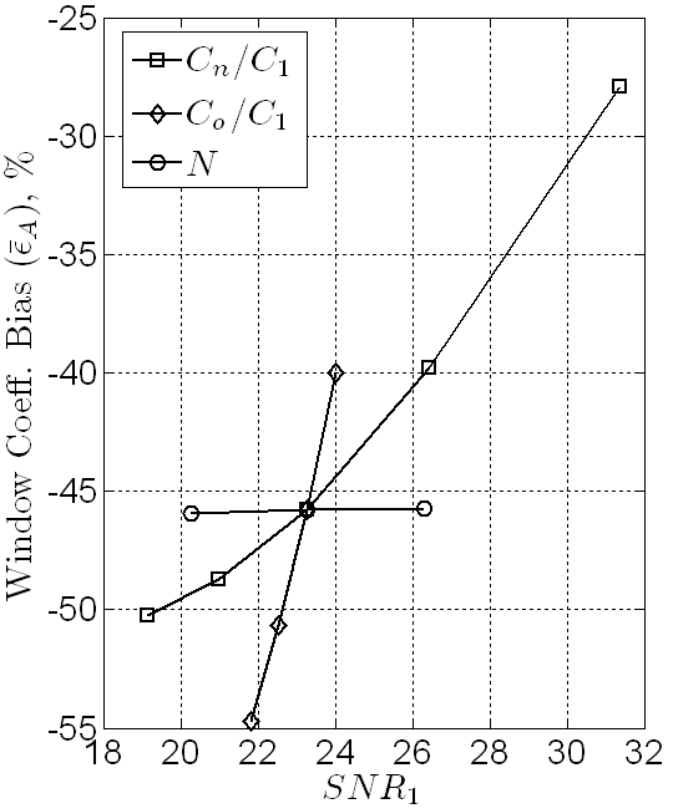

Figure B.22: $\bar{\epsilon}_A$ vs. SNR_1. SNR_1 computed by varying parameters: C_n/C_1, C_o/C_1, and N about the baseline case.

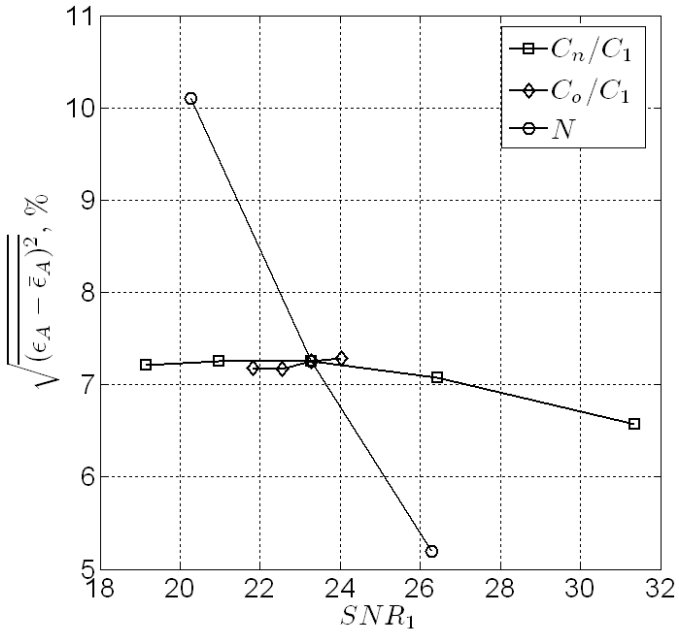

Figure B.23: $\sqrt{\overline{(\epsilon_{\hat{A}} - \bar{\epsilon}_{\hat{A}})^2}}$ vs. SNR_1. SNR_1 computed by varying parameters: C_n/C_1, C_o/C_1, and N about the baseline case.

from the laser sheet. To study how the presence of multiple signals effects $\epsilon_{\hat{t}}$ and $\epsilon_{\hat{A}}$, several simulation cases were carried out with multiple signals. To model a burst with multiple signals, several single burst signals (equation B.3.1) were superimposed before the noise was added. Tables of these cases are listed in figures B.24-B.26.

Simulations revealed that peak time and sheet time ($\hat{t}_s$) bias errors are negligible, but the standard deviations of these errors increase with the number of signals on a channel. The window coefficient bias increases with the number of signals as well. However, the standard deviation of ϵ_A seems to approach a maximum of 8%. These results are plotted in figures B.27, B.28, B.29, and B.30.

Parameters	Baseline	Perturbations from Baseline
Number of Samples (N)	4096	-
Time Dependent Noise Level (C_n)	3.0	5.0, 4.0, 2.0, 1.0
Constant Noise Level (C_o)	0.15	-
Signals 1 & 2		
Fraction of half sample rate ($\hat{f}_1, \hat{f}_2$)	0.55, 0.35	
Signal Window Coefficient (A_1, A_2)	-15	-
Peak Time ($\hat{t}_{p,1}, \hat{t}_{p,2}$)	-0.1 to 0.1, uniform distribution	
Peak Amplitude (C_1, C_2)	1.0	-
Filter Order	200	-
Filter Bandwidth (fraction of half sample rate)	0.10	-
Percentage of Burst for Gaussian Fit	45	-

Figure B.24: Table of simulation parameters for two superimposed signals

Parameters	Baseline	Perturbations from Baseline
Number of Samples (N)	4096	-
Time Dependent Noise Level (C_n)	3.0	5.0, 4.0, 2.0, 1.0
Constant Noise Level (C_o)	0.15	-
Signals 1, 2, & 3		
Fraction of half sample rate ($\hat{f}_1, \hat{f}_2, \hat{f}_3$)	0.55, 0.35, 0.75	
Signal Window Coefficient (A_1, A_2, A_3)	-15	-
Peak Time ($\hat{t}_{p,1}, \hat{t}_{p,2}, \hat{t}_{p,3}$)	-0.1 to 0.1, uniform distribution	
Peak Amplitude ($C1$, $C2$, $C3$)	1.0	-
Filter Order	200	-
Filter Bandwidth (fraction of half sample rate)	0.10	-
Percentage of Burst for Gaussian Fit	45	-

Figure B.25: Table of simulation parameters for three superimposed signals

Parameters	Baseline	Perturbations from Baseline
Number of Samples (N)	4096	-
Time Dependent Noise Level (C_n)	3.0	5.0, 4.0, 2.0, 1.0
Constant Noise Level (C_o)	0.15	-
Signals 1, 2, & 3		
Fraction of half sample rate ($\hat{f}_1, \hat{f}_2, \hat{f}_3$)	0.55, 0.35, 0.75	
Signal Window Coefficient (A_1, A_2, A_3)	-15	-
Peak Time ($\hat{t}_{p,1}, \hat{t}_{p,2}, \hat{t}_{p,3}$)	-0.1 to 0.1, uniform distribution	
Peak Amplitude ($C1$, $C2$, $C3$)	1.0	-
Filter Order	200	-
Filter Bandwidth (fraction of half sample rate)	0.10	-
Percentage of Burst for Gaussian Fit	45	-
Laser Sheet		
Fraction of half sample rate ($\hat{f}_s$)	0.00001	
Signal Window Coefficient (A_s)	-1000	-
Peak Time ($\hat{t}_{p,s}$)	-0.1 to 0.1, uniform distribution	
Peak Amplitude (C_s)	2.0	1.0, 3.0
Filter Order	200	-
Filter Bandwidth (fraction of half sample rate)	0.0001	-

Figure B.26: Table of simulation parameters for three superimposed signals and laser sheet

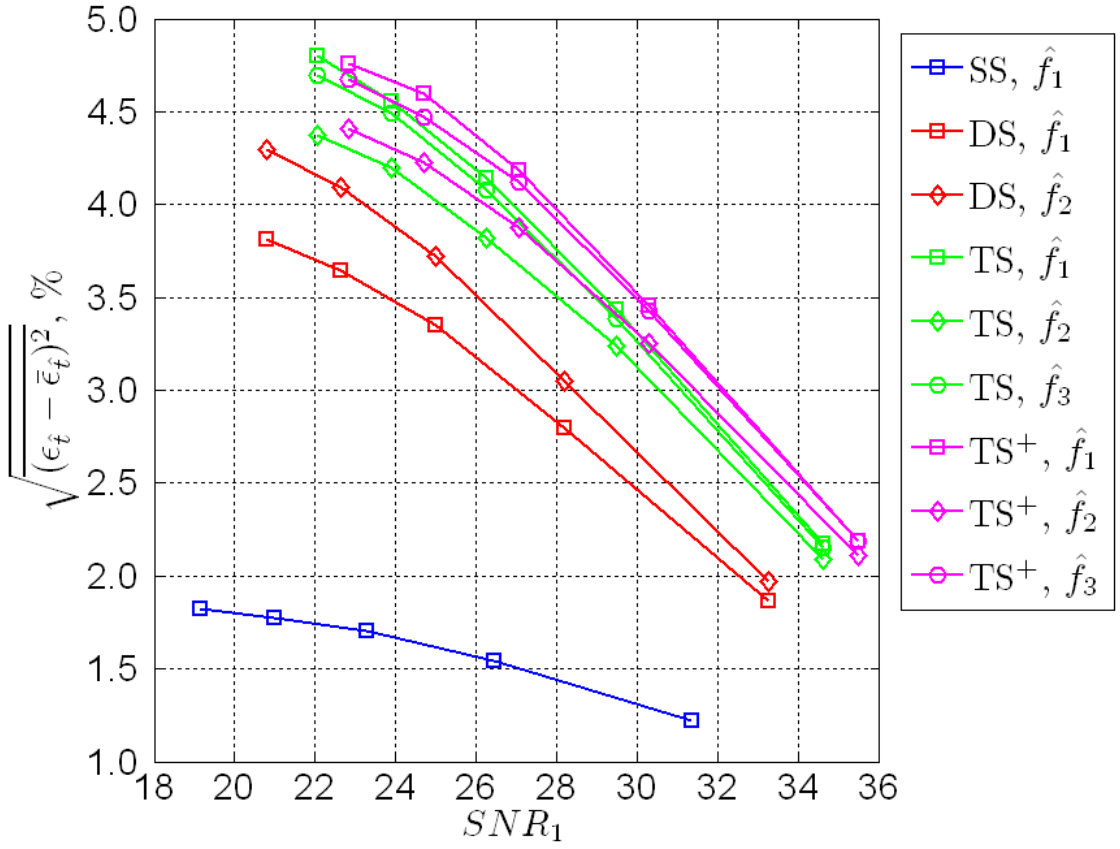

Figure B.27: $\sqrt{\overline{(\epsilon_{\hat{f}} - \bar{\epsilon}_{\hat{f}})^2}}$ vs. SNR_1 for multiple signals. SNR_1 computed by varying parameters C_n/C_1. SS-Single Signal, DS-Double Signal, TS-Triple Signal, TS$^+$-Triple Signal plus Laser Sheet

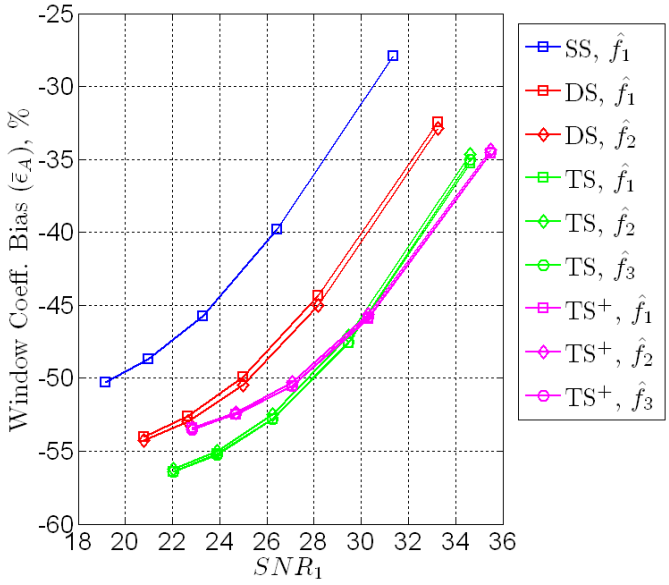

Figure B.28: $\bar{\epsilon}_A$ vs. SNR_1 for multiple signals. SNR_1 computed by varying parameters C_n/C_1. SS-Single Signal, DS-Double Signal, TS-Triple Signal, TS$^+$-Triple Signal plus Laser Sheet

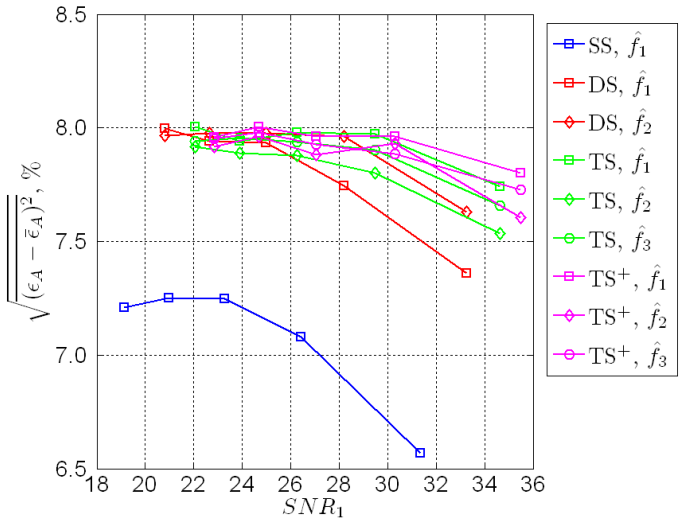

Figure B.29: $\sqrt{\overline{(\epsilon_A - \bar{\epsilon}_A)^2}}$ vs. SNR_1 for multiple signals. SNR_1 computed by varying parameters C_n/C_1. SS-Single Signal, DS-Double Signal, TS-Triple Signal, TS$^+$-Triple Signal plus Laser Sheet

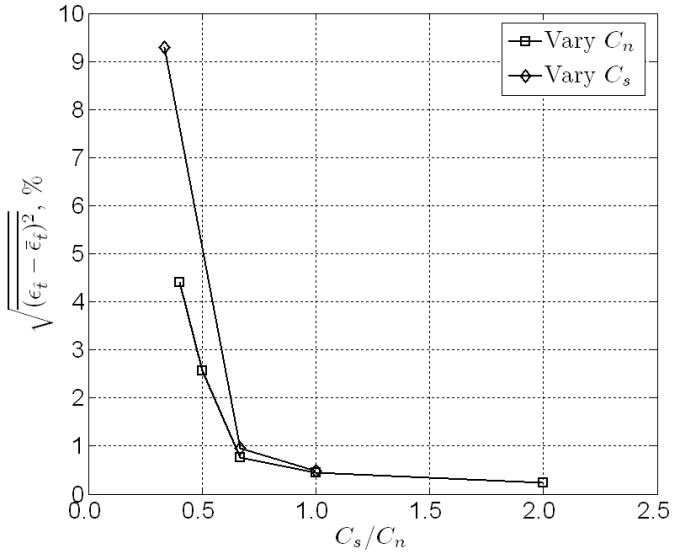

Figure B.30: Standard deviation of sheet time error $\left(\sqrt{\overline{(\epsilon_t - \bar{\epsilon}_t)^2}}\right)$ when three Doppler signals are present vs. ratio of laser sheet amplitude to time dependent noise level (C_s/C_n)

Appendix C

Measurement Volume Truncation

Figure C.1 shows a schematic of an LDV measurement volume being truncated by the wall. The vertical position of the measurement volume as recorded by the encoder is denoted by y_e, which is measured in reference to some datum value, y_d, from the true wall location. Therefore, y_s describes the distance from the true wall location to the geometric center of the measurement volume which is achieved by shifting the encoder values by the datum location $(y_e - y_d)$. The origin of the coordinate y' represents the geometric center of the measurement volume and moves with the measurement volume. When the measurement volume is truncated the true center of the measurement volume, as defined by the average location of a statistically sufficient number of seed particles that pass through the volume, is not longer the geometric center. The correct value, y, is computed using equation C.0.1 by considering the probability distribution of wall-normal crossing locations of a statistically sufficient number of seed particles $g(y')$.

$$y = \frac{1}{\int_{-y_s}^{a} g(y')dy'} \int_{-y_s}^{a} y' g(y')dy' + y_s \ , \quad 0 \leq y \leq a \tag{C.0.1}$$

If a uniform distribution is assumed for $g(y')$, the integrals in equation C.0.1 is simple and results in the following expression for y.

$$y = \frac{1}{2}(y_s + a) \ , \quad 0 \leq y \leq a \tag{C.0.2}$$

Suppose, however, a different distribution is chosen that results in an arbitrary slope α in equation C.0.2 such that equation C.0.3 is the result.

$$y = \alpha(y_s + a) \ , \quad 0 \leq y \leq a \tag{C.0.3}$$

By substituting equation C.0.3 into equation 3.4.3 and rearranging, it can be shown how a linear fit to the measured sublayer profile can be used to find both m and y_d.

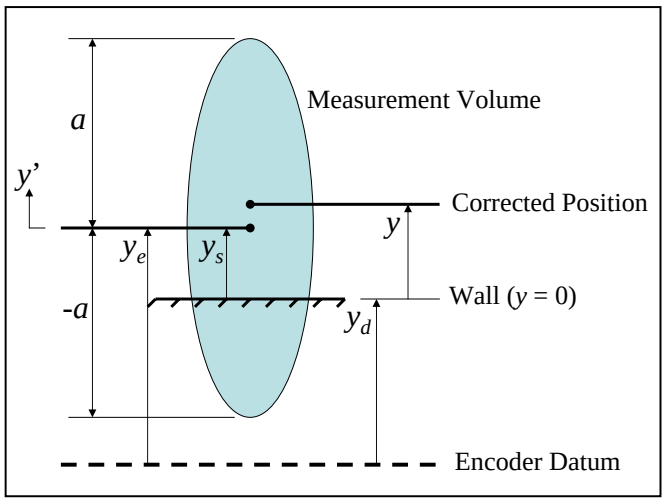

Figure C.1: Schematic of Measurement Volume Truncation

$$\begin{aligned} U &= My_e + B \\ M &= m\alpha \ , \quad B = M(y_d + a) \end{aligned} \tag{C.0.4}$$

Assuming a uniform distribution for $g(y')$ is a logical choice. The distribution of particles themselves is uniform, only the cross-section of the measurement volume will cause in a non-uniform distribution for $g(y')$. If the cross-section of the measurement volume is assumed to be elliptical [124], then

$$g(y') = \frac{2}{\pi a}\sqrt{1-(\frac{y'}{a})^2} \ , \quad -d \leq y \leq d \tag{C.0.5}$$

Given this distribution, equation C.0.1 becomes

$$\begin{aligned} y &= \frac{1}{C}\frac{2a}{3\pi}\left[1-(\frac{y_s}{a})^2\right]^{3/2} + y_s \\ C &= \frac{1}{2} + \frac{y_s}{\pi a}\sqrt{1-(\frac{y_s}{a})^2} - \frac{1}{\pi}\arctan\left[\frac{-y_s}{a\sqrt{1-(\frac{y_s}{a})^2}}\right] \end{aligned} \tag{C.0.6}$$

Figure C.2 shows the true wall-normal location as a function of y_e for both the uniform and elliptic distributions. Substituting equation C.0.6 into equation 3.4.3 and performing a curve fit to the measured values of U and y_e to compute m and y_d will result in a system of nonlinear equations that must be iteratively solved. The solution of which is not guaranteed however, as the Jacobian matrix quickly becomes singular using a Newton nonlinear algorithm to solve

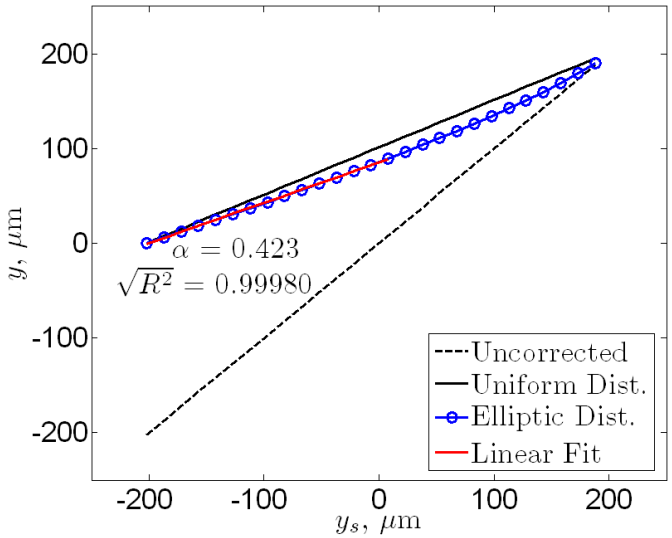

Figure C.2: Effect of measurement volume truncation on true wall-normal location

the system. However, as seen in figure C.2, most of the near wall points are a near linear function of y_e. A linear fit to these points results in a value for α of 0.423 in equation C.0.3.

For the profile examined in section 3.4.2, both values of α were used to estimate the friction velocity ($u_\tau = \sqrt{\nu m}$). The results from section 2.1.2 were used to estimate a value for a. The uniform distribution agreed closely with the friction velocity computed from the Reynolds shear stress and the simple fit method. However, the elliptic distribution with linear fit near the wall resulted in an estimate that was high by about 10%. A possible explanation for this is that the receiving volume is much smaller than the intersection volumes of the laser beams and 'sees' a light intensity field that is more uniformly distributed than elliptic.

Bibliography

[1] S. Glegg and W. Devenport, "The far-field sound from rough-wall boundary layers," *Proceedings of the Royal Society A*, vol. 465, pp. 1717–1734, 4 March 2009.

[2] B. S. Smith, W. N. Alexander, W. Devenport, S. A. L. Glegg, and D. L. Grissom, "The Relationship Between Roughness Noise and the Near-Field Pressure Spectrum," in *14th AIAA/CEAS Aeroacoustic Conference*, (Vancouver, British Columbia Canada), AIAA-2008-2904, 5-7 May 2008.

[3] R. L. Simpson and Y. T. Chew, "Measurements in Steady and Unsteady Separated Turbulent Boundary Layers," in *Laser Velocimetry and Particle Sizing* (H. D. Thompson and W. H. Stevenson, eds.), pp. 179–196, 1979.

[4] J. P. Bons, R. P. Taylor, S. T. McClain, and R. B. Rivir, "The Many Faces of Turbine Surface Roughness," *Journal of Turbomachinery*, vol. 123, pp. 739–748, October 2001.

[5] B. D. Matheis and A. P. Rothmayer, "Impact of Surface Roughness on Local Aerodynamics Using a Three-Dimensional Navier-Stokes Solver," in *42nd AIAA Aerospace Sciences Meeting and Exhibit*, (Reno, Nevada), AIAA-2004-58, 5-8 January 2004.

[6] J. Nikuradse, "Strmungsgesetze in rauhen Rohren," *VDI-Forschchungsheft*, vol. 361, 1933. English translation, "Laws of flow in rough pipes," NACA TM 1292, 1950.

[7] R. L. Townsin, D. Byrne, T. E. Svensen, and A. Milne, "Estimating the Technical and Economic Penalties of Hull and Propeller Roughness," *Transactions of the Society of Naval Architects and Marine Engineers*, vol. 89, p. 295, 1981.

[8] H. Darcy, "Recherches experimentales relatives au mouvement de l'eau dans les tuyaux," *Mem. Savants etrangers*, vol. 15, p. 141, 1858.

[9] C. S. Subramanian, T. M. Ostrem, and S. N. Gangadharan, "Noncontact Measurement of Marine Biofouling Roughness," *Marine Technology*, vol. 41, pp. 67–73, April 2004.

[10] J. Counihan, "Adiabatic atmospheric boundary layers: A review and analysis of data from the period 1880-1972," *Atmospheric Environment*, vol. 9, pp. 871–905, October 1975.

[11] H. Cheng and I. P. Castro, "Near wall flow over urban-like roughness," *Boundary-Layer Meteorology*, vol. 104, pp. 229–259, August 2002.

[12] D. W. Bechert, M. Bruse, W. Hage, J. G. T. Van Der Hoeven, and G. Hoppe, "Experiments on drag-reducing surfaces and their optimization with an adjustable geometry," *Journal of Fluid Mechanics*, vol. 338, pp. 59–87, 1997.

[13] V. C. Patel, "Perspective: Flow at High Reynolds Number and Over Rough Surfaces - Achilles Heel of CFD," *Journal of Fluids Engineering*, vol. 120, pp. 434–444, September 1998.

[14] F. R. Hama, "Boundary-Layer Characteristics for Smooth and Rough Surfaces," in *Transactions of the Society of Navel Architects and Marine Engineers*, vol. 62, pp. 333–358, 1954.

[15] J. Jimnez, "Turbulent Flows over Rough Walls," *Annual Review of Fluid Mechanics*, vol. 36, pp. 173–196, 2004.

[16] J. George, *Structure of 2-D and 3-D Turbulent Boundary Layers with Sparsely Distributed Roughness Elements*. PhD thesis, Virginia Polytechnic Institute and State University, 2005.

[17] J. L. Bennington, "Effects of Various Shaped Roughness Elements in Two-Dimensional High Reynolds Number Turbulent Boundary Layers," Master's thesis, Virginia Polytechnic Institute and State University, 24 August 2004.

[18] A. E. Perry, W. H. Schofield, and P. N. Joubert, "Rough wall turbulent boundary layers," *Journal of Fluid Mechanics*, vol. 37, no. 2, pp. 383–413, 1969.

[19] P. R. Bandyopadhyay and R. D. Watson, "Structure of rough-wall turbulent boundary layers," *Physics of Fluids*, vol. 31, pp. 1877–1883, July 1988.

[20] L. Prandtl, "Recent Results of Turbulence Research," TM 720, NACA TM 720, 1933.

[21] F. H. Clauser, "Turbulent Boundary Layers in Adverse Pressure Gradients," *Journal of the Aeronautical Sciences*, vol. 21, pp. 91–108, February 1954.

[22] R. A. Antonia and P.-. Krogstad, "Turbulence structure in boundary layers over different types of surface roughness," *Fluid Dynamics Research*, vol. 28, pp. 139–157, February 2001.

[23] S. Leonardi, P. Orlandi, R. J. Smalley, L. Djenidi, and R. A. Antonia, "Direct numerical simulations of turbulent channel flow with transverse square bars on one wall," *Journal of Fluid Mechanics*, vol. 491, pp. 229–238, 2003.

[24] W. L. Moore, *An Experimental Investigation of the Boundary-Layer Development Along a Rough Surface*. PhD thesis, University of Iowa, August 1951.

[25] C. D. Tomkins, *The Structure of Turbulence Over Smooth and Rough Walls*. PhD thesis, University of Illinois at Urbana-Champaign, 2001.

[26] R. L. Simpson, "Characteristics of turbulent boundary layers at low Reynolds numbers with and without transpiration," *Journal of Fluid Mechanics*, vol. 42, no. 4, pp. 769–802, 1970.

[27] A. A. Townsend, *The Structure of Turbulent Shear Flow*. Cambridge University Press, 1976.

[28] A. E. Perry and C. J. Abell, "Asymptotic similarity of turbulence structures in smooth- and rough-walled pipes," *Journal of Fluid Mechanics*, vol. 79, p. 785, 1977.

[29] A. Ashrafian and H. I. Andersson, "The structure of turbulence in a rod-roughened channel," *International Journal of Heat and Fluid Flow*, vol. 27, pp. 65–79, 2006.

[30] G. J. Kunkel, J. Allen, James, and J. Smits, Alexander, "Further support for Townsends Reynolds number similarity hypothesis in high reynolds number rough-wall pipe flow," *Physics of Fluids*, vol. 19, 2007.

[31] S. Nakagawa, Y. Na, and T. J. Hanratty, "Influence of a wavy boundary on turbulence. i. highly rough surface," *Experiments in Fluids*, vol. 35, pp. 422–436, 2003.

[32] R. A. Antonia, "The Effect of Different Types of Surface Conditions on a Turbulent Boundary Layer," in *1st International Conference on Flow Interaction*, (Hong Kong), 5-9 September 1994.

[33] D. J. Bergstrom, O. G. Akinlade, and M. F. Tachie, "Skin Friction Correlation for Smooth and Rough Wall Turbulent Boundary Layers," *Transactions of ASME*, vol. 127, pp. 1146–1153, November 2005.

[34] L. Keirsbulck, A. Mazouz, L. Labrago, and C. Tournier, "Influence of the surface roughness on the third-order moments of velocity fluctuations," *Experiments in Fluids*, vol. 30, pp. 592–594, 2001.

[35] P. . Krogstad and R. A. Antonia, "Structure of turbulent boundary layers on smooth and rough walls," *Journal of Fluid Mechanics*, vol. 277, p. 1, 1994.

[36] D. Poggi, A. Porporato, and L. Ridolfi, "Analysis of the small-scale structure of turbulence on smooth and rough walls," *Physics of Fluids*, vol. 15, pp. 35–46, January 2003.

[37] O. M. Bakken, p.-A. Krogstad, A. Ashrafian, and H. I. Andersson, "Reynolds number effects in the outer layer of the turbulent flow in a channel with rough walls," *Physics of Fluids*, vol. 17, 2005.

[38] L. F. Moody, "Friction factors for pipe flow," *Transactions of ASME*, vol. 66, pp. 671–684, 1944.

[39] H. Schlichting, "Experimental investigation of the problem of surface roughness," TM 823, NACA TM 823, 1937.

[40] D. Bettermann, "Contribution a l'etude de la couche limite turbulente de long de plaques rugueuses," Tech. Rep. 65-6, Centre National de la Recherche Scientifique, Paris, France, 1965.

[41] F. A. Dvorak, "Calculation of Turbulent Boundary Layers on Rough Surfaces in Pressure Gradient," *AIAA Journal*, vol. 7, no. 9, pp. 1752–1759, 1969.

[42] D. R. Waigh and R. J. Kind, "Improved Aerodynamic Characterization of Regular Three-Dimensional Roughness," *AIAA Journal*, vol. 36, no. 6, pp. 1117–1119, 1998.

[43] R. L. Simpson, "A Generalized Correlation of Roughness Density Effects on Turbulent Boundary Layer," *AIAA Journal*, vol. 11, no. 2, pp. 242–244, 1973.

[44] P. S. Jackson, "On the displacement height in the logarithmic velocity profile," *Journal of Fluid Mechanics*, vol. 111, pp. 15–25, 1981.

[45] D. O. Stewart, "Effects of Spacing and Geometry of Distributed Roughness Elements on a Two-Dimensional Turbulent Boundary Layer," Master's thesis, Virginia Polytechnic Institute and State University, 2005.

[46] C. F. Colebrook and C. M. White, "Experiments with Fluid Friction in Roughened Pipes," *Proceedings of the Royal Society London A*, vol. 161, pp. 367–381, 3 August 1937.

[47] P.-. Krogstad, H. I. Andersson, O. M. Bakken, and A. Ashrafian, "An experimental and numerical study of channel flow with rough walls," *Journal of Fluid Mechanics*, vol. 530, pp. 327–352, 2005.

[48] R. L. Webb, E. R. G. Eckert, and R. J. Goldstein, "Heat Transfer and Friction in Tubes with Repeated-Rib Roughness," *International Journal of Heat and Mass Transfer*, vol. 14, pp. 601–617, April 1971.

[49] M. Acharya, J. Bornstein, and M. P. Escudier, "Turbulent boundary layers on rough surfaces," *Experiments in Fluids*, vol. 4, pp. 33–47, 1986.

[50] P. R. Bandyopadhyay, "Rough-wall turbulent boundary layers in the transition regime," *Journal of Fluid Mechanics*, vol. 180, pp. 231–266, July 1987.

[51] D. W. Bechert, M. Bruse, and W. Hage, "Experiments with three-dimensional riblets as an idealized model of shark skin," *Experiments in Fluids*, vol. 28, pp. 403–412, May 2000.

[52] F. Pineau, V. D. Nguyen, J. Dickinson, and J. Belanger, "Study of Flow Over a Rough Surface With Passive Boundary Layer Manipulators and Direct Wall Drag Measurements," in *AIAA 25th Aerospace Sciences Meeting*, (Reno, Nevada), AIAA, 12-15 January 1987.

[53] J. A. Schetz and B. Nerney, "Turbulent Boundary Layer with Injection and Surface Roughness," *AIAA Journal*, vol. 15, pp. 1288–1294, September 1977.

[54] R. A. Antonia and R. E. Luxton, "The response of a turbulent boundary layer to a step change in surface roughness Part 1. Smooth to rough," *Journal of Fluid Mechanics*, vol. 48, no. 4, pp. 721–761, 1971.

[55] B. E. Lee and B. F. Soliman, "An Investigation of the Forces on Three Dimensional Bluff Bodies in Rough Wall Turbulent Boundary Layers," *Journal of Fluids Engineering*, vol. 99, pp. 503–510, September 1977.

[56] B. G. Brzek, R. B. Cal, G. Johansson, and L. Castillo, "Near Wall Measurements in Smooth/Rough Turbulent Boundary Layers," in *45th AIAA Aerospace Sciences Meeting*, (Reno, Nevada), AIAA-2007-531, 8-11 January 2007.

[57] P. . Krogstad, R. A. Antonia, and L. W. B. Browne, "Comparison between rough- and smooth-wall turbulent boundary layers," *Journal of Fluid Mechanics*, vol. 245, pp. 599–617, 1992.

[58] M. C. Goody and R. L. Simpson, "Surface Pressure Fluctuations Beneath Two- and Three-Dimensional Turbulent Boundary Layers," *AIAA Journal*, vol. 38, pp. 1822–1830, October 2000.

[59] W. K. Blake, "Turbulent boundary-layer wall-pressure fluctuations on smooth and rough walls," *Journal of Fluid Mechanics*, vol. 44, no. 4, pp. 637–660, 1970.

[60] F. A. Aupperle and R. F. Lambert, "Effect of Roughness on Measured Wall-Pressure Fluctuations beneath a Turbulent Boundary Layer," *Journal of the Acoustical Society of America*, vol. 47, no. 1, pp. 359–370, 1970.

[61] B. Smith, *Wall Jet Boundary Layer Flows Over Smooth and Rough Surfaces*. PhD thesis, Virginia Polytechnic Institute and State University, April 2008.

[62] W. N. Alexander, "Normalization of Roughness Noise on the Near-Field Wall Pressure Spectrum," Master's thesis, Virginia Polytechnic Institute and State University, 2009.

[63] J. George and R. L. Simpson, "Some effects of sparsely distributed three-dimensional roughness elements on two-dimensional turbulent boundary layers," in *38th AIAA Aerospace Sciences Meeting and Exhibit*, no. 2000-0915, (Reno, NV), AIAA-2000-915, 10-13 January 2000.

[64] G.-K. Kerevanian, A. Sidorenko, E. Benard, R. K. Cooper, S. R. Raghunathan, F. Saeed, I. Paraschivoiu, and F. Kafyeki, "Effect of Height and Density of Roughness Elements on Turbulent Boundaries Layers," in *41st AIAA Aerospace Sciences Meeting and Exhibit*, (Reno, NV), AIAA-2003-645, 6-9 January 2003.

[65] P. C. Miles, "Geometry of the fringe field formed in the intersection of two Gaussian beams," *Applied Optics*, vol. 35, pp. 5887–5895, 20 October 1996.

[66] B. Lehmann, H. Nobach, and C. Tropea, "Measurement of acceleration using the laser Doppler technique," *Measurement Science and Technology*, vol. 13, pp. 1367–1381, July 2002.

[67] H.-E. Albrecht, M. Borys, N. Damaschke, and C. Tropea, *Laser Doppler and Phase Doppler Measurement Techniques*. Experiemental Fluid Mechanics, Springer, 2003.

[68] H.-E. Albrecht, M. Borys, N. Damaschke, and C. Tropea, "The imaging properties of scattering particles in laser beams," *Measurement Science and Technology*, vol. 10, pp. 564–574, 1999.

[69] S. M. lmen and R. L. Simpson, "A five-velocity-component laser-doppler velocimeter for measurements of a three-dimensional turbulent boundary layer," *Measurement Science and Technology*, vol. 6, pp. 702–716, June 1995.

[70] K. T. Lowe and R. L. Simpson, "An advanced laser-Doppler velocimeter for full-vector particle position and velocity measurements," *Measurement Science and Technology*, vol. 20, April 2009.

[71] K. T. Lowe, *Design and application of a novel Laser Doppler Velocimeter for turbulence structural measurements in turbulent boundary layers*. PhD thesis, Virginia Polytechnic Institute, 2006.

[72] B. Liu, K. Whitby, and H. Yu, "A Condensation Aerosol Generator for Producing Monodispersed Aerosols in the Size Range, 0.036μ to 1.3μ," *Journal de Recherches Atmosphriques*, vol. 2, pp. 397–406, 1966.

[73] K. A. Shinpaugh, R. L. Simpson, A. L. Wicks, S. M. Ha, and J. L. Fleming, "Signal-processing techniques for low signal-to-noise ratio laser Doppler velocimetry signals," *Experiments in Fluids*, vol. 12, pp. 319–328, 1992.

[74] R. L. Simpson, M. Ghodbane, and B. E. McGrath, "Surface pressure fluctuations in a separating turbulent boundary layer," *Journal of Fluid Mechanics*, vol. 177, pp. 167–186, 1987.

[75] M. C. Goody, *An Experimental Investigation of Pressure Fluctuations in Three-Dimensional Turbulent Boundary Layers*. PhD thesis, Virginia Polytechnic Institute and State University, 1999.

[76] N. K. Agarwal and R. L. Simpson, "A new technique for obtaining the turbulent pressure spectrum from the surface pressure spectrum," *Journal of Sound and Vibration*, vol. 135, no. 2, pp. 346–350, 1989.

[77] M. P. Schultz and K. A. Flack, "Outer layer similarity in fully rough turbulent boundary layers," *Experiments in Fluids*, vol. 38, pp. 328–340, 2005.

[78] T. Ikeda and P. A. Durbin, "Direct simulations of a rough-wall channel flow," *Journal of Fluid Mechanics*, vol. 571, pp. 235–263, 2007.

[79] P. Bradshaw, "'Inactive' motion and pressure fluctuations in turbulent boundary layers," *Journal of Fluid Mechanics*, vol. 30, pp. 211–258, 2 1967.

[80] M. Goody, "Empirical Spectral Model of Surface Pressure Fluctuations," *AIAA Journal*, vol. 42, pp. 1788–1794, September 2004.

[81] O. G. Akinlade, D. J. Bergstrom, M. F. Tachie, and L. Castillo, "Outer flow scaling of smooth and rough wall turbulent boundary layers," *Experiments in Fluids*, vol. 37, pp. 604–612, October 2004.

[82] J. Andreopoulos and P. Bradshaw, "Measurements of Tubulence Structure in the Boundary Layer on a Rough Surface," *Boundary-Layer Meteorology*, vol. 20, pp. 201–213, 1981.

[83] D. J. Bergstrom, N. A. Kotey, and M. F. Tachie, "The Effects of Surface Roughness on the Mean Velocity Profile in a Turbulent Boundary Layer," *Journal of Fluids Engineering*, vol. 124, pp. 664–670, September 2002.

[84] D. Bettermann, "Contribution a l'Etude de la Convection Forcee Turbulente le Long de Plaques Rugueses," *International Journal of Heat and Mass Transfer*, vol. 9, pp. 153–164, 1966.

[85] L. Djenidi, R. Elavarasan, and R. A. Antonia, "The turbulent boundary layer over transverse square cavities," *Journal of Fluid Mechanics*, vol. 395, p. 271, 1999.

[86] K. A. Flack, M. P. Schultz, and T. A. Shapiro, "Experimental support for Townsend's Reynolds number similarity hypothesis on rough walls," *Physics of Fluids*, vol. 17, 2005.

[87] Y. Furuya and H. Fujita, "Turbulent Boundary Layers on Wire-Screen Roughnesses," *Bulletin of the Japanese Society of Mechanical Engineers*, vol. 10, no. 37, pp. 77–86, 1967.

[88] Y. Furuya, M. Miyata, and H. Fujita, "Turbulent Boundary Layer and Flow Resistance on Plates Roughened by Wires," in *Gas Turbine and Fluids Engineering Conference*, (New Orleans, La.), ASME, 21-25 March 1976.

[89] I. S. Gartshore and K. A. De Croos, "Roughness Element Geometry Required for Wind Tunnel Simulations of the Atmospheric Wind," in *Transactions of the ASME*, pp. 480–485, The American Society of Mechanical Engineers, September 1977.

[90] J. George and L. Simpson, Roger, "Some Three-Dimensional Rough-Wall Turbulent Boundary Layers," in *40th AIAA Aerospace Sciences Meeting and Exhibit*, no. 2002-0580, (Reno, NV), AIAA-2002-580, 14-17 January 2002.

[91] A. J. Grass, "Structural features of turbulent flow over smooth and rough boundaries," *Journal of Fluid Mechanics*, vol. 50, no. 2, pp. 233–255, 1971.

[92] M. H. Hosni, H. W. Coleman, and R. P. Taylor, "Measurement and Calculation of Fluid Dynamic Characteristics of Rough-Wall Turbulent Boundary-Layer Flows," *Journal of Fluids Engineering*, vol. 115, pp. 383–388, September 1993.

[93] L. Keirsbulck, L. Labraga, A. Mazouz, and C. Tournier, "Surface Roughness Effects on Turbulent Boundary Layer Structures," *Journal of Fluids Engineering*, vol. 124, p. 127, March 2002.

[94] N. A. Kotay, D. J. Bergstrom, and M. F. Tachie, "Power laws for rough wall turbulent boundary layers," *Physics of Fluids*, vol. 15, pp. 1396–1404, June 2003.

[95] P.-. Krogstad and R. A. Antonia, "Surface roughness effects in turbulent boundary layers," *Experiments in Fluids*, vol. 27, pp. 450–460, 1999.

[96] W. Li, R. K. Decker, J. W. Lew, and W. Naughton, Jonathan, "Characteristics of Turbulent Boundary Layers on Rough Surfaces with Favorable Pressure Gradients," in *31st AIAA Fluid Dynamics Conference*, (Anaheim, CA), AIAA-2001-2915, 11-14 June 2001.

[97] P. M. Ligrani and R. J. Moffat, "Structure of transitionally rough and fully rough turbulent boundary layers," *Journal of Fluid Mechanics*, vol. 162, p. 69, 1986.

[98] J. K. Marshall, "Drag measurements in roughness arrays of varying density and distribution," *Agricultural Meteorology*, vol. 8, pp. 269–292, 1971.

[99] N. P. Mikhailova, E. U. Repik, and Y. P. Sosedko, "Permissible Height of the Surface Roughness in a Turbulent Boundary Layer with a Streamwise Pressure Gradient," *Fluid Dynamics*, vol. 38, no. 1, pp. 32–42, 2003.

[100] S. Nakagawa and J. Hanratty, Thomas, "Particle image velocimetry measurements of flow over a wavy wall," *Physics of Fluids*, vol. 13, pp. 3504–3507, November 2001.

[101] A. E. Perry and P. N. Joubert, "Rough-wall boundary layers in adverse pressure gradients," *Journal of Fluid Mechanics*, vol. 17, pp. 193–211, 1963.

[102] A. E. Perry and J. D. Li, "Experimental support for the attached-eddy hypothesis in zero-pressure-gradient turbulent boundary layers," *Journal of Fluid Mechanics*, vol. 218, pp. 405–438, September 1990.

[103] A. E. Perry, K. L. Lim, and S. M. Henbest, "An experimental study of the turbulence structure in smooth- and rough-wall boundary layers," *Journal of Fluid Mechanics*, vol. 177, pp. 437–466, April 1987.

[104] M. R. Raupach, A. S. Thom, and I. Edwards, "A wind-tunnel study of turbulent flow close to regularly arrayed rough surfaces," *Boundary-Layer Meteorology*, vol. 18, pp. 373–397, June 1980.

[105] J. A. van Rij, B. J. Belnap, and P. M. Ligrani, "Analysis and Experiments on Three-Dimensional, Irregular Surface Roughness," *Journal of Fluids Engineering*, vol. 124, pp. 671–677, September 2002.

[106] M. P. Schultz, "Turbulent Boundary Layers on Surfaces Covered With Filamentous Algae," *Journal of Fluids Engineering*, vol. 122, pp. 357–363, June 2000.

[107] M. P. Schultz and K. A. Flack, "Turbulent Boundary Layers Over Surfaces Smoothed by Sanding," *Journal of Fluids Engineering*, vol. 125, pp. 863–870, September 2003.

[108] L. Sirovich and S. Karlsson, "Turbulent drag reduction by passive mechanisms," *Nature*, vol. 388, pp. 753–755, 21 August 1997.

[109] R. J. Smalley, R. A. Antonia, and L. Djenidi, "Self-preservation of rough-wall turbulent boundary layers," *European Journal of Fluid Mechanics B - Fluids*, vol. 20, pp. 591–602, 2001.

[110] C. S. Subramanian, P. I. King, M. F. Reeder, S. Ou, and R. B. Rivir, "Effects of Strong Irregular Roughness on the Turbulent Boundary Layer," *Flow, Turbulence, and Combustion*, vol. 72, pp. 349–368, 2004.

[111] M. F. Tachie, D. J. Bergstrom, and R. Balachandar, "Rough Wall Turbulent Boundary Layers in Shallow Open Channel Flow," *Journal of Fluids Engineering*, vol. 122, pp. 533–541, September 2000.

[112] Y. Tsuji, "Large-scale anisotropy effect on small-scale statistics over rough wall turbulent boundary layers," *Physics of Fluids*, vol. 15, pp. 3816–3828, December 2003.

[113] T. Pfister, L. Bttner, and J. Czarske, "Laser Doppler sensor employing a single fan-shaped interface fringe system for distance and shape measurement of laterally moving objects," *Applied Optics*, vol. 48, pp. 140–154, 1 January 2009.

[114] T. Pfister, L. Bttner, and J. Czarske, "Laser Doppler profile sensor with submicrometre position resolution for velocity and absolute radius measurements of rotating objects," *Measurement Science and Technology*, vol. 16, pp. 627–641, 31 January 2005.

[115] K. Shirai, T. Pfister, L. Bttner, J. Czarske, H. Mller, S. Becker, H. Lienhart, and F. Durst, "Highly spatially resolved velocity measurements of a turbulent channel flow by a fiber-optic heterodyne laser-Doppler velocity-profile sensor," *Experiments in Fluids*, vol. 40, pp. 473–481, March 2006.

[116] L. Bttner and J. Czarske, "Determination of the axial velocity component by a laser-Doppler velocity profile sensor," *Journal of the Optical Society of America A*, vol. 23, pp. 444–454, February 2006.

[117] L. Bttner and J. Czarske, "Spatial resolving laser Doppler velocity sensor using slightly tilted fringe systems and phase evaluation," *Measurement Science and Technology*, vol. 14, pp. 2111–2120, 9 October 2003.

[118] L. Bttner and J. Czarske, "A multmode-fibre laser-doppler anemometer for highly spatially resolved velocity measurements using low-coherence light," *Measurement Science and Technology*, vol. 12, pp. 1891–1903, 9 October 2001.

[119] J. Czarske, L. Büttner, T. Razik, and H. Müller, "Boundary layer velocity measurements by a laser Doppler profile sensor with micrometre spatial resolution," *Measurement Science and Technology*, vol. 13, pp. 1979–1989, November 2002.

[120] J. Czarske, "Laser Doppler velocity profile sensor using a chromatic coding," *Measurement Science and Technology*, vol. 12, no. 1, pp. 52–57, 2001.

[121] A. M. R. Hopkins, *Fluid Dynamics and Surface Pressure Fluctuations of Turbulent Boundary Layers Over Densely Distributed Roughness*. PhD thesis, Virginia Polytechnic Institute and State University, 2010.

[122] A. V. Oppenheim and R. W. Schafer, *Discrete-Time Signal Processing*. Prentice-Hall, 1989.

[123] P. B. Coates, "Photomultiplier noise statistics," *Journal of Physics D: Applied Physics*, vol. 5, pp. 915–930, May 1972.

[124] L. H. J. Absil, *Analysis of the Laser Doppler Measurement Technique for Application in Turbulent Flows*. PhD thesis, Technische Universiteit Delft, 1995.